Des otolithes aux satellites : méthodes et applications du traitement du signal et des images pour l'observation de l'océan

Ronan Fablet

▶ **To cite this version:**

Ronan Fablet. Des otolithes aux satellites : méthodes et applications du traitement du signal et des images pour l'observation de l'océan. Traitement du signal et de l'image [eess.SP]. Université de bretagne occidentale, 2012. tel-00693172

HAL Id: tel-00693172
https://theses.hal.science/tel-00693172

Submitted on 2 May 2012

HAL is a multi-disciplinary open access archive for the deposit and dissemination of scientific research documents, whether they are published or not. The documents may come from teaching and research institutions in France or abroad, or from public or private research centers.

L'archive ouverte pluridisciplinaire **HAL**, est destinée au dépôt et à la diffusion de documents scientifiques de niveau recherche, publiés ou non, émanant des établissements d'enseignement et de recherche français ou étrangers, des laboratoires publics ou privés.

Des otolithes aux satellites : méthodes et applications du traitement du signal et des images pour l'observation de l'océan.

Mémoire présenté pour obtenir

l'Habilitation à Diriger des Recherches

par

Ronan Fablet
Maître de Conférence Institut Télécom/Telecom Bretagne
LabSTICC (UMR CNRS-Télécom Bretagne-UBO-UBS)

Jury:
Jean-Marc Boucher
Patrick Bouthemy
Gilles Burel - rapporteur
Jean-Marc Fromentin - rapporteur
Alain Hillion
Frédéric Jurie - rapporteur
Josiane Zerubia - rapporteur

Mars 2012

Résumé

Ce document présente une synthèse des activités de recherche menées depuis une dizaine d'années en premier lieu dans le cadre du Laboratoire Ifremer-IRD de Sclérochronologie des Animaux Aquatiques et du département Sciences et Technologies Halieutiques de l'Ifremer puis au sein du département Signal & Communications de Telecom Bretagne et du Laboratoire en Sciences et Techniques de l'Information, de la Communication et de la Connaissance.

De manière générale, ces activités se situent à l'interface des STIC[1] et de l'océanographie. Dans le cadre d'approches interdisciplinaires, ces travaux ont visé à exploiter et développer des outils et méthodes de traitement du signal et des images pour (i) fournir de nouvelles représentations des processus/scènes observés, (ii) exploiter ces représentations pour inférer ou reconstruire des informations d'intérêt du point de vue thématique. Trois domaines thématiques relevant de la télédétection de l'océan au sens large ont été privilégiés : initialement, les otolithes comme marqueurs des traits de vie individuels des poissons et la télédétection acoustique des fonds marins et de l'écosystème pélagique, et plus récemment la télédétection satellitaire de la surface de l'océan. Ces problématiques conduisent notamment à aborder différentes problématiques génériques du traitement du signal et des images telles que l'analyse de la géométrie de signaux multivariés (y compris des formes), l'analyse et la reconnaissance de textures, l'interpolation de données manquantes, la reconnaissance de scènes et d'objets à travers différents cadres méthodologiques (modèles probabilistes, inférence bayésienne, approches variationnelles, apprentissage statistique,...).

A partir de cette expertise est envisagé le potentiel, encore largement inexploré, d'une exploration des bases d'observations multi-échelles et multi-modales de l'océan, pour la caractérisation et la modélisation des processus clés déterminant les dynamiques des écosystèmes marins. Cette analyse met en évidence les enjeux réels du traitement de l'information dans ce contexte thématique et permet de dégager des problématiques scientifiques que l'on cherchera à développer dans les prochaines années.

Mots-clés : modèles probabilistes et variationnels des signaux et des images, géométrie des signaux et des images, analyse de texture, classification et segmentation, applications à l'écologie marine et à l'océanographie incluant la sclérochronologie, la télédétection acoustique des fonds marins et de l'écosystème pélagique et la télédétection spatiale de la surface de l'océan.

[1] STIC: Sciences et technologies de l'information et de la communication

Abstract

This document presents a synthesis of my research activities over the last 10 years initially within the Ifremer-IRD schlerochronology laboratory and the Fisheries Science and Technology department at Ifremer, and then at the Signal & Communication Department of Telecom Bretagne.
My research activities were undertaken at the interface of Information Science and Technology and Oceanography. In the framework of interdisciplinary approaches, my research work addressed the development of new image and signal processing tools and methods with a view to (1) providing new representations of the obsvered scenes or processes, (2) exploiting these representations to infer or reconstruct patterns of interest for the considered thematic objectives. Three thematic issues were addressed in the field of the remote sensing of the ocean (in a broad sense): initially the otoliths as recorders of the individual life traits of fish and the acoustic sensing of the seabed and of the pelagic ecosystem, and more recently the satellite-based remote sensing of the ocean surface. This research involved generic methodological developments in the field of information processing and pattern recognition such as the analysis of the geometry of multivariate signals (including shape analysis), texture analysis and recognition, missing data interpolation, object and scene reocgnition using various methodological frameworks (probabilistic models, Bayesian and variational inference, statistical learning,...).
From this expertise I wish to explore the potential, widely unexplored, of the existing databases of multimodal and multiscale observations of the ocean for the characterization and the modelling of the dynamics of marine ecosystems. These thematic issues involve key information processing challenges which will be at the core of the multidisciplinary research I will undertake in the coming years.

Keywords : probabilistic and variational signal and image models, signal and image geometry, texture analysis, classification and segmentation issus, applications to marine ecology and physical oceanography including fish otolith research, acoustic seabed and pelagic ecosystem sensing, satellite ocean surface sensing

Table des matières

Avant-propos **11**

Remerciements **11**

I Introduction : observation de l'océan et traitement de l'information **13**

II Les otolithes comme archives individuelles des comportements et réponses individuelles des poissons **15**
II.1 Extraction d'informations géométriques dans les images d'otolithes **16**
II.1.1 Extraction d'informations géométriques élémentaires dans les images d'otolithes 17
II.1.2 Reconstruction de la morphogenèse de l'otolithe à partir d'une image 20
II.2 Modélisation de la formation des otolithes **22**
II.2.1 Approche expérimentale pour la compréhension des mécanismes de la biominéralisation de l'otolithe 22
II.2.2 Modèle conceptuel et numérique de la formation de l'otolithe 24
II.3 Méthodes et outils de reconstruction de traits de vie individuels **27**
II.3.1 Collecte et qualité des données individuelles d'âge et de croissance des poissons 27
II.3.2 Méthodes robustes d'analyse quantitative de signaux extraits des otolithes 28
II.4 Synthèse **31**
II.5 Sélection de publications représentatives de ce chapitre **31**

III Méthodes d'imagerie sonar pour l'observation des écosystèmes marins **67**
III.1 Classification et segmentation des textures sonar pour l'aide à la cartographie des fonds marins **68**
III.1.1 Caractérisation et reconnaissance des textures sonar 70
III.1.2 Segmentation basée texture pour la cartographie sonar des fonds marins 72
III.2 Méthodes d'analyse de l'imagerie sonar de la colonne d'eau **74**
III.2.1 Apprentissage de modèle de classification des cibles biologiques 75
III.2.2 Méthode d'analyse globale des échogrammes sonar de la colonne d'eau 77
III.3 Synthèse **78**
III.4 Sélection de publications représentatives de ce chapitre **79**

IV Exploitation des bases d'observation de l'océan : quels outils de traitement de l'information pour l'aide à la caractérisation et la modélisation des dynamiques des écosystèmes marins ? **121**
IV.1 Tera-octets de données d'observation de l'océan : quel potentiel ? Quels enjeux et quels outils nécessaires ? **121**
IV.2 Analyse et modélisation de la structuration géométrique multi-échelle de signaux multivariés **124**
IV.3 Super-résolution spatio-temporelle de champs géophysiques à partir de données multi-modales d'observation de l'océan **127**
IV.4 Stratégie de fouille dans les bases d'observation de l'océan **129**
IV.5 Valorisation des travaux et insertion locale **131**

V Bibliographie **132**

ANNEXES **141**

A Curriculum vitae **143**

B Activités d'enseignement **144**

C Activités d'encadrement de la recherche **145**

D Activités d'administration de la recherche **149**

E Production et valorisation scientifique **151**

F Acronymes **159**

Liste des Figures

Figure 1. L'otolithe comme archive individuelle de la vie des poissons et de leur environnement 15
Figure 2. Illustration du principe des contours subjectifs (ici, le triangle blanc) 17
Figure 3. Illustration de l'ambiguïté de l'interpolation de données angulaires. 18
Figure 4. Interpolation AMLE d'orientations pour l'image Lena. 19
Figure 5. Interpolation AMLE d'orientation pour une image d'otolithe 19
Figure 6. Reconstruction de la morphogénèse de l'otolithe 20
Figure 7. Application de la reconstruction de la morphogenèse de l'otolithe à l'extraction de structures géométriques dans les images d'otolithe 21
Figure 8. Analyse d'un otolithe en microspectrométrie Raman. 23
Figure 9. Modèle de formation de l'otolithe. 25
Figure 10. Comparaison de données d'opacité de l'otolithe de morues élevées suivant deux types de conditions d'alimentation et de temperature à des simulations du modèle DEB-otolithe 26
Figure 11. Comparaison d'images d'otolithes réels et virtuels représentatifs de deux stocks de morue (mer du nord et mer de Barents) 26
Figure 12. Estimation conjointe de l'âge et de la croissance de l'otolithe. 27
Figure 13. Evaluation quantitative du critère proposé sur la base de formes MPEG-7, en termes de performances de reconnaissance et indexation, et aux méthodes de l'état de l'art 29
Figure 14. Analyse des séquences migratoires des anguilles en Gironde 30
Figure 15. Schéma de principe de la formation d'image acoustique des fonds marins par des émissions/réceptions d'un sondeur de fond multifaiscaeaux 67
Figure 16. Illustration du principe de la construction d'une cartographie des fonds marins lors d'une campagne acoustique sonar 68
Figure 17. Illustration de la diversité des textures sonar associées à différents types de fonds marins 69
Figure 18. Distorsions de contraste et de géométrie observées dans les images acoustiques des fonds marins acquises par des sondeurs multi-faisceaux 70
Figure 19. Caractérisation de textures sonar à partir des caractéristiques des distributions de points d'intérêt 70
Figure 20. Illustration de l'intérêt de la caractérisation conjointe des caractéristiques visuelles et spatiales des distributions de points d'intérêt 72
Figure 21. Evaluation quantitative de différents méthodes de segmentation sur des mosaïques de textures correspondant à différents niveaux de complexité 73
Figure 22. Comparaison des segmentations de texture par des approches markoviennes et variationnelles pour l'image B2 74
Figure 23. Exemple d'imagerie sonar de la colonne d'eau acquise par des échosondeurs à 18KHz et 200Hz 75
Figure 24. Principe de l'apprentissage faiblement supervisé itératif 77
Figure 25. Exemple d'application de la caractérisation de la distribution des bancs de poisson dans les échogrammes sonar à la discrimination des zones d'anchoix juéveniles et adultes le long des côtes péruviennes 78
Figure 26. Diversité des données d'observations satellitaires et in situ de l'océan 122
Figure 27. Les déformations géométriques comme marqueurs des dynamiques de différentes composantes d'un écosystème 124
Figure 28. Analyse multi-échelle des déformations géométriques le long d'une trajectoire 126
Figure 29. Observations satellitaires multi-modales de l'océan et données maquantes 127
Figure 30. Principe de l'émulation haute-résolution de champs de vent à la surface de l'océan par apprentissage statistique 128

Avant-propos

Des otolithes aux satellites. Ou plutôt des satellites aux otolithes puis des otolithes aux satellites. Lorsqu'en septembre 2002 je pose mes valises à l'Ifremer et plus particulièrement au laboratoire Ifremer-IRD de sclérochronologie des animaux aquatiques, je viens tout juste de découvrir ce que sont les otolithes, de petites concrétions calcaires de l'oreille interne des poissons, mais je n'en ai encore jamais vu et j'aurai été bien en peine d'en trouver un par moi-même. L'ingénierie aéronautique comme la vision par ordinateur préparent évidemment à beaucoup d'imprévus, mais de là à traiter des otolithes.... Me voilà donc plonger dans une matrice pluridisciplinaire pour percer les secrets de ces petits "cailloux". Dix ans plus tard dans le cadre des activités du département Signal & Communications de Telecom Bretagne et de l'équipe TOMS de l'UMR LabSTICC, ma démarche scientifique continue à se nourrir de cette matrice pluridisciplinaire et je poursuis mon exploration d'échelles d'observation de l'océan menant des otolithes aux satellites à travers un filtre "traitement de l'information". Ce document présente une synthèse de ces différentes activités de recherche ainsi que les prolongements envisagés.

Remerciements

Trugarez vras à tous ceux qui m'ont accompagné, suivi et soutenu depuis plus de 10 ans de l'IRISA à Telecom Bretagne, en passant par Brown University, le LASAA, l'Ifremer Brest, l'IMARPE et l'IRD à Lima. La liste serait trop longue pour ne pas en oublier. Merci à tous.
Je voudrais également remercier chaleureusement les membres du jury, en particulier les rapporteurs, pour leurs commentaires, analyses et suggestions.

I Introduction : observation de l'océan et traitement de l'information

L'océan un territoire encore aujourd'hui largement inexploré et inconnu. Là où les technologies spatiales permettent d'observer la plus petite parcelle de terre et de voir toujours plus loin dans l'univers, l'océan et le monde vivant sous-marin conservent bien des mystères. Plusieurs milliers de nouvelles espèces marines ont ainsi été recensés récemment dans le cadre d'un projet international (www.coml.org) mené sur une dizaine d'années, et pas nécessairement dans des milieux extrêmes, telles que les milieux profonds peu accessibles. Sait-on que l'on connaît très mal les migrations de nombreuses espèces marines? L'émergence récente des techniques de marquage-recapture et de marquage électronique a par exemple mis en évidences des migrations de plusieurs centaines de kilomètres pour des espèces telles que la beaudroie et la plie, espèces dont les caractéristiques morphologiques laissent peu penser qu'elles puissent être des lignées de grands voyageurs (Hunter, Metcalfe et al. 2003; Landa, Quincoces et al. 2008). Ces techniques de marquage électronique ont également permis des avancées significatives pour la compréhension des structures spatiales et temporelles d'espèces emblématiques telles que les thonidés (Block, Teo et al. 2005).

Des modalités de télédétection de l'océan. Ces quelques exemples pris dans le domaine de l'écologie halieutique pourraient être complétés par de nombreux autres concernant aussi bien la cartographie des fonds marins, le comportement des prédateurs supérieurs ou plus largement la connaissance des processus physiques et biogéochimiques en jeu dans l'océan et leurs interactions, etc.... Ils illustrent tous un aspect fondamental de l'étude du milieu marin et des océans, la difficulté à disposer de moyens d'observation *in situ* de la même manière que pour les milieux terrestres. L'observation *in situ* est fortement limitée par les contraintes de plongée de même que les modalités de télédétection dans la mesure où le milieu marin est un canal fortement dispersif pour les ondes électromagnétiques. L'océanographie a longtemps reposé sur l'échantillonnage *in situ* de paramètres géophysiques, biogéochimiques et/ou biologiques dans le cadre de campagnes océanographiques. C'est finalement assez récemment (depuis une trentaine d'années) qu'ont pu être développés des moyens opérationnels de télédétection de l'océan, le terme télédétection étant pris au sens large en termes de mesure à distance de paramètres de l'océan, notamment avec l'émergence de l'océanographie spatiale et le développement de l'acoustique sous-marine :

- A partir des années 80, des systèmes satellite opérationnels permettent de mesurer en continu des paramètres de l'océan (e.g., hauteur de mer, température de surface, couleur de l'eau,...) en surface ou subsurface (typiquement quelques mètres de profondeur) (Block, Teo et al. 2005). De nouveaux capteurs viennent enrichir la gamme de paramètres géophysiques qui peuvent être mesurés, comme par exemple la salinité en surface grâce à la mission européenne SMOS lancée en 2009 et la mission américaine Aquarius dont le lancement est prévu en 2012. Pour compléter ces données associées à des résolutions en général supérieures au kilomètre (à l'exception des capteurs SAR pour des paramètres géophysiques associés à la rugosité de surface), les technologies de géolocalisation et transmission par satellite ont pu être combinées au développement de bouées et profileurs dérivants (e.g., bouées ARGO) pour mesurer des paramètres géophysiques à haute résolution temporelle (de l'ordre de l'heure) le long de trajectoires (y compris des profils verticaux dans le cas des profileurs) (Gould, Roemmich et al. 2004; Gaillard, Autret et al. 2009).
- L'acoustique sous-marine permet d'accéder à une vision complémentaire sous la surface d'autres composantes des écosystèmes marins, en particulier l'écosystème pélagique (i.e., les composantes biologiques (e.g., poissons, plancton) dans la colonne d'eau) et la nature des fonds marins pour les technologies sonar. Déployés dans le cadre de campagnes océanographiques et plus récemment d'observatoires sous-marins (point fixe), les systèmes sonar (Lurton 2002; Simmonds, MacLennan 2005) permettent par exemple d'accéder à l'échelle d'un écosystème à la distribution spatiale de différentes espèces de plancton et de poissons. Ces systèmes sonar constituent ainsi l'une des méthodes privilégiées pour l'évaluation des stocks pélagiques tels que les stocks d'anchois du golfe de Gascogne et des côtes péruviennes depuis plus de 20 ans (Petitgas, Masse et al. 2003; Gutierrez, Schwartzman et al. 2007). Récemment il a également été montré que les données sonar permettent d'estimer des paramètres géophysiques clés tels que la profondeur de la couche superficielle de l'océan (Bertrand, Ballon et al. 2010).

L'observation et la caractérisation des comportements à l'échelle individuelle sont également des éléments essentiels pour appréhender les dynamiques et interactions à l'échelle d'un écosystème. Depuis le début des années 1990, l'utilisation de marqueurs individuels des organismes marins a connu des développements croissants et a profondément modifié la perception de nombreux processus écologiques, en particulier concernant les dynamiques spatio-temporelles des populations (e.g., (Hunter, Metcalfe et al. 2003; Block, Teo et al. 2005)). Outre les technologies de marquage électronique évoqués précédemment, les marqueurs "naturels", notamment des marqueurs biochimiques et génétiques, fondés sur l'analyse de tissus ou d'autres parties des

organismes constituent des sources inestimables d'information à l'échelle individuelle. Parmi ces marqueurs naturels, les biocarbonates (e.g., squelette de coraux, otolithes des poissons, coquilles des bivalves) sont de véritables archives individuelles des traits de vie (e.g., âge, migrations, origine natale) et des paramètres de l'environnement dans lequel l'organisme a vécu (e.g., température, salinité, pollution métallique,... (Mitsuguchi, Matsumoto et al. 1996; Panfili, de Pontual et al. 2002; Chauvaud, Lorrain et al. 2005)).

Contributions et synthèse présentées. L'exploitation de ces différentes modalités et échelles d'observation pour caractériser et modéliser les dynamiques et interactions de composantes physiques, biogéochimiques et/ou biologiques d'un écosystème marin constitue le contexte thématique des activités de recherche présentées ici. Dans le cadre d'approches pluridisciplinaires, nous nous intéressons plus spécifiquement aux problématiques sous-jacentes de traitement de l'information. Les contributions méthodologiques associées s'organisent suivant deux aspects principaux :

- **l'analyse de la géométrie des signaux et des images** (e.g., analyse de la géométrie locale des images, extraction de structures géométriques, analyse de formes, distribution de signatures locales dans les images) ;
- des applications de **reconnaissance et classification de signaux et images** (e.g., reconnaissance et segmentation de textures, classification de formes, apprentissage statistique).

Ces travaux de recherche, initialement centrés du point de vue thématique sur l'exploitation du potentiel d'archive individuelle des otolithes de poisson et le traitement des données acoustiques sonar dans le cadre d'approches pluridisiciplinaires développées à l'Ifremer, et plus particulièrement au sein du LASAA, visent aujourd'hui dans le cadre du département Signal & Communications de Telecom Bretagne et de l'équipe TOMS de l'UMR LabSTICC à développer des solutions originales pour l'exploitation des bases d'observation de l'océan vis-à-vis de problématiques de caractérisation, compréhension et modélisation de processus géophysiques et écologiques d'intérêt en collaboration étroite avec des thématiciens (e.g., collaborations avec les départements NSE, STH et LOS de l'Ifremer, les UMR LEMAR et EME).

Afin de couvrir la plus grande partie des activités de recherche menées au cours des dix dernières années (cf. cv fourni en annexe), cette synthèse s'appuie tout d'abord sur une structuration thématique suivant deux axes :

- **L'otolithe, archive individuelle de l'environnement et des traits de vie des poissons (Partie II)** ;
- **L'imagerie sonar des fonds marins et de la colonne d'eau** (**Partie III**).

puis développe les **axes de recherche envisagés portant sur la fouille de données dans les bases d'observation de l'océan**, en s'appuyant notamment sur des illustrations fournies par différents résultats préliminaires (**Partie IV**).

Cette synthèse est complétée par des annexes :

- un **cv court** comportant une liste de publications représentatives accessibles sur la page web suivante : perso.telecom-bretagne.eu/ronanfablet (**Annexe A**) ;
- une description des **activités d'enseignement** (**Annexe B**) ;
- une description des **activités d'encadrement de la recherche** ((co-)encadrement d'étudiants, thèses et chercheurs) (**Annexe C**) ;
- une description des **activités d'administration de la recherche** (participation à et coordination de programmes nationaux et internationaux) (**Annexe D**) ;
- la synthèse de la **production scientifique** (**Annexe E**).

II Les otolithes comme archives individuelles des comportements et réponses individuelles des poissons : outils d'analyse, modélisation et interprétation

Les otolithes, concrétions calcaires de l'oreille interne des poissons (plus précisément des poissons téléostéens), constituent de véritables archives biologiques et environnementales (Campana 2001; Panfili, de Pontual et al. 2002). A l'instar des troncs d'arbre, leur croissance sur un mode accrétionnel (i.e., couche par couche) produit généralement des marques successives, dont la rythmicité peut aller de l'infradien au circannuel (un exemple d'alternance de structures opaques et translucides saisonnières peut être observée en Figure 5). Ce processus de biominéralisation de l'otolithe résulte d'un contrôle physiologique strict par l'organisme, mais est influencé par les conditions du milieu dans lequel il vit. Ainsi, température, salinité d'une part et variations saisonnières du métabolisme, état reproducteur, âge d'autre part peuvent influencer le processus de biominéralisation en modifiant les vitesses de dépôt et/ou l'incorporation dans les fractions minérales et organiques d'éléments chimiques. En outre, contrairement à d'autres pièces calcifiées comme les écailles, l'otolithe reste généralement stable dans le temps. Son analyse offre donc un potentiel unique de reconstitution, à une résolution temporelle allant du jour à l'année, à la fois des paramètres environnementaux et des traits de vie des poissons.

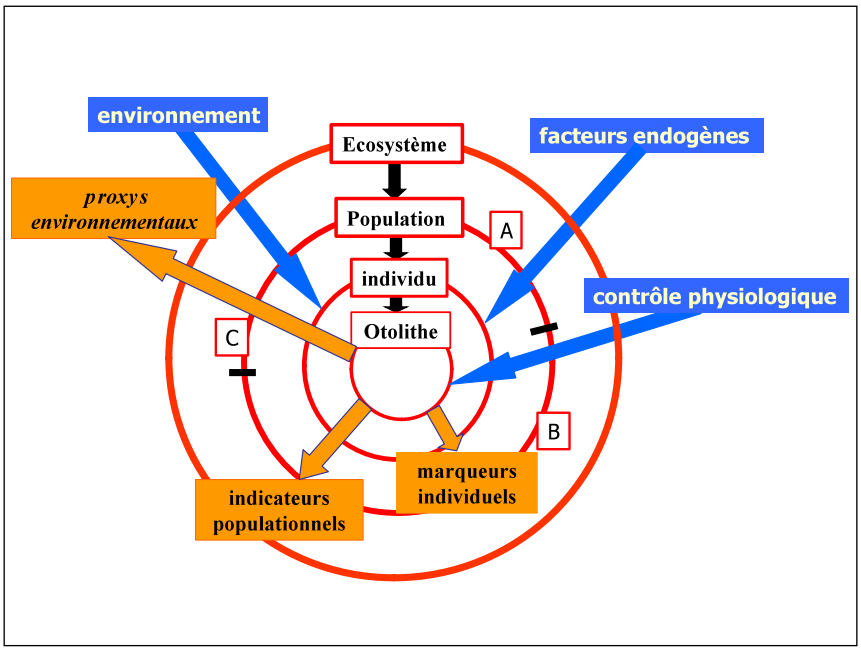

Figure 1. L'otolithe comme archive individuelle de la vie des poissons et de leur environnement. Sa formation accrétionelle, soumise à un contrôle physiologique strict, est sous l'influence de facteurs endogènes et environnementaux. En conséquence, l'otolithe offre un potentiel unique pour l'identification de marqueurs individuels (e.g., âge, croissance, migrations), d'indicateurs populationnels (structure en âge, structuration spatio-temporelle de différentes populations (ici, A, B, C)) et de marqueurs environnementaux (eg température, salinité). D'après (de Pontual 2009).

L'otolithe peut ainsi fournir des informations à différentes échelles (cf. Figure1): 1) à l'échelle individuelle en termes d'histoires individuelles de croissance, de reproduction ou de migration ; 2) à l'échelle d'une population, les données "otolithes" permettent d'aborder les processus de recrutement, de mortalité et peut révéler les structurations spatio-temporelles des stocks et populations de poissons; 3) au niveau de l'écosystème, l'otolithe permet de reconstruire des informations sur les conditions environnementales passées à travers l'effet de ces conditions sur les processus physiologiques qui contrôlent sa formation. A titre d'exemple, plusieurs millions d'otolithes sont ainsi étudiés chaque année à l'échelle mondiale (dont plus de 40000 à l'IFREMER) principalement pour des problématiques d'évaluation et gestion des ressources halieutiques. Si l'analyse des otolithes est reconnue à l'heure actuelle comme une source considérable d'information, ce potentiel d'archive est encore largement sous-exploité. Certaines études récentes montrent même que les principes d'interprétation des

signatures otolithes restent largement empiriques et conduisent dans certains cas à des interprétations erronées. Le cas de l'estimation de la croissance du merlu de l'Atlantique Nord-Est à partir de l'analyse des otolithes en est un exemple frappant (de Pontual, Bertignac et al. 2003). Les résultats issus de campagnes de marquage-recapture ont ainsi démontré que les schémas d'interprétation des otolithes (agréés au niveau européen mais non validés) étaient erronés et avaient conduit à une sous-estimation d'un facteur 2 de la croissance. Cet exemple illustre les limites d'une démarche scientifique principalement fondée sur la mise en évidence de liens statistiques entre un paramètre de l'environnement et des informations structurales ou chimiques contenues dans les otolithes, et plus largement les biominéraux (coraux, coquilles de bivalves,...). Ainsi, en dépit de résultats parfois indiscutables, comme par exemple la calibration du signal $\delta_{18}O$ (rapport des fractions isotopiques 16 et 18 de l'oxygène dans l'otolithe) comme proxy[2] de la température, le signal "otolithe", bien qu'existant, reste souvent indéchiffrable.

Pour dépasser ces difficultés, deux approches complémentaires ont été envisagées dans le cadre pluridisciplinaire du Laboratoire Ifremer-IRD de Sclérochronologie des Animaux Aquatiques en soutien aux activités opérationnelles de l'Ifremer de collecte des paramètres biologiques des espèces marines exploitées :

- le développement d'une approche mécaniste de modélisation de la formation de l'archive (Partie II.2) permet de dépasser les carences conceptuelles actuelles. Derrière l'otolithe se trouve un organisme (derrière l'archive, un archiviste) en interaction avec l'environnement, dont le fonctionnement contrôle l'information carbonatée. Ainsi, les approches mécanistes intégrant la biologie d'espèces modèles, s'avèrent aujourd'hui indispensables pour une calibration des archives biologiques marines tels que les otolithes, les coraux, les coquilles de bivalves ;
- le développement d'outils et méthodes de calibration et reconstruction de traits de vie individuels (Partie II.3). Il s'agit ici de déployer une analyse quantitative et non-subjective pour exploiter le potentiel d'archive de l'otolithe.

Ces deux aspects s'appuient sur une étape préalable d'extraction de signatures structurelles et/ou chimiques de l'otolithe. Nous nous focalisons ici plus particulièrement sur l'extraction d'informations géométriques dans les images d'otolithes (Partie II.1).

Ces différents travaux se sont articulés autour de la coordination de plusieurs projets (notamment, la coordination des projets ANR JC OTOCAL (2005-2008) et EU STREP AFISA (2007-2009)) ainsi que différentes collaborations nationales et internationales (notamment, IRISA/INRIA Rennes (F. Cao), Univ. de Bergen (H. Hoie), DanishTech. Univ. (H. Mosegaard), Vrije Univ. Amsterdam (S. Kooijman), IMEDEA (B. Morales-Nin), CEMAGREF (F. Daverat), LEMAR (A. Lorrain))

II.1 Extraction d'informations géométriques dans les images d'otolithes

L'interprétation de l'information structurelle (i.e., l'information relative aux anneaux ou structures) observée sur des otolithes entiers ou sur des coupes sert de base à l'exploitation des otolithes pour la reconstruction des traits de vie individuels, en particulier l'estimation de l'âge et de la croissance. Le développement des techniques d'imagerie et de traitement numérique des images a ouvert de nouvelles perspectives d'automatisation de ces interprétations et d'aide à l'interprétation. Des exemples d'images d'otolithe permettent d'apprécier ci-après différents niveaux de complexité en termes de forme et de contraste des structures ou anneaux observés sur les otolithes ou les coupes d'otolithe (cf. Fig. 5, 6, 7, 11 & 12). En amont de la phase d'interprétation proprement dite, la phase d'extraction et de caractérisation de l'information structurelle, qui consiste à identifier et caractériser les structures géométriques d'intérêt (centre de croissance, axes de croissance, anneaux,…), est fondamentale.

L'une des caractéristiques importantes des travaux menés relativement à l'état de l'art a consisté à explicitement différencier ces étapes d'extraction et d'interprétation. En outre, ces travaux ont eu pour objectif général d'améliorer la robustesse des algorithmes proposés notamment afin de traiter des images de complexité supérieure et d'élargir la gamme des structures géométriques extraites, jusqu'ici focalisé sur les anneaux, notamment à la détection du centre et des axes de croissance et de la séquence d'évolution de la forme de

[2] En écologie, un proxy est une mesure ou signature (ici de l'otolithe) permettant de prédire un paramètre de l'environnement. Par exemple, le rapport isotopique des fractions 16 et 18 de l'oxygène des biominéraux (coraux, coquilles de bivalves, otolithes) est un proxy de la température de la masse d'eau dans laquelle l'organisme se développe, i.e. il permet de prédire cette température (dans ce cas par une relation linéaire Devereux, I. (1967). Temperature measurements from oxygen isotope ratios of fish otoliths. Science, 155: 1684-1685.).

l'otolithe. Ces travaux se sont notamment appuyés sur le co-encadrement des travaux de thèses d'Anatole Chessel (2004-2007) et de Kamal Nasrredine (2006-2010).

Cette synthèse met plus particulièrement l'accent sur deux aspects :

- l'extraction d'informations géométriques élémentaires dans les images d'otolithes (Partie I.1.1) ;
- la reconstruction de la morphogenèse de l'otolithe (Partie I.1.2).

II.1.1 Extraction d'informations géométriques élémentaires dans les images d'otolithes

Synthèse des contributions: *Nos travaux sur ce thème ont porté sur l'extraction de différents types d'informations et structures géométriques dans les images d'otolithes - centre et axes de croissance, orientation locale de croissance. Nous avons notamment proposé des méthodes d'interpolation du champ dense des orientations locales dans une image, décrites ci-après.*

De manière générale, des solutions d'extraction automatique des structures d'intérêt (centres et axes de croissance, marques de croissance, marques de stress,...) ont été proposées pour des images d'otolithe de complexité peu élevée (typiquement, les images d'otolithe de plie) (e.g., (Robertson, Morison 1999; Troadec, Benzinou et al. 2000; Campana 2001; Panfili, de Pontual et al. 2002; Fablet, Le Josse 2005)). L'application de ces techniques à des images d'otolithe de complexité moyenne ou élevée (eg, otolithes de morue, otolithes de merlu) n'est généralement pas pleinement satisfaisante, d'où la nécessité de développer de nouvelles approches. On peut notamment citer la difficulté rencontrée dans l'extraction des anneaux de croissance, car ceux-ci sont peu contrastés et souvent incomplets. Ce problème est connu en psychovision sous le concept de contours subjectifs (Kanizsa 1996), qui décrit notre aptitude à reconstruire des contours complets à partir d'informations partielles (Fig. 2). La communauté de vision par ordinateur s'est récemment intéressée à des implémentations partielles de ce processus de complétion (Desolneux, Moisan et al. 2003; Desolneux, Moisan et al. 2008).

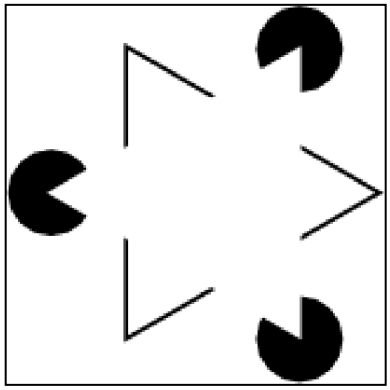

Figure 2. Illustration du principe des contours subjectifs (ici, le triangle blanc). D'après (Kanizsa 1996)

Dans un premier temps, une méthode d'extraction de structures partielles (i.e , d'anneaux non-fermés) (Fablet 2006) a été proposée, là où les travaux antérieurs s'attachaient à détecter des anneaux de croissance fermés. Du fait de l'existence de zones aveugles de faible contraste, l'approche proposée rend le problème plus facilement résolvable. L'exploitation d'un filtrage orienté adapté lui assure une plus grande robustesse vis-à-vis des travaux antérieurs, notamment dans le cas des images d'otolithes de plie comme l'a démontré une application à l'estimation automatique de l'âge et de la croissance détaillée ci-dessous. L'extension à des images de complexité supérieure (eg, les images d'otolithes de morue et de merlu) reste toutefois limitée dans la mesure où cette approche est fondée sur l'hypothèse que la croissance de l'otolithe est radiale, hypothèse le plus souvent peu réaliste. Ces premiers résultats, en particulier les limites d'application des méthodes proposées, y compris nos premiers travaux (Robertson, Morison 1999; Troadec, Benzinou et al. 2000; Panfili, de Pontual et al. 2002; Fablet, Le Josse 2005; Fablet 2006), nous ont conduit à reformuler, en collaboration avec l'IRISA/INRIA Rennes (F. Cao et C. Kervrann), le problème de l'extraction des macro-structures dans les images d'otolithe en nous inspirant de la vision humaine et notamment des méthodes de détection a contrario introduits par Desolneux et al. (Desolneux, Moisan et al. 2003; Desolneux, Moisan et al. 2008). Cette collaboration s'est notamment appuyée sur le co-encadrement du doctorat d'Anatole Chessel (2004-2007).

Une première application des méthodes de détection a contrario a permis de proposer une solution robuste de détection du centre de croissance des otolithes sur la base de critères géométriques simples (Cao, Fablet 2006). Concernant l'extraction des anneaux, on peut remarquer que la connaissance des orientations locales des structures géométriques dans les images joue un rôle clé dans le processus psychovisuel d'identification de ces

structures à partir d'informations élémentaires (segments, coins, jonctions,…). Dans le cas des images de pièces calcifiées, deux approches ont été adoptées jusqu'ici : soit ces orientations locales sont calculées à partir du gradient d'intensité des images, soit elles sont implicitement considérées comme connues (par exemple, en supposant que la croissance est radiale). La première solution n'est en général pas satisfaisante du fait du bruit observé dans les données de gradient d'intensité, et la seconde est clairement limitée aux situations les plus simples. Nous avons donc proposé une approche originale de reconstruction dense de champs d'orientations locales dans les images (Chessel, Cao et al. 2006; Chessel 2007). Le problème est formulé comme une interpolation de données manquantes à partir d'un ensemble de données d'orientation connues.

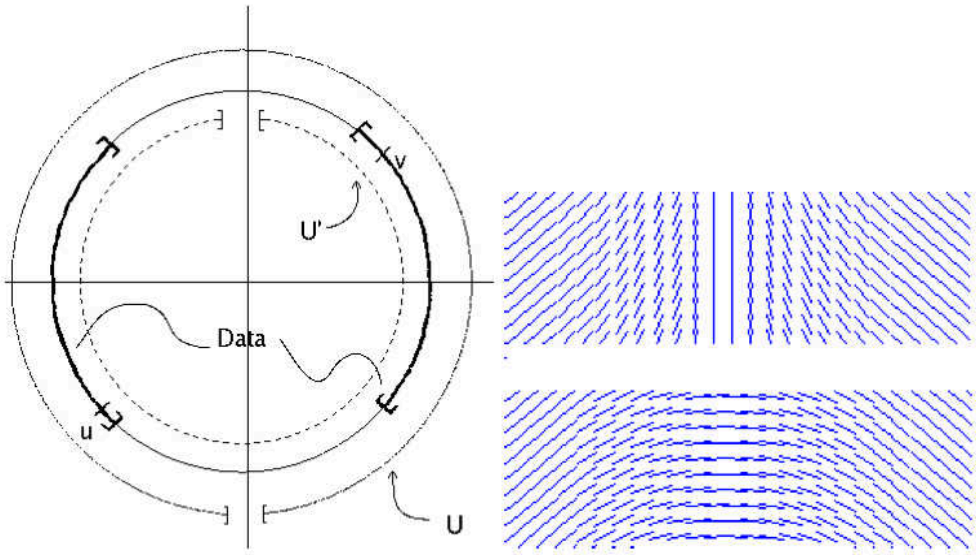

Figure 3. Illustration de l'ambiguïté de l'interpolation de données angulaires : à gauche, pour des données angulaires éparses réparties sur deux intervalles disjoints (en gras), il existe deux manières de joindre ces deux intervalles (respectivement, U et U') ; à droite, illustration de cette ambiguïté pour le cas $u-v=\pi/2[\pi]$. D'après (Chessel 2007)**.**

Comme illustré (Figure 3), l'interpolation de données d'orientation présente une ambiguïté fondamentale liée à la nature intrinsèquement périodique de ces données. L'interpolation comporte donc deux problèmes :

- l'un consistant à déterminer la carte locale d'orientations (i.e., intervalle de la forme $[\theta-\pi/2, \theta+\pi/2]$) dans laquelle la solution est recherchée ;
- le deuxième déterminant la solution recherchée au sens d'un certain critère dans la carte locale.

Cette deuxième étape revient à une interpolation scalaire classique, la première étant elle spécifique aux données d'orientation. Deux techniques d'interpolation ont été envisagées: une approche fondée sur des voisins naturels utilisant une triangulation de Delaunay et une approche axiomatique associée à un opérateur aux dérivées partielles (Chessel 2007). Des évaluations expérimentales (Chessel 2007) ont démontré que cette deuxième technique présente de meilleures performances pour les images d'otolithes pour lesquelles peu de singularités locales sont attendues, alors que la première approche semble plus robuste pour des images naturelles.

Nous mettons ici succinctement l'accent sur le cadre axiomatique proposé. Il consiste en une application du cadre axiomatique développé pour l'interpolation d'images scalaires (Caselles, Morel et al. 1998; Sole, Caselles et al. 2004). Cette approche repose sur la prise en compte de quatre propriétés principales que doit respecter l'interpolant :

- l'invariance à la rotation ;
- l'invariance à la translation ;
- l'invariance au changement d'échelle ;
- un principe de comparaison assurant que l'interpolant respecte localement une relation d'ordre.

Les trois premières propriétés imposent une invariance géométrique au point de vue. La quatrième propriété correspond dans le cas de l'interpolation scalaire à une invariance au changement de contrastes (Caselles, Morel et al. 1998). Dans le cas de l'interpolation d'orientations, elle contraint la régularité locale de l'opérateur d'interpolation et empêche la présence d'oscillations dans la solution recherchée. En suivant une démarche similaire au cas de l'interpolation scalaire, on peut déterminer les opérateurs aux dérivées partielles vérifiant ces propriétés (complétées par des propriétés techniques de régularité et stabilité). Parmi ceux-ci, l'opérateur AMLE

(Absolutely Minimizing Lipshitz Extension) (Caselles, Morel et al. 1998) présente les caractéristiques les plus intéressantes pour notre application pour reconstruire la géométrie des structures géométriques observées dans les images d'otolithe. Cet opérateur peut notamment être défini de manière équivalente comme l'opérateur qui minimise la norme L_∞ du gradient, c.-à-d. l'interpolant régulier (c.-à-d., minimisant une norme du gradient de u) le moins régulier. Formellement, il s'agit de l'opérateur d'interpolation qui minimise l'énergie suivante :

$$\lim_{p\to\infty}\left(\int \|\nabla u\|^p\right)^{1/p}$$

où u est le champ d'orientation. Numériquement, l'opérateur AMLE est mis en œuvre suivant l'équation de diffusion suivante :

$$\begin{cases} \dfrac{\partial u}{\partial t} = \nabla u^t \left[\nabla\nabla^t u\right]\nabla u \\ u_{|D} = u_0 \end{cases}$$

où t est une variable temporelle algorithmique représentant les itérations de la diffusion, ∇u est le gradient du champ u et $\nabla\nabla^t u$ son hessien, D est le domaine sur lequel les valeurs d'orientation sont connues (ici, l'ensemble des points de l'image où l'orientation est connue) et u_0 l'ensemble de ces valeurs connues. L'existence et l'unicité de l'opérateur AMLE sont connues dans le cas scalaire. De tels résultats ne peuvent être étendus directement au cas des données angulaires. Les évaluations numériques ont toutefois démontré la stabilité du schéma numérique proposé. Afin de prendre en compte l'ambiguïté topologique illustrée en Fig.3 une approche multi-résolution a été développée. La construction initiale de la pyramide multi-résolution exploite uniquement les données connues. Puis, l'opérateur AMLE est appliqué à chaque niveau de résolution à partir d'une initialisation des informations reconstruites au niveau précédent. Des résultats d'interpolation AMLE de l'orientation sont données pour l'image Lena (Figure 4) ainsi qu'une image d'otolithes (Figure 5). Ils exploitent deux critères différents de sélection des données initiales, c.-à-d. des points de l'image pour lesquels l'information d'orientation du gradient de l'image est jugée fiable : le résultat d'un détecteur de contour Canny-Deriche (Deriche 1987) et une détection *a contrario* des points où l'orientation du gradient est localement cohérente (Chessel 2007). Ce dernier critère s'est révélé plus approprié aux images d'otolithes qui présentent des niveaux de gradient relativement faibles.

Figure 4. Interpolation AMLE d'orientations pour l'image Lena : image originale (gauche), ensemble des points de contours sélectionnés par un filtre de Canny-Deriche (milieu), visualisation du champ d'orientation reconstruit par l'opérateur AMLE en utilisant comme données initiales l'orientation du gradient aux points sélectionnés. (droite). Le champ d'orientation est visualisé à travers ses lignes de champ. D'après (Chessel 2007).

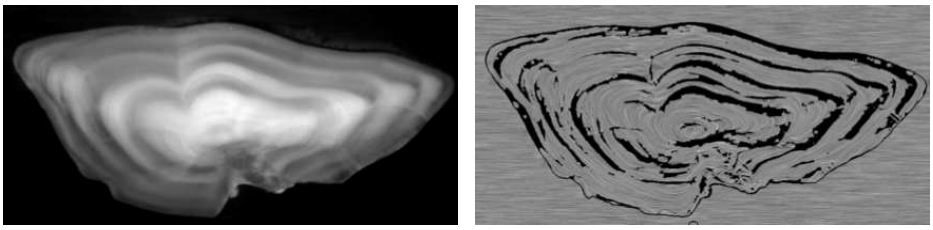

Figure 5. Interpolation AMLE d'orientation pour une image d'otolithe : image d'un otolithe de lieu noir (gauche), champ d'orientation interpolé par AMLE et données initiales (en noir) (droite). Les données initiales résultent d'une détection *a contrario* des points présentant des orientations de gradient localement cohérentes. Le champ d'orientation est visualisé à travers ses lignes de champ. D'après (Chessel 2007).

Les champs d'orientation interpolés fournissent les informations nécessaires pour différentes applications telles que le filtrage orienté, l'extraction de structures curvilinéaires pour les images naturelles ou l'extraction des anneaux et des axes de croissance pour les images d'otolithes (Chessel, Cao et al. 2006; Chessel 2007). Dans la partie suivante, nous présentons plus particulièrement une application à la reconstruction de la morphogenèse 2D de l'otolithe.

II.1.2 Reconstruction de la morphogenèse de l'otolithe à partir d'une image

Synthèse des contributions: *Nous présentons ici une approche variationnelle de reconstruction de la morphogenèse de l'otolithe dans un plan de coupe à partir d'une image et des applications à l'extraction de structures géométriques (anneaux, axes de croissance). L'approche proposée repose sur une représentation de type "level-set" de la déformation de la forme de l'otolithe au cours du temps.*

L'analyse de la forme des otolithes a constitué l'une des premières applications des techniques de traitement d'images et de reconnaissances de formes à l'otolithométrie. Elle a notamment été largement employée depuis une quinzaine d'années pour des problèmes de discrimination de stocks dans la mesure où il a été observé que les caractéristiques de l'environnement influent sur la forme des otolithes d'une espèce donnée (Campana, Casselman 1993; Panfili, de Pontual et al. 2002).

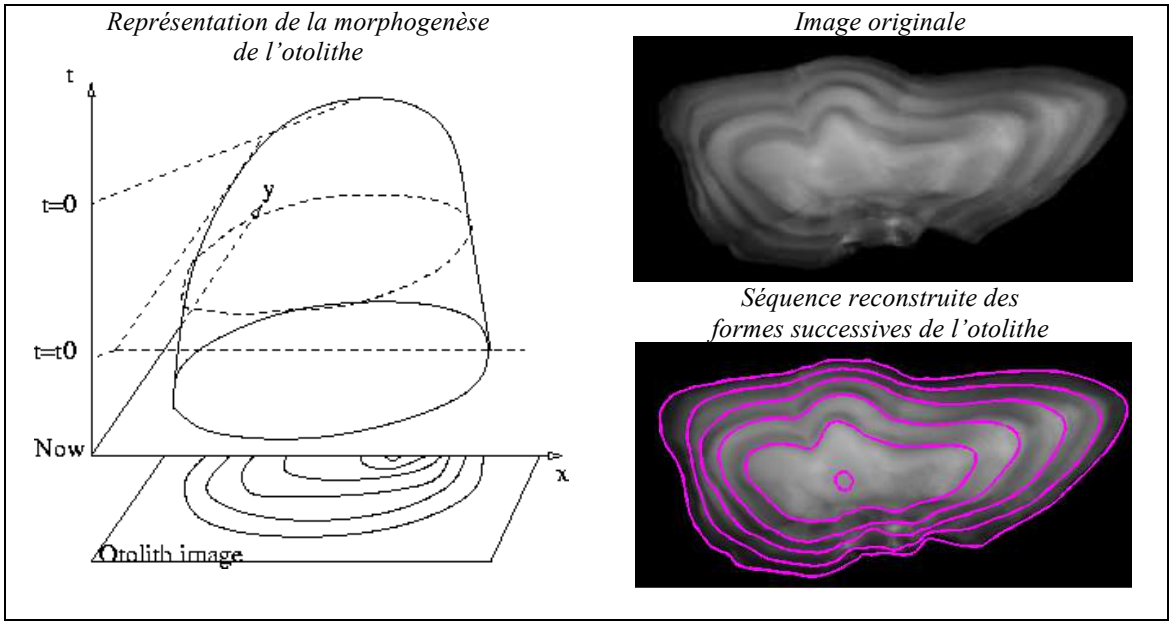

Figure 6. Reconstruction de la morphogénèse de l'otolithe *:* représentation de la morphogenèse de l'otolithe par une fonction potentiel dont les lignes de niveaux représentent les formes successives de l'otolithe (gauche) ; image d'un otolithe de lieu noir (droite, haut), séquence reconstruite des formes de l'otolithe superposée à l'image originale (droite, bas)

Alors que les travaux antérieurs sur l'analyse de la forme des otolithes se limitent à la caractérisation du pourtour de l'otolithe dans un plan de coupe, la présence des anneaux internes permet potentiellement d'aborder la reconstruction de l'évolution de la forme de l'otolithe au cours de la vie du poisson. De la connaissance de la morphogenèse pourrait être déduit des éléments de compréhension et de modélisation de l'effet des facteurs environnementaux et endogènes sur la formation de l'archive. En nous appuyant, sur l'extraction du champ AMLE des orientations locales, une méthode de reconstruction de l'évolution temporelle de la forme de l'otolithe dans un plan a été développée (Figure 6). Cette application, à notre connaissance originale, repose sur la modélisation de la morphogénèse de l'otolithe comme une surface tels que les lignes de niveaux de cette surface correspondent aux formes successives de l'otolithe. L'ajustement de ce modèle à une image est formulé dans un cadre variationnel de telle manière que les lignes de niveaux du modèle f soient aussi tangentes que possible aux structures de l'image, i.e. au champ dense des orientations des structures reconstruites par l'opérateur AMLE. Formellement le critère variationnel considéré est de la forme suivante :

$$E(U) = \int_{t\in[0,T]} \int_{p\in\Gamma_t(U)} \left[(1-\gamma) + \gamma \left\| \left\langle \frac{\nabla U(p)}{\|\nabla U(p)\|}, \omega(p) \right\rangle \right\|_\rho dpdt \right]$$

où γ pondère l'importance relative des deux termes d'énergie, U est la fonction de $\mathcal{R}^2$ dans $\mathcal{R}$ représentant l'évolution de la forme de l'otolithe, $\Gamma_t(U)$ est la forme de l'otolithe au temps t, i.e. la ligne de niveau t de la fonction U définie par

$$\Gamma_t(U) = \left\{ p \in \Re^2 / U(p) = t \right\}.$$

La direction du gradient de U, est la normale à la ligne de niveau de U passant au point p et ω(p) l'orientation locale estimé au point p pour l'image considérée. Nous utilisons une norme robuste (en pratique une approximation de la valeur absolue de type $\|x\|_\rho=(\varepsilon+x^2)^{1/2}$) afin de prendre en compte la présence éventuelle de valeurs aberrantes (Black, Rangarajan 1996).

Le premier terme d'énergie correspond à une contrainte de régularité des formes en minimisant la longueur des courbes. Le deuxième terme cherche à faire correspondre chaque courbe de niveaux aux orientations locales de l'image. Il faut noter que ce critère variationnel est invariant vis-à-vis de la dynamique de contraste de la fonction U. Ceci impose de considérer une contrainte additionnelle sur cette dynamique, typiquement une distribution uniforme des valeurs du champ U, pour effectuer la minimisation du critère variationnel. Elle repose sur la dérivation des équations d'Euler-Lagrange associé et la mise en œuvre d'une descente de gradient. Le détail des ces équations et de leur résolution numérique peut être trouvé dans (Fablet, Pujolle et al. 2008). Les équations aux dérivées partielles associées sont proches des solutions envisagées pour le filtrage anisotrope d'images faisant intervenir des opérateurs de courbure (Tschumperlé 2006). Comme illustré ci-dessus (Fig. 6), la formulation variationnelle proposée associée au champ d'orientation interpolé par l'opérateur AMLE permet de reconstruire l'évolution de la forme de l'otolithe. Des résultats complémentaires montrent que l'utilisation directe des données de gradient conduit à des estimations trop bruitées (cf. Fig. 6, Fablet, Pujolle et al. 2008 en annexe à ce chapitre).

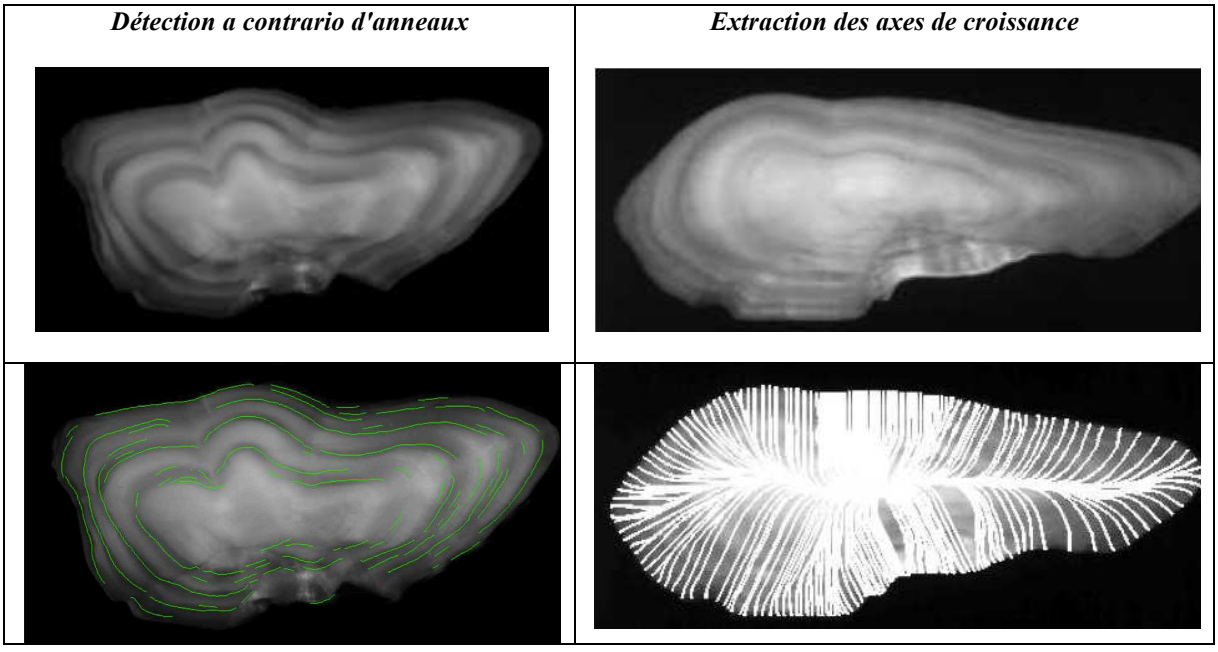

Figure 7. Application de la reconstruction de la morphogenèse de l'otolithe à l'extraction de structures géométriques dans les images d'otolithe : extraction des anneaux dans une image formulée comme la détection de zones de vallées cohérentes vis-à-vis de la géométrie estimée par la reconstruction variationnelle de la morphogenèse (gauche), reconstruction des axes de croissance extraits comme des structures curvilinéaires entre le centre et le bord de l'otolithe localement orthogonales aux orientations locales estimées (droite). D'après (Chessel 2007).

Du point de vue applicatif, cette reconstruction de la morphogenèse de l'otolithe ouvre de nouvelles perspectives, en premier lieu en termes d'extraction des structures géométriques dans les images d'otolithe (axes de croissance, anneaux partiels). Il a notamment été envisagé une approche itérant successivement, interpolation

d'orientation, reconstruction de la morphogenèse et détection des anneaux (Chessel 2007; Chessel, Fablet et al. 2008). Cette dernière étape de détection est formulée comme un problème de détection de structures curvilinéaires correspondant à des zones de crêtes ou vallées de l'image. La méthode proposée repose notamment sur les principes de la détection a contrario (Desolneux, Moisan et al. 2008) et utilise comme ensemble de courbes candidates les lignes de niveaux de la fonction de morphogenèse reconstruite U. Une description détaillée peut être trouvée dans (Chessel 2007; Chessel, Fablet et al. 2008). Il peut être noté que la procédure itérative proposée conduit à des améliorations significatives des informations géométriques reconstruites. A titre d'illustration, nous fournissons ici des exemples de résultats obtenus pour deux exemples d'images d'otolithes en termes d'extraction des anneaux et de reconstruction des axes de croissance (Figure 7).

Associée à une calibration temporelle d'images d'otolithes, i.e. des images interprétées par des experts ou des images d'échantillons issus d'expériences de marquage/recapture[3] (de Pontual, Bertignac et al. 2003), elle fournit également les outils nécessaires pour l'analyse et la modélisation de la morphogenèse de l'otolithe (cf. Partie II.3). Elle permet également de définir un référentiel adapté à la croissance de l'otolithe pour l'analyse intra- et inter-échantillons de différentes informations extraites sur un même otolithe. A titre d'illustration, un exemple d'analyse conjointe de l'information structurelle et de la signature isotopique $\delta^{18}O$ de l'otolithe peut être visualisée à l'adresse suivante : http://public.enst-bretagne.fr/~rfablet/mottolith.html.

II.2 Modélisation de la formation des otolithes

La validation et la calibration de proxys environnementaux et de marqueurs des traits de vie individuels extraits de l'otolihe reposent principalement sur l'établissement de lien statistique significatif entre des signatures de l'otolithe et des conditions ontogéniques ou environnementales spécifiques. Même si cette démarche empirique a conduit à des avancées indéniables, le potentiel d'archive des otolithes reste largement inexploité et nécessite de mieux comprendre et de mieux caractériser les mécanismes de formation de l'otolithe. La collaboration développée par l'Ifremer (H. de Pontual) avec le CSM (D. allemand) et l'Université de Nice-Sophia-Antipolis (D. Allemand et P. Payan) a démontré la nécessité de passer d'une caractérisation descriptive et conceptuelle du processus de biocalcification à une caractérisation plus quantitative de ce processus et de son évolution vis-à-vis de paramètres environnementaux et métaboliques, ceci devant se concrétiser par la modélisation numérique de la formation de l'otolithe.

Cette question scientifique a constitué la trame du montage et de la coordination du projet ANR JC OTOCAL. Elle nécessite de considérer deux aspects complémentaires :

- La mise en oeuvre d'une approche expérimentale pour la compréhension des mécanismes de la biominéralisation de l'otolithe (Partie I.2.1) ;
- La modélisation de la formation de l'otolithe (Partie I.2.2).

Il faut souligner le caractère extrêmement novateur de cette démarche multidisciplinaire qui à notre connaissance n'a pas été développée par d'autres laboratoires et a conduit à des résultats extrêmement intéressants détaillés ci-dessous (e.g., (Fablet, Pecquerie et al. 2011)).

II.2.1 Approche expérimentale pour la compréhension des mécanismes de la biominéralisation de l'otolithe

> ***Synthèse des contributions:*** *Nos objectifs de compréhension et modélisation du processus de biominéralisation de l'otolithe se sont appuyés sur une approche expérimentale, à la fois en termes d'expérimentation zootechnique en milieu contrôlé et de techniques d'analyse et caractérisation à petite échelle (micron) des fractions minérales et organiques de l'otolithe.*

La caractérisation de processus fins tels que les processus de biocalcification nécessite de développer une approche expérimentale en milieu contrôlé. Dans cette optique, nous nous sommes appuyés sur les infrastructures d'aquaculture de l'Ifremer qui ont assuré les développements zootechniques nécessaires au maintien en captivité d'un stock de merlus sur lesquels les protocoles expérimentaux propres à nos thématiques

[3] Le principe des expériences de marquage/recapture pour des populations de poissons consiste à capturer des individus que l'on pourvoie de marques externes, de "marques" internes chimiques et/ou de marques électroniques (Fromentin, Ernande, et al. 2009). Ces individus sont ensuite relachés dans le milieu. Les marques externes permettent notamment d'identifier ces individus lors de leur recapture pour qu'ils puissent être adressés aux scientifiques.

sont mis en œuvre (Jolivet, de Pontual et al. 2012). Le choix du modèle merlu est motivé par la volonté de coupler cette approche expérimentale en milieu contrôlé à l'analyse des échantillons issus du milieu naturel, et plus particulièrement des programmes de marquage-recapture par marques électroniques coordonnés par l'Ifremer (de Pontual, Jolivet et al. Soumis).

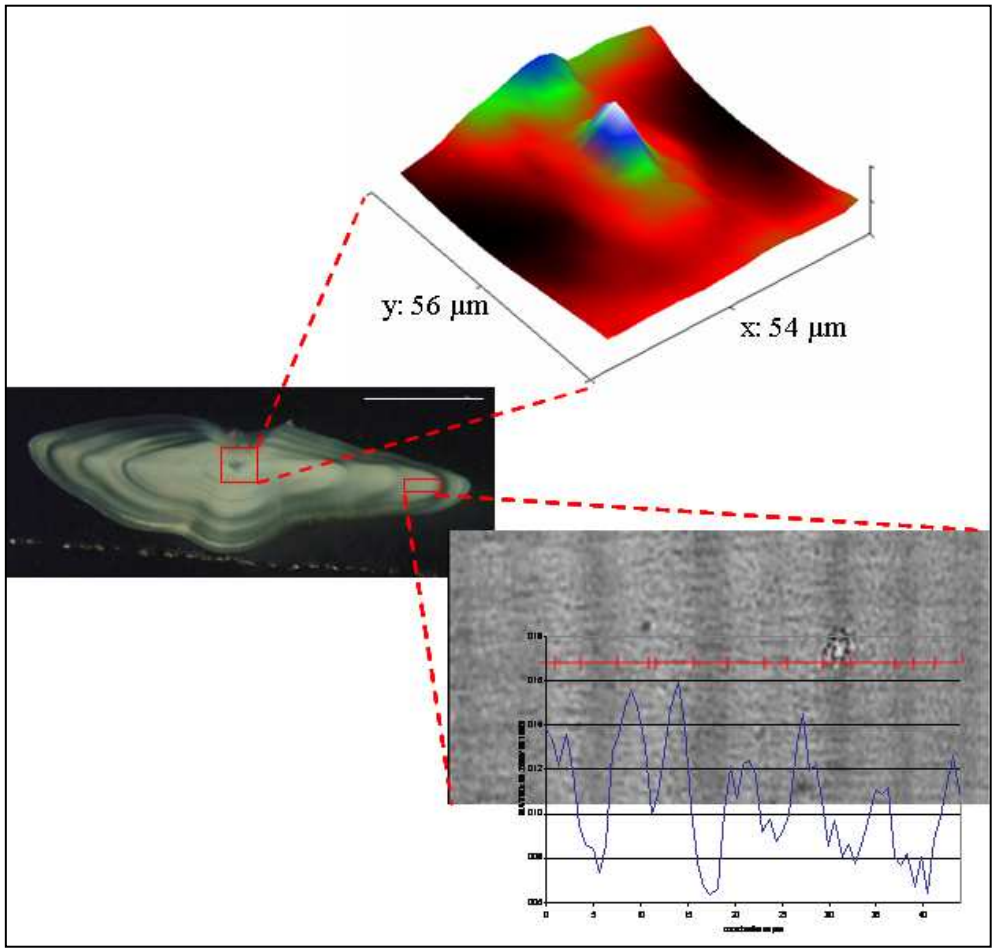

Figure 8. Analyse d'un otolithe (milieu) en microspectrométrie Raman. La microscopie Raman permet de quantifier localement (à l'échelle du micron) les concentrations des fractions minérales et organiques de l'otolithe. La cartographie 2D (en haut) de la zone du nucleus (centre de croissance de l'otolithe) montre une plus grande concentration en matière organique également observée dans la région sulcale (zone située au-dessus du nucleus dans l'image à droite). Le rapport entre les fraction organique et minérale (ici le rapport des signatures RAMAN du groupement CH et de l'aragonite (en bleu) suit l'alternance des microstructures opaques et translucides (droite). D'après (Jolivet, Bardeau et al. 2008).

Ces expériences en milieu contrôlé ont fourni le cadre de la thèse d'A. Jolivet co-encadrée avec H. de Pontual. Au-delà des données sur la variabilité de la croissance du merlu pour différentes conditions de température, elles ont mis en évidence les relations entre croissance somatique du poisson et croissance de l'otolithe et opacité de l'otolithe, fournissant ainsi un des éléments conceptuels pour le modèle numérique décrit par la suite (Fablet, Pecquerie et al. 2011). De manière générale, la croissance de l'otolithe est largement corrélée à la croissance du poisson (appelée croissance somatique), l'otolithe maintenant toutefois sa croissance lors des arrêts de croissance somatique, par exemple dus à des périodes de jeune. L'un des résultats intéressants de ces travaux expérimentaux résident dans la mise en évidence d'une relation linéaire entre l'opacité de l'otolithe et la fraction de croissance de l'otolithe expliquée par la croissance somatique (Jolivet 2009).

Il est largement admis que la fraction organique de l'otolithe joue un rôle central dans le processus de biominéralisation (Allemand, Mayer-Gostan et al. 2007). Du fait des méthodologies analytiques retenues, nécessitant le plus souvent une grande quantité d'échantillons en solution, les connaissances disponibles (Dannevig 1956; de Pontual, Geffen 2002) ne permettent pas d'appréhender de manière qualitative et quantitative la variabilité spatiale des fractions minérale et organique des structures de l'otolithe, tant les micro-

que les macro-structures (Jolivet, Bardeau et al. 2008). Dans ce contexte, la thèse d'A. Jolivet a développé une nouvelle technique d'analyse des otolithes fondée sur la microspectrométrie Raman (méthode non destructive d'analyse in situ et à haute résolution spatiale (i.e., de l'ordre du micron)) (Figure 8). Ces travaux ont abouti à la remise en cause de la définition classique des microstructures de l'otolithe (cf. glossaire de (Panfili, de Pontual et al. 2002)) dites respectivement « mineral-rich » et « organic-rich ». Elle montre aussi que l'opacité peut être prédite à partir de signatures Raman spécifiques des fractions minérales et organiques (Jolivet 2009).

II.2.2 Modèle conceptuel et numérique de la formation de l'otolithe

Synthèse des contributions : *en nous appuyant sur le cadre mécaniste de la théorie DEB ("Dynamic Energy Budget"), le modèle bio-énergétique de formation de l'otolithe (croissance et opacité) proposé permet de formuler les interactions entre des facteurs clés, le métabolisme de l'individu, les conditions de température et disponibilité alimentaire de l'environnement. Nous présentons une calibration du modèle sur des données expérimentales et une application à l'interprétation de variabilités de "patterns" d'otolithes d'une même espèce pour deux stocks différents.*

L'interprétation des signaux de croissance et d'opacité des otolithes vis-à-vis des paramètres physiologiques des stocks et/ou espèces comme de la variabilité environnementale reste largement empirique et semble conduire à des conclusions contradictoires dans certains cas (cf., cas des otolithes de morue de mer du Nord et de mer de Barents). La modélisation de la formation de l'otolithe constitue ainsi un défi prioritaire pour l'otolithométrie (Panfili, de Pontual et al. 2002). Différents modèles ont été proposés dans la littérature (Romanek, Gauldie 1996; Gauldie, Romanek 1998; Hussy, Mosegaard 2004) mais leur portée reste limitée. Alors que les hypothèses de contrôle par la dynamique des précurseurs ioniques considérées dans (Romanek, Gauldie 1996; Gauldie, Romanek 1998) sont mises en défaut par des résultats expérimentaux récents (Allemand, Mayer-Gostan et al. 2007), le modèle proposé par Hussy et al. repose principalement sur une approche empirique qui ne permet pas d'identifier les facteurs clés intervenant dans la biominéralisation de l'otolithe.

A partir des connaissances disponibles dans la littérature ainsi que de résultats expérimentaux illustrés précédemment, nous proposons de relier, dans le cadre de la théorie DEB (Dynamic Energy Budget) (Kooijman 2010), les variations de croissance et d'opacité de l'otolithe aux variations des conditions métaboliques de l'individu et de son environnement (Fablet, Pecquerie et al. 2011). Le schéma de principe du modèle proposé est illustré (Figure 9). La théorie DEB est une théorie générale de l'organisation métabolique qui décrit comment un individu assimile et utilise l'énergie au cours de son cycle de vie. Le principe-clé de notre modèle est l'application du concept de produit métabolique, tel que défini par la théorie DEB, aux otolithes de poissons, de cela découlant un grand nombre de caractéristiques largement documentés de l'otolithe telles que la corrélation entre croissance de l'otolithe et respiration (Wright, Fallon-Cousins et al. 2001), et les phénomènes de corrélation et décorrélation entre la croissance de l'otolithe et la croissance somatique durant les périodes de forte et faible croissance (Campana 1990; Høie, Folkvord et al. 2008). Les fractions minérales et organiques de l'otolithe sont définies comme deux produits métaboliques impliquant des contributions potentiellement différentes des flux métaboliques élémentaires définis par la théorie DEB, en particulier le flux de croissance somatique (p_G) et le flux de dissipation (p_D), associé à des processus de maintenance (Figure 9). Les variations d'opacité résultent des variations relatives de ces deux fractions (Hussy, Mosegaard 2004). Etant donné que la précipitation in-vitro de carbonate de calcium sous sa forme aragonitique est directement dépendante de la température (Romanek, Gauldie 1996), les variations de température agissent également directement sur la dynamique de la fraction minérale. Mathématiquement, la croissance et de l'opacité de l'otolithe sont des fonctions, modulées par un effet température, des flux métaboliques p_G et p_D dont les dynamiques sont données par les équations différentielles ordinaires définies par la théorie DEB. La température du milieu et les conditions d'alimentation de l'individu sont les deux variables forçantes de la dynamique bio-énergétique DEB. Les simulations 1D du modèle DEB-otolithe sont étendues à des simulations d'images d'otolithes en exploitant un modèle calibré de la déformation de l'otolithe dans un plan transverse, modèle obtenu grâce aux outils de traitement d'images présentés en partie II.1.

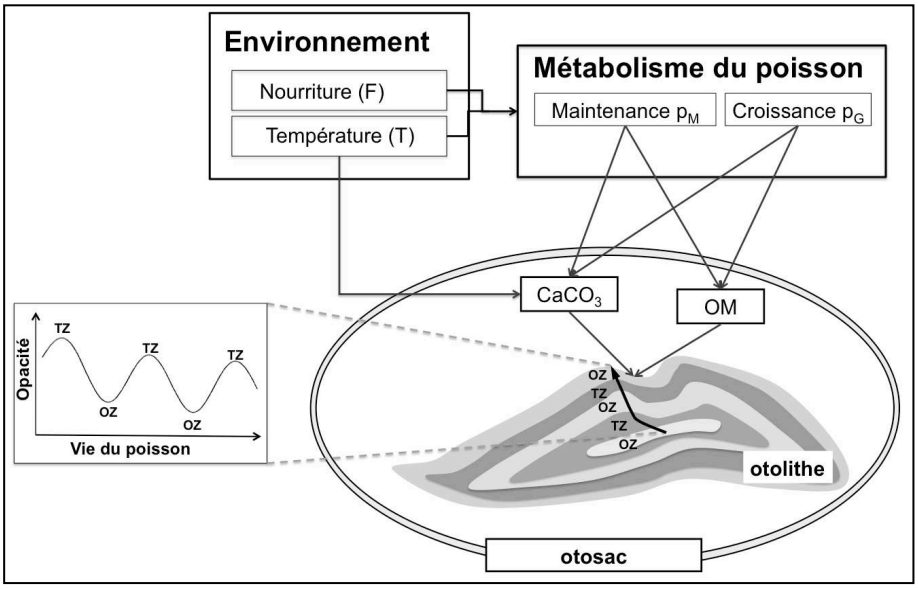

Figure 9. Modèle de formation de l'otolithe : La formation de l'otolithe suit un mode accrétionnel de dépôt de couches successives de carbonate de calcium (CaCO3). Cette accrétion implique une matrice organique (MO) composé d'éléments organiques présents dans l'endolymphe, le fluide interne dans l'épithélium sacculaire, et présente généralement une alternance de couches opaques et translucides. Ici, nous proposons de définir l'otolithe comme un produit métabolique, tel que défini par la théorie DEB ("Dynamic Energy Budget"). La formation de l'otolithe est alors déterminée par les flux métaboliques élémentaires, i.e. le flux de croissance somatique et le flux de maintenance, avec un facteur additionnel de régulation directe de la précipitation minérale par la température. Les flux métaboliques dépendent de l'état de l'individu et des conditions dans lesquelles il évolue. La modulation directe ou indirecte de la biominéralisation de l'otolithe par les paramètres de l'environnement (notamment, la température et la nourriture) se traduit généralement par une alternance de bandes opaques (OZ) et translucides (TZ). D'après (Fablet, Pecquerie et al. 2011).

Nous avons mené la calibration et l'évaluation du modèle DEB-otolithe sur des données expérimentales fournies par l'IMR et l'Université de Bergen (Hans Hoie). La qualité des correspondances entre les simulations du modèle et les données expérimentales suggère la pertinence du modèle conceptuel envisagé (Figure 10). Ce modèle constitue une avancée significative dans la compréhension des interactions complexes entre le métabolisme et les facteurs environnementaux dans les signatures archivées par l'otolithe. Comme illustré ci-après, il ouvre de nombreuses perspectives en termes d'analyse de "patterns" de l'otolithe et de reconstruction de traits de vie individuel. Les résultats obtenus doivent amener à valider les hypothèses de modélisation retenues par des travaux expérimentaux sur les mécanismes de biominéralisation.

Le modèle DEB-otolithe ouvre de nombreuses perspectives en termes d'interprétation et reconstruction de traits de vie individuels à partir des signatures structurelles et chimiques de l'otolithe. Nous en fournissons une première illustration (Figure 11) pour une problématique de compréhension des différences observées entre les signaux d'opacité pour des stocks d'une même espèce. Nous considérons le cas des stocks de morue de la mer de Barents et de la mer du nord. Les otolithes de ces deux stocks présentent des "patterns" d'opacité en opposition de phase. En particulier, les otolithes de morue de mer du nord n'obéissent pas à l'hypothèse généralement admise de formation d'une zone opaque au printemps et d'une zone translucide en hiver. Nous montrons ici que le modèle DEB-otolithe permet de prédire ces différences par les différences des conditions environnementales (alimentation et température) rencontrées par les deux stocks (Fablet, Pecquerie et al. 2011). Dans le cas du stock de mer de Barents la formation de la zone opaque au printemps s'explique par la conjonction d'une migration vers des eaux plus chaudes et une plus grande accessibilité des proies. Quant au stock de mer du nord, le pic de température en fin d'été est associé à un stress alimentaire se traduisant par la formation d'une zone translucide.

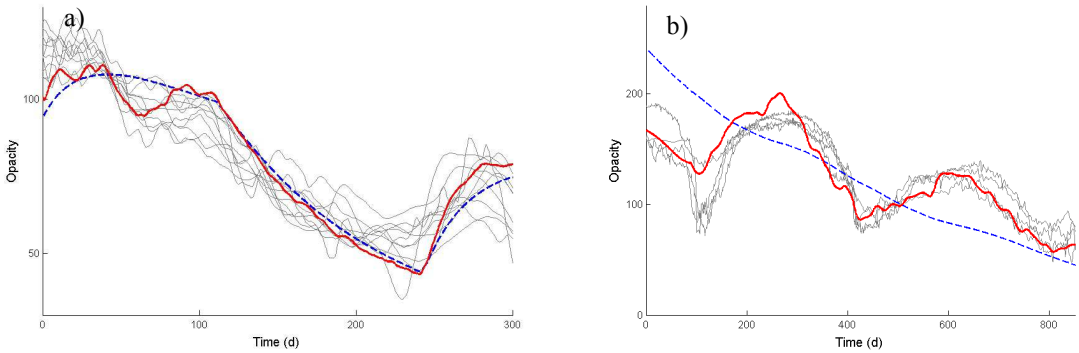

Figure 10. Comparaison de données d'opacité de l'otolithe de morues élevées suivant deux types de conditions d'alimentation et de temperature à des simulations du modèle DEB-otolithe : (a) une forte baisse des conditions d'alimentation après 100 jours d'expérimentation avec une variation saisonnière de la temperature, (b) une alimentation constante avec une variabilité saisonnière de la temperature sur une période de deux ans et demi. Nous rapportons les données d'opacité (gris) ainsi que les simulations du modèle sans effet direct de la température sur la précipiattion de la fraction minérale (bleu) et avec cet effet direct (rouge). D'après (Fablet, Pecquerie et al. 2011).

La formulation mathématique du modèle DEB (en termes de système dynamique) et sa relative parcimonie (de l'ordre d'une dizaine de paramètres) permet également d'envisager des applications de reconstruction de traits de vie individuels formulée comme un problème d'inversion du système dynamique. Une première application en ce sens a été envisagée pour reconstruire l'information de densité des proies à partir du signal d'opacité (Pecquerie, Fablet et al. 2012). Il peut être noté que la formulation mathématique du modèle DEB se prête à une formulation de ces problèmes d'inversion dans le cadre de l'assimilation variationnelle (Lions 1971; Le-Dimet, Talagrand 1986), que nous exploitons par ailleurs (cf. Partie IV.2).

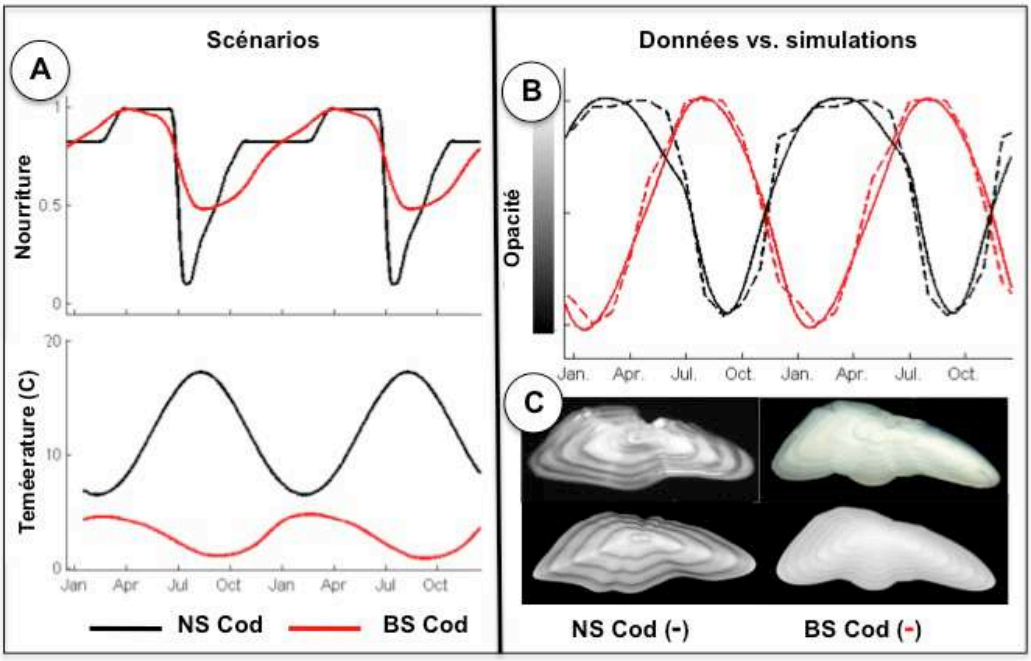

Figure 11. Comparaison d'images d'otolithes réels (en bas à gauche) et virtuels (en bas à droite) représentatifs de deux stocks de morue (mer du nord (NS Cod) et mer de Barents (BS Cod)) : Les simulations 1D (B,-) s'appuient sur des scénarios de conditions environnementales issus des données de litérature (A). Elles sont comparées aux "patterns" saisonniers d'opacité observés sur les otolithes des deux stocks (B, --). Les images simulées (C, bas) sont également comparées à des images d'otolithes réélles (C, haut). D'après (Fablet, Pecquerie et al. 2011). Une animation présentant ces résultats peut être visualisée à partir du lien http://www.plosone.org/article/info%3Adoi%2F10.1371%2Fjournal.pone.0027055.

II.3 Méthodes et outils de reconstruction de traits de vie individuels

II.3.1 Collecte et qualité des données individuelles d'âge et de croissance des poissons

Synthèse des contributions: *Nous avons proposé différentes approches (segmentation, analyse temps-fréquence, apprentissage statistique) d'estimation automatique des données individuelles d'âge et croissance des poissons à partir de l'analyse des images d'otolithes.*

La qualité des données individuelles d'âge et de croissance est critique pour l'application des modèles de dynamique des populations, sur laquelle se fondent largement l'évalaution et la gestion des stocks halieutiques. Le développement de méthodes automatiques d'estimation de l'âge et de la croissance des poissons à partir des images d'otolithes a pour objectif d'apporter une réponse en termes d'assurance qualité et de contrôle qualité. De manière générale, ce problème est abordé suivant trois approches complémentaires :

- L'estimation automatique de l'âge par apprentissage statistique reposant sur la classification des images d'otolithes vis-à-vis des différentes classes d'âge. Cette formulation par classification repose sur une représentation globale de l'information structurelle contenue dans une image et la définition d'une métrique ou mesure de similarité associée. La solution originale proposée (Fablet, Le Josse 2005) exploite des classifieurs à noyaux gaussiens (SVM, Support Vector Machine) ;
- L'estimation paramétrique de la croissance individuelle par une analyse temps-fréquence du contenu des images (Fablet, Benzinou et al. 2003). Les transformations temps-fréquence permettent d'analyser finement les signaux non-stationnaires modulés en fréquence. Dans le cas où la périodicité annuelle du dépôt des macrostructures de l'otolithe est validée, le signal d'intensité sur un axe de croissance entre le noyau et le bord de l'otolithe présente une modulation fréquentielle associée à la loi de croissance. L'approche proposée exploite plus particulièrement une représentation paramétrique de type exponentiel de la loi de croissance individuelle et une technique d'estimation robuste des paramètres de ce modèle paramétrique dans le plan temps-fréquence ;
- L'estimation conjointe de l'âge et de la croissance (Fablet 2006) reposant sur une interprétation explicite des marques structurelles observées dans les images d'otolithes (Figure 12). L'approche proposée repose sur une sélection bayésienne, parmi un ensemble de courbes géométriques extraites, du sous-ensemble de courbes le plus pertinent vis-à-vis d'un a priori formulé sur la variabilité des lois de croissance individuelles.

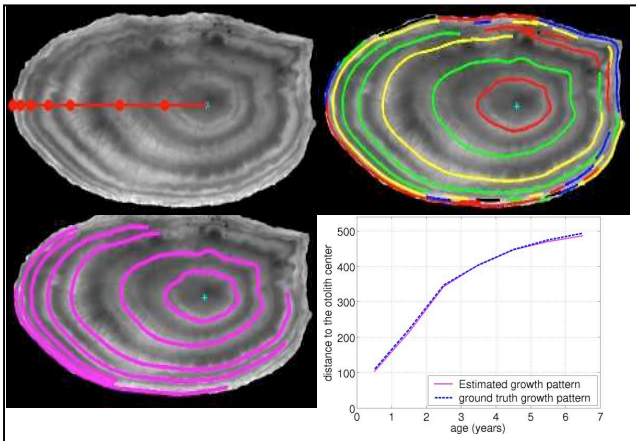

Estimation conjointe de l'âge et de la croissance d'un otolithe par approche bayésienne : image d'otolithe de plie et interprétation associée de l'expert (haut gauche), extraction automatique de structures géométriques significatives (haut, droite), configuration des structures sélectionnées (bas gauche), lois de croissance estimées (bas droite).

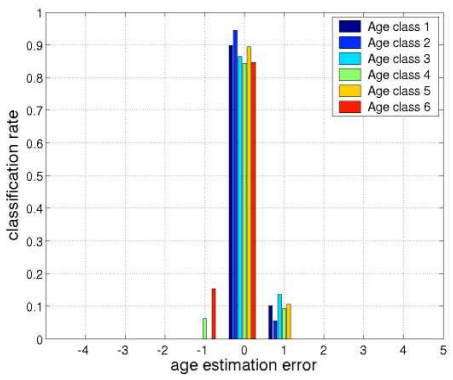

Performances de l'estimation automatique de l'âge : taux de bonne estimation automatique de l'âge par l'approche bayésienne proposée, relativement à l'interprétation de l'expert, pour une base de 200 otolithes de plie.

Figure 12. Estimation conjointe de l'âge et de la croissance de l'otolithe. D'après (Fablet 2006).

Ces différents développements méthodologiques ont été validés sur une base de 200 otolithes de plies des groupes d'âge 1 à 6 prélevés au 4ème trimestre en 1993 et 2000. Les taux de bonne estimation de l'âge sont de l'ordre de 80/90%, la référence étant fournie par l'interprétation d'un expert (Figure 12). Ces résultats sont illustrés pour la méthode d'estimation conjointe de l'âge et de la croissance. L'agrément à l'interprétation fourni

par l'expert (en termes de positionnement des marques) est supérieur à 95% dans le cas où l'âge est correctement estimé. Ces résultats sont pertinents pour un transfert vers l'opérationnel. Une validation à plus grande échelle doit être conduite pour déterminer les conditions d'application opérationnelle de ces développements, étant entendu qu'une prise en charge intégrale des estimations d'âge réalisées par les experts n'est pas envisageable (à la fois du fait de la nécessité de conserver une expertise interne mais également du fait même des caractéristiques intrinsèques de ces méthodes qui repose sur un apprentissage à partir de bases d'échantillons interprétés).
Ces travaux ont été réalisés dans le cadre d'une action incitative jeune chercheur 2003-2004 soutenu par la direction scientifique de l'Ifremer et poursuivi au sein du GdR Ifremer ACOMAR. Ils s'articulent autour d'une collaboration avec l'ENIB, les experts en estimation d'âge de l'Ifremer, et avec l'UPC (V. Parisi) dans le cadre du projet européen IBACS. Ces différents travaux ont également constitué la base du montage et de la coordination du projet UE STREP AFISA (2007-2009).

II.3.2 Méthodes robustes d'analyse quantitative de signaux extraits des otolithes

Synthèse des contributions: *Nous avons proposé différentes méthodes quantitatives d'analyse de signatures de l'otolithe (e.g., formes 2D, signaux d'opacité, signaux chimiques) pour la reconstruction de traits de vie individuels (analyse de séquences de macrostructures, discrimination d'espèces à partir de la forme de l'otolithe, reconstruction de profils migratoires à partir segmentation bayésienne de signaux chimiques de l'otolithe).*

Comme l'illustre partiellement les parties précédentes, la reconstruction des traits de vie individuels des poissons (e.g., âge, croissance, migrations, origine natale,...) ou de paramètres de leur environnement (e.g., température, salinité) à partir de l'analyse des otolithes a connu un essor important depuis plus d'une vingtaine d'années (Panfili, de Pontual et al. 2002). Les avancées récentes mettent en évidence la nécessité de développer des outils et méthodes plus puissants pour pleinement exploiter le potentiel des différentes de signatures structurelles et chimiques de l'otolithe (Fromentin, Ernande et al. 2009).

Dans ce contexte, nous nous sommes intéressés à la prise en compte des variabilités individuelles dans l'interprétation des signatures des otolithes. Deux applications ont plus particulièrement envisagées :

- l'analyse des séquences des macrostructures (anneaux) observées sur les otolithes pour des espèces pour lesquelles il n'existe pas de schéma d'interprétation validée de ces macrostructures (Courbin, Fablet et al. 2007);
- l'analyse de la forme de l'otolithe (Nasreddine, Benzinou et al. 2009; Nasreddine, Benzinou et al. 2010).

Ces deux applications reposent sur un principe similaire de définition d'une mesure de similarité prenant en compte les variabilités individuelles et exploitent des méthodes de recalage de signaux 1D. Nous en donnons ici le principe pour la caractérisation et la classification des formes 2D, thématique abordée dans le cadre de la thèse de K. Nasreddine (co-encadrement avec A. Benzinou, ENIB).

La forme de l'otolithe peut être utilisée pour identifier l'espèce voire le stock d'un individu. Ceci a constitué l'une des premières exploitations opérationnelles de l'otolithe comme marqueurs individuels (Campana, Casselman 1993; Panfili, de Pontual et al. 2002). La méthodologie employée consiste en général à représenter les formes 2D par des coefficients de Fourier à partir desquels sont conduits une classification (e.g., (Campana, Casselman 1993; Begg, Brown 2000; Duarte-Neto, Lessa et al. 2008)). Ces méthodes sont analogues aux approches de décomposition des formes sur des bases de fonction telles que les bases de Fourier ou les moments de Zernike, largement employées dans le domaine de la reconnaissance de formes (e.g., (Kim, Kim 2000; Zhang, Lu 2003)). Récemment, des mesures de similarité des formes fondées sur des critères de mises en correspondance ont rencontré un intérêt grandissant, du fait de leur capacité à gérer des invariances à des transformations géométriques plus complexes (par exemple des transformations affines ou non-rigides) (Younes 2000; Latecki, Lakamper 2002; Sebastian, Klein et al. 2003). L'approche proposée (Nasreddine, Benzinou et al. 2009; Nasreddine, Benzinou et al. 2010) consiste en une extension de (Younes 2000) et repose formellement sur la définition du critère variationnel suivant

$$D(F_1,F_2) = \min_{\Phi\in\Omega} \int_0^1 \sqrt{\Phi(s)} \cos\left[\left\|\theta_{F_1}(s) - \theta_{F_2}(\Phi(s))\right\|\right] ds$$

où F_1 et F_2 sont deux formes planes fermées, s l'abscisse curviligne de la courbe F_i considérée, $\theta_F(s)$ l'orientation de la tangente à la forme F_i au point s et Φ la fonction la fonction de mise en correspondance entre les deux formes. Les fonctions de mise en correspondance appartiennent l'ensemble des transformations admissibles Ω, c.-à.-d. des fonctions croissantes de [0,1] dans [0,1]. Des contraintes de régularité sont en outre imposées aux fonctions de recalage.

Exemples de formes de la base d'évaluation considérée (base MPEG-7)

Synthèse de l'évaluation quantitative de la méthode proposée par rapport à l'état de l'art

Method	Retrieval accuracy	Classification rate
Proposed scheme	**89.05%**	**98.86%**
String of symbols [Daliri and Torre, 2008]	85.92%	98.57%
Zernike moments [Direkoglu and Nixon, 2008; Kim and Kim, 2000]	70.22%	90%
Multiscale FD 2D [Direkoglu and Nixon, 2008]	*NA*	95.5%
Elliptic FD [Direkoglu and Nixon, 2008; Nixon and Aguado, 2007]	*NA*	82%
Shape tree [Felzenszwalb and Schwartz, 2007]	87.7%	*NA*
Inner-distance shape context (IDSC) [Ling and Jacobs, 2007]	85.40%	*NA*
Fixed correspondence + aggregated-pose chance probability functions [Super, 2006]	84%	97.4%
Fixed correspondence + Chance probability functions [Super, 2006]	83.04%	97.2%
Fixed correspondence [Super, 2006]	80.78%	97%
Hierarchical procruste matching [McNeill and Vijayakumar, 2006]	86.35%	95.71%
Multilayer eigenvectors [Super, 2006]	70.33%	*NA*
Normalized squared distance [Super, 2003]	79.36%	96.9%
Racer [Super, 2003]	79.09%	96.8%
Optimized CSS [Mokhtarian and Bober, 2003]	81.12%	*NA*
Curve edit distance [Sebastian et al., 2003]	78.17%	*NA*
Shape context [Belongie et al., 2002]	76.51%	*NA*
Parts correspondence [Latecki, 2002; Latecki and Lakamper, 2000]	76.45%	*NA*
Visual parts [Latecki and Lakamper, 2000]	76.45%	*NA*
Skeleton DAG [Lin and Kung, 1997]	60%	*NA*
Curvature Scale Space [Mokhtarian et al., 1996]	75.44%	*NA*
Wavelet [Chuang and Kuo, 1996]	67.76%	*NA*

Figure 13. Evaluation quantitative du critère proposé sur la base de formes MPEG-7, en termes de performances de reconnaissance et indexation, et aux méthodes de l'état de l'art : exemples de formes indexées dans la base MPEG-7 (haut), performances de reconnaissance de formes et de précision de recherche pour différences méthodes. D'après (Nasreddine, Benzinou et al. 2010).

Ce critère étend la proposition initiale de (Younes 2000) et améliore la robustesse aux erreurs locales de recalage, résultant par exemple d'occlusions partielles, à travers l'utilisation d'une norme robuste (ici, un estimateur de Leclerc est considéré (Black, Rangarajan 1996)). Ce critère étant défini à partir des orientations locales, il est naturellement invariant en translation et changement d'échelle. L'invariance en rotation est obtenue par la prise en compte dans l'ensemble des fonctions admissibles des rotations dans le plan. Cela revient en pratique à ne pas donner de contraintes sur la position de l'origine de chaque courbe (i.e., s=0). L'évaluation numérique du critère $D(F_1,F_2)$ résulte d'une minimisation par un schéma incrémental. L'évaluation de la méthode proposée conduite à la fois sur des bases génériques de traitement d'images et des bases d'images d'otolithes et d'autres biocarbonates démontre la robustesse du critère proposé vis-à-vis des solutions de l'état de l'art. A titre d'illustration est fournie la comparaison d'une méthode de classification de formes 2D, exploitant le critère proposé ci-dessus évalué à différentes échelles d'analyses d'une forme individuelle, à un ensemble de méthodes de l'état de l'art (Figure 13). Il faut souligner l'intérêt de la mesure de similarité de formes proposées tant vis-à-vis de techniques utilisant des critères locaux (e.g., Curvature Scale Space (Mokhtarian, Mackworth

1986)) que d'approches globales (e.g., descripteurs de Fourier (Campana, Casselman 1993; Begg, Brown 2000; Zhang, Lu 2003), moment de Zernike (Kim, Kim 2000)).

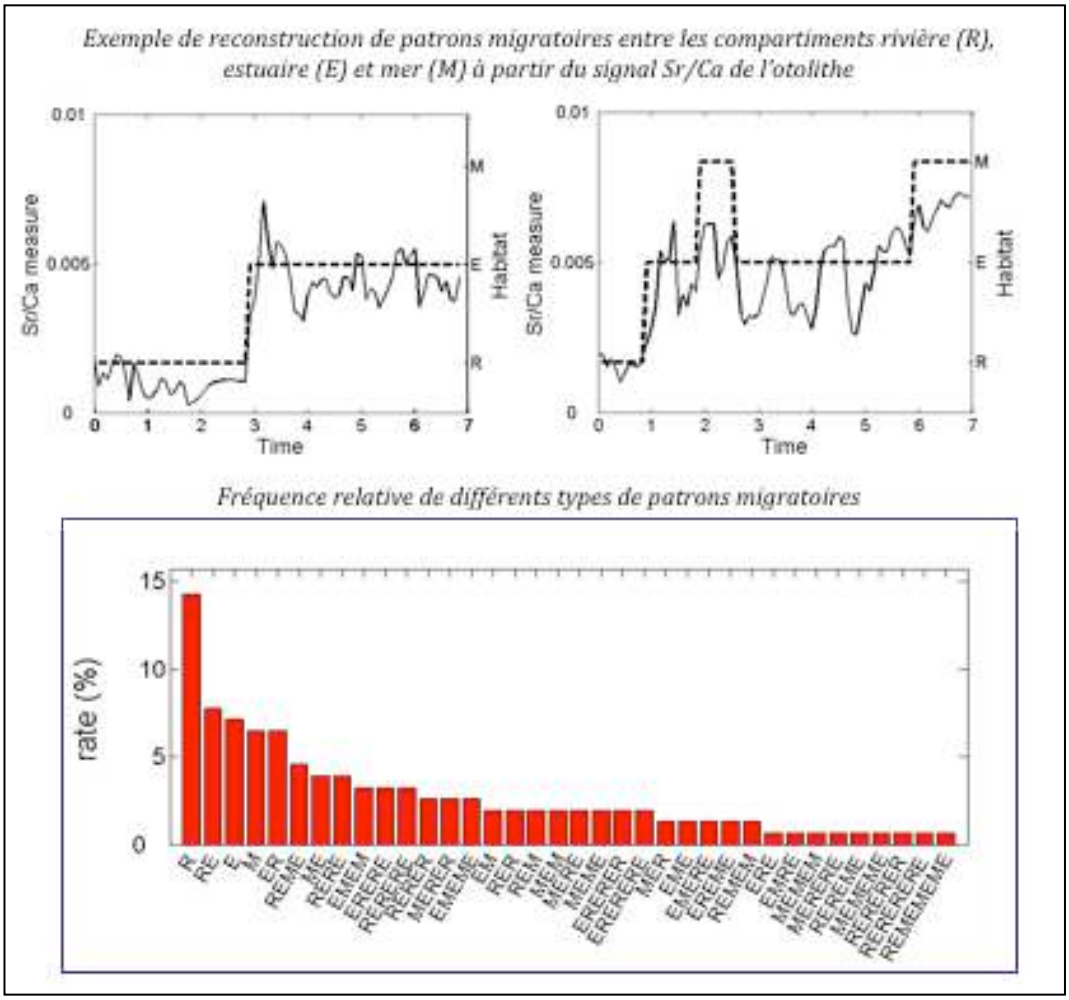

Figure 14. Analyse des séquences migratoires des anguilles en Gironde : exemples de reconstruction des séquences temporelles des migrations individuelles à travers les compartiments Rivière (R), Estuaire (E) et Mer (M), à partir de mesures du ratio Sr/Ca échantillonnées entre le nucleus et le bord de l'otolithe (haut) ; catégorisation automatique des trajectoires migratoires individuelles à partir des séquences de migrations et fréquences relatives de chaque type de tactique (e.g., la catégorie R correspond à un poisson qui est toujours resté dans le compartiment rivière, RE signifie que le poisson a passé une première phase en rivière puis a migré vers l'estuaire (bas). D'après (Fablet, Daverat et al. 2007).

Lorsque des marques (structurelles ou chimiques) sont indicatrices de changements d'état, il est critique de pouvoir disposer de méthodes robustes permettant la détection de ces changements dans une séquence temporelle et de reconstruire les séquences d'états successifs. A titre d'exemple, dans le cas de gradients importants des conditions environnementales, il a été montré pour un grand nombre d'espèces de poisson que l'otolithe est une archive du circuit migratoire réalisé par le poisson. Cette utilisation du potentiel d'archive de l'otolithe repose généralement sur l'analyse de signatures chimiques (eg, rapport Sr/Ca, isotopes du strontium,…) de l'otolithe sur un axe de croissance de référence (de Pontual, Geffen 2002; Elsdon, Gillanders 2006; Elsdon, Wells et al. 2008). Les travaux antérieurs se limitent toutefois le plus souvent à la démonstration du potentiel de l'archive, sans procéder à une reconstruction explicite des patrons migratoires par une approche quantitative. Nous avons proposé de formuler ce problème comme un problème inverse de traitement du signal : l'habitat (ou la zone géographique) étant considéré comme une variable cachée que l'on cherche à estimer à partir des observations (ici, les caractéristiques chimiques de l'otolithe sur un axe de croissance de référence). En exploitant un cadre bayésien non-supervisé (chaîne de Markov cachée), largement exploité en traitement du signal notamment pour la parole (Rabiner 1989), nous avons développé une méthode de reconstruction des séries temporelles des migrations individuelles à travers un nombre de compartiments finis à partir d'une séquence de signatures de l'otolithe. L'un des intérêts de cette méthode est d'introduire explicitement un modèle probabiliste des transitions entre compartiments. Dans le cadre d'une collaboration avec le CEMAGREF de Bordeaux (F.

Daverat), cette contribution méthodologique a été appliquée à la caractérisation des tactiques migratoires des anguilles dans l'estuaire de la Gironde. Il en résulte une analyse quantitative et une catégorisation non-supervisée des patrons migratoires d'un échantillon de 190 otolithes anguilles (Figure 14). Cette catégorisation ouvre de nouvelles perspectives pour l'étude des interactions entre tactiques migratoires et variations des traits de vie individuels (âge, croissance). Une extension multivariée de ce modèle dans le cas de signaux multi-élémentaires a également été proposée (Daverat, Martin et al. 2010). Il peut également être souligné que le modèle d'observation peut exploiter une prédiction linéaire fondée sur des informations complémentaires (e.g., régime du fleuve, saison, âge,...).

II.4 Synthèse

Ses propriétés d'archive des traits de vie individuels et des paramètres de l'environnement font de l'otolithe un outil particulièrement pertinent pour aborder de nombreuses questions d'intérêt en écologie halieutique, notamment pour comprendre et prédire les réponses des individus et des populations aux forçages naturels (changement climatique, acidification des océans, ...) et anthropiques (pêche, pollutions, ...). Son utilisation comme marqueur individuel dans un nombre croissant d'études publiées en est la parfaite illustration.
Dans ce contexte, les outils et méthodes développées constituent des contributions significatives à trois niveaux:

- en termes d'**extraction d'information** : nous avons notamment proposé la première méthode permettant de reconstruire la morphogenèse 2D de l'otolithe à partir d'une image (Fablet, Pujolle et al. 2008) et développé de l'utilisation de la spectrométrie RAMAN pour caractériser à une résolution très fine les fractions organiques et minérales de l'otolithe (Jolivet, Bardeau et al. 2008);
- en termes de **modélisation et calibration des signatures de l'otolithe** : nous avons introduit un modèle bioénergétique de formation de l'otolithe permettant de relier la formation de l'otolithe aux conditions environnementales rencontrées par le poisson (Fablet, Pecquerie et al. 2011). Cet outil constitue une plate-forme extrêmement prometteuse tant pour la simulation et prédiction des signatures des otolithes que pour la reconstruction de traits de vie individuels (Pecquerie, Fablet et al. 2012);
- en termes de **reconstruction de traits de vie individuels** : nous avons introduit différents outils conduisant à des améliorations significatives de l'exploitation du potentiel d'archive de l'otolithe en exploitant des outils avancés de traitement du signal et des images (apprentissage statistique, modèle bayésien, méthodes variationnelles) par exemple pour la discrimination d'espèces, la reconstruction de profils migratoires ou encore l'estimation de l'âge et de la croissance individuelle.

Le cadre multidisciplinaire du LASAA a constitué un élément déterminant pour conduire ces travaux, dont on peut souligner le caractère générique et la portée vis-à-vis des autres biocarbonates (e.g., coraux, coquilles de bivalves,...).

II.5 Sélection de publications représentatives de ce chapitre

Les publications suivantes sont des exemples représentatifs des contributions méthodologiques et thématiques relevant de ce chapitre :

- R. Fablet, F. Daverat, H. de Pontual. Unsupervised Bayesian reconstruction of individual life histories from otolith signatures: case study of Sr:Ca transects of eel (Anguilla anguilla) otoliths. Canadian Journal of Fisheries and Aquatic Science. 64:152-165, 2007.
- R. Fablet, S. Pujolle, A. Chessel, A. Benzinou, F. Cao 2D Image-based reconstruction of shape deformation of biological structures using a level-set representation. Computer Vision and Image Understanding, 111(3): 295-306, 2008.
- R. Fablet, L. Pecquerie, H. de Pontual, H. Hoie, R. Millner, H. Mosegaard, S.A.L.M Kooijman. Shedding light on fish otolith biomineralization using a bioenergetic approach. PLoS ONE, 2011.

Ces Publications sont fournies ci-après.

Available online at www.sciencedirect.com
ScienceDirect
Computer Vision and Image Understanding 111 (2008) 295–306
Computer Vision and Image Understanding
www.elsevier.com/locate/cviu

2D Image-based reconstruction of shape deformation of biological structures using a level-set representation

R. Fablet [a,*], S. Pujolle [a], A. Chessel [a], A. Benzinou [b], F. Cao [c]

[a] *Ifremer/LASAA, Otolith Research Laboratory, BP 70, Technopôle Brest-Iroise, 29280 Plouzane, France*
[b] *ENIB/RESO, Signal Processing Laboratory, Technopôle Brest-Iroise, 29280 Plouzane, France*
[c] *IRISA/VISTA, Computer Vision Group, Campus de Beaulieu, 35014 Rennes, France*

Received 11 August 2006; accepted 24 December 2007
Available online 15 January 2008

Abstract

This paper copes with the reconstruction of accretionary growth sequence from images of biological structures depicting concentric ring patterns. Accretionary growth shapes are modeled as the level-sets of a potential function. Given an image of a biological structure, the reconstruction of the sequence of growth shapes is stated as a variational issue derived from geometric criteria. This variational setting exploits image-based information, in terms of the orientation field of relevant image structures, which leads to an original advection term. The resolution of this variational issue is discussed. Experiments on synthetic and real data are reported to validate the proposed approach.
© 2008 Elsevier Inc. All rights reserved.

Keywords: Shape matching; Accretionary morphogenesis; Level-set representation; Inverse problem

1. Introduction and problem statement

A number of biological structures, for instance corals, seashells, fish otoliths,[1] tree trunks or vertebrae grow according to an accretionary process. In other words, they can be viewed as a succession of three-dimensional concentric layers (with respect to an initial core). The composition of these layers, in terms of crystalline organization and chemical features, vary according to endogenous and exogenous factors [27]. Often, the accretionary process is associated with a periodic, mainly daily or seasonal, scheme, such that the observation of these biological structures in an observation plane going through the initial core depict concentric ring patterns, also called growth marks, as illustrated in Fig. 1. These characteristics provide the basis for exploiting these structures as biological archives to define environmental proxies (e.g., for instance to reconstruct temperature and salinity sequences) [10] or to reconstruct individual life traits (e.g., individual age and growth information or migration paths) [19]. To further stress the key importance of these biological structures in marine ecology, it can be pointed out for instance that several millions of fish otoliths are analyzed each year for fisheries management.

New computational tools [18,19] are sought to improve the understanding, the modeling and the decoding of these biological archives. Their shape characteristics have been extensively exploited [5]. Though the presence of internal growth rings provide the mean for back-tracking the temporal evolution of the shape from the core to the outline, the actual analysis and reconstruction of this morphogenesis sequence have not been investigated. From an image processing perspective, the reconstruction of the morphogenesis of the considered biological structures within an observation plane[2] can be viewed as the reconstruction of

* Corresponding author. Fax: +33 298224653.
E-mail addresses: rfablet@ifremer.fr (R. Fablet), achessel@ifremer.fr (A. Chessel), benzinou@enib.fr (A. Benzinou), fcao@irisa.fr (F. Cao).
URLs: http://www.ifremer.fr/lasaa/rfablet (R. Fablet), http://www.enib.fr (A. Benzinou), http://www.irisa.fr (F. Cao).

[1] Fish otoliths are calcified structures present in fish inner ears.

[2] In the subsequent, the term "observation plane" will only refer to an observation plane containing the initial core of the analyzed biological structure.

1077-3142/$ - see front matter © 2008 Elsevier Inc. All rights reserved.
doi:10.1016/j.cviu.2007.12.005

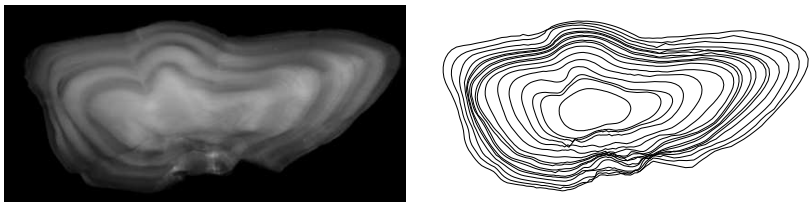

Fig. 1. Illustration of the goal of the paper: image of a pollock otolith in a given observation plane containing the growth center (left); reconstructed series of the evolved shapes (right).

the shape deformation history from the initial circular core to the observed outline as illustrated in Fig. 1. Mathematically sound solutions [8,35] have been proposed to determine the deformation path between any two shapes. The application of these schemes would however first require extracting the internal growth rings. Whereas the detection of the growth center and the detection of the external shape may be automated [6], the automated extraction of internal growth rings is a particularly complex task due to the presence of blind areas and so-called subjective contours [18,21]. As exemplified in Fig. 2, the application of techniques, such as edge filters [16], watershed transforms [2], level-set image transforms [24] or anisotropic diffusion [28], does not permit straightforwardly solving for this ring extraction issue. Low-level cues, in particular local image orientations [11], however, convey relevant information on the shape of thegrowth rings (Fig. 1).

The goal of this paper is to develop a well-founded variational scheme to combine such low-level cues with a view to reconstructing the accretionary growth shape history. Given that local image orientations can be regarded as estimations of the local growth directions, the determination of an accretionary growth shape sequence is stated as the estimation of the sequence of shape deformations from the initial core to the outline such that any intermediary shape should be normal to local image orientations. We adopt a level-set representation to model the accretionary growth process. Coupling a priori constraints on shape regularity and image-based information in terms of local shape orientation, the considered issue resorts to a varia-

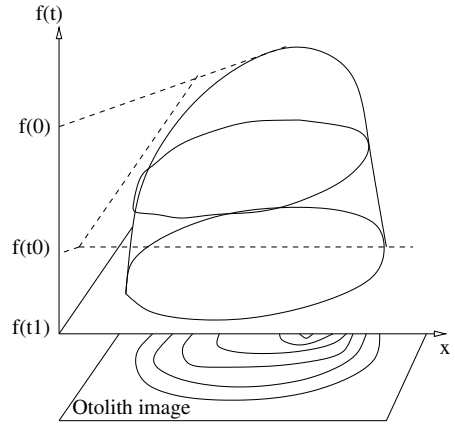

Fig. 3. Level-set representation of the accretionary growth process: the evolution of the shape is described by a potential function U, such that the growth shape at time t is given by level-line $\Gamma_t(U) = \{p \in \mathcal{R}^2 \text{ such that } U(p) = f(t)\}$ with f a continuous and strictly monotonic function.

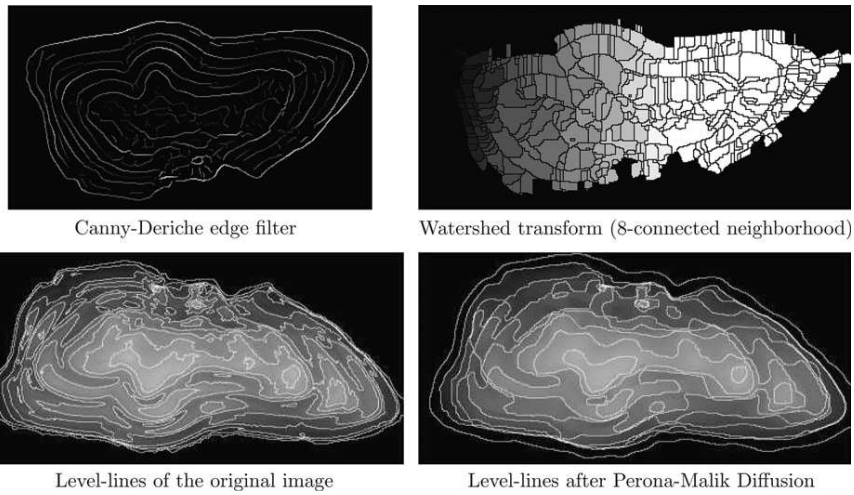

Fig. 2. Illustration of the complexity of the considered issue: result from the processing of the otolith image depicted Fig. 1 using standard line and region extraction techniques applied to the otolith image depicted in Fig. 1 (from top left to bottom right, Canny–Deriche edge filter [16], watershed transform [2], level-line extraction within the original image [24], level-line extraction after an anisotropic Peron–Malik diffusion [28]).

tional interpolation. This paper is organized as follows. Section 2 details the proposed variational framework. Minimization issue is described in Section 3. Experiments and concluding remarks are reported in Sections 4 and 5.

2. Proposed approach

2.1. Level-set setting

As suggested in the seminal work of Thompson [32], we adopt a level-set setting to represent the accretionary growth process (Fig. 3). It comes to introduce a potential function U defined over $\mathcal{R}^2$ such that the shape $\Gamma_t(U)$ of the considered biological structure within a given observation plane at time t is given by the level-set of U:

$$\Gamma_t(U) = \{p \in \mathcal{R}^2 \text{ such that } U(p) = f(t)\}, \quad (1)$$

where f is a strictly monotonic continuous function. Given U, the sequence of level-sets $\{\Gamma_t(U)\}_{[0,T]}$ represents the evolution of the shape from time 0 to time T. This representation conforms to the classical assumption that accretionary growth is locally normal to the shape. The growth increment at any point p is indeed inversely proportional to $\nabla U(p)$, which is, by definition, normal in p to level-set $\Gamma_{U(p)}(U)$.

Let us stress that this level-set representation is generic. Convex as well as non-convex shapes can be represented. Besides, secondary growth centers could also be taken into account, though this point is not investigated in this paper. In the field of computer vision, level-set representations are widely exploited, especially as contrast-invariant representations issued from the fast level-set transform [24], or as a tool to solve for variational segmentation issues [31]. In the latter case, the potential function is evolved according to a PDE such that its zero level-set corresponds to the boundary of the region interest. In our case, we do not only focus on a particular level-set but the overall series of level-sets is of interest as it represents the deformation history of the observed biological structures.

2.2. Geometric priors and orientation-based constraints

Given an image of the considered biological structure in a given observation plane, our goal is to reconstruct the potential function U associated with the underlying accretionary growth. Let us stress that the proposed level-set representation provides a relevant framework to solve for the inverse problem, since it intrinsically conveys the key geometric properties of the accretionary growth: concentricity and local parallelism of the successive level-sets. Besides, as shown below, such a representation offers a powerful tool to transform a purely geometric setting to a variational minimization issue.

Formally, we assume that we are given with some boundary conditions as illustrated in Fig. 4a: at least the shapes at times 0 and T, but additional constraints can be considered such as internal partial or complete growth rings. These conditions are stated as a set of points or curves for which the potential value is known. Let us denote by $\mathcal{B}$ this point set and $G_{\mathcal{B}}$ the associated potential values. By convention, potential value assigned to the shape at time T is zero and $G_{\mathcal{B}}$ also convey that U has to be null beyond the shape at time T. Solving for the reconstruction of U is then stated as the computation of its extension from $\mathcal{B}$ to the whole domain $\mathcal{R}^2$.

In addition, the image conveys relevant local geometric information in terms of orientations of the ring structures. Formally, we assume that an orientation field normal to local growth orientations is provided as illustrated in Fig. 4b. The interpolation of level-set representation U is then be constrained to be locally tangent to this orientation field. A first solution consists in considering orientation field $\omega(I) = \nabla I^{\perp}/|\nabla I|$ with I the image intensity. Obviously, for low gradient values, the computation of the orientation is highly noisy. However, the module of the image gradient can be considered as a meaningful relevance weight [26]. Hence, a confidence map $\alpha(I)$ is defined as $g(|\nabla I|)$, where g is a continuous stepwise function rescaled between 0 and 1. A second solution resorts to computing the orientation field as the s (Absolutely Minimizing Lipschitz Extension) of the orientations normal to the gradient measures selected by a thresholded Canny–Deriche edge filter [11,16]. As shown in [11], this procedure guarantees to extract smooth orientation field, which is expected to better constrain the reconstruction of the 2D morphogenesis. Let us denote by $\omega(I)$ the orientation field issued from image I and $\alpha(I)$ the associated local confidence map. When using AMLE orientation fields, confidence map $\alpha(I)$ is set to one.

Given boundary constraints $\{\mathcal{B}, G_{\mathcal{B}}\}$ and orientation constraints $\{\omega(I), \alpha(I)\}$, the extension of U to the whole

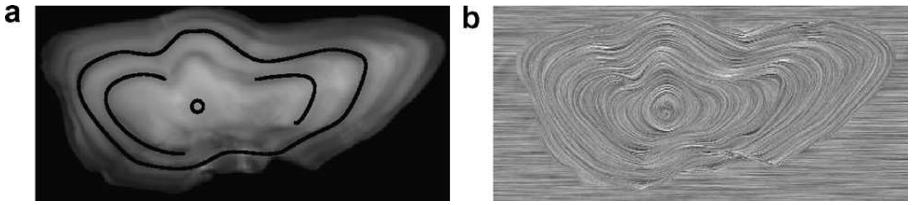

Fig. 4. Geometric priors and orientation-based information exploited to constrain the reconstruction of the accretionary morphogenesis: (a) example of boundary conditions given as a point or curve set for which potential values are known (depicted as black curve superimposed to the image of the considered biological structure), (b) example of orientation field computed from the image of the considered biological structure (the orientation field is visualized via its field line using LIC [4]).

domain $\mathcal{R}^2$ is defined as the minimization of an energy criterion E:

$$\widehat{U} = \arg \min_{U \in \mathcal{U}(G_{\mathcal{B}})} E(U), \tag{2}$$

where $\mathcal{U}(G_{\mathcal{B}})$ is the set of the functions from $\mathcal{R}^2$ to $\mathcal{R}$ whose restriction to $\mathcal{B}$ is $G_{\mathcal{B}}$. Energy $E(U)$ is split into two terms: a regularization term issued from a geometric shape prior and a data-driven term setting orientation-based constraints,

$$E(U) = (1-\gamma)E_R(U) + \gamma E_O(U,I), \tag{3}$$

where $E_R(U)$ is a shape regularity term, $E_O(U,I)$ a data-driven term and γ is a weighting factor balancing the relative influence of each term.

The chosen regularity criterion resorts to minimizing the perimeter of any growth shape $\Gamma_t(U)$. Hence, $E_R(U)$ is defined as the sum over all level-sets of the unity function:

$$E_R(U) = \int_{t\in[0,T]} \int_{p\in\Gamma_t(U)} 1 \tag{4}$$

The second energy term $E_O(U,I)$ evaluates how level-lines of U conform to local growth orientations $\omega(I)$. Any shape $\Gamma_t(U)$ is expected to be normal to orientation field $\omega(I)$. Given that $\Gamma_t(U)$ is a level-line of U, this is equivalent to the orthogonality between growth directions $\nabla U/|\nabla U|$ and orientations $\omega(I)$ along $\Gamma_t(U)$. Therefore, summing over all level-lines of U, $E_O(U,I)$ is defined as

$$E_O(U) = \int_{t\in[0,T]} \int_{p\in\Gamma_t(U)} \alpha(I,p)\cdot\rho\left(\left\langle \frac{\nabla U(p)}{|\nabla U(p)|}, \omega(I,p)\right\rangle\right), \tag{5}$$

where ρ is an error function. In order to account for outliers, a robust function is exploited [22]. Compared to a classical quadratic term, it ensures the robustness to local incoherences within orientation field w. In the subsequent, ρ is set as $\rho(x) = |x|$. For the sake of simplicity, fields $\omega(I)$ and $\alpha(I)$ are referred to as ω and α in the subsequent.

2.3. Variational framework

The above definition of the energy criterion is issued from the summation over all level-lines of U. The direct minimization of $E(U)$ from this formulation is then infeasible since it first implies to extract all level-lines of U. The solution comes from the co-area formula which supplies us with an equivalent computation over $\mathcal{R}^2$. More precisely, for any function Ψ, the following result applies [23]:

$$\int_{t\in[0,\inf]} \int_{p\in\Gamma_t(U)} \Psi = \int_{p\in\mathcal{R}^2} |\nabla U|\Psi. \tag{6}$$

Norm $|\nabla U|$, inherited from the co-area transform, can be viewed as a weight which gives more influence to points where the gradient of the level-set representation is high (conversely, where the growth is slow).

Using the formulations of energy terms $E_R(U)$ and $E_RO(U)$, we resort to the following variational issue:

$$\widehat{U} = \arg \min_{U\in\mathcal{U}(G_{\mathcal{B}})} \int_{p\in\mathcal{R}^2} (1-\gamma)\cdot|\nabla U| + \gamma\cdot\alpha\cdot|\langle\nabla U,\omega\rangle|. \tag{7}$$

The reconstruction of the series of growth shapes can then be regarded as a variational interpolation of the potential field U given boundary constraints $G_{\mathcal{B}}$. The minimization to be solved for involve two classical terms that are encountered in the resolution of inverse problems for two-dimensional data, for instance in image analysis [30]. The first term is as regularization term computed as a function of the norm of the image gradient. Here, we resort to the total variation criterion, widely exploited for image denoising [17,30]. Contrarily to a quadratic criterion, the minimization of the total variation is associated to an anisotropic diffusion, better accounting for geometric image structures. The second term, often referred as the data-driven term, aims at aligning the orientation field of U to orientation constraints ω. A similar term has been used for the reconstruction of dense orientation fields in fingerprint images within a quadratic Markovian setting [15]. We may also stress that the summation over $\mathcal{R}^2$ in criterion (7) is naturally restricted to the actual image domain as the search space $\mathcal{U}(G_{\mathcal{B}})$ for function U is constrained to functions being null beyond the shape at final time T. Hence, minimizing criterion (7) over $\mathcal{R}^2$ and over the actual image domain is formally equivalent.

2.4. Additional constraints

Minimization (7) is issued from purely geometric constraints. As level-set representations are contrast invariant (i.e., a contrast change does not affect the geometry of the level-sets but only the indexes of the level-sets) [24], additional constraints on U are needed to numerically solve for Eq. (7). For instance, if the boundary set is given by the growth center at time 0 and the final shape at time T, solving for Eq. (7) converges to an unstable solution constant everywhere except at the point corresponding to the growth center.

To account for this issue, a theoretical solution would be that the surface between two successive level-lines $\Gamma_t(U)$ and $\Gamma_{t+\mathrm{d}t}(U)$ is constrained by the instantaneous accretionary deposit at time t. Since the actual instantaneous growth rate is generally unknown, we cannot straightforwardly exploit this constraint. However, the relationship between this growth function and the partition function of U can be exploited. More precisely, the surface of the shape $\Gamma_t(U)$ can be evaluated as the surface of the domain for which the potential function U is above $U(t)$. The growth function of the shape $\Gamma_t(U)$ is then proportional to the partition function P_U of U, defined by:

$$P_U(\lambda) = \int_{p\in\mathcal{R}^2 \text{ such that } U(p)>\lambda} \mathrm{d}p.$$

Hence, setting constraints on the growth rate of the surface of $\Gamma_t(U)$ is equivalent to considering a prior on the first-order statistics p_U of U. For the sake of simplicity, the uniform distribution has been selected in this work, but other priors might be relevant. Let us stress that changing from one prior to another simply consists in a contrast change.

Hence, the variational interpolation finally comes to solve for

$$\min_{U\in\mathcal{U}(G_B)} \int_{p\in\mathcal{R}^2} (1-\gamma)\cdot|\nabla U| + \gamma\cdot\alpha\cdot|\langle\nabla U,\omega\rangle|, \tag{8}$$

subject to $p(U)$ is uniform.

3. Numerical resolution

To solve for the above constrained minimization, we adopt a two-step iterative approach: the first step comes to project the current solution onto the set of level-representations with uniform first-order statistics. We detail below the unconstrained minimization. To improve the convergence, a multiresolution framework is adopted.

3.1. Unconstrained minimization

To solve for the minimization of E with respect to U, Euler–Lagrange equations [1] provide the expression of the gradient of E. Given that the L1 norm is not derivable in zero, it is approximated as $\sqrt{\epsilon^2+x^2}$. We let the reader refer to [30] for the analysis of the total variation criterion whose gradient is given by:

$$\frac{(\epsilon_R^2+U_x^2)U_{xx} - 2U_yU_xU_{xy}^2 + (\epsilon_R^2+U_y^2)U_{yy}}{(\epsilon_R^2+\nabla U^2)^{3/2}}. \tag{9}$$

Neglecting the variations of the weight α,[3] the second energy term leads to the following gradient:

$$\begin{aligned}\Psi(U) &= div\left(\frac{\langle\nabla U,\omega\rangle\omega}{(\epsilon_D^2+\langle\nabla U,\omega\rangle^2)^{1/2}}\right)\\ &= \frac{div(\omega)\langle\nabla U,\omega\rangle}{(\epsilon_D^2+\langle\nabla U,\omega\rangle^2)^{1/2}} + \frac{\epsilon_D^2\langle\nabla\nabla U\cdot w+\nabla\omega\cdot\nabla U,\omega\rangle}{(\epsilon_D^2+\langle\nabla U,\omega\rangle^2)^{3/2}},\end{aligned} \tag{10}$$

where div is the divergence operator, $\nabla\nabla U_p$ the Hessian matrix of U at point p, and $\nabla\omega(p)$ the gradient matrix $(\nabla w_{p,x};\nabla w_{p,y})$ with $\omega_{p,x}$ and $\omega_{p,y}$ the horizontal and vertical component of ω_p.

The expression of $\Psi(U)$ can be compared to PDEs proposed for anisotropic image smoothing which reduces to $div(\langle\nabla U,\omega\rangle\omega)$ in the case of the smoothing along a single direction ω [33,34]. The first term is a weighted version of advection term $\langle\nabla U,\omega\rangle$. This advection equation corresponds to the transport of a scalar quantity U preserved by a vector field ω, for instance the transport of temperature by wind and currents in meteorology and oceanography. The weighting factor depends on $div(\omega)$. If ω is issued from the actual morphogenesis potential function, $div(\omega)$ is the curvature of the true (but unknown) successive growth shapes to be reconstructed. The second term involved in the expression of $\Psi(U)$ is a weighted version of the diffusion operator along the field lines of ω, $\omega^T\nabla\nabla Uw+\omega^T\nabla\omega\nabla U$, as proposed in [33] for curvature-based regularization of images.

Assuming $div(\omega)\neq 0$, the steady-state of the evolution equation $dU/dt=\Psi(U)$ reduces to an advection equation

$$\langle\nabla U,\omega\rangle = 0. \tag{11}$$

Let us recall that $\sqrt{\epsilon^2+x^2}$ is used as a numerical approximation of the L1 norm $\|x\|$, such that $|\epsilon_D|\ll sup(x)$. Solutions to $dU/dt=0$ should then be valid for any value $0<\epsilon_D\lll sup(x)$. Hence, any function U such that $\langle\nabla U,\omega\rangle\neq 0$ on a given neighborhood could not satisfied $\Psi(U)=0$ for some values of $\epsilon_D\lll sup|\langle\nabla U,\omega\rangle|$. Besides, functions verifying $\langle\nabla U,\omega\rangle=0$ are obvious solutions of the steady-state equation $dU/dt=0$. The assumption that $div(\omega)\neq$ is further discussed and motivated below.

From this steady-state equation, the existence and the uniqueness (up to a contrast change) of the solution of the considered inverse problem can be derived.

Proposition 1. *Let ϕ be a potential function such that $\nabla\phi\neq 0$ and $div(\nabla\phi^\perp/|\nabla\phi|)\neq 0$. Let ω be the orientation field tangent to the level-lines of Φ.*

Let U be a potential function such that $\nabla U\neq 0$. U is a solution of Eq. (11) if and only if it exists a strictly monotonic continuous and derivable function g such that $U=g(\Phi)$.

Proof. As $\omega=\nabla\phi^\perp/|\nabla\Phi^\perp|$, $div(\omega)\neq 0$. Hence, Eq. (11) is equivalent to $\langle\nabla U,\omega\rangle=0$. As the level-lines of a field U can be defined as the lines tangent to $\nabla U^\perp$, the latter equation imposes level-lines of U and Φ to be aligned. It then exists a continuous and derivable function g such that $U=g(\Phi)$. Given that $\nabla U\neq 0$ and $\nabla\phi\neq 0$, g is strictly monotonic.

Reciprocally, potential function $U=g(\Phi)$, with g a strictly monotonic continuous and derivable function, is a solution of Eq. (11) □.

This proposition guarantees that, if direction field ω is the direction field of an unknown potential function, the solutions of Eq. (11) are transformed versions of this unknown potential function with respect to a contrast change. Note also that this is only valid for a domain on which $div(\nabla\phi^\perp/|\nabla\phi|)\neq 0$. Assuming that only isolated points do not fulfill this condition, this results can be extended to the whole domain by continuity. Condition $div(\nabla\phi^\perp/|\nabla\phi|)\neq 0$ indeed resorts to considering that the curvature of the level-lines is not null. Formally, such an assumption seems reasonable for the studied biological phenomena: they rather involve round or elliptic growth shapes and the formation of growth shapes involving perfect straight lines seems unlikely. From a numerical point of view, numerical unstabilities have however been observed

[3] It should be stressed that this confidence map is actually exploited only with orientation fields computed from image gradients.

in practice when using directly the gradient-descent issued from Euler–Lagrange equations. These numerical unstabilities may be due to weighting factor $div(\omega)$ since growth shapes far from the growth center tend to become locally closer to straight lines. Consequently, to ensure a better numerical resolution, we prefer exploiting an explicit Gauss-Seidel scheme. Given that Eq. (11) does not lead to a linear system, the Gauss-Seidel scheme is derived from the discrete version of the considered variational criterion. Considering a finite difference approximations of $|\nabla U|$ similar to Markovian setting [20,25], we resort to:

$$(1-\gamma)\sum_{(p,q)\in\mathcal{N}}\rho_{\epsilon_R}(U_p-U_q)+\gamma\sum_{p\in\mathcal{R}^2}\alpha_p\cdot\rho_{\epsilon_D}(\langle\nabla U_p,\omega_p\rangle), \tag{12}$$

where $\mathcal{N}$ is the four-neighborhood system and (i.e., the neighborhood of a point is given its four western, northern, eastern and southern neighbors in the image). The minimization of the discrete energy involving robust functions is carried out using an iterated reweighted least square (IRLS) scheme, which iterates two steps: the computation of robust weights

$$\beta_R(p,q)=\phi_R(U_p-U_q) \tag{13}$$

and

$$\beta_D(p)=\phi_D(\langle\nabla U_p,\omega_p\rangle), \tag{14}$$

where function ϕ is the influence function associated with robust estimator ρ computed as $\phi(x)=\rho'(x)/x$ (these robust weights are low for high residual error, i.e., outliers, and high for low residuals); and solving for the weighted least square minimization

$$\min_{U\in\mathcal{U}(G_B)}(1-\gamma)\sum_{(p,q)\in\mathcal{N}}\beta_R(p,q)\cdot|U_p-U_q|^2+\gamma\sum_{p\in\mathcal{R}^2}\alpha_p\cdot\beta_D(p)\cdot\langle\nabla U_p,\omega_p\rangle^2 \tag{15}$$

given robust weight maps β_R and β_D. This least square estimation is indeed solved for using a Gauss-Seidel scheme. U_p is iteratively updated by explicitly solving for the quadratic minimization (15) under the assumption that U is constant except at point p. The associated computations based on a centered numerical approximation of ∇U_p are detailed in Annex. It might be stressed that this explicit Gauss-Seidel scheme automatically adapts to the range of values chosen for potential function U. Only the stopping criterion of this minimization procedure should be set wrt the difference between the maximum and minimum values of U (that is to say the values of U for the shape at time 0 and T). In our implementation, the stopping criterion is set to 0.001 times this difference.

3.2. Reprojection onto the constrained subspace

The projection of the current solution U onto the set of level-set representation with uniform first-order statistics can be viewed as an histogram equalization. As histogram equalization can be implemented as a PDE scheme [7], constrained minimization (8) could be solved by coupling the PDE issued from the gradient of E to the one proposed in [7]. However, as stressed above, such a PDE-based scheme is numerically unstable and a discrete Gauss-Seidel minimization scheme is preferred. The histogram equalization is applied as a second step after the Gauss-Seidel loop. Given $\widetilde{U}$, the distribution of the potential values $p(\widetilde{U}$ is computed as well as their cumulative distribution $F(\widetilde{U})$. Aligning $F(\widetilde{U})$ to line $y=x$ provides us with a contrast change approximately leading to a uniform distribution $p(U)$. As stressed previously, this transformation does not modify the geometry of the level-lines but only their relative potential values.

3.3. Multiresolution minimization

Minimization (7) is obviously not convex. To ensure a better robustness to the initialization, a multiresolution scheme is used. Given a Gaussian pyramid of the orientation field ω [3], the multiresolution approach comes to solve for the estimation of the potential function U at successive resolutions, from the coarsest resolution to the finest one. The final estimate at a given resolution serves as the initialization at the next resolution. In practice, Gaussian pyramids with four levels were exploited.

3.4. Initialization

The computation of a relevant initialization to the proposed gradient-based multiresolution scheme is important to ensure a fast and relevant convergence. The initialization is delivered by the scalar AMLE (Absolutely Minimizing Lipschitz Extension) of the boundary conditions to the whole domain [9]. Since the AMLE resorts to the minimization of the L_∞ norm, the AMLE can be viewed as the less smooth interpolation operator among all smooth interpolation operator. The AMLE is implemented as gradient descent $\partial U/\mathrm{d}t=U_{\nabla\nabla}$ where $U_{\nabla\nabla}$ is the second-order derivative in the direction of the gradient of U. It is shown to converge to the unique AMLE. The key properties of the AMLE is that it is an artifact-free and oscillation-free interpolant actually capable of taking into account isolated boundary points as well as curves.

4. Results

4.1. Extraction of the orientation fields

The proposed approach initially relies on the extraction of orientation field ω. As detailed previously, orientation field $\omega=\nabla I/|\nabla I|$ computed from the image gradient ∇I is first investigated. The second solution comes to computing ω as the AMLE of the orientations of the gradient measures selected by a thresholded Canny–Deriche edge filter [11,16]. Fig. 5 reports the orientation fields issued from

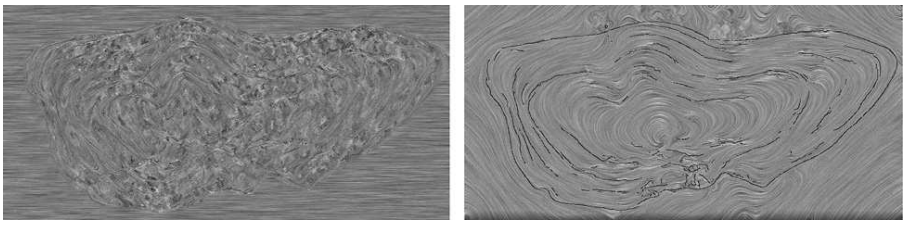

Fig. 5. Examples of extracted growth orientation fields from local image orientations for the image of a pollock (*Pollachius pollachius*) otolith depicted in Fig. 1: visualization of the orientation field issued from the image gradient (left), visualization of the orientation field computed as the AMLE (Absolutely Minimizing Lipschitz Extension) of automatically selected gradient measures depicted by black lines (right). Orientation fields are visualized via their field lines using LIC) [4].

these two schemes for the image depicted in Fig. 1. These orientation fields are visualized via their field lines, using Line Integral Convolution (LIC) [4]. As expected, orientation field $\omega = \nabla I/|\nabla I|$ is not globally coherent and only orientation information along image contours may be meaningful. On the contrary, the AMLE orientation field is much smoother. It conveys relevant geometric cues, which are expected to better constrain the reconstruction of the 2D morphogenesis.

4.2. Examples of reconstruction of the series of growth shapes

To illustrate the different steps of our approach, we first display the reconstruction of the history of growth shapes for the pollock otolith image previously depicted in Fig. 1. The results of the reconstructions of the morphogenesis associated with the orientation fields issued from the image gradient and the AMLE scheme are compared in Fig. 6. Besides, reconstructions issued for two different configurations of boundary constraints G_B: the first example only involves the position of the growth center, whereas the growth center as well as the first translucent ring is given in the second example. Parameters γ, ϵ_R and ϵ_D are, respectively, set to 0.6, 0.1 and 0.1 for the first case and to 0.9, 0.1 and 0.1 for the latter. Equally sampled level-lines $\{\Gamma_t(U)\}$ superimposed to the otolith image are reported. Due to the weaker coherence of the gradient-based orientation field, the minimization of the variational criterion does not lead to very regular level-lines in that case. If only the growth center is provided, such orientation information is not sufficient to reconstruct relevant growth shapes, especially for the first two rings. The additional boundary constraint given as the first bright ring permits to greatly improve the reconstruction of the series of growth shape. The results issued from the AMLE orientation field clearly depict more regular shapes which fit to the internal otolith structures. In addition, the two boundary constraints lead to very similar results: few differences can be observed and mainly occur in the ventral lobe (left part) of the first translucent ring. Concerning computational time, the proposed scheme is implemented as a C code under linux and runs in about half a minute for a 500×1000 image. To illustrate the role of the two energy terms involved in the proposed variational formulation, results are reported for the two configurations processed in Figs. 7 and 8 setting

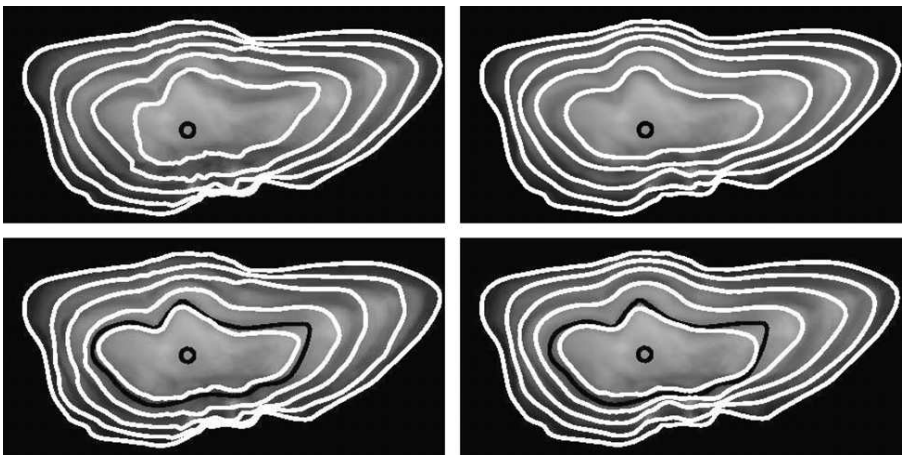

Fig. 6. Reconstruction of the series of growth shapes for the pollock (*Pollachius pollachius*) otolith image depicted above: first row, reconstruction given the otolith center using the gradient-based (left) and AMLE (right) orientation fields; second row, reconstruction given the otolith center and the first opaque ring using the gradient-based (left) and AMLE (right) orientation field. Parameter ϵ is set to 0.1. The constraints (i.e., the otolith center and the first opaque ring) are superimposed to the otolith image as black curves, and the equally sampled level-sets of the reconstructed potential function U as white curves.

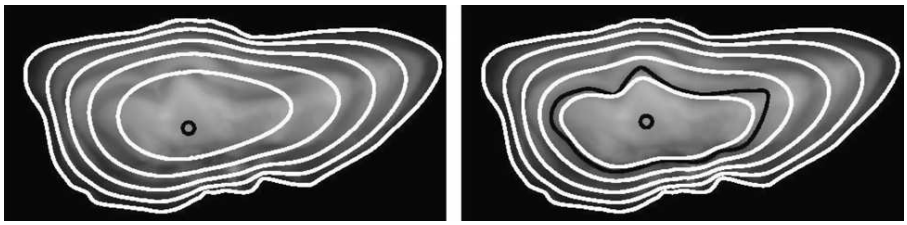

Fig. 7. Reconstruction of the series of growth shapes for the pollock (*Pollachius pollachius*) otolith image depicted above setting γ to 0 (i.e., using only the regularization term): left, given the otolith center; right, given the otolith center and the first opaque ring. In both cases, the constraints (i.e., the otolith center and the first opaque ring) are superimposed to the otolith image as black curves, and the equally sampled level-sets of the reconstructed potential function U as white curves.

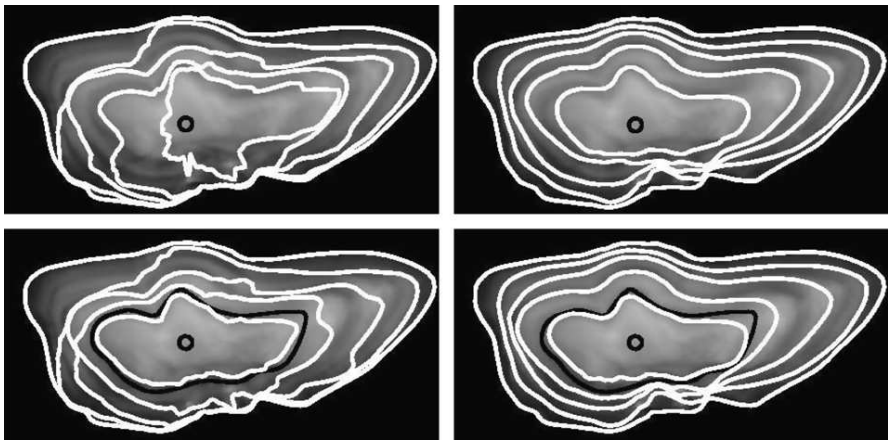

Fig. 8. Reconstruction of the series of growth shapes for the pollock (*Pollachius pollachius*) otolith image depicted above setting γ to 1 (i.e., using only the data-driven term): first row, results are obtained knowing the position of the growth center using the gradient-based (left) and AMLE (right) orientation fields; second row, reconstruction knowing the otolith center and the first opaque ring using the gradient-based (left) and AMLE (right) orientation field. Parameter ϵ is set to 0.1 and weighting factor. The constraints (i.e., the otolith center and the first opaque ring) are superimposed to the otolith image as black curves, and the equally sampled level-sets of the reconstructed potential function U as white curves.

γ to 0 and 1. If only the regularization term is exploited, the reconstruction of the shapes only relies on the geometric prior set in terms of shape regularity and can be viewed as a shape matching example [8,35]. Such prior does not however permit to reconstruct relevant shape deformations if only the growth center and the otolith outline is provided. The quality of the reconstruction clearly improves if additional boundary constraints are added. While results reported using the AMLE orientation field appear very similar for $\gamma = 1$ (Fig. 8) and $\gamma = 0.9$ (Fig. 6). It is however preferable to impose some minimum regularity (i.e., $\gamma < 1$) in order to deal with potential local incoherences of the AMLE orientation field. This is indeed further illustrated when the gradient orientation field are used, since the minimization of the variational criterion with $\gamma = 1$ does not lead to a meaningful configuration even if the first translucent ring is provided (Fig. 8). Practically, a trade-off has to be achieved between regularity and conformity to the orientation field.

With a view to investigating this aspect, experiments are carried out for synthetic data. The synthetic image is created as follows. For the otolith image depicted in Fig. 1, the boundary constraints defined by the set of all translucent rings were exploited to extract a sequence of otolith shapes using only the regularization term (i.e., $\gamma = 0$). The values of potential function U are then converted to intensity using a modulated sinusoidal mapping to generate an image depicting a sequence of dark and bright rings. This image is corrupted by a centered Gaussian noise with a standard deviation of 10. This test image is associated with a reference potential function U_{GT} which can be used as a reference for performing a quantitative evaluation. Such a quantitative evaluation is reported in Fig. 9. Both the performances of the variational setting combined to gradient-based and AMLE orientation fields were evaluated as a function of the weighting factor γ. These results further stress that the AMLE scheme is more robust and more stable. As confirmed empirically for real images, γ values between [0.8,1[correspond to the best trade-off between regularity and conformity to orientation data.

To further illustrate the flexibility of the proposed scheme, an example of reconstruction of the growth shapes is carried out using additional constraints given as annotated segments of an internal ring (Fig. 10). This example demonstrates the capability of the proposed variational scheme to take such constraints into account in order to

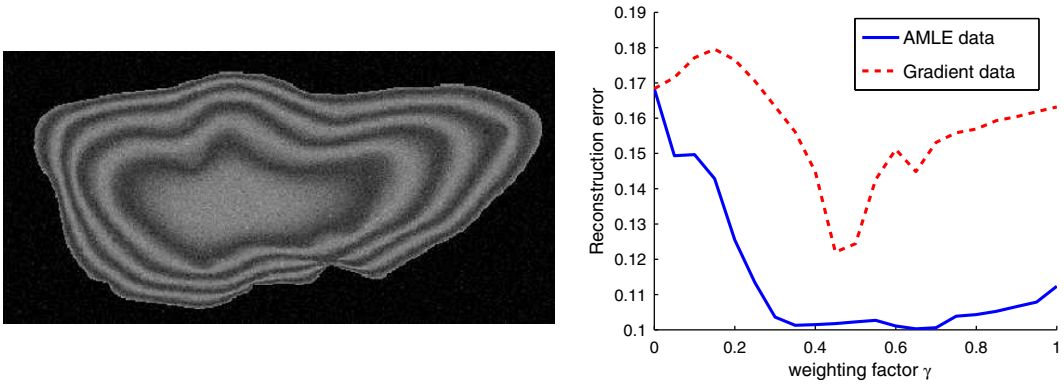

Fig. 9. Influence of the weighting factor γ on the reconstruction error for a synthetic otolith image: left, noisy synthetic otolith image; right, reconstruction error using gradient-based and AMLE orientation field as a function of the weighting factor γ.

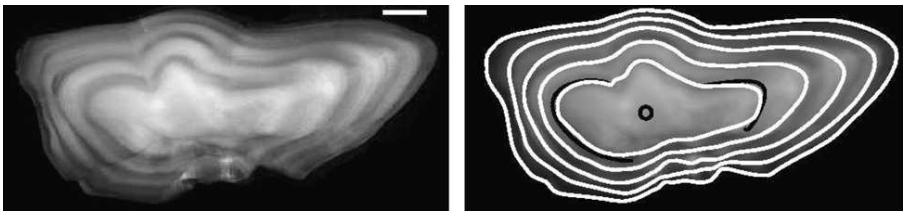

Fig. 10. Reconstruction of the series of growth shapes for the pollock (*Pollachius pollachius*) otolith processed for boundary constraints given by the position of the growth center and two segments of the first opaque ring: original image (left), series of shape superposed to the otolith image (right column). These experiments have been carried out using the AMLE orientation field to compute the data-driven term. Boundary constraints are depicted as black curves in the images.

improve the reconstruction of the shapes compared to the results reported above.

Experiments for three other fish species, namely plaice (*Pleuronectes platessa*), cod (*Gadhus morua*) and hake (*Merluiccius merluccius*), as well as the section of a tree trunk, are presented in Figs. 11 and 12). Obviously, better results are recovered for the plaice otolith and the section of a tree trunk, which involves the clearest structure. The

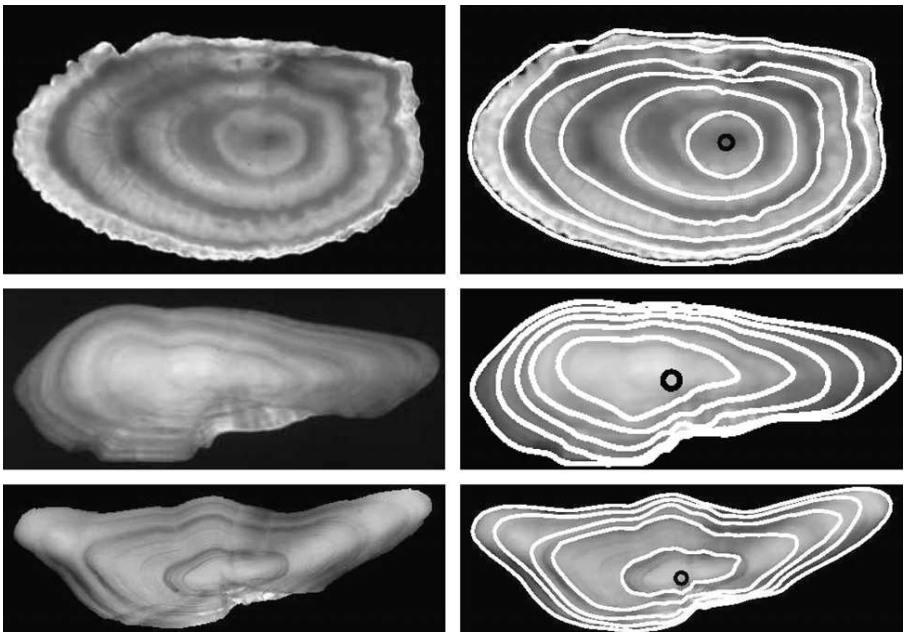

Fig. 11. Reconstruction of the series of growth shapes for three examples of fish otoliths: a plaice (*Pleuronectes platessa*) otolith (first row), a cod (*Gadhus morua*) otolith (second row), and a whiting (*Merlangius merlangus*) otolith (third row. For each row, the otolith image and the series of shape superposed to the otolith image are reported. The same parameter setting as in the previous experiments is used.

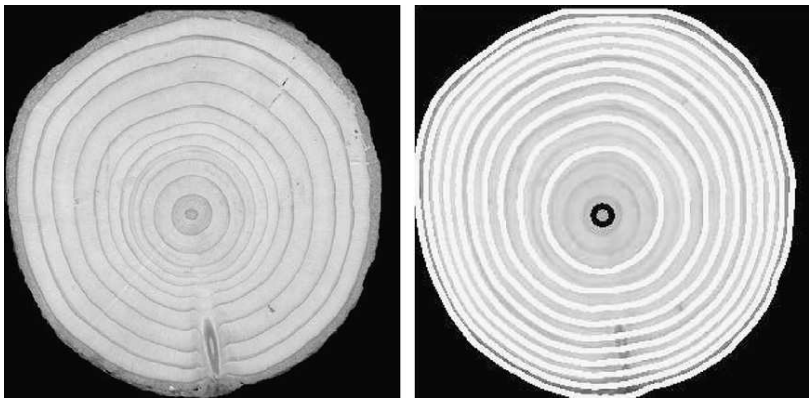

Fig. 12. Reconstruction of the series of growth shapes of the section of a tree trunk: original image (left), reconstructed potential function U (left column), series of shape superposed to the image of the section of the tree trunk (right column). These experiments have been carried out using the AMLE orientation field to compute the data-driven term. The growth center is depicted as a black circle.

results reported for the whiting (*Gadhus morua*) and cod (*Merlangius merlangus*) otoliths demonstrate that we are also capable of approximately recovering the complex and non-uniform evolution of such shapes from lower-contrasted images.

5. Discussion

We have proposed a scheme aimed at reconstructing from an image the evolution of the shape of biological structures involving accretionary growth process. Its key feature is a level-set representation, which intrinsically accounts for the major characteristics of the accretionary growth process. From purely geometric criteria on shape regularity and on local orientation coherence with respect to the observed image, a variational formulation is derived. The associated minimization is efficiently solved for within a discrete robust multiresolution framework. Reported results on synthetic and real data provides a validation of the proposed approach. In particular, it demonstrates that AMLE orientation fields should be preferred to the orientation of image gradient since it conveys more relevant geometric information on image structures than image gradients.

As far as the comparison to related work is concerned, the proposed approach is, to our knowledge, the first contribution aimed at reconstructing accretionary growth sequences of biological structures from images. As shown in Fig. 2, the application of computer vision techniques, such as edge filters [16], watershed transforms [2], level-set image transforms [24] applied to the original grey-level image or to the image pre-processed by an anisotropic diffusion [28], cannot straightforwardly lead to the reconstruction of the growth level lines. The considered class of biological images depict rather simple geometric structures. Due to a low-contrast of these geometric structures and the presence of subjective contours and/or blind areas, the reconstruction of the geometric information is far from trivial and motivates the development of a computationally more involved approach as presented in this paper.

In future work, several refinements and extensions will be investigated. Whereas uniformity constraints set to the distribution of potential function U are exploited to solve for minimization (7), other constraints more closely related to growth dynamics (for instance, a mean growth model) might also be exploited. New regularization term $E_R(U)$ will also be investigated to encode a priori knowledge on shape statistics, for instance using an exemplar-based setting [13,14,29]. Our specific interest will be in shape priors encoding the dynamics of the growth of the shape. 3D morphogenesis reconstruction may also be considered as an extension of this work from the joint analysis of several observation planes. Besides, improvements should be obtained from iterations between the extraction of the low-level cues (the orientation fields) and the reconstruction of the shape deformation history. Such iterated process would benefit from orientation-adapted processing of the original image [12,33] to extract the considered low-level cues given a current estimate of the shape deformation history. This contribution also provides the basis for the development of improved pre-processing (for instance, orientation-based image filtering) and information extraction (growth axis, growth rings) tools [12] for the considered biological images. In the field of marine ecology, new issues can also be investigated in terms of understanding and modeling of biocalcification and accretionary growth process.

Acknowledgments

We are grateful to A. Alvarez, A. Christensen, H. Mosegaard, M. Palmer and H. de Pontual for fruitful discussions. We also thank the anonymous referees for their helpful comments on the early version of the manuscript. This work has been carried out with the financial support from the Commission of the European Communities, spe-

cific program "Specific Support to Policies", SSP8-044132 "AFISA". It does not necessarily reflect its views and in no way anticipates the Commission's future policy in this area. This work has also been supported by national ANR grant "OTOCAL".

Appendix. Potential update

The local update of potential U at point p to solve for Eq. (15) relies on a centered gradient approximation and is computed as:

$$U_p = \frac{(1-\gamma)\sum_{q\in\mathcal{N}_p}\beta_R(p,q)\cdot U_q + \gamma\sum_{q\in\mathcal{N}_p^H}\beta_D(q)\omega_{q,x}\langle A_{p,q},\omega_q\rangle + \gamma\sum_{q\in\mathcal{N}_p^V}\beta_D(q)\omega_{q,y}\langle B_{p,q},\omega_q\rangle}{(1-\gamma)\sum_{q\in\mathcal{N}_p}\beta_R(p,q) + \gamma\sum_{q\in\mathcal{N}_p^H}\beta_D(q)\omega_{q,x}^2 + \gamma\sum_{q\in\mathcal{N}_p^V}\beta_D(q)\omega_{q,y}^2}, \tag{16}$$

where $\mathcal{N}_p$ comprises the four neighbors of p, $\mathcal{N}_p^H$ its two horizontal neighbors and $\mathcal{N}_p^H$ its two vertical ones. $\omega_{q,x}$ and $\omega_{q,y}$ are, respectively, the horizontal and vertical component of vector ω_q. Vector $A_{p,q}$ for point $p=(i,j)$ and its horizontal neighbor $q=(i,j+k)$, $k=\mp 1$, is defined as $(U_{i,j+2k},(-1)^{\frac{k+1}{2}}(U_{i+1,j+k}-U_{i-1,j+k}))^t$. Similarly, vector $B_{p,q}$ for point $p=(i,j)$ and its vertical neighbor $q=(i+k,j)$, $k=\mp 1$, is defined as $(U_{i,j+2k},(-1)^{\frac{k+1}{2}}(U_{i+1,j+k}-U_{i-1,j+k}))^t$.

References

[1] G. Aubert, P. Kornprobst, Mathematical Problems in Image Processing, Springer-Verlag, New York, USA, 2002.

[2] S. Beucher, F. Meyer, The morphological approach to segmentation: the watershed transformation, in: E.R. Dougherty (Ed.), Mathematical Morphology in Image Processing, vol. 12, Marcel Dekker, New York, 1993, pp. 433–481.

[3] P.J. Burt, The Pyramid as a Structure for Efficient Computation, in: A. Rosenfeld (Ed.), Springer-Verlag, 1984, pp. 6–35.

[4] B. Cabral, L.C. Leedom, Imaging vector field using line integral convolution, Computer Graphics Proceedings (1993) 263–270.

[5] S. Campana, J. Casselman, Stock discrimination using otolith shape analysis, Canadian Journal of Fisheries Research and Aquatic Sciences 50 (1993) 1062–1083.

[6] F. Cao, R. Fablet, Automatic morphological detection of otolith nucleus, Pattern Recognition Letters 27 (6) (2006) 658–666.

[7] V. Caselles, G. Sapiro, Histogram modification via partial differential equations, Journal of Differential Equations 135 (1997) 238–268.

[8] V. Caselles, R. Kimmel, G. Sapiro, Geodesic active contours, International Journal of Computer Vision 22 (1) (1997) 61–79.

[9] V. Caselles, J.-M. Morel, C. Sbert, An axiomatic approach to image interpolation, IEEE Transactions on Image Processing 7 (1998) 376–386.

[10] L. Chauvaud, The shell of the Great Scallop Pecten maximus as a tool for high frequency paleoenvironmental reconstruction, Geochemistry, Geophysics, Geosystems 6 (2005) Q08001, doi:10.1029/2004GC000890.

[11] A. Chessel, F. Cao, R. Fablet, Interpolation of orientation: an axiomatic approach, in: Proceedings of European Conference on Computer Vision, ECCV06, LNCS 3954, Graz, May 2006, pp. 241–254.

[12] A. Chessel, R. Fablet, F. Caoand C. Kervrann, Orientation interpolation and applications, in: Proceedings of 13th International Conference on Image Processing, ICIP'2006, Atlanta, October 2006.

[13] D. Cremers, S.J. Osher, S. Soatto, Kernel density estimation and intrinsic alignment for shape priors in level set segmentation, International Journal of Computer Vision 69 (3) (2006) 335–351.

[14] D. Cremers, C. Schnörr, Statistical shape knowledge in variational motion segmentation, Image and Vision Computing 21 (1) (2003) 77–86.

[15] S. Dass, Markov random field models for directional field and singularity extraction in fingerprint images, IEEE Transactions on Image Processing 13 (10) (2004) 1358–1367.

[16] R. Deriche, Using canny's criteria to derive a recursively implemented optimal edge detector, International Journal of Computer Vision 1 (2) (1987) 167–187.

[17] S. Durand, J. Froment, Reconstruction of wavelet coefficients using total variation minimization, SIAM Jal Scientific Computing 24 (5) (2003) 1754–1767.

[18] R. Fablet, Semi-local extraction of ring structures in images of biological hard tissues: application to the bayesian interpretation of fish otoliths for age and growth estimation, Canadian Journal on Fisheries and Aquatic Sciences 43 (6) (2006) 1414–1428.

[19] R. Fablet, F. Daverat, H. de Pontual, Unsupervised bayesian reconstruction of individual life histories chronologies from otolith signatures: case study of Sr:Ca transects of eel (anguilla anguilla) otoliths, Canadian Journal of Fisheries Research and Aquatic Sciences 64 (2007) 152–165.

[20] S. Geman, D. Geman, Stochastic relaxation, Gibbs distribution and the Bayesian restoration of images, IEEE Transactions on Pattern Analysis and Machine Intelligence 6 (6) (1984) 721–741.

[21] A. Guillaud, A. Benzinou, H. Troadec, V. Rodin, J. Le Bihan, Autonomous agents for edge detection and continuity perception on otolith images, Image and Vision Computing 20 (13–14) (2002) 955–968.

[22] P. Huber, Robust Statistics, John Wiley & Sons, 1981.

[23] F. Lin, X. Yang, Geometric Measure Theory: An Introduction, International Press, 2002.

[24] P. Monasse, F. Guichard, Fast computation of a contrast invariant representation, IEEE Transactions on Image Processing 9 (5) (2000) 860–872.

[25] E. Mémin, P. Pérez, A multigrid approach for hierarchical motion estimation, in: Proceedings of Sixth IEEE International Conference on Computer Vision, ICCV'98, Bombay, January 1998, pp. 933–938.

[26] J.M. Odobez, P. Bouthemy, Separation of moving regions from background in an image sequence acquired with a mobile camera, in: H.H. Li, S. Sun, H. Derin (Eds.), Video Data Compression for Multimedia Computing, Kluwer, 1997, pp. 295–311 (Chapter 8).

[27] J. Panfili, H. De Pontual, H. Troadec, P.J.Wright, Manual of Fish Sclerochronology, Editions Ifremer, 2003.

[28] P. Perona, J. Malik, Scale-space and edge detection using anisotropic diffusion, IEEE Transactions on Pattern Analysis and Machine Intelligence 12 (7) (1990) 629–639.

[29] M. Rousson, N. Paragios, R. Deriche, Implicit active shape models for 3d segmentation in mr imaging, in: C. Barillot, D.R. Haynor, P. Hellier (Eds.), Seventh International Conference on Medical Image Computing and Computer-Assisted Intervention, MICCAI'2004, Lecture Notes in Computer Science, vol. 3216, Saint-Malo, France, 2004, pp. 209–216, September.

[30] L. Rudin, S. Osher, E. Fatemi, Nonlinear total variation based noise removal algorithms, Physica D 60 (1–4) (1992) 259–268.
[31] J.A. Sethian, Level Set Methods and Fast Marching Methods: Evolving Interfaces in Computational Geometry, Fluid Mechanics, Computer Vision and Materials Science, Cambridge University Press, 1999.
[32] D.W. Thompson, On Growth and Form, Cambridge University Press, 1917.
[33] D. Tschumperlé, Fast anisotropic smoothing of multi-valued images using curvature-preserving PDE's, International Journal of Computer Vision 68 (1) (2006) 65–82.
[34] J. Weickert, Anisotropic Diffusion in Image Processing, Teubner-Verlag, Stuttgart, 1998.
[35] L. Younès, Optimal matching between shapes via elastic deformations, Image and Vision Computing 17 (1999) 381–389.

OPEN ACCESS Freely available online

PLoS one

Shedding Light on Fish Otolith Biomineralization Using a Bioenergetic Approach

Ronan Fablet[1]*, Laure Pecquerie[2], Hélène de Pontual[3], Hans Høie[4,5], Richard Millner[6], Henrik Mosegaard[7], Sebastiaan A. L. M. Kooijman[8]

1 Institut TELECOM, TELECOM Bretagne, Lab-STICC, Brest, France, **2** Department of Ecology, Evolution and Marine Biology, University of California Santa Barbara, Santa Barbara, California, United States of America, **3** Ifremer, Departement of Fisheries Sciences and Technology, Plouzane, France, **4** Department of Biology, University of Bergen, Bergen, Norway, **5** Institute of Marine Research, Bergen, Norway, **6** CEFAS, Lowestoft, Suffolk, United Kingdom, **7** National Institute of Aquatic Resources, Technical University of Denmark, Charlottenlund, Denmark, **8** Department of Theoretical Biology, Vrije Universiteit, Amsterdam, The Netherlands

Abstract

Otoliths are biocalcified bodies connected to the sensory system in the inner ears of fish. Their layered, biorhythm-following formation provides individual records of the age, the individual history and the natural environment of extinct and living fish species. Such data are critical for ecosystem and fisheries monitoring. They however often lack validation and the poor understanding of biomineralization mechanisms has led to striking examples of misinterpretations and subsequent erroneous conclusions in fish ecology and fisheries management. Here we develop and validate a numerical model of otolith biomineralization. Based on a general bioenergetic theory, it disentangles the complex interplay between metabolic and temperature effects on biomineralization. This model resolves controversial issues and explains poorly understood observations of otolith formation. It represents a unique simulation tool to improve otolith interpretation and applications, and, beyond, to address the effects of both climate change and ocean acidification on other biomineralizing organisms such as corals and bivalves.

Citation: Fablet R, Pecquerie L, de Pontual H, Høie H, Millner R, et al. (2011) Shedding Light on Fish Otolith Biomineralization Using a Bioenergetic Approach. PLoS ONE 6(11): e27055. doi:10.1371/journal.pone.0027055

Editor: Peter Roopnarine, California Academy of Sciences, United States of America

Received April 13, 2011; **Accepted** October 10, 2011; **Published** November 14, 2011

Copyright: © 2011 Fablet et al. This is an open-access article distributed under the terms of the Creative Commons Attribution License, which permits unrestricted use, distribution, and reproduction in any medium, provided the original author and source are credited.

Funding: This study was partially funded by National Science Foundation (NSF) grants EF-0742521 and DEB-0717259 to L.P. and ANR grant OTOCAL to R.F. No additional external funding was received for this study. The funders had no role in study design, data collection and analysis, decision to publish, or preparation of the manuscript.

Competing Interests: The authors have declared that no competing interests exist.

* E-mail: ronan.fablet@telecom-bretagne.eu

Introduction

Otoliths, biomineralized aragonite bodies in the fish inner ear, have long been recognized as key biological archives. Many species deposit seasonally alternating opaque and translucent zones (Fig. 1) that provide proxies of age critical in fish population dynamics [1]. By providing dated morphological, structural and chemical signatures, otoliths are also keys for past and present environment reconstructions [2] and life trait characterization [3,4,5,6]. Such data are critical for marine ecosystem and fisheries monitoring. Due to the poor understanding of biomineralization mechanisms, otolith proxies however often lack validation and are open to subjective interpretations [1,7]. Inaccurate otolith-based age estimation of orange roughy off New Zealand [8] and walleye pollock in the Bering Sea [9] are among the most striking examples of misinterpretations that have contributed to the overexploitation of fish populations.

Both metabolism and temperature are known to play key roles in otolith biomineralization [1,10,11]. As highlighted by meta-analyses [1,12], disentangling these two factors is however challenging. In temperate waters, the formation of translucent zones is generally considered to occur during winter whereas opaque zones would be formed during rapid growth periods in spring and summer (Fig. 1). However, this statement is often not valid. Opposite patterns have been reported as well as additional non-periodical zones that may lead to erroneous age and growth estimations [13]. Neither experimental studies monitoring temperature and feeding conditions [10,11] nor proposed otolith biomineralization models [14,15,16] have been able to explain the complex interplay between fish metabolism and temperature on otolith formation. In particular, consideration of mineral factors alone [15] has been challenged by recent characterizations of the role of organic compounds in otolith biomineralization [17].

We here propose a bioenergetic model of otolith biomineralization in the framework of the Dynamic Energy Budget (DEB) theory [18] (Fig. 1). This general theory for metabolic organization describes how an organism assimilates and utilizes energy throughout its life cycle. The key feature here is the application of the concept of metabolic product, as defined by DEB theory [18]. The mineral and organic fractions of the otolith are regarded as individual metabolic products involving contributions from somatic growth (p_G) and maintenance (p_M) DEB energy fluxes (Fig. 1), and otolith opacity variations result from variations in the ratio between these two fractions [19]. Given that in vitro aragonite precipitation is temperature-dependent [15], temperature variations also directly act on the dynamics of the mineral fraction (Fig. 1). Mathematically, given the parameterization of metabolic fluxes p_G and p_M defined by DEB theory [18], otolith growth (Eq. 1) and opacity (Eq. 3) can be regarded as functions of the state of the individual (reserves and length) and of its environment (temperature and food density). The 1D simulation of otolith formation may be transformed into a 2D transverse

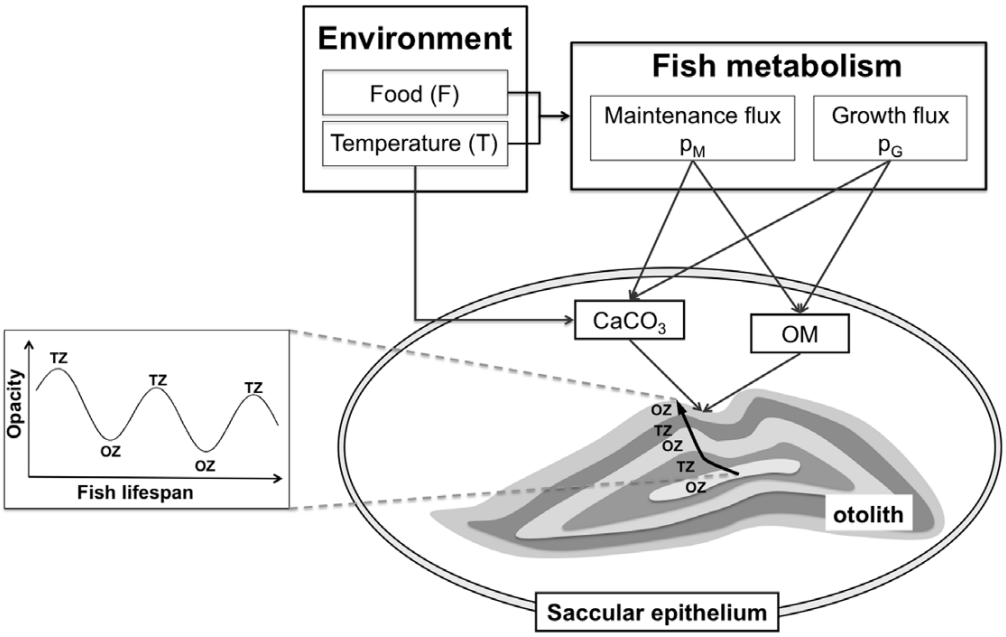

Figure 1. Model for otolith biomineralization. Otolith formation corresponds to an accretion of successive layers of calcium carbonate ($CaCO_3$) embedded in an organic matrix (OM) which precursors are synthesized by the saccular epithelium. At a yearly scale seasonal environmental and physiological variations induce opacity changes with an alternated deposition of translucent (TZ) and opaque (OZ) zones appearing respectively as dark and bright zones under reflected light. We here state the otolith as a metabolic product as defined by the Dynamic Energy Budget (DEB) theory for metabolic organization [18]; Otolith formation is driven by fish growth (p_G) and maintenance (p_M) metabolic fluxes which depend on the individual state and the temperature and feeding conditions the fish experiences. We also account for the temperature-dependent dynamics of $CaCO_3$ precipitation [15].
doi:10.1371/journal.pone.0027055.g001

section image of a growing otolith using calibrated shape deformation algorithms for otolith images [20].

Results and Discussion

Model calibration and validation were carried out from two experimental cod otolith datasets. The calibration relied on a 300-day experiment on juvenile cod which experienced a shift to lower feeding conditions and varying temperatures (Fig. 2a; Fig. S1 & S2 and Table S1 & S2). The validation involved a 800-day experiment on juvenile cod which experienced seasonal temperature variations and constant feeding (Fig. 2b; Fig. S3 & S4). Metabolic effects alone induced most of the opacity variations in the first experiment but could not explain seasonal opacity signals in the second experiment (Fig. 2; Fig. S2 & S4). Temperature factor $c_C(T)$ was negatively correlated to opacity in the first experiment (Fig. 2, left column) and could not account for the overall decreasing opacity trend in the second experiment (Fig. S4). Only the interplay between the metabolic and temperature factors led to a reliable prediction ($R^2>0.9$, $p<0.001$ in both cases). These results also outlined the different dynamics of feeding and temperature effects. Whereas temperature acted immediately through the regulation factor $c_C(T)$, food-induced effects were typically smoothed out, the reserves of the individual acting as a buffer.

The proposed model opens up new prospects for the understanding of differences in otolith patterns of a given species within different ecosystems (Fig. 3). As an illustration, we considered two cod populations respectively in the Barents Sea (BS) and in the southern North Sea (NS) (Fig. 3). Their otoliths depict antiphasic seasonal opacity patterns (Fig. 3B). BS cod follows the general pattern with a winter translucent zone and an summer opaque zone, while NS cod forms an opaque zone in spring and a translucent one in late summer [21]. In addition, NS cod otolith images are much more contrasted than BS cod ones (Fig. 3C). By forcing the calibrated model with population-specific feeding and temperature scenarios stated from data available in the literature (Fig. S5, and Video S1), we explained these two population-specific characteristics. The smaller variations in both feeding and temperature conditions experienced by the BS cod result in otolith images with a lower contrast well redrawn by the model (Fig. 3C). Observed seasonal patterns (dashed lines, Fig. 3B), given as the relative proportions of opaque edges in monthly sampled otolith sets [21], were compared to normalized versions of the simulated opacity patterns (solid lines, Fig. 3B; Fig. S6). The model convincingly reproduced the seasonal patterns ($R^2>0.96$ $p<0.001$). Neither of the two populations conforms to the generally assumed interpretation, i.e. slow-growth winter translucent zones and fast-growth summer opaque ones [1]. BS cod forms a late winter translucent zone which is induced by migration to warmer waters rather than slow-growth conditions (Fig. S8). The opposite pattern of the NS cod results from the late summer formation of a translucent zone due to low feeding activity with simultaneous high temperatures (Fig. S7). Besides, we showed that similar seasonal opacity patterns for different populations, here Barents sea cod and Norwegian coast cod populations, might not necessarily refer to similar feeding and temperature conditions but might also be observed with different population-specific scenarios (Fig. S9). These results highlight the complex interplay between temperature and feeding conditions each of

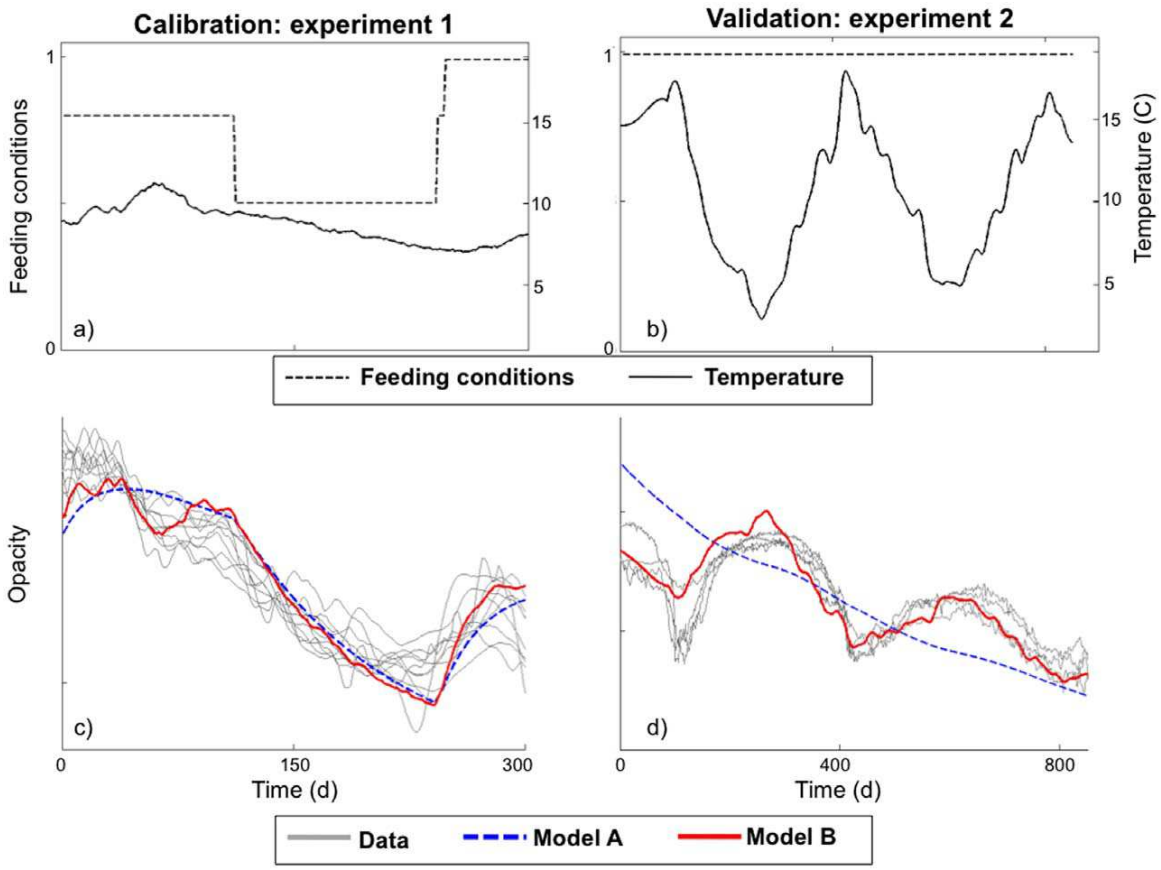

Figure 2. Model calibration and validation on cod otoliths using two experimental datasets: 1) reduced feeding conditions (day 110 to day 220) with seasonal temperature variations (left column), and 2) constant feeding with seasonal temperature cycles over a two-and-a-half-year period (right column). We report temperature and feeding conditions (a, b) and the comparison between model simulations and opacity data (c, d). We display opacity data (Data, gray) and model simulations without the temperature effect on calcium carbonate precipitation (Model A, blue) and with this temperature effect (Model B, red).
doi:10.1371/journal.pone.0027055.g002

which may individually have a positive or a negative effect on otolith growth and opacity. These interactions as well as the above-mentioned differences in their relative response dynamics explain why empirical studies have reached contradictory conclusions on the regulation of the formation of otolith structures among species and stocks [12].

Improving the reliability of otolith-based individual and population data is critical to population dynamics and ecology. In this respect, our model provides a conceptual basis to interpret well-known but poorly understood otolith characteristics:

- The coupling between otolith growth and fish somatic growth during high feeding periods [10,22] results from the large contribution of the somatic growth flux ($\alpha_{CpG} >> \beta_{CpG}$, Eq. 1). In contrast, low feeding periods [10,22] lead to a decoupling due to the weaker but significant contribution of the maintenance flux in otolith growth ($\alpha_{CpG} \sim 0$ and $\beta_{CpG} > 0$, Eq. 1);
- The correlation between otolith growth and fish respiration [23] follows naturally as CO_2 production is also modelled as a weighted sum of metabolic processes in a DEB context [18];
- The differences in the relative contributions from the somatic and maintenance fluxes (Eq. 3) result in metabolism-induced opacity changes; improved feeding conditions lead to a more opaque accretion [21]. They also explain the lifespan decrease of opacity as the growth flux decreases as the individual gets closer to its asymptotic size [19];
- The greater otolith accretion at higher temperatures [11,24] is a direct outcome of the temperature-dependent dynamics of the precipitation of aragonite (Eq. 1). This mechanism also accounts for the formation of a more opaque otolith zone when the fish experiences colder temperatures [11,24].

Beyond these new mechanistic interpretations, scenario-based model simulations are of primary interest to interpret and predict otolith characteristics in response to environmental changes (e.g. climate). For instance, they provide new means for the discrimination of seasonal vs. non-seasonal otolith structures, a crucial issue for the improvement of the accuracy of individual age data [1]. Direct model inversion also presents a great potential for the reconstruction of individual life traits from otolith patterns. For instance, given temperature records obtained from data storage tags or estimated from the oxygen isotopic ratios of the otolith, modeled otolith accretion and opacity may be fitted to the recorded macrostructures of real otoliths by tuning individual feeding dynamics and growth. To our knowledge, the

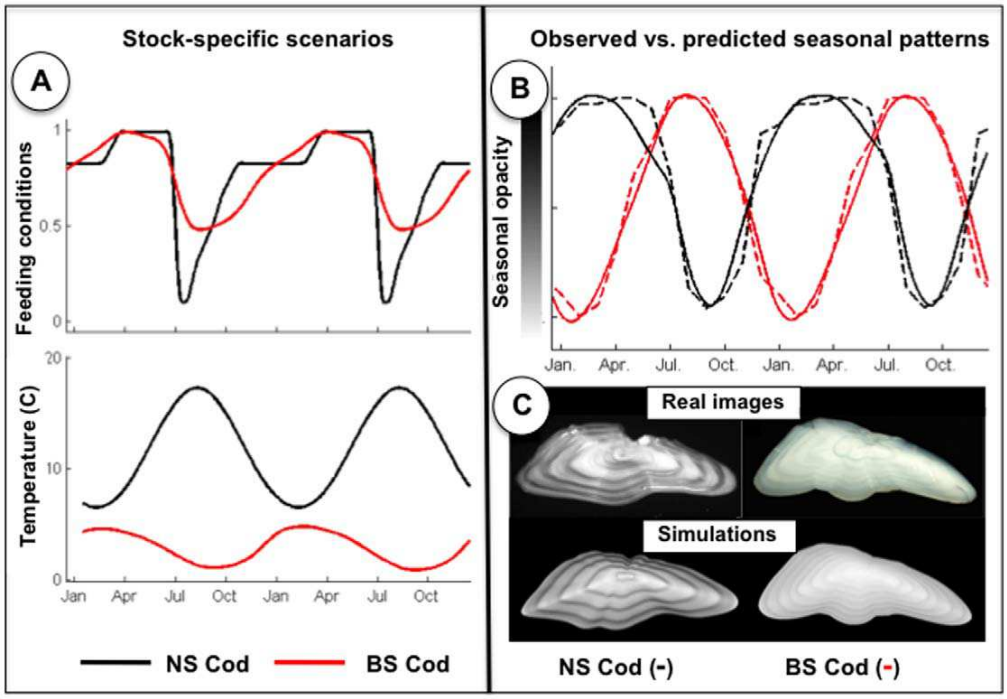

Figure 3. Resolving the non-synchronous seasonality of opacity patterns of Barents Sea (BS) and southern North Sea (NS) cod otoliths: Feeding and temperature conditions (panel A) that explain otolith opacity patterns observed for southern North Sea (NS, black) and Barents Sea (BS, red) cod (panels B and C). Observed seasonal patterns (dashed lines), given as the relative proportions of opaque edges in the monthly sampled otolith sets [21], are compared to normalized simulated opacity patterns (solid lines). Model simulations reproduce both the opposite seasonal opacity patterns (panel B) and the remarkable differences in the contrast of the otolith images of the two populations (panel C). The Supp. Mat. details the stock-specific scenarios (Text S1 & Fig. S5) and animated model simulations are provide as an electronic appendix (Video S1).
doi:10.1371/journal.pone.0027055.g003

acquisition of feeding dynamics at the individual scale remains a challenge in non-monitored environments, but it is particularly important for the understanding and prediction of food web dynamics. The analysis of otolith chemical composition could also benefit from the proposed framework. Both element and isotopic signatures provide invaluable information on fish migration and population connectivity [4,6]. However, they often depict complex interactions between endogenous and environmental factors [7] that may be deciphered by extensions of our approach.

The biomineralization of other structures such as coral skeletons and bivalve shells also lacks a comprehensive understanding. The proposed framework provides a generic basis for modeling their formation. The biomineralization mechanisms we considered, a metabolism-driven control parameterized by somatic growth (assumption A1) and maintenance energy fluxes and a temperature-specific effect on precipitation dynamics and (assumption A2) are generic and their implementation exploits a theory for metabolic organization already applied to fish, bivalves and corals [25,26]. DEB-based biomineralization models could then provide simulation tools to addres the effects of climate change on a large variety of calcifying organisms [27]. Furthermore, by providing a framework where pH conditions could impact *i)* metabolic processes and *ii)* $CaCO_3$ precipitation directly and indirectly via their impact on metabolic processes, we strongly believe that these models represent a promising starting point to investigate the consequences of ocean acidification on biocalcifying organisms [28].

Methods

A generic model of otolith formation

The biomineralization of otoliths is primarily controlled by organic compounds in the endolymph [17]. These organic compounds being synthesized by specialized cells of the saccular epithelium, we here relate otolith formation to fish bioenergetics in the framework of the DEB theory [18]. Our model relies on two basic assumptions:

- *A1-Both the aragonite fraction and the organic matrix of an otolith are metabolic products.* In DEB theory, such compounds are formed during metabolic processes but do not require maintenance and are not used to fuel other metabolic processes [18]. This applies to fish otoliths as they are inert biomineralized structures whose formation is primarily controlled by physiological factors [17];
- *A2-The precipitation of the mineral fraction of the otolith is temperature-dependent.* This assumption is supported by in-vitro analysis of aragonite precipitation [15].

From (A1), the dynamics of the volumes of the mineral and organic fractions of the otolith, respectively $V_C\,(\mu m^3)$ and $V_P\,(\mu m^3)$, are derived as functions of the somatic growth flux (p_G, $J.d^{-1}$) and the maintenance flux (p_M, $J.d^{-1}$) of an individual fish:

$$\frac{dV_C}{dt} = c_C(T)\cdot[\alpha_C p_G + \beta_C p_M] \qquad (1)$$

$$\frac{dV_P}{dt} = \alpha_P p_G + \beta_P p_M \quad (2)$$

where α_C, β_C, α_P, β_P ($\mu m^3.J^{-1}$) are model parameters. The regulation factor $c_C(T)$, stated as an Arrhenius law (Text S1, Section 1), accounts for the temperature effect on mineral precipitation dynamics (A2). As defined by DEB theory [18], the growth and maintenance fluxes (p_G and p_M) are functions of the state of the individual (reserves and length) and of its environment (temperature and food density) (Text S1, Section 1). Given that the organic fraction accounts for less than 5% of the otolith volume [17], we neglect its contribution and the otolith volume is predicted by the volume of the mineral fraction.

Otolith opacity O relates to variations in the ratio between the volumes ΔV_P and ΔV_C of the organic and mineral fractions of the newly precipitated material [19]:

$$O = \frac{\Delta V_P}{\Delta V_C} \approx \frac{dV_P/dt}{dV_C/dt} = \frac{1}{c_C(T)} \cdot \frac{\alpha_P p_G + \beta_P p_M}{\alpha_C p_G + \beta_C p_M} \quad (3)$$

The temporal simulation of otolith formation is transformed into a 2D transverse section image of an otolith using calibrated shape deformation algorithms [20]. This allows comparing simulated otolith images to real ones. We let the reader refer to the Supp. Mat. for further details on the modeling assumptions (Text S1, Section 1) and model parameters (Table S1 & S2).

Model validation and calibration

We used otolith data from two different cod rearing experiments for model calibration and validation. In Experiment 1, one-year-old fish ranging from 30 to 35 cm were reared under seasonal temperature variations in high feeding conditions for 100 days, lower feeding conditions for the subsequent 120 days and ad libitum conditions for the last 80 days [10]. In Experiment 2, fish were 7 months old at the start of the experiment. They were fed ad libitum for 22 months and experienced seasonal temperature conditions [29]. In both cases, calibrated otolith data (i.e., time-referenced otolith growth and opacity data) were available along with the fish growth data.

The otolith data from Experiment 1 along with published data [30] were used to calibrate the DEB otolith model and the dataset from Experiment 2 was used as a validation dataset. The Supp. Mat. (Text S1, Table S1 & S2) further details model calibration and validation and reports calibrated model parameters.

Analysis of seasonal otolith patterns

We applied the calibrated cod otolith model to the analysis of the opposite seasonal opacity patterns of two cod populations, namely Barents Sea cod and Southern North Sea cod [21]. The definition of two population-specific feeding and temperature scenarios relied on data available in the literature (Fig. S5):

- For the NS cod population, the yearly temperature conditions are given by the dynamics of surface temperatures in the southern North Sea [21]. Following [31], mid-level and high-level feeding conditions were respectively assumed from December to February and between March and July while a low feeding behaviour corresponding to temperature highs was considered from August to October;
- For the BS cod population, the considered temperature conditions were issued from records of data storage tags [32] showing a long southward migration to warmer temperatures in winter. In accordance with this seasonal migration, we assumed that feeding conditions improved in the winter and spring with a peak in feeding conditions, corresponding to the seasonal feeding on capelin in March–April [33], followed by lower feeding conditions form August to November prior to the start of the southward migration in December.

For the two populations, we compared simulated otolith images to real ones as well as the observed and predicted seasonal opacity patterns. These observed seasonal opacity patterns from [21] were given as the percentage of opaque otolith edges for monthly sampled cod otolith sets. The seasonal patterns of the model simulations were issued as detrended and normalized version of the predicted opacitie series.

Supporting Information

Figure S1 Model simulations for a shift in feeding conditions (Exp. 1): first row, feeding conditions, temperature conditions (a–b); second row somatic and otolith distal radius (c–d). Model simulations (red) are compared to otolith data (gray) for the known feeding and temperature conditions. The model parameters are given in Tables S1 and S2.
(TIF)

Figure S2 Model simulations for a shift in feeding conditions (Exp. 1): otolith data (gray, thin solid lines) for the known feeding and temperature conditions are compared to the model simulations for two parameter settings: a model with no temperature-specific effect (i.e., parameter T_{AC} set to 0) ($R^2 = 0.93$, $p<0.001$, blue dashed line) and the calibrated otolith model (Table S1 & S2) ($R^2 = 0.96$, $p<0.001$, red, solid line).
(TIF)

Figure S3 Model simulation for constant feeding conditions and seasonal temperature cycles (Exp. 2): first row (from left to right), feeding and temperature conditions (a–b); second row, somatic growth and otolith distal radius (c–d). The simulation of the calibrated model (red) is compared to individual data (gray).
(TIF)

Figure S4 Simulation of opacity patterns for constant feeding conditions and seasonal temperature cycles (Exp. 2). Real opacity data (gray, thin solid lines) are compared to three different simulations: a simulation of the calibrated model (Table S1 & S2) (red, solid line), a simulation with no temperature regulation (blue, dashed line) and a simulation where otolith opacity depends only on temperature (magenta, dashed-dotted line). The correlation coefficients with the real data were $R^2 = 0.90$, $R^2 = 0.66$ and $R^2 = 0.43$, respectively ($p<0.001$ in all cases).
(TIF)

Figure S5 Model simulations for Southern North Sea cod (NS, black) and Barents Sea cod (BS, red): food density series (a), temperature series (b), somatic growth patterns (c), and otolith opacity patterns (d). The somatic growth data (panel c, dashed lines) were obtained from Bolle et al. (Jørgensen 1992) for the both populations.
(TIF)

Figure S6 Seasonality of the timing of otolith zone formation for the simulated and real data for NS and BS cod: feeding conditions (a), temperature conditions

(b), and seasonal opacity patterns (c). BS cod are represented by red and NS cod by black. We compared the average proportions of translucent otolith edges for real otoliths taken from Høie et al. (Høie, Millner et al. 2009) (dashed lines) to identify simulated seasonal opacity patterns (solid lines).
(TIF)

Figure S7 Seasonal otolith opacity patterns for NS cod with constant and non-constant feeding conditions: feeding conditions (a), temperature conditions (b), and seasonal opacity patterns (c). We display two simulations: the one reported in Fig. S6 (solid lines, $R^2 = 0.96$, $p>0.001$) and a scenario assuming a constant feeding with the temperature conditions used in Fig. S6 (dotted lines, $R^2 = 0.64$, $p>0.001$). Simulated opacity patterns are compared to the otolith data (dashed, see Fig. S5).
(TIF)

Figure S8 Seasonal otolith opacity patterns for BS cod with constant and non-constant feeding conditions: feeding conditions (a), temperature conditions (b), and seasonal opacity patterns (c). We display two simulations: the one reported in Fig. S6 (solid lines, $R^2 = 0.96$, $p>0.001$) and a scenario assuming a constant feeding with the temperature conditions used in Fig. S6 (dotted lines, $R^2 = 0.54$, $p>0.001$). The simulated opacity patterns are compared to the real otolith data (dashed line, see Fig. S5).
(TIF)

Figure S9 Seasonality of the timing of otolith zone formation for BS and Norwegian coastal (NC) cod: feeding conditions (a), temperature conditions (b) and seasonal opacity patterns (c). BS cod are shown in red and NC cod in magenta. Both populations are known to display the same seasonal otolith opacity pattern. We compared the average proportions of translucent otolith edges for real otoliths taken from Høie et al. (Høie, Millner et al. 2009) (dashed lines) with simulated seasonal opacity patterns (solid lines).
(TIF)

Text S1 This Supplementary Text provides further details and analysis regarding the key aspects of the proposed bioenergetic model of otolith biomineralization. It is organized as a report and involves three main sections:

- **1. A generic bioenergetic model of otolith biomineralization.** This section further details model assumptions and equations.
- **2. Model calibration and validation.** This section details calibration and validation dataset and results, and report calibrated model parameters.
- **3. Resolving the seasonal timing of the formation of opaque and translucent zones in fish otoliths of different cod populations.** This section details the analysis, from model simulations, of the non-synchronous and synchronous seasonal opacity otolith patterns of several cod populations, namely Barrents Sea, Southern North Sea and Norwegian coast cod populations.

(DOC)

Table S1 Variables, parameter values and equations for individual growth and somatic maintenance in a standard DEB model.
(TIFF)

Table S2 Variables, parameter values and equations for otolith biomineralization.
(TIFF)

Video S1 Animated version of model simulations reported in Fig. 3.
(MOV)

Acknowledgments

We thank P. Klein, R.M. Nisbet for comments on the manuscript.

Author Contributions

Conceived and designed the experiments: RF LP HdP. Performed the experiments: RF LP. Analyzed the data: RF LP HH RM. Contributed reagents/materials/analysis tools: RF LP SALMK HH RM. Wrote the paper: RF LP HdP HM.

References

1. Campana SE (2001) Accuracy, precision and quality control in age determination, including a review of the use and abuse of age validation methods. J Fish Biol 59: 197–242.
2. Ivany LC, Patterson WP, Lohmann KC (2000) Cooler winters as a possible cause of mass extinctions at the eocene/oligocene boundary. Nature 407: 887–890.
3. Carpenter SJ, Erickson JM, Holland FD (2003) Migration of a Late Cretaceous fish. Nature 423: 70–74.
4. Rooker JR, Secor DH, De Metrio G, Schloesser R, Block BA, et al. (2008) Natal Homing and Connectivity in Atlantic Bluefin Tuna Populations. Science 322: 742–744.
5. Thorrold SR, Latkoczy C, Swart PK, Jones CM (2001) Natal homing in a marine fish metapopulation. Science 291: 297–299.
6. Tsukamoto K, Nakai I, Tesch WV (1998) Do all freshwater eels migrate? Nature 396: 635–636.
7. Elsdon TS, Wells BK, Campana SE, Gillanders BM, Jones CM, et al. (2008) Otolith chemistry to describe movements and life-history measurements of fishes: hypotheses, assumptions, limitations, and inferences using five methods. Oceanography and Marine Biology: an Annual Review 46: 297–330.
8. Andrews AH, Tracey DM, Dunn MR (2009) Lead–radium dating of orange roughy (Hoplostethus atlanticus): validation of a centenarian life span. Can J Fish Aq Sc 66: 1130–1140.
9. Beamish RJ, McFarlane GA (1996) A discussion of the importance of aging errors, and an application to walleye pollock: the world's largest fishery. In: Secor DH, et al. (1996) Recent Developments in Fish Otolith Research University of South Carolina Press. pp 545–565.
10. Høie H, Folkvord A, Mosegaard H, Li L, Clausen LAW, et al. (2008) Restricted fish feeding reduces cod otolith opacity. J App Ichthyol 24: 138–143.
11. Neat FC, Wright P, Fryer RJ (2008) Temperature effects on otolith pattern formation in Atlantic cod Gadus morhua. J Fish Biol 73: 2527–2541.
12. Beckman DW, Wilson AW (1996) Seasonal timing of opaque zone formation in fish otoliths. In: Secor DH, et al. (1996) Recent developments in fish otolith research Univ. of South Carolina Press. pp 27–43.
13. de Pontual H, Groison AL, Piñeiro C, Bertignac M (2006) Evidence of underestimation of European hake growth in the Bay of Biscay, and its relationship with bias in the agreed method of age estimation. ICES J Mar Sci 63: 1674–1681.
14. Hussy K, Mosegaard H (2004) Atlantic cod (Gadus morhua) growth and otolith accretion characteristics modelled in a bioenergetics context. Can J Fish Aquat Sci 61: 1021–1031.
15. Romanek CS, Gauldie RW (1996) A predictive model of otolith growth in fish based on the chemistry of the endolymph. Comp Biochem Phys A, Physiology 114: 71–79.
16. Schirripa MJ, Goodyear CP (1997) Simulation of alternative assumptions of fish otolith-somatic growth with a bioenergetics model. Ecol Mod 102: 209–223.
17. Allemand D, Mayer-Gostan N, de Pontual H, Boeuf G, Payan P (2007) Fish Otolith Calcification in Relation to Endolymph Chemistry. In: al. Be, ed. Handbook of biomineralization Wiley. pp 291–308.
18. Kooijman SALM (2010) Dynamic Energy Budget theory for Metabolic Organisation Cambridge University Press.
19. Hussy K, Mosegaard H, Jessen F (2004) Effect of age and temperature on amino acid composition and the content of different protein types of juvenile Atlantic cod (Gadus morhua) otoliths. Can J Fish Aquat Sci 61: 1012–1020.
20. Fablet R, Pujolle S, Chessel A, Benzinou A, Cao F (2008) 2D Image-based reconstruction of shape deformation of biological structures using a level-set representation. Comp Vis Im Und 111: 295–306.

21. Høie H, Millner R, McCUllyc S, Nedreassb KH, Pilling GM, et al. (2009) Latitudinal differences in the timing of otolith growth: A comparison between the Barents Sea and southern North Sea. Fish Res 96: 319–322.
22. Campana SE (1990) How Reliable are Growth Back-Calculations Based on Otoliths? Can J Fish Aquat Sci 47: 2219–2227.
23. Wright PJ, Fallon-Cousins P, Armstrong JD (2001) The relationship between otolith accretion and resting metabolic rate in juvenile Atlantic salmon during a change in temperature. J Fish Biol 59: 657–666.
24. Mosegaard H, Titus R (1987) Daily growth rates of otoliths in yolk sac fry of two salmonids at five different temperatures. In: al. Ke, ed. pp 221–227.
25. Cardoso J, van der Veer HW, Kooijman SALM (2006) Body-size scaling relationships in bivalve species: A comparison of field data with predictions by the Dynamic Energy Budget (DEB) theory. J Sea Res 56: 125–139.
26. Muller E, Kooijman SALM, Edmunds PJ, Doyle FJ, Nisbet RM (2009) Dynamic Energy Budgets in syntrophic symbiotic relationships between heterotrophic hosts and photoautotrophic symbionts. J Theor Biol 259: 44–57.
27. Millner RS, Pilling GM, McCully S, Høie H (2010) Changes in the timing of otolith zone formation in North Sea cod from otolith records: an early indicator of climate-induced temperature stress? Marine Biology.
28. Checkley DM, Dickson AG, Takahashi M, Radich JA, Eisenkolb N, et al. (2009) Elevated CO2 Enhances Otolith Growth in Young Fish. Science 324: 1683–1683.
29. IBACS (2006) WP6 report: Long time rearing for monitoring of near natural conditions. IBACS project (Integrated Approach to the Biological Basis of Age Estimation in Commercially Important Fish Species, QQLRT-2001-01610).
30. van der Veer H, Freitas V, Cardosa J, Lika K, Campos J, et al. (2010) Temperature tolerance and energetics, a Dynamic Energy Budget-based comparison of North Atlantic marine species. Philosophical Transactions of the Royal Society B: Biological Sciences Special issue "Developments in Dynamic Energy Budget theory and its applications".
31. Pilling GM, Millner RS, Easey MW, Maxwell DL, Tidd AN (2007) Phenology and North Sea cod Gadus morhua L.: has climate change affected otolith annulus formation and growth? J Fish Biol 70: 584–599.
32. Godø OR, Michalsen K (2000) Migratory behaviour of north-east Arctic cod, studied by use of data storage tags. Fish Res 48: 127–140.
33. Yaragina NA, Marshall CT (2000) Trophic influences on interannual and seasonal variation in the liver condition index of Northeast Arctic cod (Gadus morhua). ICES J Mar Sci 57: 42–55.

Unsupervised Bayesian reconstruction of individual life histories from otolith signatures: case study of Sr:Ca transects of European eel (*Anguilla anguilla*) otoliths

Ronan Fablet, Françoise Daverat, and Hélène De Pontual

Abstract: The reconstruction of individual life histories from chemical otolith measures is stated as an unsupervised signal-processing issue embedded in a Bayesian framework. This computational methodology was applied to a set of 192 European eel (*Anguilla anguilla*) otoliths. It provided a robust and unsupervised analysis of the individual chronologies of habitat use (either river, estuary, or coastal) from Sr:Ca measures acquired along an otolith growth axis. Links between Sr:Ca values and habitat, age, and season and the likelihood of the transitions from one habitat type to another were modelled. Major movement characteristics such as age at transition between habitats and time spent in each habitat were estimated. As a straightforward output, an unsupervised classification of habitat use patterns showed great variability. Using a hidden Markov model, 37 patterns of habitat use were found, with 20 different patterns accounting for 90% of the sample. In accordance with literature, residence behaviour was observed (28% of the eels). However, about 72% changed habitat once or several times, mainly before age 4. The potential application of this method to any other measures taken along an otolith growth axis to reconstruct individual chronologies gives a new insight in life history tactics analysis.

Résumé : Nous considérons ici la reconstitution des histoires de vies d'après des mesures chimiques d'otolithes comme un problème de traitement d'un signal non supervisé dans un cadre bayésien. Cette méthode numérique a été appliquée à un jeu de 192 données d'otolithes d'anguilles (*Anguilla anguilla*). Une analyse robuste et non supervisée des chronologies d'utilisation des habitats (soit de rivière, d'estuaire ou de milieu côtier) a été obtenue à partir des mesures Sr:Ca acquises le long d'un axe de croissance de l'otolithe. Les liens entre les valeurs Sr:Ca, les habitats, l'âge, la saison et les probabilités de transition d'un habitat à un autre ont été modélisés. Des caractéristiques importantes, telles que l'âge à la transition entre habitats et le temps passé dans un habita, ont été estimées. En résultat immédiat, une classification non supervisée des patrons d'utilisation d'habitat montre une grande variabilité. En utilisant un modèle de Markov caché, 37 patrons d'utilisation d'habitat ont été trouvés 20 représentant 90 % de l'échantillon. En accord avec la littérature, un comportement résident a été observé chez 28 % des anguilles. Cependant, 72 % des anguilles ont changé d'habitat une ou plusieurs fois, surtout avant l'âge de 4 ans. L'application potentielle de cette méthode à d'autres types de mesure prises sur un axe de croissance d'un otolithe pour reconstituer des chronologies individuelles ouvre une perspective nouvelle pour l'analyse des tactiques d'histoire de vie.

Introduction

The recent bloom of ecology studies using otolith microchemistry emphasises the remarkable potential of the otolith for investigating fish life history traits. The use of otolith chemistry to trace migration pathways is premised on a significant correlation between the elemental composition of otoliths and physicochemical properties of the ambient environment (Thorrold et al. 1997; Campana 1999; Martin and Thorrold 2005). Hence, sequential elemental measures acquired along an otolith growth axis are thought to record environmental information along the fish life span (Elsdon and Gillanders 2003). River basin origin are inferred from strontium isotope ratios (Thorrold and Shuttleworth 2000; Milton and Chenery 2003), whereas salinity level has been inferred from strontium to calcium ratios (Sr:Ca) (Tzeng et al. 1994). With more than 200 research articles published, Sr:Ca is the most popular microchemistry application to fish ecology, where it is used as a tool to track movements across water masses of different salinities for at least 20 fish species. To date, more than 28 published studies rely on the analysis of Sr:Ca for the characterization of life histories of

Received 9 January 2006. Accepted 12 August 2006. Published on the NRC Research Press Web site at http://cjfas.nrc.ca on 30 January 2007.
J19093

R. Fablet[1] and H. De Pontual. Ifremer/LASAA, BP 70, 29280 Plouzane, France.
F. Daverat. Cemagref, 50 Avenue de Verdun, 33612 Cestas, France.

[1]Corresponding author (e-mail: rfablet@ifremer.fr).

 doi:10.1139/F06-173 © 2007 NRC Canada

eel species (*Anguilla* spp.). Data acquisition of otolith chemistry remains technically demanding, time consuming, and costly. Hence, the challenge has first been a matter of data acquisition rather than a matter of data interpretation. So far, the interpretation of transects of otolith chemical signatures generally relies on a visual evaluation of each signal. Whenever formalised, the treatment of sequential Sr:Ca measures of eel otoliths data consists of the calculation of the mean values for each individual eel (Tsukamoto and Arai 2001; Tzeng et al. 2002). For instance, Tzeng et al. (2002) classified eel life histories from the number of years assigned to a specific water mass according to the mean value of Sr:Ca measures. This is questionable, as each Sr:Ca otolith measure is a specific indicator of a water mass, so that the mean of two different water masses has no ecological meaning. Also, the temporal dimension of the data is lost. In other studies, individual Sr:Ca values, plotted against age-class graphs, are assigned to a water mass according to their level (Morrison et al. 2003). Because of the nonlinearity of the otolith growth pattern, this is not satisfactory either; the otolith growth pattern during the first years of the fish's life has a finer spatial resolution than that of the last years. As a consequence, evenly spaced Sr:Ca transects result in an inequal number of measurements for each year of the fish's life. In addition, the classification of individual migratory behaviours relied on a priori classes, which may not account for the actual diversity observed in the processed data set (Tzeng et al. 2002; Daverat and Tomas 2006). For instance, in Daverat and Tomas (2006), the visual interpretation of Sr:Ca signals is carried out to classify 270 eels according to six a priori categories of movement patterns. Although time consuming, such a scheme also appears rather subjective.

This overview of previous work emphasizes the need for an unsupervised and well-founded computational method dedicated to the analysis of otolith signatures in terms of environmental information (here the habitat visited by the fish). Such a contribution is expected to account for the temporal nature of the signatures sampled along otolith transects. It is also intended to provide robust and objective (as opposed to expert subjectivity) tools to perform a quantitative analysis of statistically meaningful data sets (typically, several hundred samples). These issues can be regarded as inverse problems within the scope of signal processing. Multidisciplinary studies have already applied signal-processing techniques to process fish otolith data for ageing purposes (Troadec et al. 2000; Fablet 2006) or other issues such as stock discrimination (Campana and Casselman 1993) or fish individual status (Cardinale et al. 2004). From a signal-processing perspective, each Sr:Ca measure is associated with a hidden state variable standing for an environmental parameter (in our case, a habitat type), and the temporal nature of the sequence of Sr:Ca measures can be restored from the otolith growth pattern. Formally, the reconstruction of the individual patterns of habitat use is stated as the Bayesian reconstruction of the temporal sequence of the hidden state variables given the observed sequence of Sr:Ca signatures. The proposed scheme mainly relies on Gaussian mixture models (GMM) and hidden Markov models (HMM). All these developments are implemented under Matlab 7 using Netlab (Nabney 2001) and CRF (Murphy 2004) toolboxes. This method is applied to the analysis of individual habitat use histories for a data set of 192 eel otolith Sr:Ca transects. The generalisation of such a method for the treatment of sequential measures acquired along an otolith growth axis is further discussed.

Materials and methods

Data sets

An eel ecology study (Daverat et al. 2005) led to the acquisition of 192 individual eel Sr:Ca series. The fish samples were collected in the Gironde River basin (southwest France) in three main habitats (water masses). Sixty-three (33%), 115 (60%), and 14 (7%) eels were collected in freshwater, estuary, and coastal habitats, respectively.

The aim of this study is to characterize the habitat use patterns of eels from the Gironde River basin during their continental growing phase as a yellow eel. Sr:Ca transects are used to track the eel movements across freshwater, brackish, and marine habitats. Hence, only the part of the otolith corresponding to the continental life of the eel is retained (from glass eel mark to the edge). The acquisition method is described in Daverat et al. (2005) and consists of electron microprobe measures of Sr and Ca concentrations in 8 μm diameter spots evenly spaced every 20 μm along the longest growth axis of the otolith from the glass eel mark to the edge. Along this transect of Sr:Ca measures, the position of each annual age mark is recorded as a distance from the glass eel mark.

Calibration over time of Sr:Ca series

The interpretation of the macrostructures, so-called "rings", laid annually (Berg 1985) and observed on the otoliths along the longest growth axis, provides an estimation of individual growth patterns. The elver mark is set as the origin of the time axis. Only the interval between the elver mark and the edge is taken into account, as the ecological issue is the continental habitat use pattern of the eel after the glass eel stage until the time of capture. Annual rings are used as time references to map Sr:Ca series acquired with respect to the distance to the elver mark to time series using a linear interpolation. The time series are interpolated at a monthly precision (i.e., a time sampling rate of 1/12). In the following, we will refer to this time axis as the age axis, as it refers to the time spent from the elver mark.

The actual temporal resolution of the Sr:Ca series depends on both the sampling resolution of the electron microprobe and, of course, the otolith growth rate. In a previous experiment (Daverat et al. 2005), a mean otolith growth rate of 20 $\mu m \cdot month^{-1}$ was found for young individuals, so that about 12 Sr:Ca measures are usually sampled for the earlier growth years, whereas from the year 6 onward, fewer measures (down to three or four) may be available because of slower growth. Therefore, the results issued from the analysis of interpolated Sr:Ca time series need to be cautiously analyzed in terms of temporal precision, especially for the last years of life of the older individuals.

Eels have a strong territorial behaviour, as stressed by tagging–recapture and telemetry experiments (Helfman and Bozeman 1983; Aoyama and Sasai 2002). Therefore, because of the temporal resolution associated with otolith

© 2007 NRC Canada

Sr:Ca signatures permits investigating eel movements within the Gironde watershed at a relevant time scale.

Determination of the habitat-related Sr:Ca model

Following Daverat et al. (2005), Sr:Ca measures are regarded as proxies for habitat type for eels of the Gironde River watershed. Three habitat categories are considered according to salinity: river, estuarine, and marine. We do not aim to reconstruct the salinity from the Sr:Ca measure but rather discriminate habitat types The variations of Sr:Ca measures due to interhabitat characteristics, including salinity, are much greater than those due to intrahabitat characteristics (e.g., spatiotemporal variations of the salinity within a given habitat type) or interindividual variability (e.g., individual growth rate) as validated by the ex situ experiment conducted in Daverat et al. (2005) for eels from the Gironde River watershed.

We further model the distribution of Sr:Ca signatures for each habitat type as a Gaussian distribution parameterized by a mean model and a standard deviation. Different models could be chosen. In this study, two different cases are investigated. The first one is a constant model parameterized by a mean value. To test for the influence of seasonality and age on the incorporation of strontium, a linear model with two explanatory variables is also considered. Formally, let us denote by $g(\cdot|\Theta_H,\sigma_H)$ the Gaussian distribution of Sr:Ca measures for habitat type H, parameterized by the mean model Θ_H and the standard deviation σ_H. Using a constant model $\Theta_H = m_H$, $g(\cdot|m_H,\sigma_H)$ is computed for a Sr:Ca measure y as

$$g(y|m_H,\sigma_H) = \frac{1}{\sqrt{2\pi\sigma_H^2}} \exp\left(-\frac{(y-m_H)^2}{2\sigma_H^2}\right)$$

Considering a linear model, model Θ_H is parameterized by the mean value m_H, the effects of age λ_A and season λ_S. For a Sr:Ca measure y at age a and hydrological season s (normalized average monthly flow), the associated likelihood $g(y|a,s,\Theta_H,\sigma_H)$ for habitat type H is given by

$$g(y|a,s,\Theta_H,\sigma_H) = \frac{1}{\sqrt{2\pi\sigma_H^2}} \times \exp\left(-\frac{(y-m_H-\lambda_A a-\lambda_S s)^2}{2\sigma_H^2}\right)$$

The constant model is a particular case of the linear model with $\lambda_A = \lambda_S = 0$; hence, in the rest of this paper, we will only detail the developments for the latter.

The first step consists of determining the associated model parameters (Θ_H,σ_H) for each habitat type H. One should note that no labelled data are available to perform this estimation, only a mixed set of Sr:Ca measures $\{y_i\}$ associated with unknown habitat types (within the three considered). The estimation of the parameters of the habitat models $\{\pi_H, \Theta_H,\sigma_H\}_{H\in\{R,E,M\}}$ is then an unsupervised issue and can be solved for using a mixture model (Bishop 1995). (Unsupervised problems are defined as having no labelled data available, whereas in supervised problems, labelled data are provided, i.e., in our case, Sr:Ca data for which the assignment to an habitat type would be known.) For the latter, model parameter estimation directly resorts to model fitting for the independent subsets of data formed by the labelled data associated with each class. In contrast, the unsupervised estimation of model parameters requires analyzing the considered set of unlabelled data as a whole (Bishop 1995).

To this end, given the Sr:Ca measures $\{y_i\}$ relative to explanatory variables $\{a_i,s_i\}$, the whole distribution of $\{y_i\}$ is modelled as a GMM issued from the superimposition of the three Gaussian habitat models:

$$p(y_i|a_i,s_i,\{\pi_H,\Theta_H,\sigma_H\}_{H\in\{R,E,M\}}) = \sum_{H\in\{R,E,M\}} \pi_h g(y_i|a_i,s_i,\Theta_H,\sigma_H)$$

where R, E, and M represent the labels relative to the three habitat types river, estuarine, and marine, respectively. π_R, π_E, and π_M are the prior probabilities or mixing proportions of the three habitat types. Given a set of unlabelled data $\{y_i\}$ and the associated explanatory variables $\{a_i,s_i\}$, we aim to estimate the parameters of the mixture model $\{\pi_H,\Theta_H,\sigma_H\}_{H\in\{R,E,M\}}$ such that $p(y|a,s,\{\pi_H,\Theta_H,\sigma_H,\}_{H\in\{R,E,M\}})$ best fits the distribution of the data set $\{y_i\}$ according to the maximum likelihood (ML) (Bishop 1995). This model estimation is carried out using the expectation maximization (EM) algorithm (Bishop 1995). The computations involved in this iterative procedure are detailed in Appendix A.

The estimated mixture parameters are assigned to each habitat type by sorting the mean values of the Gaussian modes. We rely on the statement that the lower the salinity of the habitat, the lower the mean Sr:Ca measure (Fig. 1).

The goodness of the fits of the constant and the linear models for each mode is compared with Akaike's information criterion (AIC) method (Awad 1996), and the influence of age and season on the Sr:Ca signature is tested according to correlation statistics between the model prediction and the data (McCullagh and Nelder 1989). The comparison of the contributions of each group of predictors permits us to evaluate the relative importance of habitat, season, and age (Silber et al. 1995). These statistical tests are performed with R software (R Development Core Team 2005).

Estimation of individual habitat use from Sr:Ca series

Our goal is to analyze the individual patterns of habitat use from the series of Sr:Ca measures as illustrated (Fig. 2). This issue is stated as the estimation of the temporal sequence of habitat types (x_t) corresponding to a given observed series of Sr:Ca measures (y_t), where x_t is a label R, E, or M, for each time t.

Formally, this labelling issue is embedded within a Bayesian framework. The term labelling comes from the signal-processing terminology (Rabiner 1989). It refers to the process of determining the sequence of labels (in our case, the sequence of habitat types) associated with a given sequence of observations (in our case, the Sr:Ca signatures). More precisely, it is regarded as the search for the best sequence $(\hat{x}_0,\ldots,\hat{x}_T)$, according to the maximum a posteriori (MAP) criterion (Rabiner 1989), over all possible habitat sequences. The MAP criterion maximizes the posterior likelihood of the habitat sequence (x_t) given an observed series of Sr:Ca measures (y_t), i.e.,

$$(1) \qquad (\hat{x}_0,\ldots,\hat{x}_T) = \arg\max_{(x_0,\ldots,x_T)} p(x_0,\ldots,x_T|y_0,\ldots,y_T)$$

© 2007 NRC Canada

Fig. 1. Distribution of Sr:Ca values (solid line) and the three modes (dashed line, dotted line, bold solid line) of the fitted Gaussian mixture model.

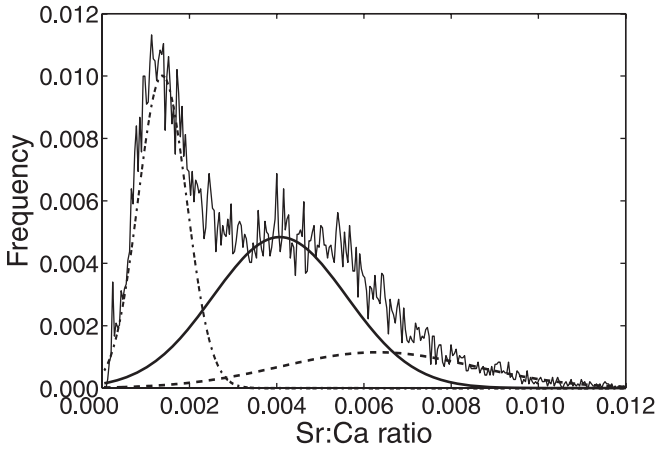

Within a Bayesian framework, posterior likelihood $p(x_0,\ldots,x_T|y_0,\ldots,y_T)$ is rewritten according to Bayes's rule (Bishop 1995) and, solving for eq. 1, is equivalent to

$$(\hat{x}_0,\ldots,\hat{x}_T) = \arg\max_{(x_0,\ldots,x_T)} p(y_0,\ldots,y_T|x_0,\ldots,x_T) \times p(x_0,\ldots,x_T)$$

where $p(y_0,\ldots,y_T|x_0,\ldots,x_T)$ is generally referred to as the data-driven term, which evaluates the likelihood of a sequence of observations given a sequence of labels, and $p(x_0,\ldots,x_T)$ is the prior specifying some a priori knowledge on the characteristics of the sequence of labels. One might note here that the proposed Bayesian method defines a prior (or hyperprior) on the temporal dynamics of the hidden variables (i.e., in our case, habitat type variables) and noton the distribution of the parameters of the observation models (in our case, the habitat-related Sr:Ca models). Though not considered here, the combination of both types of priors could be investigated.

We first specify the data-driven term $p(y_0,\ldots, y_T|x_0,\ldots, x_T)$. As Sr:Ca measures ($y_t$) primarily depend on state variables (x_t), it can be assumed that y_t are conditionally independent of x_t. Hence, data-driven likelihood $p(y_0,\ldots,y_T|x_0,\ldots, x_T)$ is factorized as the product of likelihoods $\prod_t p(y_t|x_t)$. Likelihood $p(y_t|x_t)$ specifies the distribution of the Sr:Ca measures for each habitat type. This information is conveyed by the estimated GMM $\{\pi_H,\Theta_H,\sigma_H\}_{H\in\{\mathrm{R,E,M}\}}$ and $p(y_t|x_t)$ is given by $g(y_t|a_t, s_t, \Theta_{x_t}, \sigma_{x_t})$.

As far as prior $p(x_0,\ldots, x_T)$ is concerned, two solutions are investigated. First, assuming that state variables (x_t) are statistically independent, eq. 1 reduces for each time t to

$$\hat{x}_t = \arg\max_{H\in\{\mathrm{R,E,M}\}} p(y_t|x_t = H)p(x_t = H) \quad (2)$$

The prior term reduces to the a priori likelihood of each habitat type and is specified by the mixing proportions $\{\pi_H\}_{H\in\{\mathrm{R,E,M}\}}$ of the estimated GMM. Equation 2 then becomes

$$\hat{x}_t = \arg\max_{H\in\{\mathrm{R,E,M}\}} \pi_H g(y_i|a_i, s_i, \Theta_{H_1}, \sigma_{H_1})$$

Given that this likelihood only depends on the Sr:Ca signature and model parameters $\{\pi_H,\Theta_H,\sigma_H\}_{H\in\{\mathrm{R,E,M}\}}$, this labelling equation can be interpreted as a threshold-based procedure for which Sr:Ca – habitat equations, derived from model parameters $\{\pi_H,\Theta_H,\sigma_H\}_{H\in\{\mathrm{R,E,M}\}}$, take into account the mean Sr:Ca model, the associated standard deviation, and the mixing proportion of each habitat type. Whereas Sr:Ca – habitat equations exploited in previous work (Elsdon and Gillanders 2003) are generally set a priori, the GMM is a method for determining such equations from an unlabelled data set.

This first model is rather simplistic, however, and does not explicitly model fish movements among habitat types. To account for these temporal dynamics, first-order Gaussian HMMs (Rabiner 1989) are used. These models were initially developed and exploited for speech analysis. As illustrated (Fig. 3), they rely on the actual modelling of the temporal dynamics of the state variables (x_t) using a first-order Markov chain. Given the sequence of state variables $(x_0, x_1,\ldots, x_{t-1})$ from time 0 to time $t - 1$, a first-order Markov chain is such that state variable x_t at time t only depends on x_{t-1},. In other words, this model only keeps the memory of its last state to jump to the next one. Formally, this leads to the property that $p(x_t|x_{t-1},\ldots, x_1, x_0) = p(x_t|x_{t-1})$ and implies that the first-order Markov chain is fully characterized by its transition matrix $\mathbf{\Gamma}$: $p(x_t = H_1|x_{t-1} = H_2) = \Gamma(H_1,H_2)$. This transition matrix specifies the likelihood that the fish switches to habitat type H_1 at time t given that it is in habitat type H_2 at time $t - 1$. By definition, the sum over each column of $\mathbf{\Gamma}$ equals one. A graphical representation of the transition matrix is provided (Fig. 3). Let us stress that some transitions may be forbidden, that is, pairs of habitats for which $\Gamma(H_1,H_2) = 0$ (for instance, the transition from A to C in Fig. 3*b*). However, this does not prevent reaching one state from another by going through other states, if there is a sequence involving several transitions with a non-null likelihood. As illustrated for an abstract example (Fig. 4), although direct transitions from A to C are impossible, paths from A to C going through B are possible. Such features are expected in our case, as it seems unrealistic that fish can switch directly from the river to the marine area without going through the estuarine area.

As far as computational aspects are concerned, we first need to specify the parameters of the Markovian prior (i.e., transition matrix $\mathbf{\Gamma}$). Here, no prior knowledge is available to set a priori these parameter values. They are estimated from the considered data set according to the ML criterion. This comes to search for transition matrix $\hat{\mathbf{\Gamma}}$ associated with the maximum likelihood for the whole set of samples

$$\hat{\mathbf{\Gamma}} = \arg\max_{\Gamma} \prod_i p(y_0^i,\ldots, y_T^i|\Gamma)$$

This maximization issue is solved for using the expectation–maximization algorithm. We let the reader refer to Rabiner (1989) for a detailed description of this estimation procedure and only review its main characteristics here. The following two steps are iterated until convergence. Given the current estimate $\mathbf{\Gamma}^k$ of the transition matrix, the expectation step computes the posterior likelihoods:

$$\xi^i_{H_1H_2}(t) = p(x_t^i = H_2, .x_{t-1}^i = H_1|y_0^i,\ldots, y_T^i, \Gamma^k)$$

$$\gamma^i_{H_1}(t) = p(.x_t^i = H_1|y_0^i,\ldots, y_T^i, \Gamma^k)$$

© 2007 NRC Canada

Fig. 2. Principle of the reconstruction of the time habitat sequence from the acquired Sr:Ca measures spatially sampled along a growth axis of the otolith: it relies on the assumption that the habitat type influences the chemical composition of the otolith such that the individual temporal sequence of habitat types can be reconstructed from otolith chemical signatures sampled along a reference growth axis.

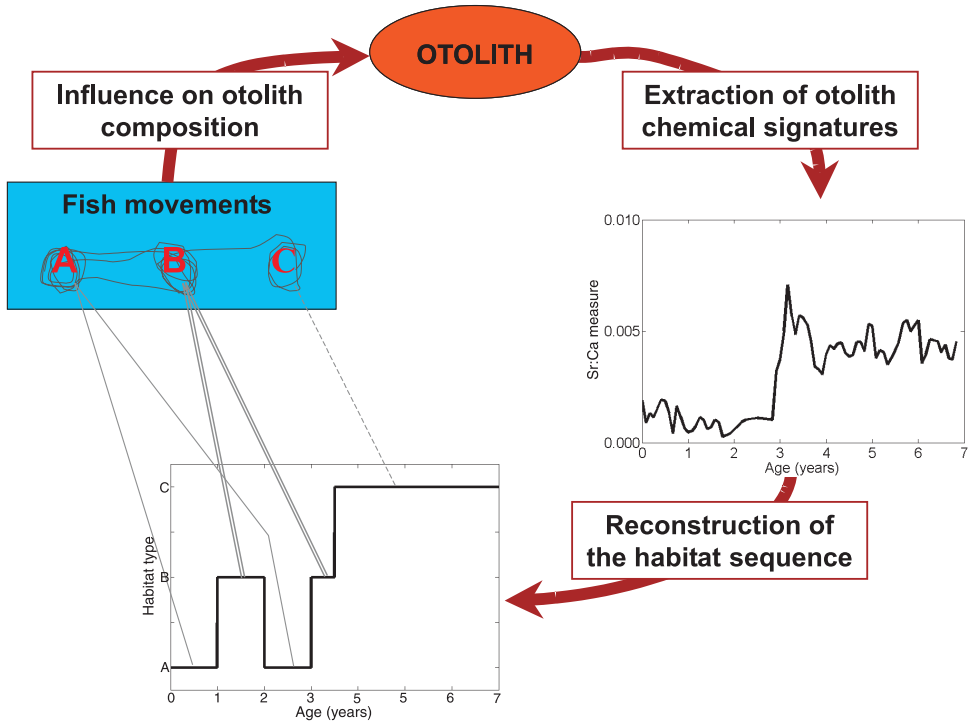

The maximization step updates the transition matrix $\mathbf{\Gamma}^{k+1}$ from these posterior likelihoods as their average over the whole data set:

$$\mathbf{\Gamma}(H_1, H_2) = \frac{\sum_{i=1}^{N}\sum_{t=0}^{T_i}\xi^i_{H_1H_2}(t)}{\sum_{i=1}^{N}\sum_{t=0}^{T_i}\gamma^i_{H_1}(t)}$$

One might stress that the analysis of the estimated transition matrix provides the mean for evaluating the relevance of the HMM, compared with the GMM, for the considered data set. As the latter reduces the temporal prior $p(x_t|x_{t-1})$ to a static prior $p(x_t)$, it can be viewed as a constrained HMM for which the transition matrix verifies $\mathbf{\Gamma}(H_1,H_2) = \mathbf{\Gamma}(H_1)$. For a given data set, the estimated transition matrix $\mathbf{\Gamma}$ of the HMM can then be compared with the transition matrix $\mathbf{\Gamma}'$ associated with the GMM (i.e., $\mathbf{\Gamma}(H_1,H_2) = \pi_{H_1}$), and it can be determined whether or not it is worth considering the generic HMM rather than the GMM.

Given the estimated HMM parameters, the reconstruction of the optimal habitat sequence $(\hat{x}_0,\ldots,\hat{x}_T)$ according to the MAP criterion comes to solve for

$$(\hat{x}_0,\ldots,\hat{x}_T) = \arg\max_{(x_0,\ldots,x_T)}\prod_{t=0}^{T} p(y_t|x_t) \times \prod_{t=1}^{T} p(x_t|x_{t-1})p(x_0)$$

This maximization can not be solved for analytically. However, the Viterbi algorithm (Rabiner 1989) guarantees to retrieve the best state sequence using an efficient forward–backward procedure. We let the reader refer to Rabiner (1989) for a complete description of the Viterbi algorithm andonly review its main steps here, which involve computations similar to the forward procedure of the EM scheme described above for the estimation of the transition matrix. More precisely, it first computes recursively (from time 0 to time T) for any habitat type H the likelihood, denoted by $\delta_H(t)$, of the most likely habitat sequence leading to habitat H at time t:

$$\delta_H(t) = \max_{(x_0,\ldots,x_{t-1})} p(y_0,\ldots,y_t,x_0,\ldots,x_{t-1},x_t = H|\Phi,\Gamma)$$

At the last step of the forward procedure (i.e., at time T), the habitat label maximizing $\delta_H(T)$ provides the optimal habitat type $\hat{x}_T$. A backward procedure then reconstructs recursively the optimal habitat sequence $(\hat{x}_0,\ldots,\hat{x}_T)$ by retrieving the state H_1 at time $t-1$, which leads to the reconstructed state $\hat{x}_t$ at time t with the maximum likelihood. Contrary to the GMM, this labelling procedure cannot be interpreted as a thresholding technique based on Sr:Ca – habitat equations. The observed sequence of Sr:Ca signatures is interpreted as a whole, not as a sequence of independent variables. Depending on temporal context, similar Sr:Ca values might then be assigned to different habitat types; meanwhile the reconstructed habitat sequence is guaranteed to be the most likely given the observed Sr:Ca sequence.

Analysis of habitat sequences

Given the set of the individual habitat sequences, a quantitative analysis of fish movements is carried out. More precisely, the movement pattern is defined as the sequence of the successive habitats visited by the fish. This sequence

© 2007 NRC Canada

Fig. 3. Graphical representation of the hidden Markov model (HMM). (*a*) Graphical representation of the conditional dependencies involved in the HMM. The horizontal arrows indicate the conditional dependencies $x_t|x_{t-1}$ modeling the temporal dynamics of the hidden state, and the vertical arrows indicate the conditional dependencies $y_t|x_t$ modeling the likelihood of measure y_t given state x_t. This graphical representation emphasizes that observations (y_t) are independent conditionally to hidden states (x_t), and that x_t is assumed independent on $(x_0,\ldots,x_{t-2})$ given x_{t-1}. (*b*) Illustration of the characteristics of the transition matrix that specifies the temporal dynamics of the state variable for a HMM with four hidden states A, B, C, and D. The transition matrix specifying the likelihoods $p(x_t|x_{t-1})$ is graphically represented as arrows linking two states with an associated likelihood. For instance, the transition from A to B, associated with likelihood $p(x_t = B|x_{t-1} = A)$ set to 0.3, is visualized by the arrow from A to B. Note that the likelihood to leave one state, i.e., the sum of all the likelihoods of the transitions issued from one state, is one. Some transitions may be forbidden, i.e., associated with a null probability, for instance, transitions from B to A. A particular case of transitions is the one corresponding to staying in the current state (for instance, transitions A to A or C to C).

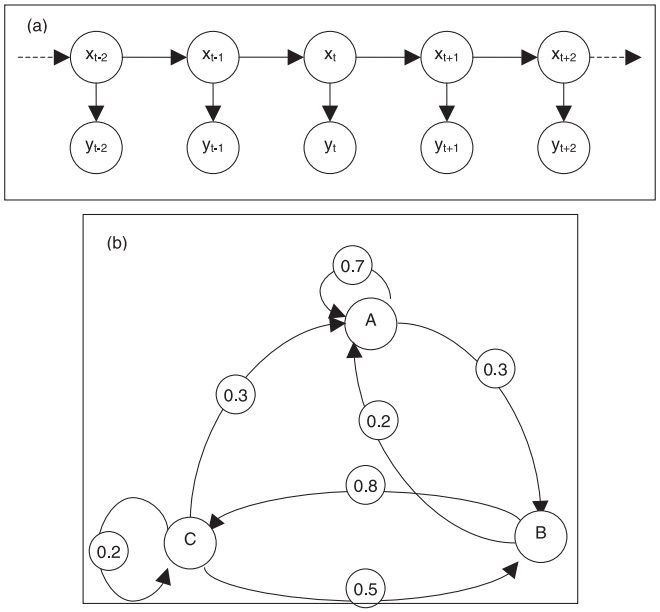

takes into account both the quality and the order of the visited habitats, for instance, the movement pattern issued from habitat sequence RRRREEEERRRRR is RER. For a given otolith set, the set of all of the associated movement patterns can be determined, as well as the corresponding relative frequencies. This procedure then leads to an automated categorization of the observed movement patterns. Contrary to previous work relying on the definition of a priori movement patterns (typically, resident behaviour, as well as migrations from one habitat type to another) (Secor 1999; Daverat and Tomas 2006), this procedure delivers an unsupervised classification of the individual movement patterns and permits investigation of the actual variability of the individual fish behaviours with a finer characterization and not ignoring unexpected behaviours. An analysis based on macrocategories, resulting from the grouping of certain movement patterns (for instance, those involving one or several movements between two habitat types), can also be used to deliver a more synthetic view of the relative occurrences of the different categories of movement patterns.

Fig. 4. Comparison of the habitat sequence reconstructed using the Gaussian mixture model (GMM) and the hidden Markov model (HMM) for a given Sr:Ca series: (*a*) GMM-based reconstruction, (*b*) HMM-based reconstruction. In each plot, the Sr:Ca signal (solid line) and the estimated habitat sequence (broken line) are reported as a function of fish age (in years).

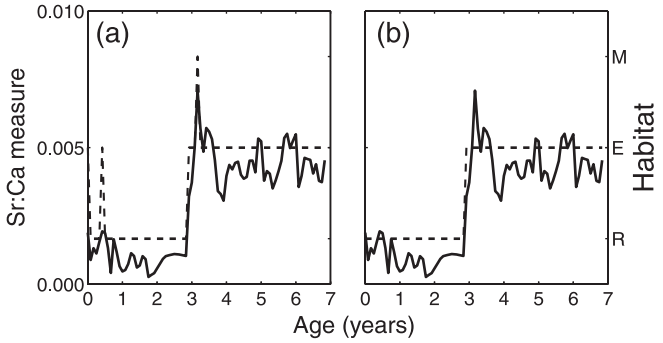

Because the habitat sequences are calibrated over time, a variety of measures can also be defined to characterize individual life traits. We focus on the analysis of the time at which the transitions from one habitat to another occurs and of the time spent in a given habitat between the two transitions. For a given type of transition from habitat type H_1 to habitat type H_2 (i.e., within the set of transitions {R to E, R to M, E to M, E to R, M to R, M to E}), the whole set of habitat sequences $\{(x_t^i)_{t\in\{0,\ldots,T_i\}}\}_{i\in\{1,\ldots,N\}}$ is analyzed to extract the set of all transitions from H_1 to H_2. These transitions are characterized by their transition times $\{t^n_{H_1H_2}\}$ and the times spent in H_2 $\{D^n_{H_1H_2}\}$. The statistical distributions of these quantities are then computed using a nonparametric technique, as they are clearly multimodal. More precisely, given a scale parameter μ and a set of quantities $\{w^n\}$, the likelihood $p(w)$ is computed as

$$p(w) = \frac{1}{Z}\sum_n \exp(-\mu(w - w^n)^2)$$

where Z is the normalization factor. The computation of the statistics of transition times $\{t^n_{H_1H_2}\}$ is performed in terms of age, month, and age group at which the transitions occur. Scale parameter μ is set to one for quantities given as monthly values and age groups and to $1/10^2$ for quantities given as ages.

Results

Comparison between constant and linear models

The linear model accounting for habitat, age, and season effects (AIC value of 45 167) outperforms the model only accounting for habitat effect (AIC value of 46 465). Habitat, age, and hydrological season (river flow) factors all have a significant influence on Sr:Ca values for each habitat ($p < 0.001$) (Table 1).

The comparison of the relative contribution of the habitat factor to the contribution of both age and season factors reveals that habitat contributes more to the variation of Sr:Ca values than age and season, with a ratio of effect standard

© 2007 NRC Canada

deviations of 4.58 (95% confidence interval (CI) 4.38–4.79) (Silber et al. 1995). Because the effect of age and season is significant in terms p statistics, we report the results of the analysis of the individual chronologies of habitat use with respect to the linear model.

Table 1. Analysis of variance (ANOVA) table for the linear model.

Factor	Likehood ratio χ^2	df	Pr(>χ^2)
Habitat	43 744	2	$<2.2\times10^{-16}$
Season	31	1	2.397×10^{-8}
Age	1 984	15	$<2.2\times10^{-16}$

Individual chronologies of habitat use

A comparison of the habitat sequences issued from the GMM and the HMM is illustrated (Fig. 5). As the GMM does not account for time coherence, the associated habitat sequences are less smooth and involve numerous short transitions. As stressed above, the GMM can be regarded as a constrained HMM for which the transition matrix verifies $\Gamma(H_1,H_2) = \Gamma(H_1)$. The transition matrix of the GMM can not approximate the one estimated for the HMM (Table 2). The latter refers to the temporal dynamics $p(x_t|x_{t-1})$ observed over the whole eel data set. It stresses that the prior likelihood of leaving a given habitat type is clearly different for each habitat type. In all cases, the resident behaviour has the highest likelihood. Whereas the likelihoods of the transitions from the estuary to the river and the marine area are roughly in the same order of magnitude, direct transitions from the river to the marine area, and vice versa, are highly unlikely (about 10 times less likely than the transitions from the river and the marine area to the estuary).

The GMM can not handle these temporal dynamics and, hence, is then less relevant than the HMM for the considered data set. An important output of this result is that the observed very short transitions observed in the GMM-based habitat sequences are highly unlikely given the overall transition statistics over the whole data set. These elements lead us to consider the HMM method as the reference method to further characterize life traits from the estimated habitat sequences. Eels sampled in the Gironde River watershed display a wide repertoire of habitat use patterns, such as lifelong residences in the same habitat, as defined in the model (river, estuary, marine area) or as single or multiple shifts among habitats (Fig. 6). From these examples, it should be stressed that the considered model is not a simple thresholding technique. The temporal Sr:Ca signal is analyzed as a whole to determine the optimal MAP habitat sequence. Because the HMM labelling results from an optimal (according to the MAP criterion) trade-off between the temporal prior and the data-driven term, similar Sr:Ca values might be associated with different habitat types.

Analysis and classification of movement patterns

From the overall analysis of the reduced habitat sequences, the different classes of movement patterns associated with the considered data set are automatically determined. Given the temporal resolution associated with the spatial sampling of Sr:Ca signatures, movement patterns are analyzed up to age 6. Also, only fish older than 4 years are analyzed, which guarantees that movement patterns can actually be compared and relevantly characterized in terms of relative frequencies. Using the HMM, 37 patterns are represented (Fig. 6). Although only the first 20 patterns account for more than 80% of the samples, the first five patterns occur with a frequency greater than 5%. Among the first four patterns, three correspond to resident behaviour. The GMM-based approach leads to 88 different patterns, within which only the first five account for more than 3% of the samples. A more synthetic view of the diversity of the movement patterns according to 10 classes is also reported (Fig. 7). This classification results from the grouping of movement patterns involving one or several transitions between two habitat types. More precisely, 10 macrocategories are formed. They comprise three classes associated with the resident behaviour in the river (R), the estuary (E), and the marine area (M), four classes corresponding to one or several movements from the river to the estuary (ER), from the estuary to the river (RE), from the estuary to the marine area (EM), and from the marine area to the estuary (ME), and two classes (REM and MER) associated with movements from the river to the estuary (respectively, from the marine area to the estuary) followed by movements from the estuary to the marine area (respectively, from the estuary to the river). The last class refers to the remaining movement patterns, all of them involving a stay in each of the three habitat types. The comparison of the GMM- and HMM-based categorizations indicates that the main differences occur for the relative frequencies evaluated for the resident behaviours (10% vs 28%) and the class "others" (21% vs 3%), which is mainly due to the presence of very short transitions in the GMM-based sequences. In particular, the resident behaviour in the estuary is only assigned to 0.6% of the samples by the GMM. This does not seem consistent with the results retrieved for the two other resident behaviours (6.5% and 3.5% of the samples classified as residents in the river and the marine area, respectively) and previous work (Tsukamoto and Arai 2001; Daverat et al. 2004, 2005). For other macrocategories, especially those involving one or several movements between two habitat types, similar results are reported for the two methods. Movement patterns between two habitat types involve about 54% of the samples. Most of these movement patterns involve movements between the river and the estuary (38% for the GMM-based scheme and 35% for the HMM-based method), whereas patterns involving movements between the estuary and the marine area account for 16% and 18% of the samples, respectively.

Focusing on the HMM-based categorization, resident behaviours account for only 28% of the samples, and 72% of the movement patterns involve at least one movement. Residents in the marine habitat account for 6.5% of the sample, which is quite consistent with the 7% of fish collected in the marine area. Although 33% of the samples have been collected in the river, only 14.3% of the samples are labelled as residents in the river habitat. Similarly, the reported categorization leads to 7.8% of residents in the estuary area, whereas our sample is composed of 60% of fish collected in the estuary. For migration behaviours, patterns involving only one migration, as well as patterns involving several migrations between two types of habitats, are encountered, but only be-

© 2007 NRC Canada

Fig. 5. Examples of estimated habitat sequences for four individual eels using the hidden Markov model (HMM) based reconstruction: (*a*) example of residency in the river ; (*b*) example of residency in the estuary ; (*c*) example of residency in the marine area ; (*d*, *e*, *f*) examples of multiple movements between the river, the estuary, and (or) the marine area. In each subplot, the Sr:Ca signal (solid line) and the estimated habitat sequence (broken line) are reported as a function of fish age (in years).

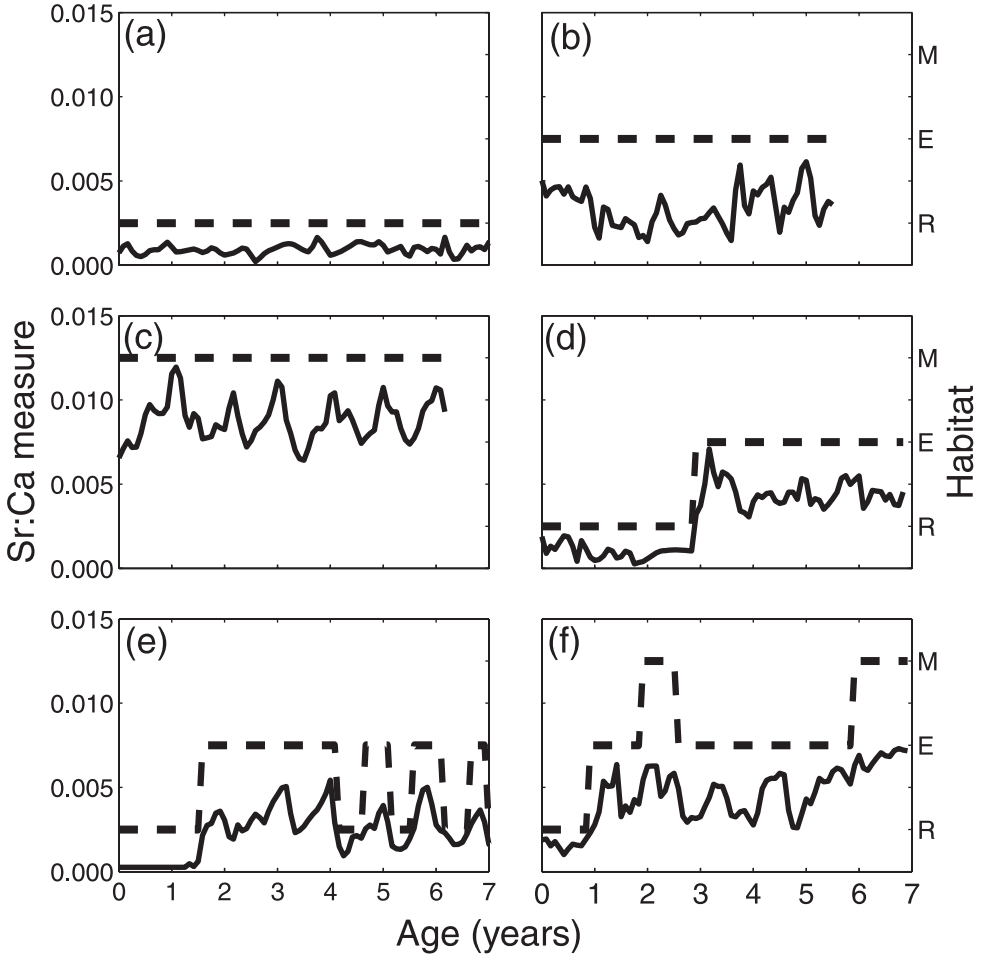

Table 2. Comparison of the transition statistics associated with the Gaussian mixture model (GMM) and the hidden Markov model (HMM).

Transitions from	Method	River	Estuary	Marine area
River	GMM	0.295	0.52	0.185
	HMM	0.903	0.096	0.001
Estuary	GMM	0.29	0.52	0.18
	HMM	0.063	0.905	0.032
Marine area	GMM	0.29	0.52	0.18
	HMM	0.009	0.274	0.717

Note: This table reports the values of the transition likelihood $p(x_t = H_1|x_{t-1} = H_2) = \Gamma(H_1,H_2)$ estimated for the considered data set. The GMM can be viewed as a constrained HMM such that $\Gamma(H_1,H_2) = \Gamma(H_1)$. The table should be read as follows: each row reports the transition likelihood from the associated habitat type.

tween the river and the estuary or the estuary and marine area. Noticeably, up to five successive migrations between the river and the estuary can be observed for the same individual before age 6. Fewer samples involve migrations among the three habitats. However, about 9% of the samples are associated with patterns including a first migration from the river to the estuary and then one or several movements between the estuary and the marine area. Conversely, very few individuals (below 2%) move from the marine area to the river after a stay in the estuary. Interestingly, the characteristics of the movement patterns seem to be different depending on the early phase of the habitat sequence. More precisely, 32% of the fish having an initial phase (according to the elver mark) in the river remain in the river, whereas 47% shift once or several times between the river and the estuary. The remaining 20% spend their last phase between the estuary and the marine area. For fish having an initial phase in the estuary, 23% remain in the estuary, 46% and 29% shift one or several times, respectively, to the river and to the marine area. Among all fish having an initial phase in the marine area, 29% remain in the marine area, 41% shift one or several times between the marine area and the estuary, and 28% move initially to the estuary (with possible returns to the marine area) and later to the river (with possible returns to the estuary).

Analysis of the transitions between habitats

As previously noted, only the first 6 years of life of the fish are considered for the rest of the analysis of the transi-

© 2007 NRC Canada

Fig. 6. Unsupervised analysis of the movement patterns: frequencies of the movement patterns extracted from the estimated habitat sequences using the hidden Markov model (HMM) framework. Each habitat sequence is represented by the sequence of the habitat types visited by the fish, e.g., a habitat sequence EEEEEERRRRRRRR would be represented by the movement pattern ER. The relative frequencies (%) of all the movement patterns present in the processed data set are reported in decreasing order.

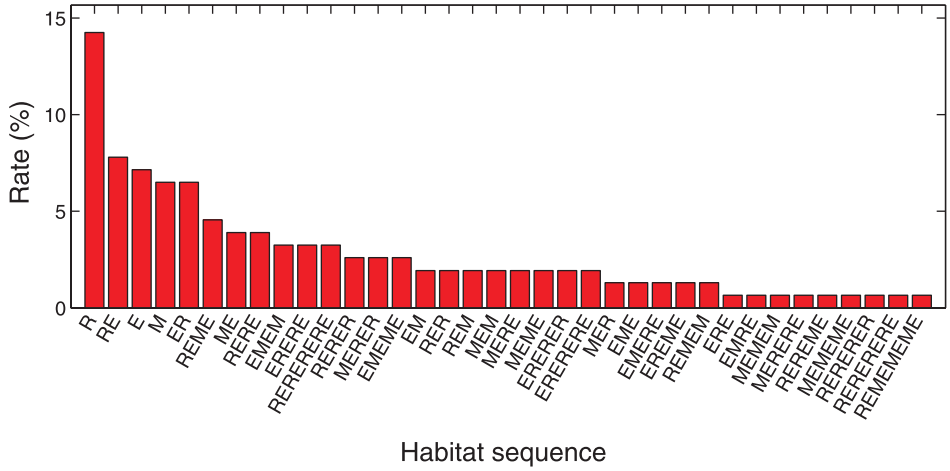

tions between habitats to keep a consistent temporal resolution throughout. The proportions of the transitions from one habitat to another are evaluated first as a function of age and then as a function of season. In the overall sample (192 eels), transitions as a function of age or as a function of season between two different habitats are less frequent than stays in the same habitat as presented, for instance, for the estuary (Figs. 8*a*, 8*b*) at the individual level. This indicates that movements among habitats are seldom compared with the residence in one habitat. Transitions between the river and the marine area do not occur. The reported results also show that the occurrence of the transition is season-dependent.

Analysis of transitions schedules and duration of habitat use

Age at transition between the river and the estuary and duration of the habitat use before changing habitat are investigated for eels more than 4 years old. Because of their absence, transitions between the marine habitat and the river are not analysed.

Transitions from the river to the estuary did not seem age-specific (Fig. 8*c*), but their frequency decreases with age, with a maximum of transitions occurring at age 1. The duration of the stay in the river is less than 2 years, with a maximum number of fish spending less than 1 year in the river before moving to the estuary (Fig. 8*d*).

Transitions from the estuary to the river and from the estuary to the marine area do not occur for a specific age of the eel, as shown (Fig. 8*e*), but decrease as the age of the fish increases. Most eels spend less than 1 year in the estuary before moving to either the river or the marine area (Fig. 8*f*).

Discussion

Spatial and temporal resolution of the analysis

The integration of the temporal dimension in the Sr:Ca series is an important issue in this study. Time series are reconstructed using resampling techniques. The spatial resolution of the analysis on the otolith is constrained by analytical requirements. In this study, a size measure of 8 µm every 20 µm provides us with an approximate temporal resolution of 1 month for the first years of life up to 3 months and more later than the 6th year. This constraint leads us to analyse only the first 6 years of life in order to keep a consistent temporal resolution. Our method is based on a yearly otolith growth model, but it would be improved by accounting for the seasonal variations of the eel otolith growth. Though the general variations of the eel otolith are known (Mounaix and Fontenelle 1994), a formalised model is, as far as we know, not available.

Habitat-related modelling of otolith signatures

In this study, a monoproxy approach is used to model habitat-related otolith characteristics. The proposed unsupervised scheme based on a mixture model permits the estimation of model parameters for each habitat zone from unlabelled data. A linear model is used to account for the significant influence on Sr:Ca values of age and season, in addition to habitat. As expected, the contribution of habitat is shown to be much greater than that of age and (or) season. Outside the metamorphosis from leptocephalus larvae into glass eel, to date, no significant effect of ontogeny due to growth or age was observed on Sr:Ca incorporation into eel otolith (Kawakami et al. 1998; Kraus and Secor 2003; Daverat et al. 2005). A validation using another fish species reared for 2 years in constant salinity has failed in detecting any age effect on Sr:Ca incorporation into otoliths (Elsdon and Gillanders 2005). Age may affect Sr incorporation at a greater time scale than a few years, especially for some eels that can spend up to 20 years in their feeding habitats. As the mean age of our sample was 7 years and only the first 6 years of life are considered, the age effect is weak compared with the habitat effect. The season effect, although weak, is explained by the seasonal variations of freshwater flows into marine water masses of the Gironde River watershed and by the variations of water temperature. Hence, seasonal variations of the river flow are introduced into the model developed here. In Daverat et al. (2005), the analysis of measures of Sr:Ca in the water collected within the

© 2007 NRC Canada

Fig. 7. Categorization of the movement patterns into 10 macrocategories (*a*) issued from the Gaussian mixture model (GMM) method and (*b*) issued from the hidden Markov model (HMM) method. The 10 macrocategories are as follows: three residency behaviours (in the river (R), estuary (E), and marine area (M)); four patterns (RE, ER, EM, and ME) corresponding to one or several movements between two areas; two patterns (REM and MER) involving one or several movements between two areas (i.e., movements from the river to the estuary (RE) or from the marine area to the estuary (ME)) followed by one or several movements between two other areas (i.e., movements from the estuary to the river (ER) or from the estuary to the marine area (EM)). The last class, denoted as "others", contains the remaining movement patterns, which all correspond to movement patterns between the three different areas. We depict the relative frequencies of the considered classes of movement patterns for the processed otolith data set.

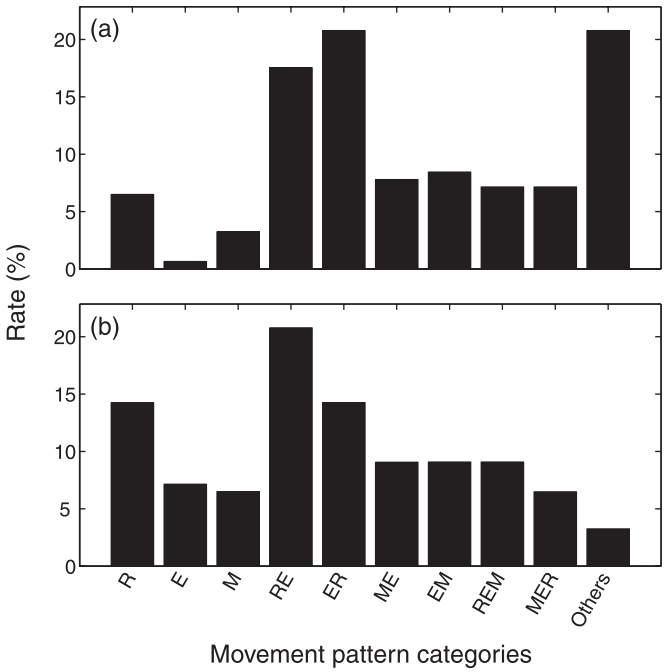

Gironde River watershed at different seasons has shown that slight seasonal fluctuations can be observed without affecting the discrimination of marine, estuarine, and riverine habitats. This is confirmed by the proposed unsupervised method. Growth rate is also known to have an effect on the Sr:Ca. In this study, only the yearly growth rates are available such that its relative effect can not be directly analyzed. Results reported in Daverat et al. (2005) for eels from the same area indicate that this effect is very weak compared with the strong relationship between habitat type and Sr:Ca value, a result validated for eels and other species using coupled experimental and field validations (Kraus and Secor 2004; Elsdon and Gillanders 2005). The effect of the growth rate on Sr:Ca might have led to misclassifications of very slow-growing eels as higher-salinity migrants (and vice versa). However, given the high salinity contrast among the three considered habitats, such situations should seldom occur.

Further applications of this model could take into account other types of effects, e.g., physiological parameters, feeding conditions, or temperature (Campana 1999; Campana et al. 2000). In addition, other kinds of parametric models (polynomial, log-normal, exponential, etc.) could also be straightforwardly used. Multiproxy approaches using multidimensional structural and (or) chemical otolith signatures may also be investigated within this framework with a view to retrieving a more precise estimation of the environments or the states experienced thought the fish's life. The combination of Sr:Ca with oxygen isotope ratios as a proxy of water temperature (Nelson et al. 1989) may, for instance, provide a more precise estimation of the temporal resolution of the measures in the example developed here.

Reconstruction of habitat use chronologies

The proposed method turned out to be particularly well adapted to the analysis of large data sets. The processed data set consists of 192 individual Sr:Ca series containing 70 points of Sr:Ca measures on average. Hence, a total of 14 649 Sr:Ca measures are analysed as 14 649 events representing a habitat use. Th proposed approach is computationally efficient, as only a few minutes are required to process the whole sample set, including both the estimation of the habitat Sr:Ca GMM and the reconstruction of all of the individual patterns of habitat use. Compared with previous work, the key feature of this quantitative framework is that a nonsubjective interpretation of individual Sr:Ca series in terms of habitat use is provided from an unsupervised analysis.

In the investigation of individual habitat use chronologies from chemical otolith signatures, the key assumption is that the temporal resolution associated with the sampling of these signatures on the otolith is a relevant scale for the analysis of fish movement. In our case, the sampled Sr:Ca measures lead to an approximately monthly resolution (for the first 6 years after the glass eel mark). Hence, movements at a finer submonthly scale can not be investigated. It should be stressed that this assumption underlies not only the present study, but also all previous work dedicated to the analysis of eel behaviour from otolith Sr:Ca. It is motivated by previous results (Helfman and Bozeman 1983; Aoyama and Sasai 2002; Cairns et al. 2004) showing that eels have a strong territorial behaviour. Exploiting the HMM framework, the estimated transition statistics indicate that short (i.e., 1 or 2 months) transitions from one habitat type to another are highly unlikely. Reconstructed habitat sequences then depict a strong temporal coherence. These results justify, from a statistical point of view, the choice of the HMM, as well as the assumption that eel movements among habitat types occur at a temporal resolution greater than 1 month, which can be analyzed from otolith chemical signatures.

The absence of known labelled data (i.e., fish for which at least partial habitat use chronologies would be known) prevents the performance of some direct validation of the proposed framework. It should be stressed that this issue is not specific to this work. It can also be noted for most previous work dedicated to the reconstruction of individual life traits from the analysis of otolith signatures (Elsdon and Gillanders 2003). Controlled experiments have been carried out to analyze and validate the combined effects of environment and ontogeny on chemical otolith features (Elsdon and Gillanders 2003; Daverat et al. 2005). Such experiments can be used to calibrate Sr:Ca – habitat equations. These equa-

© 2007 NRC Canada

Fig. 8. Analysis of transition features for the processed otolith data set: (*a–b*) relative frequencies (in log scale) of the instantaneous transitions from the estuarine state to one of the three states (namely, riverine (dotted lines), estuarine (solid lines), marine (broken lines)) as a function of (*a*) age or (*b*) season; (*c*) distribution of ages at transition from the river (R) to the estuary (E); (*d*) distribution of the duration of the stay in the riverine (R) state prior to the transition to the estuary (E); (*e*) distribution of ages at transition from the estuary (E) to the river (R; solid line) and the marine area (M; broken line); (*f*) distribution of the duration of the stay in the estuarine (E) state prior to the transition to the river (R; solid line) and the marine area (M; broken line).

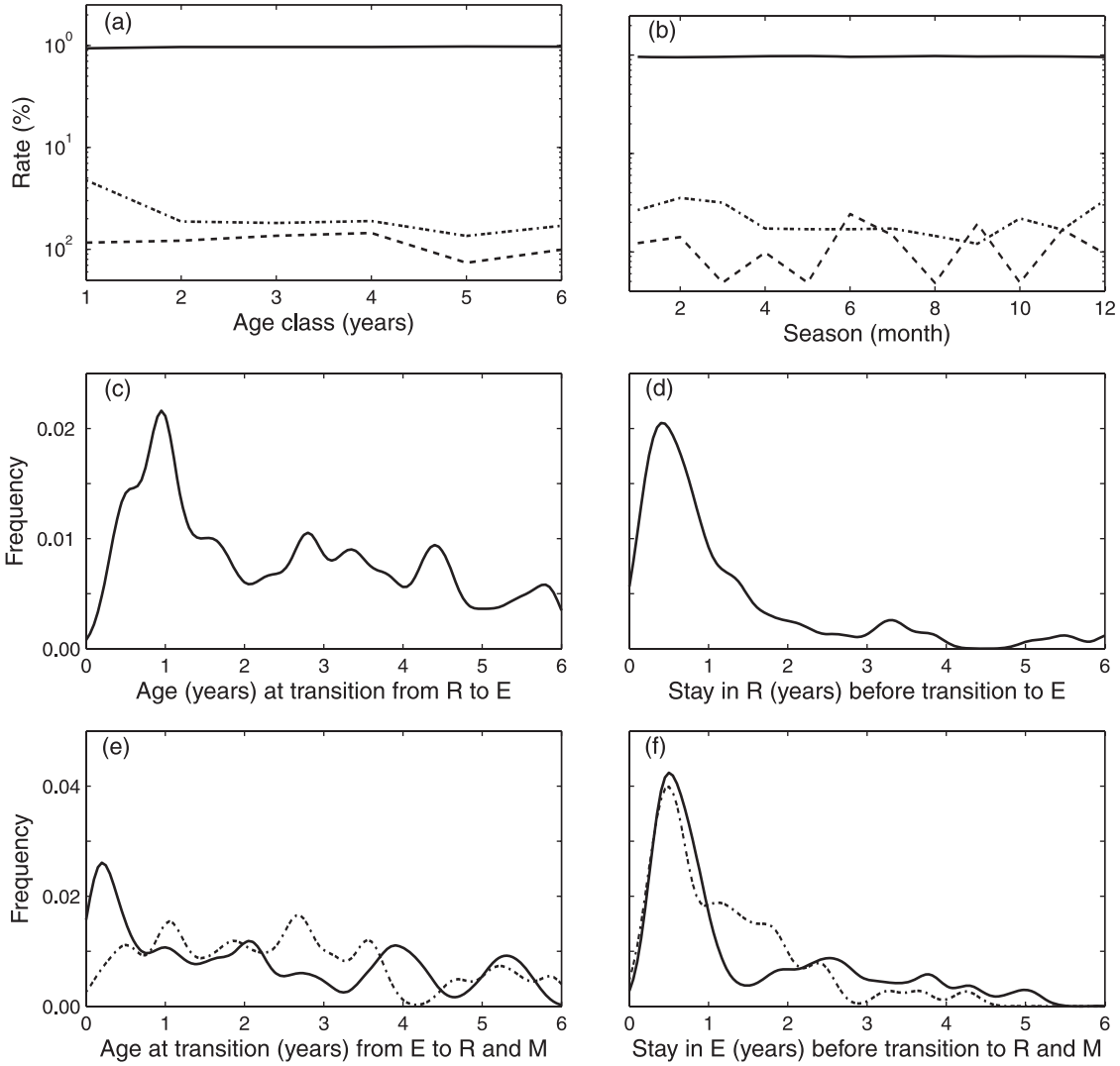

tions cannot necessarily be extended to samples from the wild, especially regarding model uncertainty (e.g., the standard deviation in Gaussian models). More importantly, such experiments do not permit the assessment of the temporal dynamics of the habitat sequence. As illustrated by the reported results, habitat sequences depict a strong temporal correlation and can not be modelled as sequences of independent variables. The HMM can be viewed as a means for combining the characterization of Sr:Ca – habitat relationship to a dynamic prior (i.e., the transition matrix) fitted to the considered data set. Though no direct validation can be reported for the individual HMM-based reconstructions of the habitat sequences, the HMM is valid from a statistical point of view in its ability to characterize and reconstruct the transitions of eels among habitat types in the Gironde River watershed.

From a methodological point of view, the proposed probabilistic models could obviously take into account other types of discrete parameters, i.e., physiological, but they might also be extended to continuous state variables (e.g., temperature). Recent developments in the field of conditional random fields (Lafferty et al. 2001) might also be investigated to take into account more complex time dynamics or continuous state sequences.

Unsupervised extraction and analysis of movement patterns

A major contribution of the proposed Bayesian framework lies in the nonsubjective, unsupervised, and thus exhaustive categorization of individual movement patterns. Thirty-seven different patterns of habitat use, with 20 patterns accounting for more than 80% of the sample, are identified within the processed sample set using the HMM scheme. Owing to the weaker temporal coherence of the GMM-based habitat sequences, the unsupervised categorization of these GMM-based sequences lead to 88 movement patterns, with only

© 2007 NRC Canada

five accounting for more than 3% of the samples. Considering macrocategories resulting from the grouping of movement patterns involving one or several migrations between two habitat types, it is shown that the results issued from GMM and HMM schemes mainly differ in the estimation of the relative frequencies of the resident behaviours (respectively, 10% and 28% of the samples). In particular, resident behaviours in the estuary account for 7.6% according to the HMM method and only 0.6% according to the GMM method. The latter result is not consistent with previous work (Tsukamoto and Arai 2001; Daverat et al. 2004, 2005) and reinforces the preference given to the HMM scheme.

Treatment of the same data set is performed according to a supervised classification in a previous study (Daverat and Tomas 2006). This categorization, based on only six classes, fails in precisely describing the repertoire of behaviour of the eels. Those six classes are defined a priori from the visual inspection of all the plots of the individual Sr:Ca series and from results for other populations found in the literature, which are not very robust. Previous work relies mainly on such supervised classification for testing a priori hypotheses on patterns of habitat use. In most cases, some individual patterns do not fit these a priori hypotheses (Tsukamoto and Arai 2001; Tzeng et al. 2002; Kotake et al. 2005) and are then withdrawn from the analysis. In contrast, the robust and unsupervised categorization of movement patterns greatly improves the investigation of unknown populations thanks to the direct determination of the diversity of the patterns of habitat use and the associated proportions.

The diversity of habitat use chronologies reported here is consistent with habitat use patterns found for *Anguilla anguilla* in the Baltic Sea (Tzeng et al. 1997; Limburg et al. 2003), as well as those of other temperate eel species such as *A. japonica* (Tsukamoto and Arai 2001; Tzeng et al. 2002), *A. rostrata* (Jessop et al. 2002; Morrison et al. 2003; Cairns et al. 2004), and *A. australis* and *A. dieffenbachii* (Arai et al. 2004). The present work confirms the existence of resident eels behaviours of their capture site (about 28%). As suggested by "transients" (Tsukamoto and Arai 2001) or "nomads" (Daverat et al. 2004, 2005), a significant number of eels (more than 72%) is reported to change habitats once or more. Interestingly, most of the fish (53%) involve habitat shifts between only two habitat types (namely, between the river and the estuary and between the estuary and the marine area). Chronologies with multiple transitions between the river and the estuary found for some eels collected in the estuary might be interpreted as an absence of movement under the seasonal fluctuations of river flows into the estuary. Though the estimated habitat-related models account for these seasonal fluctuations and Sr:Ca distributions are well discriminated whatever the season, the GMM-based reconstruction may be affected by these fluctuations. In the HMM-based reconstruction, the temporal prior estimated by the HMM imposes a strong temporal coherence. Consequently, the reconstruction of such mislabelled HMM-based habitat sequences is unlikely, so that the hypothesis of patterns with multiple or seasonal movements is confirmed by the present study.

As a by-product of the proposed approach, statistical descriptors of the fish movements between habitats, such as the distribution of the transition time from one habitat to another or the distribution of time spent in a given habitat after a transition, are evaluated for the considered data set. This results in a significant gain in analysis time and power compared with previous methods that require the information from each Sr:Ca series to be retrieved individually. The analysis of the transitions reveals that movements between two different habitats are not as frequent as residence in the same habitat throughout the fish's life. The same result is reported for studies using mark–recapture techniques (Jellyman et al. 1996; Morrison and Secor 2003) and telemetry (Parker 1995), which show that most yellow eels tend to adopt a resident behaviour. Transitions are rare temporal events throughout the fish's life, which makes them difficult to observe directly. In this study, the frequency of transitions between two different habitats decreases as the age of the eel increase. Similar results are known for *A. japonica* (Tzeng et al. 2002) and *A. rostrata* (Morrison et al. 2003), as well as *A. anguilla* (Daverat and Tomas 2006). It is also revealed that most eels spent less than 1 year in one habitat before changing again.

The unsupervised categorization framework enlarges the scope of possible analysis in terms of fish ecology. Further developments of the analysis of eel habitat use could consist of comparing individual parameters (size at age, age at maturity) of the different habitat use patterns. Such analysis could also focus on a specific stage of the fish (age or size class). More generally, it provides a powerful tool for assessing the relative efficiency of individual tactics in terms of fitness. At a broader scale, the proposed approach demonstrates the actual interest in using advanced processing techniques to fully exploit the rich potential of individual biological archives, such as fish otoliths, to characterize individual life traits. A wide range of applications for the analysis of individual life traits might be stated as such a Bayesian reconstruction of the time series of a state sequence from a set of chemical and structural measures.

Acknowledgement

We thank the anonymous referees for helpful comments on an earlier version of the manuscript.

References

Arai, T., Kotake, A., Lokman, P.M., Miller, M.J., and Tsukamoto, K. 2004. Evidence of different habitat use by New Zealand freshwater eels *Anguilla australis* and *A. dieffenbachii*, as revealed by otolith microchemistry. Mar. Ecol. Prog. Ser. **266**: 213–225.

Awad, A.M. 1996. Properties of the Akaike information criterion. Microelectron. Reliab. **36**: 457–464.

Aoyama, J., and Sasai, S. 2002. A preliminary study of the movements of yellow and silver eels, *Anguilla japonica*, in the estuary of the Fukui River, Japan, as revealed by acoustic tracking. Hydrobiologia, **470**: 31–36.

Berg, R. 1985. Age determination of eels, *Anguilla anguilla* (L.): comparison of field data with otolith ring patterns. J. Fish Biol. **26**: 537–554.

Bishop, C. 1995. Neural networks for pattern recognition. Oxford University Press, Oxford, UK.

Cairns, D.K., Shiao, J.C., Iizuka, Y., Tzeng, W.N., and MacPherson, C.D. 2004. Movement patterns of American eels in an impounded

© 2007 NRC Canada

watercourse, as indicated by otolith microchemistry. N. Am. J. Fish. Manag. **24**: 452–458.

Campana, S.E. 1999. Chemistry and composition of fish otoliths: pathways, mechanisms and applications. Mar. Ecol. Prog. Ser. **188**: 263–297.

Campana, S.E., and Casselman, J.M. 1993. Stock discrimination using otolith shape analysis. Can. J. Fish. Aquat. Sci. **50**: 1062–1083.

Campana, S.E., Chouinard, G.A., Hanson, J.M., Frechet, A., and Brattey, J. 2000. Otolith elemental fingerprints as biological tracers of fish stocks. Fish. Res. **46**: 343–357.

Cardinale, M., Doering-Arjes, P., Kastowsky, M., and Mosegaard, H. 2004. Effects of sex, stock, and environment on the shape of known-age Atlantic cod (*Gadus morhua*) otoliths. Can. J. Fish. Aquat. Sci. **61**: 158–167.

Daverat, F., and Tomas, J. 2006. Tactics and demographic attributes of the European eel (*Anguilla anguilla*): the case study of the Gironde watershed (Southwest France). Mar. Ecol. Prog. Ser. **307**: 247–257.

Daverat, F., Elie, P., and Lahaye, M. 2004. Microchemistry contribution to a first approach to the diversity of life histories of eels from the lower part of the Gironde Garonne Dordogne watershed. Cybium, **28**: 83–90.

Daverat, F., Tomas, J., Lahaye, M., Palmer, M., and Elie, P. 2005. Tracking continental habitat shifts of eels using otolith Sr/Ca ratios: validation and application to the coastal, estuarine and riverine eels of the Gironde–Garonne–Dordogne watershed. Mar. Freshw. Res. **56**: 619–627.

Elsdon, T.S., and Gillanders, B.M. 2003 Reconstructing migratory patterns of fish based on environmental influences on otolith chemistry. Rev. Fish Biol. Fish. **13**: 219–235

Elsdon, T.S., and Gillanders, B.M. 2005. Consistency of patterns between laboratory experiments and field-collected fish in otolith chemistry: an example and applications for salinity reconstructions. Mar. Freshw. Res. **56**: 609–617.

Fablet, R. 2006. Semi-local extraction of ring structures in images of biological hard tissues: application to the Bayesian interpretation of fish otoliths for age and growth estimation. Can. J. Fish. Aquat. Sci. **63**(6): 141–1428.

Helfman, G.S., and Bozeman, E.L. 1983. Ultrasonic telemetry of American eel in a tidal creek. Trans. Am. Fish. Soc. **112**: 105–110.

Jellyman, D.J., Glova, G.J., and Todd, P.R. 1996. Movements of shortfinned eels, Anguilla australis, in Lake Ellesmere, New Zealand: results from mark–recapture studies and sonic tracking. N.Z. J. Mar. Freshw. Res. **30**: 371–381.

Jessop, B.M., Shiao, J.-C., Iizuka, Y., and Tzeng, W.-N. 2002. Migratory behaviour and habitat use by American eels *Anguilla rostrata* as revealed by otolith microchemistry. Mar. Ecol. Prog. Ser. **233**: 217–229.

Kawakami, Y., Mochioka, N., Morishita, K., Tajima, T., Nakagawa, H., Toh, H., and Nakazono, A. 1998. Factors influencing otolith strontium/calcium ratios in *Anguilla japonica* elvers. Environ. Biol. Fishes, **52**: 299–303.

Kotake, A., Okamura, A., Yamada, Y., Utoh, T., Arai, T., Miller, M.J., Oka, H., and Tsukamoto, K. 2005. Seasonal variation in the migratory history of the Japanese eel *Anguilla japonica* in Mikawa Bay, Japan. Mar. Ecol. Prog. Ser. **293**: 213–225.

Kraus, R.T., and Secor, D.H. 2003. Response of otolith Sr:Ca to a manipulated environment in young American eels. Am. Fish. Soc. Symp. **33**: 79–85.

Kraus, R.T., and Secor, D.H. 2004. Incorporation of strontium into otoliths of an estuarine fish. J. Exp. Mar. Biol. Ecol. **302**: 85–106.

Lafferty, J., McCallum, A., and Pereira, F. 2001. Conditional random fields: probabilistic models for segmenting and labeling sequence data. In Proceedings of the 18th International Conference on Machine Learning (ICML'2001), 28 June – 1 July 2001, Williamstown, Mass. *Edited by* C.E. Brodley and A.P. Danyluk. Morgan Kaufmann Publishers Inc., San Francisco.

Limburg, K.E., Svedang, H., Elfman, M., and Kristiansson, P. 2003. Do stocked freshwater eels migrate? Evidence from the Baltic suggests "yes". *In* Biology, management and protection of catadromous eels. Am. Fish. Soc. Symp. **33**: 275–284.

Martin, G.B., and Thorrold, S.R. 2005. Temperature and salinity effects on magnesium, manganese, and barium incorporation in otoliths of larval and early juvenile spot *Leiostomus xanthurus*. Mar. Ecol. Prog. Ser. **293**: 223–232.

McCullagh, P., and Nelder, J.A. 1989. Generalized linear models. Chapman and Hall, London.

Milton, D.A., and Chenery, S.R. 2003. Movement patterns of the tropical shad hilsa (*Tenualosa ilisha*) infered from transects of $^{87}Sr/^{86}Sr$ isotope ratios in their otoliths. Can. J. Fish. Aquat. Sci. **60**: 1376–1385.

Morrison, W.E., and Secor, D.H. 2003. Demographic attributes of yellow-phase American eels (*Anguilla rostrata*) in the Hudson River estuary. Can. J. Fish. Aquat. Sci. **60**: 1487–1501.

Morrison, W.E., Secor, D.H., and Piccoli, P.M. 2003. Estuarine habitat use by Hudson River American eels as determined by otolith strontium:calcium ratios. *In* Biology, management and protection of catadromous eels. Am. Fish. Soc. Symp. **33**: 87–100.

Mounaix, B., and Fontenelle, G. 1994. Anguilles estuariennes et fluviales: apports de l'otolithométrie. Bull. Fr. Peche Piscic. **335**: 67–80.

Murphy, K. 2004. Conditional random field (CRF) toolbox for Matlab [online]. Available from www.cs.ubc.ca/~murphyk/Software/CRF/crf.html [updated 23 May 2006].

Nabney, I. 2001. Netlab: algorithms for pattern recognition. Springer-Verlag, New York.

Nelson, C.S., Northcote, T.G., and Hendy, C.H. 1989. Potential use of oxygen and carbon isotopic composition of otoliths to identify migratory and non-migratory stocks of the New Zealand common smelt: a pilot study. N.Z. J. Mar. Freshw. Res. **23**: 337–344.

Parker, S.J. 1995. Homing ability and home range of yellow phase American eels in a tidally dominated estuary. J. Mar. Biol. Assoc. U.K. **75**: 127–140.

Rabiner, L.R. 1989. Tutorial on hidden Markov models and selected applications in speech recognition. Proc. IEEE, **77**: 257–286.

R Development Core Team. 2005. R: a language and environment for statistical computing. R Foundation for Statistical Computing, Vienna, Austria.

Secor, D.H. 1999. Specifying divergent migrations in the concept of stock: the contingent hypothesis. Fish. Res. **43**: 13–34.

Silber, J.H., Rosenbaum, P.R., and Ross, R.N. 1995. Comparing the contribution of groups of predictors: which outcomes vary with hospital rather than patient characteristics? J. Am. Statist. Assoc. **90**: 7–18.

Thorrold, S.R., and Shuttleworth, S. 2000. In situ analysis of trace elements and isotope ratios in fish otoliths using laser ablation sector field inductively coupled plasma mass spectrometry. Can. J. Fish. Aquat. Sci. **57**: 1232–1242.

Thorrold, S.R., Jones, C.M., and Campana, S.E. 1997. Response of otolith microchemistry to environmental variations experienced by larval and juvenile Atlantic croaker (*Micropogonias undulatus*). Limnol. Oceanogr. **42**: 102–111.

Troadec, H., Benzinou, A., Rodin, V., and Le Bihan, J. 2000. Use of deformable template for two-dimensional growth ring detection of otoliths by digital image processing: application to plaice (*Pleuronectes platessa*) otoliths. Fish. Res. **46**: 155–163.

© 2007 NRC Canada

Tsukamoto, K., and Arai, T. 2001. Facultative catadromy of the eel *Anguilla japonica* between freshwater and seawater habitats. Mar. Ecol. Prog. Ser. **220**: 265–276.

Tzeng, W.N., Wu, H.F., and Wickstrom, H. 1994. Scanning electron microscopic analysis of annulus microstructure in otolith of European eel, *Anguilla anguilla*. J. Fish Biol. **45**: 479–492.

Tzeng, W.N., Severin, K.P., and Wickstrom, H. 1997. Use of otolith microchemistry to investigate the environmental history of European eel *Anguilla anguilla*. Mar. Ecol. Prog. Ser. **149**: 73–81.

Tzeng, W.N., Shiao, J.C., and Iizuka, Y. 2002. Use of otolith Sr:Ca ratios to study the riverine migratory behaviors of Japanese eel *Anguilla japonica*. Mar. Ecol. Prog. Ser. **245**: 213–221.

Appendix A

EM parameter estimation for Gaussian mixture models

The estimation of the parameters of the Gaussian mixture models is carried out according to the maximum likelihood (ML) criterion. It resorts to the following maximization issue:

$$\{\hat{\pi}_H, \hat{\Theta}_H, \hat{\sigma}_H\}_{H\in\{\mathrm{R,E,M}\}} = \arg \max_{\{\pi_H, \Theta_H, \sigma_H\}_{H\in\{\mathrm{R,E,M}\}}} \times \prod_i p\,(y_i | a_i, s_i, \{\pi_H, \Theta_H, \sigma_H\}_{H\in\{\mathrm{R,E,M}\}}$$

To solve for this maximization issue, we use the expectation–maximization (EM) algorithm (Bishop 1995). Let us denote by x_i the variable stating that the ith sample is issued from habitat x_i. The EM algorithm iterates two steps until convergence. At iteration k, the E step computes the posterior likelihood $p(x_i | y_i, a_i, s_i, \{\pi_H^k, \Theta_H^k, \sigma_H^k\}_{H\in\{\mathrm{R,E,M}\}}$ of assigning x_i to habitat H given the observed measure y_i and the current estimate of the mixture parameters $\{\pi_H^k, \Theta_H^k, \sigma_H^k\}_{H\in\{\mathrm{R,E,M}\}}$:

$$p(x_i = H_1 | y_i, a_i, s_i, \{\pi_H^k, \Theta_H^k, \sigma_H^k\}_{H\in\{\mathrm{R,E,M}\}}) = \frac{\pi_{H_1}^k p(y_i | a_i, s_i, \Theta_{H_1}^k, \sigma_{H_1}^k)}{\sum_{H_2\in\{\mathrm{R,E,M}\}} \pi_{H_2}^k p(y_i | a_i, s_i, \Theta_{H_2}^k, \sigma_{H_2}^k)}$$

Given the posterior probabilities, the M step aims at updating model parameters $\{\pi_H^{k+1}, \Theta_H^{k+1}, \sigma_H^{k+1}\}_{H\in\{\mathrm{R,E,M}\}}$. To simplify the notations, let us denote by τ_{iH} the posterior $p(x_i | y_i, a_i, s_i, \{\pi_H^k, \Theta_H^k, \sigma_H^k\}_{H\in\{\mathrm{R,E,M}\}}$. The new priors $\{\pi_H^{k+1}\}_{H\in\{\mathrm{R,E,M}\}}$ are updated as

$$\pi_H^{k+1} = \frac{1}{\mathrm{N}} \sum_i \tau_{iH}$$

The new model parameters $\Theta_H^{k+1} = (m_H, \lambda_H, \mu_H)$ are estimated as the solution of the following weighted least-square problem, where the weights are give by posterior likelihoods τ_{iH}:

$$\Theta_H^{k+1} = \arg \min_{\Theta} \left[\sum_i \tau_{iH} (y_i - Z_i^t \Theta)^2 \right]$$

where $\boldsymbol{Z}_i$ is the vector defined by $[1, a_i, s_i]$. This weighted linear regression leads to

$$\Theta_H^{k+1} = \left[\sum_i \tau_{iH} Z_i^t Z_i \right]^{-1} \sum_i \tau_{iH} y_i Z_i$$

Then, the updated standard deviations $\{\sigma_H^{k+1}\}_{H\in\{\mathrm{R,E,M}\}}$ are computed from the weighted average of the squared residual error $r_{iH} = y_i - Z_i^t \Theta_H^{k+1}$ with respect to the prediction issued from the current model estimate:

$$\pi_H^{k+1} = \sqrt{\frac{1}{N} \sum_i \tau_{iH} r_{iH}^2}$$

© 2007 NRC Canada

III Méthodes d'imagerie sonar pour l'observation des écosystèmes marins

De part les caractéristiques de propagation des ondes acoustiques dans l'eau, les moyens acoustiques constituent des technologies de premier ordre dans le domaine sous-marin. A titre d'exemple, nous pouvons citer :

- Les communications acoustiques sous-marines, aussi bien exploitées par les animaux marins que par des systèmes de transmission de données (Kilfoyle, Baggeroer 2000; Socheleau, Laot et al. 2011);
- La surveillance du milieu marin par écoute acoustique passive (Nystuen, Selsor 1997; Roy, Simard et al. 2010);
- La tomographie acoustique du milieu sous-marin pour analyser des caractéristiques géophysiques du milieu (Rabaste, Chonavel 2007; Iturbe, Roux et al. 2009);
- La caractérisation des fonds marins (e.g., habitats marins, guerre des mines) à partir de données acquises par des écosondeurs (Kenny, Cato et al. 2003; Blondel 2009);
- L'analyse de l'écosystème pélagique (e.g., plankton, poissons pélagiques) à partir de sonars ou échosondeurs (Koslow 2009; Bertrand, Ballon et al. 2010; Ballon, Bertrand et al. 2011).

Nos travaux se situent davantage dans le cadre des deux derniers domaines d'application avec une orientation privilégiée vers les aspects d'observation et suivi de l'état des écosystèmes marins. Dans ce contexte, l'acoustique constitue un outil qualitatif et quantitatif non-intrusif sans équivalent. Le principe général des échosondeurs est donné ci-dessous (Figure 15). Il s'agit d'une émission d'une onde acoustique dont l'écho reçu est analysé. Les caractéristiques de l'écho, en termes de retard et d'intensité, fournissant des indications sur la distance à l'émetteur et le type de cible (fond, bancs de poissons, couches de plankton,…) (Lurton 2002; Blondel 2009). Le plus souvent, ces modalités acoustiques conduisent à la formation d'images par la concaténation de pings, correspondant à des émissions acoustiques dans différentes directions (sondeur multifaisceaux) et/ou à des émissions successives couvrant des zones différentes du fait du déplacement du capteur qui est souvent soit remorqué par le navire soit monté sur la quille du navire.

De manière générale, l'apport des méthodologies de traitement du signal et des images que nous avons proposé se situe dans l'extraction et la classification de l'information d'intérêt (e.g., types de fond, catégorie de cibles biologiques) à partir du signal acoustique reçu par des approches de type classification et/ou segmentation. Nous détaillons dans la suite ces contributions pour les deux domaines d'application privilégiés, la cartographie des fonds marins et l'observation sonar de la colonne d'eau.

Ces travaux ont été principalement conduits dans le cadre de collaborations entre Telecom Bretagne, les départements STH et NSE de l'Ifremer, les UMRs LEMAR et EME et l'IMARPE, notamment à travers les thèses de I. Karoui, R. Lefort et H.G. Nguyen.

Figure 15. Schéma de principe de la formation d'image acoustique des fonds marins par des émissions/réceptions d'un sondeur de fond multifaiscaeaux : émission/réception à partir de l'échosondeur (haut), image formée par concaténation des acquisitions acoustiques transversalement au déplacement du capteur (milieu), distribution des angles d'incidence associées à la dimension horizontale de l'image formée (bas). D'après (Karoui 2007).

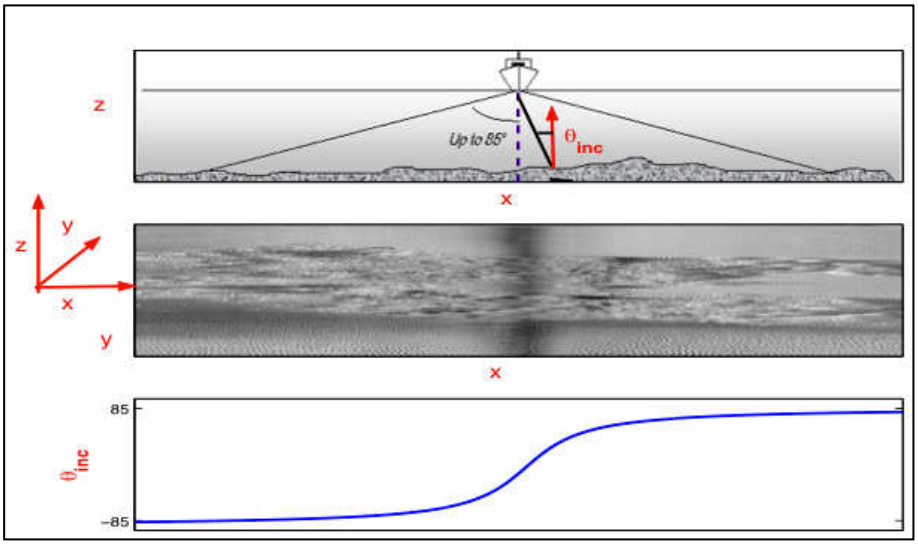

III.1 Classification et segmentation des textures sonar pour l'aide à la cartographie des fonds marins

La cartographie des fonds marins (Figure 16) consiste en la photo-interprétation d'images acoustiques géoréférencées acquises par des sondeurs. La technologie des sondeurs multifaisceaux qui est la plus répandue consiste à émettre des signaux acoustiques dans différentes directions réparties suivant un cône pour éclairer une certaine fauchée (Lurton 2002; Blondel 2009). L'énergie acoustique rétrodiffusée par le fond pour chaque angle émission permet de former un profil d'émission. Le niveau d'énergie rétrodiffusé dépend typiquement de l'angle d'incidence, du micro-relief et des caractéristiques d'absorption du fond. A partir d'un ensemble de profils angulaires consécutifs, il est possible, en tenant compte du déplacement du capteur, y compris des phénomènes de tangage et roulis, de former une image acoustique du fond.

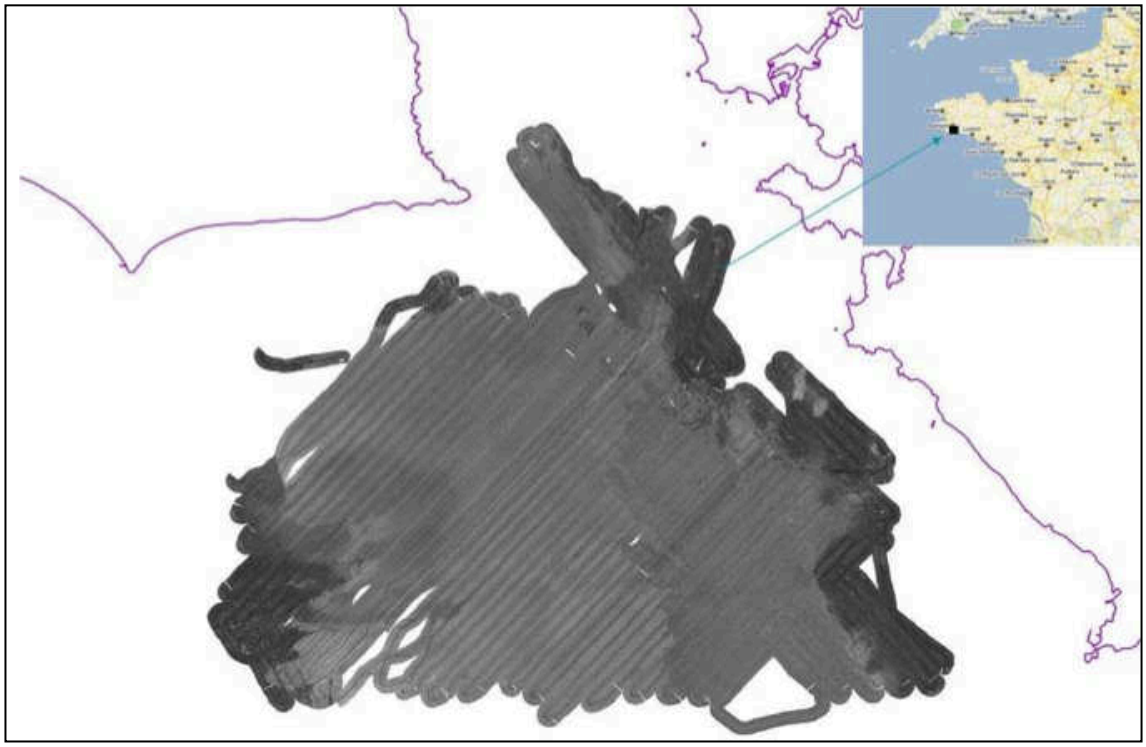

Figure 16. Illustration du principe de la construction d'une cartographie des fonds marins lors d'une campagne acoustique sonar (données Ifremer**)**.

Du fait de leur mode de formation, ces images présentent des caractéristiques spécifiques. Alors que les types de fonds marins se distinguent par des critères texturaux comme illustré ci-dessous (Figure17), il est également notable que ces images présentent des variabilités angulaires. Ainsi la zone spéculaire correspondant à des angles d'émission proche de la verticale est caractérisée par de forte énergie rétrodiffusée, voire une saturation de la réponse acoustique, et l'énergie rétrodiffusée diminue le long de la fauchée (Figure 18, gauche). Cette variation de contraste interne à l'image s'accompagne également de distorsions géométriques induites par l'observation d'une surface 3D (le fond) présentant un certain relief à des angles de rasance différents. Par exemple, au plus grands angles de rasance, les phénomènes d'ombrages sont nécessairement plus importants à même relief ce qui conduit à la génération de structures géométriques plus larges (Figure 18, droite). Outre ces deux types de distorsion, les images acoustiques du fond sont caractérisées par un niveau de bruit de chatoiement ("speckle") qui traduit des phénomènes d'incohérence de phase des ondes acoustiques rétrodiffusées par des les réflecteurs élémentaires de la surface (Lurton 2002, Maître 2008).

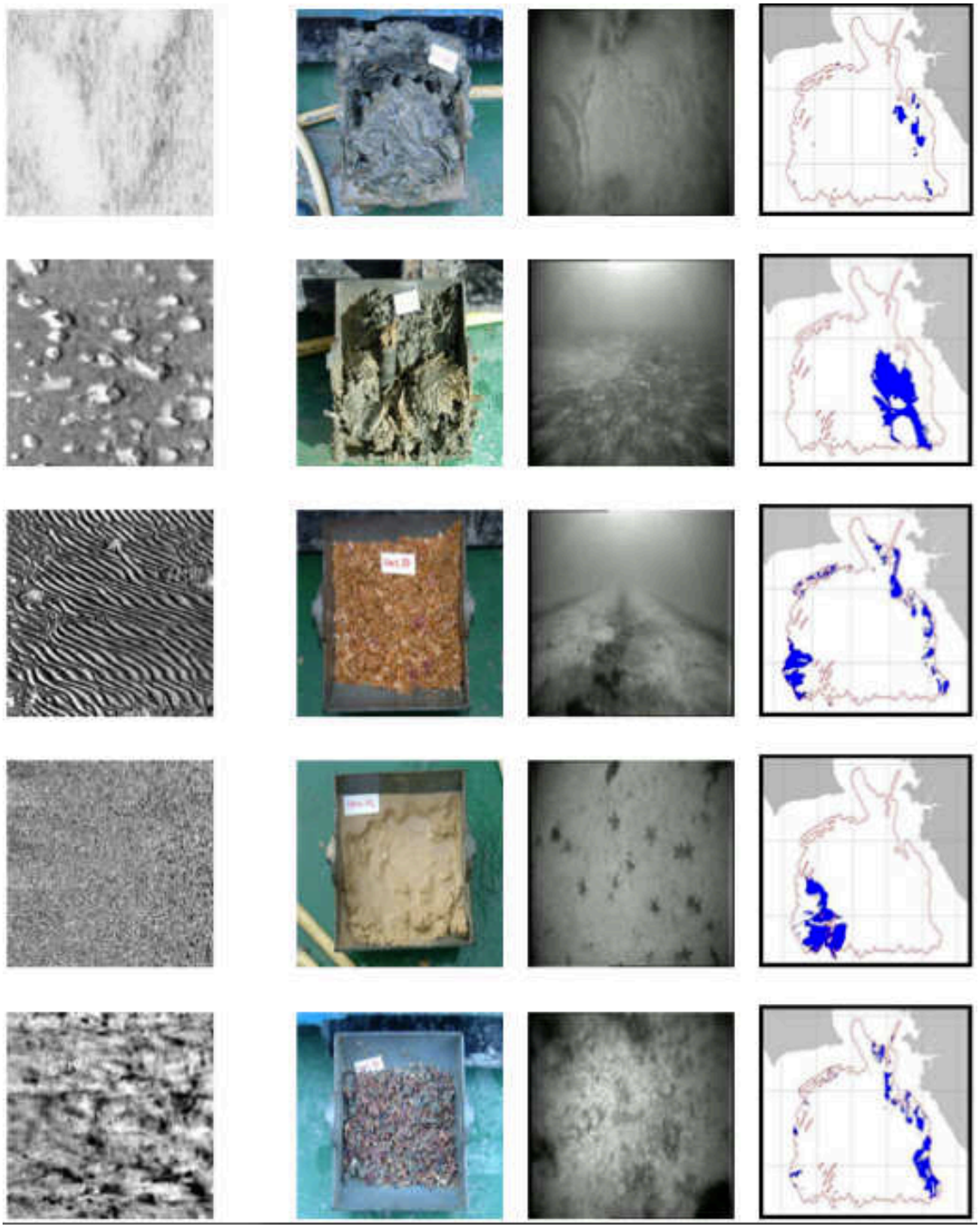

Figure 17. Illustration de la diversité des textures sonar associées à différents types de fonds marins : de gauche à droite, textures sonar, illustration d'un carottage, image optique du fond, cartographie du type de fond associé (Données Ifremer). D'après (Nguyen 2011).

Les méthodes de traitement de ces images acoustiques du fond développées ont cherché à intégrer ou tirer partie de ces propriétés vis-à-vis des problématiques de reconnaissance et classification des fonds considérées. Du point du traitement d'images, les problématiques à considérer s'apparente à des problématiques génériques de bruit, variations locales de contraste et distorsion géométrique. Trois aspects ont plus particulièrement été abordés : le pré-traitement des images acoustiques, incluant les phases de débruitage et calibration (Fablet, Augustin et al. 2005; Fablet, Augustin 2006), la caractérisation et la reconnaissance des textures sonars (Karoui, Fablet et al. 2008; Nguyen, Fablet et al. 2012) et la segmentation des types de fond marin (Karoui, Fablet et al. 2009; Karoui, Fablet et al. 2010). Nous mettons dans la suite plus particulièrement l'accent sur ces deux derniers aspects qui ont l'objet des contributions les plus significatives.

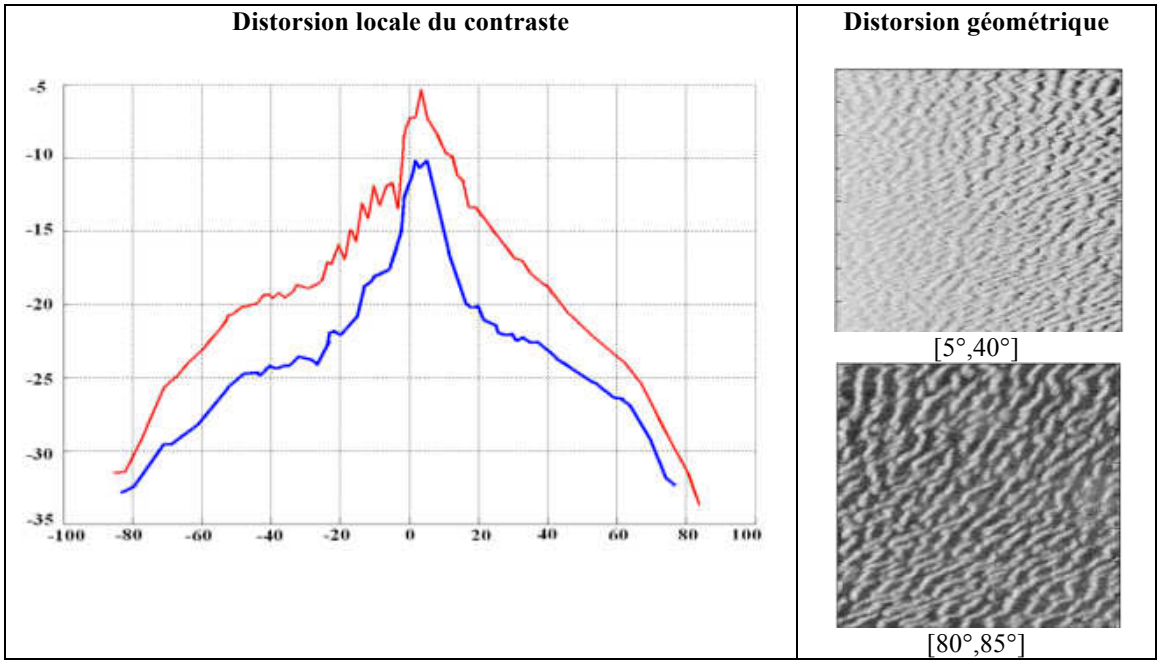

Figure 18. Distorsions de contraste et de géométrie observées dans les images acoustiques des fonds marins acquises par des sondeurs multi-faisceaux : évolution de l'indice de rétrodiffusion du fond en fonction de l'angle d'incidence pour deux types de fonds de sable (gauche), images sonar de rides de sable pour des gammes d'angle d'incidence différentes (droite).

III.1.1 Caractérisation et reconnaissance des textures sonar

Synthèse des contributions: *Nos travaux ont porté sur le développement de nouvelles méthodes de caractérisation et reconnaissance de textures sonars, suivant deux axes principaux, 1) la capacité à tirer partie de manière optimale de plusieurs signatures texturales (e.g., cooccurrences, Gabor,...), 2) la caractérisation et la modélisation de la distribution spatiale de signatures locales élémentaires (points d'intérêt).*

L'un des éléments clés pour développer une chaîne de traitement d'images dédiée à la cartographie des fonds marins est de déterminer des caractéristiques pertinentes et discriminantes des différents types de fonds marins (cf. Figure 17). Les descripteurs texturaux, fondés sur des caractéristiques d'ordre supérieur des images sonar (par opposition aux statistiques d'ordre un telles que la moyenne et la variance du BS (Backscaterring Strength) sur une zone (Hellequin, Boucher et al. 2003; Le Chenadec, Boucher 2007)), semblent bien adaptés à cet objectif. Comme illustré ci-dessus (Figure 18), il s'agit d'un problème difficile du fait des variabilités des réponses acoustiques observées pour un même type de fond. Il faut noter que ces problématiques de caractérisation invariante des textures sonars vis-à-vis de transformation géométrique et de variations locales du contraste recoupent largement celles abordées dans le cadre de l'analyse des textures naturelles, dont l'analyse a connu récemment un regain d'intérêt dans ce contexte de représentation invariante (Lazebnik, Schmid et al. 2005; Xu, Ji et al. 2009; Xia, Delon et al. 2010) notamment avec l'émergence de méthodes fondées sur l'extraction de points d'intérêt locaux (Mikolajczyk, Schmid 2005; Mikolajczyk, Tuytelaars et al. 2005).

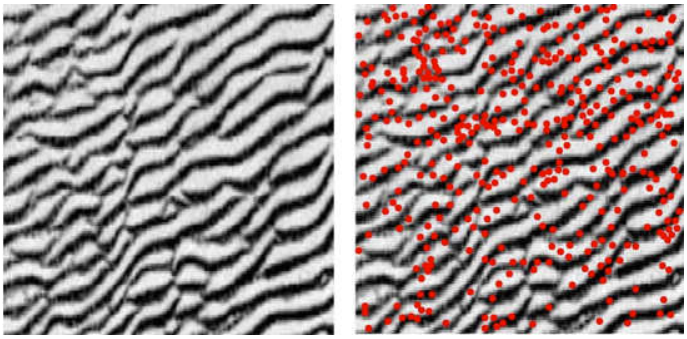

Figure 19. Caractérisation de textures sonar à partir des caractéristiques des distributions de points d'intérêt : exemple de texture sonar (gauche), détection associée de points d'intérêt (ici, points d'intérêt DoG (Mikolajczyk, Tuytelaars et al. 2005)). D'après (Nguyen, 2011).

A travers les thèses d'I. Karoui et de H.G. Nguyen, nous avons abordé ces problématiques suivant deux angles différents. Dans le cadre de la thèse d'I. Karoui, nous nous sommes intéressés à la formulation d'une mesure de similarité de texture permettant de tirer partie de différents types de descripteurs texturaux statistiques (distribution de co-occurrences, de coefficients d'ondelettes, de coefficients de Gabor,…) (Karoui, Fablet et al. 2008). Un critère supervisé de maximisation de la séparation des différentes classes de textures est exploité pour ajuster la mesure de similarité à la complexité du problème traité. La prise en compte de la modulation angulaire propre aux images sonar traitées a également été proposée. Différentes évaluations expérimentales ont démontré l'intérêt d'un couplage de plusieurs types de caractérisation statistique des textures en termes de performances de discrimination des différents types de fonds marins.

Dans le cadre des travaux de thèse de H.G. Nguyen, nous avons envisagé une stratégie alternative fondée sur l'utilisation de points d'intérêt (Nguyen 2011) (Figure 19). Notre contribution se situe dans la proposition de descripteurs de texture combinant à la fois l'information visuelle associée aux points d'intérêt ainsi que l'organisation spatiale des ensembles de points d'intérêt détectés là où les approches proposées n'utilisent généralement que l'information visuelle (e.g., (Lazebnik, Schmid et al. 2005; Zhang, Marszalek et al. 2007)). Formellement, cela revient à considérer les ensembles de points d'intérêt détectés dans une image comme des réalisations de processus ponctuels marqués (Stoyan, Stoyan 1994). Ce tyoe de modélisation par processus ponctuels a fait l'objet d'un certain nombre d'applications en traitement d'images, mais principalement pour des aspects de détection et segmentation d'objets (cf., (Descombes 2011) pour une synthèse récente). Ici, des statistiques descriptives de ces processus, par exemple des statistiques spatiales du deuxième ordre, peuvent être considérées. Ces statistiques se ramènent à des mesures de dénombrement d'occcurrences de points dans des boules de rayons variables autour d'un point de la réalisation. Dans le cas de processus ponctuel marqués, ces statistiques spatiales peuvent être étendues à des occurrences de points d'une catégorie donnée dans une boule centrée en un point de la réalisation d'une autre catégorie :

$$\Gamma_{u,v}(R) = \frac{1}{N} \sum_{p \neq q} \partial_u(S_p) \partial_v(S_q) . 1\left[\|p - q\| < R\right]$$

où N est le nombre des points d'intérêt, u et v des catégories de points d'intérêt, p et q des points d'intérêt de l'image considérée, caractérisé par des signatures S_p et S_q, et R le rayon d'analyse. La mesure $\delta_u(S_p)$ évalue si le point p est associé à la catégorie de signatures u. Ces catégories de signatures sont issues d'une étape de groupement non-supervisé de type K-moyennes appliquée à l'ensemble des signatures des points d'intérêt. Il faut noter que l'estimation de ces moments du second-ordre est biaisée dans le cas d'une estimation sur un support fini. La mise en œuvre de ces statistiques intègre donc des corrections de ces effets de bord (Nguyen, Fablet et al. 2010). En pratique, le descripteur de texture est formé par un ensemble de ces statistiques du second-ordre évaluées pour différentes valeurs de rayon d'analyse. Les caractéristiques d'invariance du descripteur de texture sont partiellement héritées des propriétés des points d'intérêt, notamment pour l'invariance en translation, rotation et contraste. L'invariance en échelle peut également être obtenu par normalisation vis-à-vis de rayons d'analyse de référence. Il est également intéressant de souligner que les statistiques du second-ordre considérées peuvent être vues comme les statistiques suffisantes d'une classe particulière de processus ponctuels, les processus de Cox log-gaussiens (Møller, Syversveen et al. 1998). Ces processus sont complètement caractérisés par une mesure d'intensité et une fonction de covariance. Outre l'intérêt de passer de statistiques descriptives à la définition d'un modèle stochastique explicite, ceci permet par une paramétrisation de la covariance de réduire la dimensionnalité du descripteur de texture (Nguyen, Fablet et al. 2011).

N_t	*Filtres de Gabor*	*Matrice de cooccurrence*	*(Dance, Willamowski et al. 2004)*	*(Ling, S. 2007)*	*(Xu, Ji et al. 2009)*	*(Zhang, Marszalek et al. 2007)*	*Aproche proposée*
1	31.22±3.14	45.33±3.03	67.25±2.75	67.62±2.93	61.14±2.90	72.53±2.45	**75.21±1.75**
5	45.14±2.54	61.58±2.14	76.38±2.15	78.42±2.33	83.33±2.07	88.62±1.33	**91.96±1.13**
10	57.37±1.93	70.67±1.72	81.22±1.72	84.14±1.72	89.68±1.65	93.17±1.15	**95.42±0.71**
15	61.25±1.52	73.85±1.34	86.35±1.20	86.38±1.25	91.34±1.45	95.33±0.98	**96.87±0.65**
20	67.78±1.28	80.12±1.30	91.28±1.15	91.87±1.38	93.85±1.31	96.67±0.93	**97.84±0.32**

Tableau 1. Evaluation de différents descripteurs de texture sur la base de textures UIUC en fonction du nombre d'images d'apprentissage (N_t).

L'évaluation de ces approches sur des bases de référence de texture visuelles (e.g., bases de texture UIUC) a démontré la pertinence de cette approche comparativement aux méthodes de l'état de l'art (Tableau 1). Comme illustré ci-dessus, cette évaluation met notamment en évidence l'intérêt de la caractérisation conjointe des informations visuelles et spatiales associées aux distributions de points d'intérêt (Figure 20). De manière complémentaire, l'analyse d'une base de textures sonar fournies par l'Ifremer permet de valider l'intérêt des techniques de points d'intérêt pour l'analyse des images sonar, avec des gains de l'ordre de 15 à 30% n termes de

bonne classification comparativement à des approches classiques (Gabor, cooccurrences) (Nguyen, Fablet et al. 2012). En termes de complexité, nous avons montré qu'il est possible de se ramener à une complexité du même ordre que les techniques fondées sur les fréquences relatives de catégories de points d'intérêt (sacs de point d'intérêt). Ceci représente un avantage significatif par rapport aux approches fondées sur l'apprentissage de classifieur de points d'intérêt (Zhang, Marszalek et al. 2007) qui conduise à la gestion de bases de données d'apprentissage de très grande taille du fait du nombre élevé de points d'intérêt détectés dans chaque image de texture (typiquement de l'ordre de 1000 points détectés pour une image 256x256).

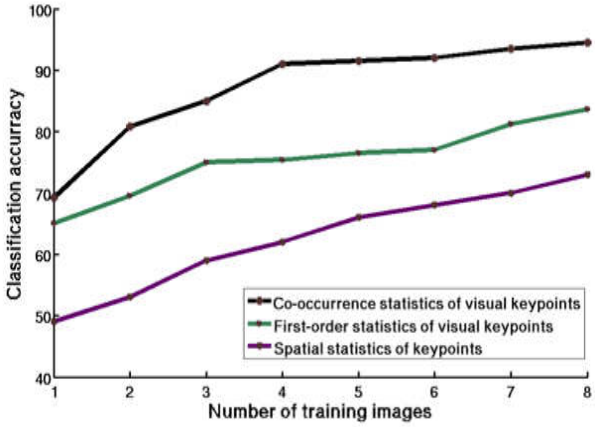

Figure 20. **Illustration de l'intérêt de la caractérisation conjointe des caractéristiques visuelles et spatiales des distributions de points d'intérêt :** comparaison des performances de reconnaissance de texture sur la base UIUC en utilisant les fréquences des catégories de points d'intérêt, les statistiques spatiales des distributions de points d'intérêt avec et sans l'intégration de l'information visuelle. D'après (Nguyen, Fablet et al. 2010).

III.1.2 Segmentation basée texture pour la cartographie sonar des fonds marins

Synthèse des contributions : *Nos travaux ont porté sur le développement et l'évaluation quantitative de différentes méthodes markoviennes et variationnelles de segmentation basée texture d'images sonar des fonds marins. Les résultats obtenus mettent notamment en exergue la pertinence des méthodes variationnelles formulées au niveau région (partition de l'image en régions) plutôt qu'au niveau pixel (étiquetage des pixels).*

L'extraction manuelle des régions d'une image sonar relativement aux différents types de fond observée est une tâche importante, mais fastidieuse, réalisée par des photo-interprètes pour la cartographie des fonds à partir d'images sonar. Dans ce contexte, le développement d'outils de segmentations des images sonar dans un but d'automatisation partielle et/ou d'aide à l'interprétation est particulièrement recherché.

Dans le cadre de la thèse d'I. Karoui, différentes techniques de segmentation supervisée et non-supervisée ont été proposées en exploitant des formulations bayésiennes (ie, champs de Markov) et variationnelles (ie, approche de type « level-set ») (Karoui, Fablet et al. 2009; Karoui, Fablet et al. 2010). L'information de texture est intrinsèquement une information non-locale définie à l'échelle d'un région. Le problème de l'application des techniques classiques de segmentation se pose alors dans la mesure où elles exploitent des descripteurs au niveau pixel (Aujol, Aubert et al. 2003). Une solution consiste à évaluer des caractéristiques texturales sur un voisinage de chaque pixel. Formulée dans un cadre bayésien exploitant les champs de Markov, cette solution nous conduit à la définition d'une énergie de la forme suivante (Karoui, Fablet et al. 2009) :

$$E(e,o) = \sum_{p} V_1\left(e_p, o_p\right) + \lambda \sum_{p,q \text{ voisins}} V_2\left(e_p, e_q\right)$$

où e est le champ des étiquettes, i.e$_p$ est la classe affectée au pixel p, o est le champ des observations, V_1 la fonction potentielle d'attache aux données et V_2 la fonction potentielle de régularisation issue définie sur des cliques d'ordre 2 (typiquement un 8-voisinage). Le premier terme d'énergie évalue la pertinence de l'observation au pixel p vis-à-vis de la classe de texture e_p alors que le deuxième terme tend à favoriser les cartes de segmentation homogène. Le paramètre de pondération λ définit l'importance relative de chaque terme. Dans le cadre de la segmentation de texture, la principale difficulté réside dans la définition du potentiel V_1 et dans le choix des caractéristiques de texture locales o_p. Nous avons proposé de considérer comme caractéristiques de texture des statistiques de réponses à différents filtres (e.g., filtres de Gabor, ondelettes, cooccurrences) et comme fonction potentielle une somme pondérée des distances entre les distributions observées localement et les distributions pour chaque classe de texture (Karoui, Fablet et al. 2008). Le cadre bayésien ainsi défini conduit à la formulation de la segmentation au sens d'un critère MPM (Maximum Posteriori Mode) plutôt que du critère MAP (Maximum A Posteriori), pour minimiser l'erreur de classification au niveau pixel. Ce formalisme fournit

également un cadre bien posé pour l'estimation des paramètres du modèle a priori (ici, le paramètre λ). Ici nous exploitons l'approche ECI (Estimation Conditionnelle Itérative) (Pieczynski 1992; Karoui 2007). L'évaluation expérimentale de cette méthode montre qu'elle permet d'atteindre des niveaux de performance pertinents mais qu'elle se révèle néanmoins relativement sensible à l'ajustement d'un paramètre critique, la taille de la fenêtre locale d'analyse pour l'évaluation des statistiques de texture (cf. Figures 21 & 22).
Une formulation variationnelle au niveau région a été envisagée pour s'affranchir de ce problème (Karoui, Fablet et al. 2010). Elle consiste non pas à formuler la segmentation comme la classification des pixels mais à voir la segmentation d'images comme la recherche d'une partition de l'image en régions disjointes optimale au sens d'un certain critère. Formellement, dans le cas supervisé, ceci conduit à la définition d'une énergie de la forme suivante :

$$E\left(\left\{\Omega_k\right\}\right) = \lambda_1 \sum_k \left|\Omega_k\right| D\left(S_k, S\left(\Omega_k\right)\right) + \lambda_2 \sum_k \left|\Gamma_k\right| + \lambda_3 E_3\left(\left\{\Omega_k\right\}\right)$$

où $\{\Omega_k\}$ forme une partition de l'image, les paramètres λ_i pondèrent l'importance relative des différentes termes d'énergie. Le premier terme évalue la similarité entre les caractéristiques de textures $S(\Omega_k)$ observées dans l'image pour la région Ω_k et les caractéristiques S_k de la classe k. Le deuxième terme est une contrainte de régularisation évaluée sur le périmètre de chaque région. Enfin le troisième terme vise à garantir la contrainte de partition de l'image. Le détail de ces différents termes est fourni dans (Karoui, Fablet et al. 2010).
Au-delà du cadre continu considéré par la formulation variationnelle par opposition à la formulation discrète de l'énergie proposée ci-dessus dans un cadre markovien, ce nouveau critère peut être vu comme une généralisation du précédent, qui correspondrait à un choix particulier de la fonction $D(S(\Omega_k),S_k)$ décomposé comme une somme sur l'ensemble des pixels. L'intérêt de la formulation au niveau région est au contraire de pouvoir spécifier l'évaluation dans son ensemble de la pertinence de la région Ω_k vis-à-vis du modèle de texture de la classe k. Ceci permet notamment de s'affranchir du choix d'une taille de fenêtre locale d'analyse et garantit dans le même temps une estimation plus robuste des statistiques de texture puisque nous disposons d'un plus grand nombre de points pour les évaluer. Formellement, la mesure de similarité $D(S(\Omega_k),S_k)$ est définie de manière analogue au critère markovien par une somme pondérée des distances entre des statistiques de texture (Karoui, Fablet et al. 2008). La principale difficulté du critère variationnel proposé est la mise en œuvre d'un schéma numérique de minimisation. Dans la mesure où la minimisation doit être réalisé sur une partition de l'image, les outils classiques de dérivation de type Euler-Lagrange ne peuvent pas être directement appliqués, mais des formes de dérivation appropriées (Jehan-Besson, Barlaud et al. 2003) doivent être considérés.

Mosaïque de textures

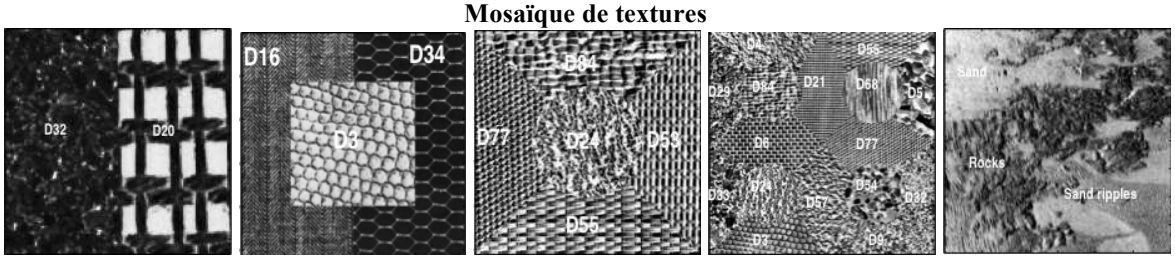

B1 **B2** **B3** **B4** **B5**

Mosaïque	*Méthode markovienne proposée 3X3*	*Méthode markovienne proposée 33X33*	*(Heiler, Schnorr 2003) 3X3*	*(Heiler, Schnorr 2003) 33x33*	*Méthode variationnelle proposée*	*(Randen, Husoy 1999)*
B1	-	-	*7%*	*10%*	***2.7%***	-
B2	*5%*	*2.7%*	*9%*	*2%*	***0.9%***	-
B3	-	*5.4%*	*70%*	*7%*	***4.9%***	*8.2%*
B4	-	*16.2%*	*80%*	*19%*	***13.9%***	*37.2M*
B5	-	*13%*	*25%*	*13%*	***7.5%***	-

Figure 21. Evaluation quantitative de différents méthodes de segmentation sur des mosaïques de textures correspondant à différents niveaux de complexité : mosaïques de textures considérées (haut), taux d'erreur de classification au niveau pixel pour différentes méthodes de segmentation, y compris les méthodes variationnelles « région » et markoviennes décrites dans le texte. Pour les méthodes markoviennes et l'approche variationnelle (Heiler, Schnorr 2003), des fenêtre d'analyse 3x3 et 33x33 sont considérées. D'après (Karoui 2007).

Comme illustré ci-dessous (Figures 21 & 22), l'intérêt de la formulation variationnelle réside à la fois dans une plus grande robustesse à l'initialisation de la segmentation et d'autre part dans la capacité à s'affranchir du choix de la taille de la fenêtre d'analyse, paramètre qui s'avère critique pour la segmentation markovienne, pour

garantir un compromis entre pertinence des statistiques de texture et précision de localisation des frontières des régions de texture. Une évaluation des schémas de classification proposés à la cartographie des fonds marins a été envisagée (Karoui, Fablet et al. 2009). Elle démontre l'apport de la similarité basée texture comparativement aux segmentations d'images sonar exploitées fondées sur des critères d'amplitude (Hellequin, Boucher et al. 2003; Le Chenadec, Boucher 2007). Afin de prendre en compte la variabilité de géométrie et de contraste des textures sonar en fonction de l'angle d'incidence (cf. Figure 18), une adaptation de la mesure de similarité proposée consiste à envisager une somme pondérée sur différents secteurs angulaires : un domaine proche du spéculaire, un domaine correspondant à des angles rasants et un domaine intermédiaire. Ceci se révèle performant du point de vue applicatif (Karoui, Fablet et al. 2009).

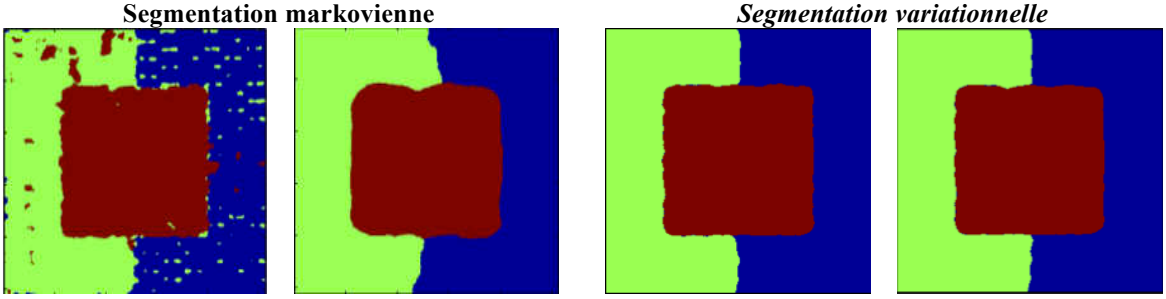

Figure 22. **Comparaison des segmentations de texture par des approches markoviennes et variationnelles pour l'image B2 :** résultat de la segmentation markovienne pour deux tailles de fenêtre d'analyse locale, respectivement 7x7 et 33x33 (bas, gauche), résultat de la segmentation variationnelle pour deux initialisations différentes, respectivement une initialisation aléatoire (A) et une initialisation (B) par maximisation d'un critère de vraisemblance locale (fenêtre d'analyse 7x7). D'après (Karoui 2007).

III.2 Méthodes d'analyse de l'imagerie sonar de la colonne d'eau

Les technologies acoustiques sonar permettent non seulement de cartographier les fonds marins mais aussi de fournir des moyens d'observation de la distribution de cibles biologiques dans la colonne d'eau. Comme illustré ci-dessous (Figure 23), les bancs de poisson, des couches de plancton ou d'autres composantes pélagiques sont associées à des valeurs significatives d'énergie acoustique rétrodiffusée (typiquement de l'ordre de -80dB à -480dB selon les types de cibles). Ces éléments fournissent le principe de l'imagerie sonar de la colonne d'eau par concaténation des données successives acquises par des échosondeurs placés sous la coque de navires se déplaçant à la surface. Les échosondeurs monofaisceau pour des fréquences de quelques dizaines à quelques centaines de Hertz sont les plus couramment utilisés et conduisent à une imagerie 1D+t, la dimension verticale correspondant à la profondeur et la dimension horizontale au déplacement en surface (Simmonds, MacLennan 2005). Plus récemment sont apparus des technologies multifaisceau dédiées à l'observation de la colonne d'eau fournissant une imagerie 2D+t voire 3D+t. Il s'agit notamment de la nouvelle génération de sondeur développée par Simrad en partenariat avec l'Ifremer (Trenkel, Mazauric et al. 2008).

L'observation sonar de la colonne d'eau constitue la seule modalité d'observation non-intrusive (ou peu intrusive) de l'écosystème pélagique permettant un suivi à l'échelle d'un écosystème (c.-à-d. de quelques dizaines ou centaines de miles nautiques) dans le cadre de campagnes océanographiques (Koslow 2009). A titre d'exemple, la gestion des stocks de poissons pélagiques tels que l'anchois repose très largement sur l'exploitation de données sonar pour évaluer la biomasse de ces stocks. De nombreuses autres applications peuvent être citées :

- la caractérisation de structures physiques telles que les déformations de la couche superficielle de l'océan, e.g. la profondeur de l'oxycline (Bertrand, Ballon et al. 2010);
- la caractérisation des communautés biologiques, e.g. zooplancton, poissons pélagiques (Petitgas, Levenez 1996; Stanton, Chu et al. 1996; Kloser, Ryan et al. 2002; Kloser, Ryan et al. 2009; Lebourges-Dhaussy, Coetzee et al. 2009; Ballon, Bertrand et al. 2011);
- la caractérisation du comportement des agrégations des poissons pélagiques (Axelsen, Anker-Nilssen et al. 2001);
- ou encore la caractérisation de la distribution spatiale des ressources pélagiques (Bertrand, Díaz et al. 2004; Gutierrez, Schwartzman et al. 2007).

Dans ce contexte applicatif, nos contributions se sont concentrées sur des deux aspects complémentaires : l'apprentissage de modèle de classification des cibles biologiques dans les échogrammes sonar de la colonne d'eau (Fablet, Lefort et al. 2009; Lefort, Fablet et al. 2010), la caractérisation de la distribution spatiale des cibles biologiques à partir d'échogrammes de la colonne d'eau (Fablet, Gay et al. Soumis). Ces développements menés

principalement dans le cadre de collaborations avec l'Ifremer et l'IRD se sont notamment appuyés sur les travaux de thèse de R. Lefort.

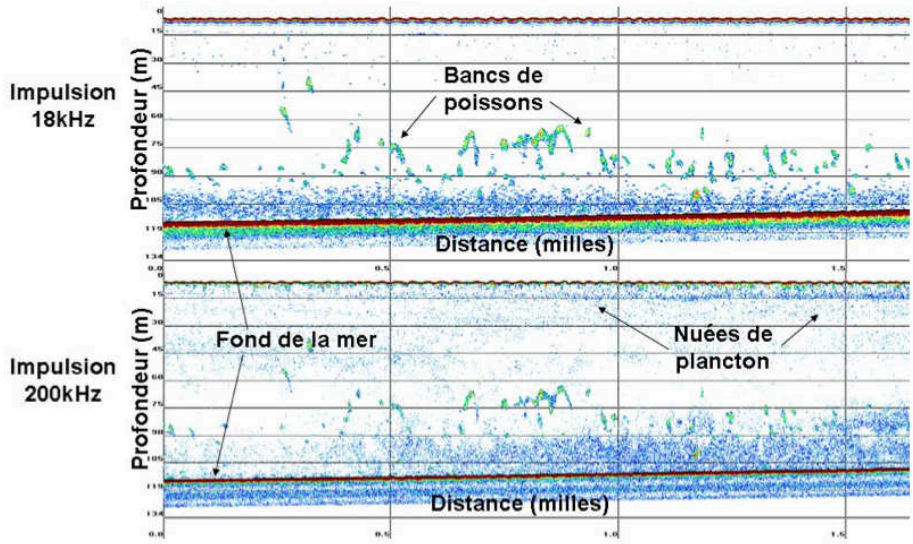

Figure 23. Exemple d'imagerie sonar de la colonne d'eau acquise par des échosondeurs à 18KHz (haut) et 200Hz. (bas) : l'énergie acoustique rétro-diffusée dans la colonne d'eau permet de détecter différentes types de cibles biologiques, par exemple ici des bancs de poissons et des couches de plankton.

III.2.1 Apprentissage de modèle de classification des cibles biologiques

> ***Synthèse des contributions :*** *Nos travaux ont porté sur le développement de modèle de reconnaissance des cibles biologiques, en particulier sur un cadre d'apprentissage faiblement supervisé permettant d'exploiter pleinement les données d'apprentissage disponible (ici, les proportions relatives des espèces dans différentes zones). Différents modèles (modèle génératif, modèle discriminant, forêts aléatoires) ont été étendus à ce cadre générique d'apprentissage faiblement supervisé.*

Comme l'illustre la Figure 23, les échogrammes sonar de la colonne d'eau mettent en évidence différents types de cibles biologiques. La discrimination de ces différents types de cibles constituent naturellement une tâche importante, par exemple pour quantifier les biomasses associées à chaque type de cibles, e.g. (Simmonds, MacLennan 2005; Ballon, Bertrand et al. 2011). En particulier, les poissons forment des agrégations ou bancs qui apparaissent comme des régions de forte densité acoustique dans les échogrammes. Le banc représente, en effet, pour les poissons pélagiques une unité essentielle des différentes phases de vie (reproduction, prédation, migration,...) (Aoki 1980). L'approche "banc" constitue donc une approche naturelle pour le traitement des échogrammes sonar (Fréon, Misund 1999; Simmonds, MacLennan 2005) et de nombreux travaux ont porté sur des méthodes de détection, caractérisation et classification des bancs de poisson (Haralambous, Georgakarakos 1996; Scalabrin, Diner et al. 1996) et ont mis en évidences des différences des caractéristiques énergétiques et géométriques des bancs en fonction de l'espèce. Par exemple, dans (Scalabrin, Diner et al. 1996), il est montré qu'il est possible d'obtenir des taux de reconnaissance des bancs d'anchois et de sardines dans le golfe de Gascogne de l'ordre de 70% . Plus récemment, le déploiement de système sonar multi-fréquence (par exemple des antennes acoustiques à des fréquence de 38KHz et 120KHz) a conduit à une amélioration significative des performances dans certaines situations et des modèles de classification non-linéaires (e.g., séparateurs à vaste marge, forêts aléatoires) ont été évalués (Anderson, Horne et al. 2007; Jech, Michaels 2007; Fernandes 2009; Korneliussen, Heggelund et al. 2009; Charef, Ohshimo et al. 2010).

Toutes ces approches exploitent un apprentissage supervisé. Sa mise en œuvre présente toutefois des limites importantes dans le cas des bases de données d'acoustique sonar. En effet, l'information de classe (espèce) associée à un banc détecté dans un échogramme peut être obtenue par une interprétation "expert" ou l'analyse de la distribution des espèces capturées par chalutage conjointement à l'acquisition de l'échogramme. Le premier cas peut évidemment présenter des biais importants et on souhaite pouvoir s'affranchir de la subjectivité potentielle de l'interprétation "expert" et de l'absence de validation directe. La deuxième solution permet d'associer une classe à un banc uniquement pour des zones dans lesquelles une seule espèce est capturée (ou de manière pratique une espèce est très largement majoritaire (e.g., > 90%) dans les captures). De manière générale,

ces configurations mono-spécifiques sont toutefois relativement rares dans de nombreux écosystèmes. A titre d'exemple, la majorité des zones chalutées dans le golfe de Gascogne se révèlent multi-spécifiques (Petitgas, Masse et al. 2003). En outre, même s'il est globalement admis que la structure du banc est mono-spécifique (Simmonds, MacLennan 2005), il n'est pas évident que le comportement grégaire des espèces de poissons, notamment en termes de caractéristiques des bancs, soient identiques dans des zones où une ou plusieurs espèces sont présentes. Ces différents éléments posent la question de la représentativité des bases de données supervisées pour ces problématiques de reconnaissance des bancs de poissons. Notre attention s'est portée sur le développement de méthodes d'apprentissage permettant de dépasser ces limites en exploitant pleinement l'ensemble des données disponibles, à savoir les bases de données d'échogrammes sonar associées à des données de chalutage. Ces données d'apprentissage peuvent être formulées en termes de présence/absence ou de proportions relatives des espèces que l'on souhaite discriminer. Cette configuration d'apprentissage est appelée "apprentissage faiblement supervisé" et peut être modélisée comme l'apprentissage de modèles de classification à partir d'un ensemble de données d'apprentissage $\{X_n,\pi_n\}_n$ où X_n correspond à l'ensemble des caractéristiques de l'élément n (ici, un banc) et π_n à l'information de classe pour l'élément n. Cette information a priori est définie comme suit :

- si la classe est connue (i.e., dans le cas supervisé)
  $\begin{cases} \pi_n(k) = 1 \text{ si l'élément n appartient à la classe k} \\ \pi_n(k) = 0 \text{ sinon} \end{cases}$

- si aucune information de classe n'est connue (i.e., dans le cas non supervisé)
  $\pi_n(k) = 1/K$ pour toutes les K classes

- si une information de présence/absence de certaines classes est connue à l'échelle de l'échogramme
  $\begin{cases} \pi_n(k) = 1/K_n \text{ si k est parmi les } K_n \text{ classes possibles} \\ \pi_n(k) = 0 \text{ sinon} \end{cases}$

- si une information de proportion relative des espèces est disponible à l'échelle de l'échogramme, elle peut être utilisée comme information a priori π_n à l'échelle de chaque banc détecté dans l'échogramme.

La prise en compte de ce cadre faiblement supervisée permet donc d'intégrer à la fois les cas supervisés (toutes les informations de classe connuées) et non-supervisés (aucune information de classe disponible) à l'échelle de chaque élément de l'ensemble d'apprentissage. Il couvre donc également les situations d'apprentissage semi-supervisé dans lesquelles les informations de classe sont connues pour un sous-ensemble des données d'apprentissage mais inconnues pour l'autre partie des données d'apprentissage (Chapelle, Schölkopf et al. 2006). On peut donc souligner le caractère générique du cadre d'apprentissage proposé directement hérité des problématiques de reconnaissance en acoustique halieutique. Il peut trouver de nombreuses applications, notamment les applications pour lesquelles l'utilisation de données de type présence/absence constitue le cadre de référence, par exemple l'apprentissage de modèle de reconnaissance d'objets à partir de bases d'images annotées, e.g. (Ulusoy, Bishop 2005; Fergus, Perona et al. 2006). Dans ce contexte applicatif, la capacité à exploiter des informations a priori continues plutôt que binaires (présence/absence) peut par exemple permettre de formuler une notion d'incertitude sur l'interprétation d'un expert et/ou d'exploiter une cascade de différentes méthodes de classification voire d'envisager des procédures itératives comme décrit ci-dessous..

Pour aborder ce problème d'apprentissage faiblement supervisé de modèle de classification, des algorithmes d'apprentissage ont été proposés pour trois classes de modèles :

- des modèles génératifs (Fablet, Lefort et al. 2009; Lefort, Fablet et al. 2011) fondés sur la modélisation de la probabilité P(X|Y) des caractéristiques X de l'objet étant donné la classe Y. La méthode d'apprentissage proposée repose sur une adaptation de l'algorithme EM (Expectation-Maximization) (Dempster, Laird et al. 1977) ;
- des modèles discriminants linéaires et non-linéaires (Lefort, Fablet et al. 2010; Lefort, Fablet et al. 2011) fondés sur la modélisation de la probabilité a posteriori P(Y|X) de la classe Y étant donné les caractéristiques X de l'objet. Différentes méthodes d'apprentissage ont été proposées notamment une adaptation du critère de Fisher (Yang, Jin et al.);
- des modèles fondés sur forêts aléatoires (Lefort, Fablet et al. 2010). La méthode d'apprentissage proposée introduit un nouveau critère d'entropie pour la construction des arbres de classification de type C4.5 (Quinlan 1993) en prenant en compte des données d'apprentissage faiblement supervisées.

Une originalité des méthodes proposées réside dans l'introduction d'une méthode itérative d'apprentissage tirant partie de la capacité des modèles de classification considérés à produire des décisions de classification probabilisées ("soft classification decisions"). Un schéma de principe de l'algorithme proposé est donnée (Figure 24).

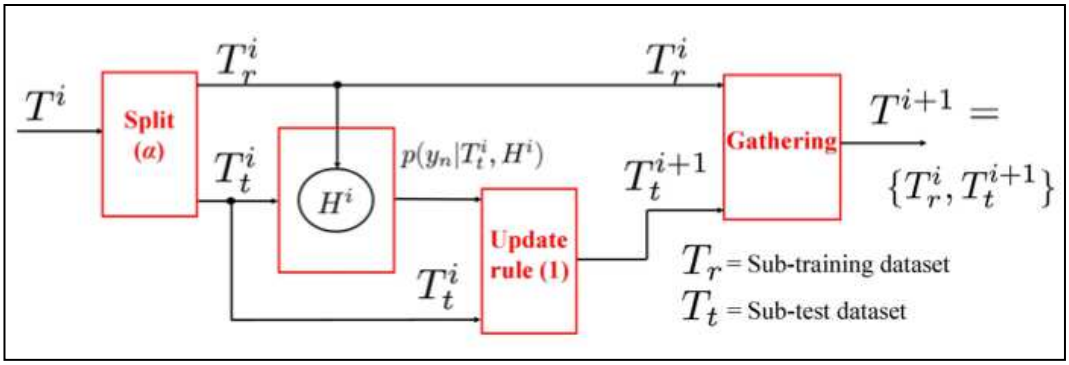

Figure 24. Principe de l'apprentissage faiblement supervisé itératif : à l'itération i, la première étape consiste à définir une partition aléatoire de l'ensemble des données faiblement supervisées T^i en un ensemble d'apprentissage T^i_r et un ensemble de test T^i_t. A partir de l'ensemble d'apprentissage T^i_r nous entrainons un nouveau modèle de classification H^i. Ce modèle est appliqué aux données de test T^i_t pour mettre à jour l'information de classe associées uniquement pour ce sous-ensemble. Le nouveau jeu de données faiblement supervisées ainsi obtenu permet d'itérer le processus. Le détail des règles de mise à jour des données de classe est donné dans (Lefort, Fablet et al. 2010).

Jeux de données	Modèles	CS	CFS A	CFS B	CNS
D1	Gen-EM	83	83	82	**19**
	Discr	90	87	86	14
	FA	**96**	85	73	14
	FA-Iter	**96**	**91**	**89**	14
	FA-Discr-Iter	**96**	89	74	14
D2	Gen-EM	94	72	36	**38**
	Discr	89	82	54	33
	FA	**97**	78	60	33
	FA-Iter	**97**	**92**	**81**	33
	FA-Discr-Iter	**97**	88	72	33
D3	Gen-EM	77	48	38	**18**
	Discr	78	63	57	16
	FA	**100**	76	63	16
	FA-Iter	**100**	**95**	**90**	16
	FA-Discr-Iter	**100**	82	74	16
D4	Gen-EM	82	48	63	**23**
	Discr	85	82	64	33
	FA	19	48	69	33
	FA-Iter	79	**82**	**78**	33
	FA-Discr-Iter	**87**	75	**78**	33
D5	Gen-EM	66	47	46	**28**
	Discr	70	72	61	27
	FA	**89**	59	35	25
	FA-Iter	**89**	47	32	25
	FA-Discr-Iter	**89**	**75**	**62**	25

Tableau 2. Evaluation des performances des méthodes d'apprentissage faiblement supervisé pour différents jeux de données et niveaux de complexité : nous évaluons cinq modèles différents, le modèle génératif (Gen-EM), le modèle discriminant (Discr), le modèle de forêt aléatoire (FA), le processus iétratif appliqué aux forêts aléatoires (FA-Iter) et le processus itératif appliqué à une combinaison modèle discriminant-forêt aléatoire (FA-Discr-Iter). Quatre jeux de données de la base UCI[4] sont considérés : jeu de données de textures naturelles (7 classes) (D1), jeu de données IRIS (3 classes), jeu de signaux temporels (6 classes) (D3), jeu de données de formes d'onde (D4) (3 classes), jeux de données de bancs de poisson (données sonar Ifremer (Scalabrin, Diner et al. 1996), 4 classes) (D5). Nous considérons les cas supervisé (CS) et non-supervisé (CSN) et deux situations faiblement supervisées de complexité différentes (CFS A & CFS B). D'après (Lefort 2010).

III.2.2 Méthode d'analyse globale des échogrammes sonar de la colonne d'eau

Synthèse des contributions : *Nous avons exploré des méthodes de caractérisation globale des échogrammes acoustiques, reposant notamment sur la caractérisation de la distribution des bancs de poissons dans un échogramme, pour des applications à l'analyse de la distribution spatiale des populations de poissons pélagiques.*

[4] A. Asuncio and D. Newman, UCI machine learning repository :

http://www.ics.uci.edu/~mlearn/MLRepository.html.

Comme indiqué précédemment, l'échelle du "banc" constitue une échelle naturelle pour analyser les échogrammes sonar de la colonne d'eau. D'autres échelles analyses, en particulier des échelles plus globales, semblent également d'intérêt pour caractériser la distribution spatiale des populations/peuplements pélagiques. Cette thématique reste relativement peu explorée et seuls quelques travaux ont proposé des méthodes de description globale de la distribution des cibles biologiques dans un échogramme acoustique (Hammond, Swartzman et al. 2001; Petitgas, Masse et al. 2003; Burgos, Horne 2008).

En exploitant une démarche similaire à l'analyse et à la modélisation des textures comme la réalisation d'un ensemble de signatures locales, nous avons proposé des descripteurs à l'échelle de l'échogramme (typiquement, des échogrammes de un à quelques miles nautiques) à partir de la caractérisation de la distribution des bancs de poissons dans l'échogramme (Lefort, Fablet et al. 2012; Fablet, Gay et al. Soumis), en particulier dans le cas des échogrammes 3D acquis par un échosondeur multifaisceau (Lefort, Fablet et al. 2012). Les résultats obtenus mettent en évidence la pertinence de l'approche proposée par rapport à d'autres types de caractéristiques, notamment des marginales des caractéristiques des bancs. Ils illustrent également le gain résultant de l'utilisation de systèmes multifaisceau qui fournissent une meilleure résolution d'observation des agrégations de poisson et modifient substantiellement la perception de la structuration spatiale des aggrégations de poissons.

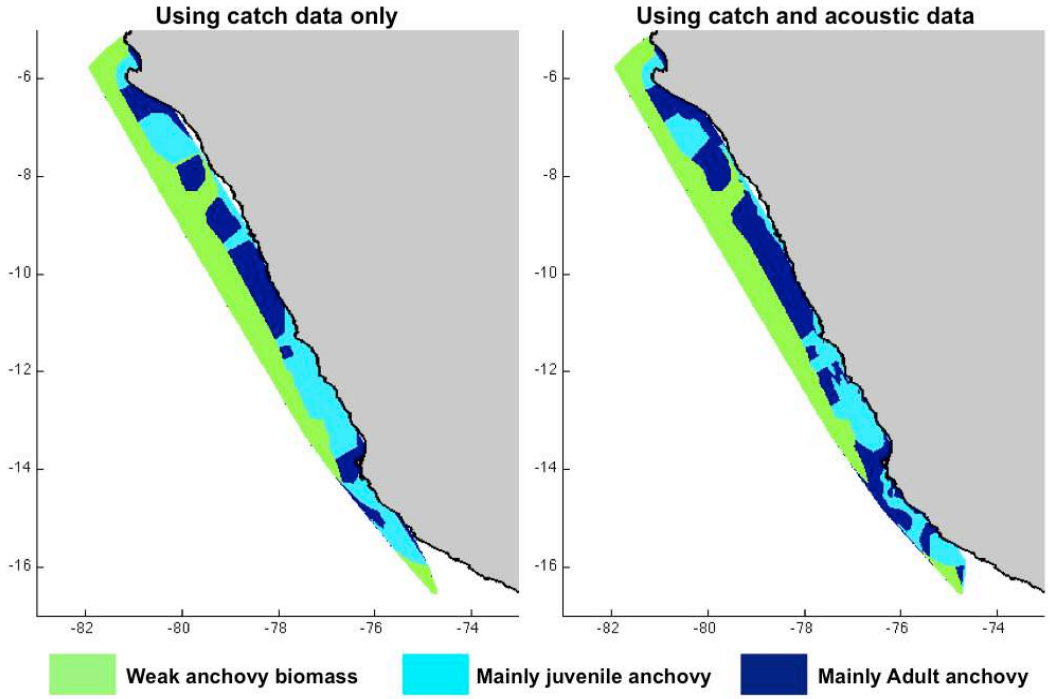

Figure 25. Exemple d'application de la caractérisation de la distribution des bancs de poisson dans les échogrammes sonar à la discrimination des zones d'anchois juvéniles et adultes le long des côtes péruviennes : carte obtenue en exploitant uniquement les données de proportions relatives issues des données de chalutage (gauche), carte obtenue en affectant chaque échogramme à des classes anchois juvénile, anchois adulte et sans anchois sur la base de descripteurs de la distribution des bancs de poisson dans l'échogramme (droite). D'après (Fablet, Gay et al. Accepté).

Nous avons également montré que ces caractéristiques évaluées à l'échelle d'un échogramme peuvent fournir des solutions d'évaluation des biomasses relatives des espèces (Fablet, Lefort et al. 2009) et qu'elles présentent également un potentiel pour discriminer différentes configurations de distribution spatiale des bancs de poisson, que cette distribution soit liée à des mélanges d'espèces différentes (Lefort, Fablet et al. 2012) soit des stades de maturité différents, par exemple pour discriminer les zones d'anchois juvéniles et adultes au large des côtes péruviennes (Fablet, Gay et al. Soumis).

III.3 Synthèse

Les caractéristiques de propagation des ondes acoustiques dans le milieu marin font des technologies acoustiques une des principales modalités de télédétection du milieu marin, tant pour l'analyse des fonds marins que pour l'observation de la colonne d'eau. Dans le cadre de nos travaux, nous nous sommes principalement concentrés

sur le traitement de données sonar pour des applications de reconnaissance et classification des fonds marins et des cibles biologiques.

Ces travaux se sont articulés autour de contributions méthodologiques, à savoir

- la caractérisation d'images à partir de statistiques descriptives et modèles probabilistes de la **distribution spatiale de signatures locales dans les images** (Nguyen, Fablet et al. 2010; Lefort, Fablet et al. 2011; Nguyen, Fablet et al. 2011);
- **la reconnaissance et la segmentation de textures** (Karoui, Fablet et al. 2008; Karoui, Fablet et al. 2010; Nguyen, Fablet et al. 2010; Nguyen, Fablet et al. 2011);
- **l'apprentissage faiblement supervisé** de modèle de classification (Lefort, Fablet et al. 2010; Lefort, Fablet et al. 2011).

Ces contributions méthodologiques ont permis de prendre en compte de caractéristiques clés des données sonar traitées (e.g., variations locales de contraste des textures sonar, données d'apprentissage disponibles en acoustique halieutique) et ont conduit à des avancées thématiques significatives par rapport à l'état de l'art. A titre d'exemple, la caractérisation invariante des textures sonar se traduit par des gains de classification de l'ordre de 15 à 30% comparativement aux méthodes utilisées classiquement. L'originalité et la généricité de ces contributions méthodologiques, généricité illustrée par des applications sur des jeux de données de référence (e.g., bases de texture UIUC, jeux de données UCI), ouvrent de nombreuses perspectives (e.g., imagerie SAR, télédétection satellitaire, reconnaissance d'objets et de scènes)

III.4 Sélection de publications représentatives de ce chapitre

Les publications suivantes sont des exemples représentatifs des contributions méthodologiques et thématiques relevant de ce chapitre :

- R. Lefort, R. Fablet, J.M. Boucher. Weakly supervised classification of objects in images using soft random forests. Proc. Eur. Conf. on Computer Vision, ECCV'2010, LNCS 6314:185-198, Heraklion, septembre 2010.
- I. Karoui, R. Fablet, J.M. Boucher, J.M. Augustin. Variational region-based segmentation using multiple texture statistics. IEEE Transactions on Image Processing, 30(3):3146-3156, 2011.
- H.-G. Nguyen, R. Fablet, J.M. Boucher, A. Erhold. Keypoint-based analysis of sonar images: application to seabed recognition. IEEE Transactions on Geoscience and Remote Sensing. Sous presse.

Ces Publications sont fournies ci-après.

Variational Region-Based Segmentation Using Multiple Texture Statistics

Imen Karoui, Ronan Fablet, Jean-Marc Boucher, *Senior Member, IEEE*, and Jean-Marie Augustin

***Abstract*—This paper investigates variational region-level criterion for supervised and unsupervised texture-based image segmentation. The focus is given to the demonstration of the effectiveness and robustness of this region-based formulation compared to most common variational approaches. The main contributions of this global criterion are twofold. First, the proposed methods circumvent a major problem related to classical texture based segmentation approaches. Existing methods, even if they use different and various texture features, are mainly stated as the optimization of a criterion evaluating punctual pixel likelihoods or similarity measure computed within a local neighborhood. These approaches require sufficient dissimilarity between the considered texture features. An additional limitation is the choice of the neighborhood size and shape. These two parameters and especially the neighborhood size significantly influence the classification performances: the neighborhood must be large enough to capture texture structures and small enough to guarantee segmentation accuracy. These parameters are often set experimentally. These limitations are mitigated with the proposed variational methods stated at the region-level. It resorts to an energy criterion defined on image where regions are characterized by nonparametric distributions of their responses to a set of filters. In the supervised case, the segmentation algorithm consists in the minimization of a similarity measure between region-level statistics and texture prototypes and a boundary based functional that imposes smoothness and regularity on region boundaries. In the unsupervised case, the data-driven term involves the maximization of the dissimilarity between regions. The proposed similarity measure is generic and permits optimally fusing various types of texture features. It is defined as a weighted sum of Kullback–Leibler divergences between feature distributions. The optimization of the proposed variational criteria is carried out using a level-set formulation. The effectiveness and the robustness of this formulation at region-level, compared to classical active contour methods, are evaluated for various Brodatz and natural images.**

***Index Terms*—Active regions, level sets, nonparametric distributions, supervised and unsupervised segmentation, texture similarity measure.**

Manuscript received January 04, 2008; revised March 26, 2010; accepted March 26, 2010. Date of publication September 02, 2010; date of current version November 17, 2010. The associate editor coordinating the review of this manuscript and approving it for publication was Dr. Ying Wu.

I. Karoui, R. Fablet and J.-M. Boucher are with the Telecom Bretagne, UMR CNRS Lab, 29238 Brest Cedex 3, France (e-mail: imen.karoui@telecom-bretagne.eu; ronan.fablet@telecom-bretagne.eu; jm.boucher@telecom-bretagne.eu).

I. Karoui and J.-M. Augustin are with the Institut Français de Recherche et dExploitation de la Mer, 29280 Plouzane, France (e-mail: jean-marie.augustin@ifremer.fr).

Color versions of one or more of the figures in this paper are available online at http://ieeexplore.ieee.org.

Digital Object Identifier 10.1109/TIP.2010.2071290

I. Introduction

TEXTURE describes a visual information which is related to local spatial variations of color, orientation and intensity in an image. It is usually described by qualitative adjectives such as smooth or rough, coarse or fine, homogeneous or random, etc. This information is fundamental in image analysis and interpretation and the segmentation of an image into homogeneous regions, in terms of textural features, remains a complex issue. An effective and efficient texture segmentation method is of key interest in numerous domains such as biomedical image analysis, industrial inspection, analysis of remote sensing images, sonar or aerial imagery [1]–[4], etc.

Pixel-based and region-based techniques can be seen as the two major categories of approaches for image segmentation. Whereas pixel-based schemes, such as k-means [5], standard Markov random fields [6], [7], consider image segmentation as a labeling issue at pixel-level, region-based approaches directly search for a relevant image partition. The main methods belonging to this second category are split-and-merge technique [8], [9], region-based Bayesian segmentation [10], active contours or deformable models [11]–[13]. As far as texture segmentation is concerned, region-based techniques appear more adapted, since texture characteristics are by nature nonlocal characteristics. Region-based approaches, especially active contours associated with a level-set setting, offer an efficient manner to cope with texture and geometrical features at the region-level. Recently, there has been a considerable amount of work that places texture segmentation in the framework of optimization theory using curve evolution techniques [2], [11], [14]–[17]. The reported results are very encouraging. In general, these methods state the segmentation problem as the minimization of an energy $E = E_1 + E_2$ composed of a data-driven term, denoted by E_1, and a regularization term denoted by E_2. The goal is to determine the image partition $\{\Omega_k\}_{k=1:K}$ that minimizes E, where $\{\Omega_k\}_k$ are image regions. Formally, the segmentation problem is expressed as follows:

$$\{\Omega_k\}_{k=1:K} = \arg\min E, \Omega_k \bigcap_{k \neq k'} \Omega_{k'} = \phi. \qquad (1)$$

Texture segmentation based upon active contour techniques involve two main categories of approaches.

- Methods that rely on the optimization either of information theoretical criteria mainly the entropy and the mutual information or of the product of pixel likelihoods. These methods assume that textural features are independent and identically distributed (i.i.d.) [11], [14]–[17].

1057-7149/$26.00 © 2010 IEEE

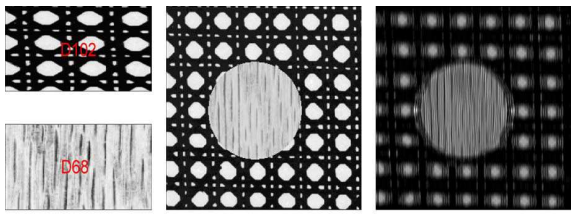

Fig. 1. Two-class Brodatz mosaic. (a) Considered Brodatz textures D102 and D68. (b) Two-class mosaic. (c) Response of the mosaic to a Gabor filter.

- Methods that exploit image neighborhoods and optimize criteria based upon neighborhood statistics [2], [3], [18], [19].

Without loss of generality, the data-term E_1 associated to all these methods can be expressed as follows:

$$E_1 = \sum_{k=1}^{K} \int_{\Omega_k} \Psi\left(p_k\right) ds \tag{2}$$

where p_k is the punctual likelihood. For the first category, this likelihood depends only upon pixel feature: $p_k\left(s\right)$. For the second category, it depends upon feature distribution in the pixel's neighborhood (that we denote by W_s): $p_k\left(s, W_s\right)$. Ψ is a function that defines the optimized criterion:

- $\Psi(x) = \log(x)$ for likelihood maximization based criterion;
- $\Psi(x) = x\log(x)$ for entropy based criterion;
- $\Psi(x) = \mathrm{dist}(x)$ for distance based criterion, where dist is a metric.

The existing methods differ in the computation of the probability p_k. Some methods are based upon parametric models. In [14], pixel likelihoods $\{p_k\left(s\right)\}$ are computed according to a Gaussian mixture of filter response statistics (Gaussian and Gabor filters). In [11] and [15], the distribution of texture features (wavelet coefficient) are modeled by generalized Gaussian models. In [19], generalized Laplacian models are considered to describe the statistics of various linear filters (the discrete cosine transform, steerable pyramids, and various orthogonal wavelets). In [17], Gaussian distributions are used to model feature channels extracted from structure tensor, etc. Other approaches rely on nonparametric distributions to evaluate pixel likelihoods such as in [18], where nonparametric neighborhood statistics were combined to an entropy-based metric. In [3], Kadir *et al.* use a nonparametric model for image intensities and in [20], the authors use nonparametric statistics to optimize image entropy and mutual information, etc.

These methods work well when texture feature distributions p_k are disjointed and may fail when these distributions significantly overlap. Fig. 1 shows an example of a mosaic composed of two Brodatz textures [21]: D102 and D68. D102 has a coarse and regular periodic texture and D68 a weakly ordered one (wood grain). These two textures depict overlapping histograms of their response to a Gabor filter (Fig. 2). Approaches based upon the punctual likelihood $p_k\left(s\right)$ [11], [14]–[17] computed from these histograms cannot correctly segment such an image. Feature distributions depict an overlap corresponding to bright patches. As the local likelihood or similarity of these bright

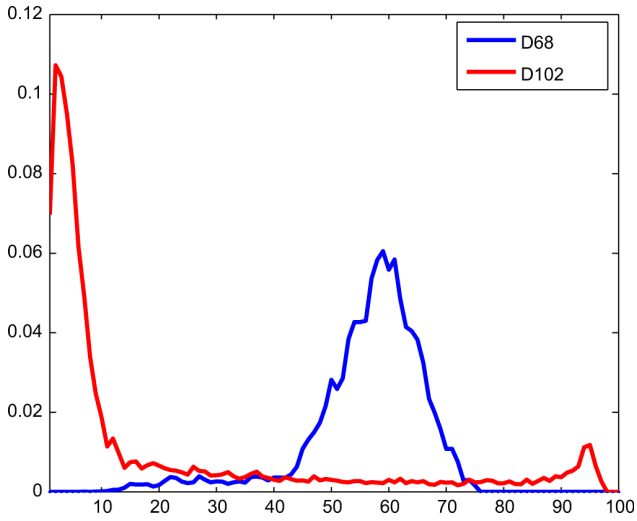

Fig. 2. Histograms of the response of the two textures (D102 and D68) to a Gabor filter.

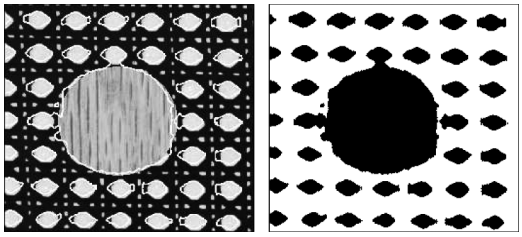

Fig. 3. Segmentation of the two-class mosaic (Fig. 1) by a classical variational approach [11], [14], [15] relying on the computation of pixel-level likelihoods of the Gabor feature.

patches in texture D102 is maximal for the model extracted form texture D68, these patches are misclassified as shown in Fig. 3. This example also stresses the dependence upon the choice of the analysis window when criterion E_1 actually exploits information in pixel neighborhoods $\{W_s\}$ [19] (Fig. 4). A 3×3 analysis window (neighborhood) is not large enough to capture the structures of texture D102, whereas a 33×33 window leads to inaccurate boundaries. $T_W = 21 \times 21$ seems to be a good tradeoff. In the general case, it is however difficult to determine an optimality criterion for the choice of the analysis window especially when the image is composed of several textures, each with a given coarseness.

The approach proposed in this paper addresses these issues as illustrated in Fig. 5. Our method uses a global criterion that combines the advantages of an efficient texture characterization with global region variational methods. The two key features are: a region-level characterization using nonparametric texture statistics and the definition of a variational observation-driven criterion from a texture-based similarity measure at region-level. Following recent works [4], [9], [22]–[24], we consider texture features computed as nonparametric statistics of filter outputs w.r.t. a varied set of filters. Observation-driven term E_1 is then defined as

$$E_1 = \sum_{k=1}^{K} \sum_{f} w_f S\left(Q_f^k, D_f\left(\Omega_k\right)\right) \tag{3}$$

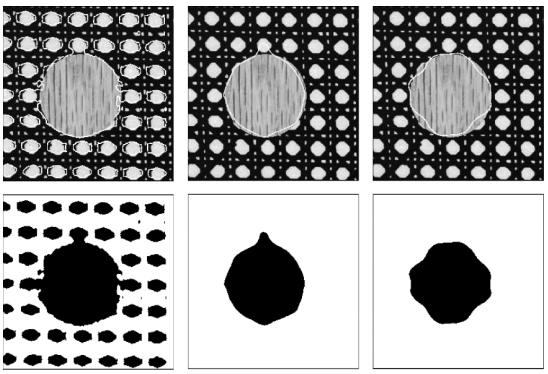

Fig. 4. Segmentation of the two-class mosaic (Fig. 1) by a classical approach [19] exploiting pixel neighborhood for different sizes of square analysis windows T_W (a) $T_W = 3 \times 3$ (b) $T_W = 21 \times 21$ (c) $T_W = 33 \times 33$.

where S is a similarity measure. Q_f^k refers to the considered texture statistics estimated from training samples for class k and feature f and $D_f(\Omega_k)$, the observed global texture statistics for region Ω_k for feature f.

Energy E_1 is minimum when the segmented regions depict texture statistics similar to prototype models. In contrast to the pixel-level formulation, our energy cannot be broken down as a sum of potential over image sites and a given site s contributes to the proposed data-driven term through its participation to the computation of region-level statistics.

The gradient-based minimization of E_1 exploits the shape derivative tools introduced in [25]. In [25], the Gâteau derivative was applied to a two class image segmentation based upon matching intensity histograms using Hellinger distance. The paper is organized as follows. Texture features and the similarity measure detailed in our previous work [26], [27] are briefly introduced in Section II. The proposed supervised segmentation criterion and its differences with classical ones are detailed in Section III. Its generalization to unsupervised case is described in Section IV. Experiments and comparisons with classical variational approaches are reported and discussed in Section V and conclusions are outlined in Section VI.

II. Texture Based Similarity Measure

Many texture features have been proposed in the literature. Co-occurrence matrices, wavelet frames, quadrature mirror filter-banks and Gabor filters have been shown to be the most effective descriptors [28]. But none of these feature classes outperforms the others for all texture categories. Each feature computed for certain parameters may emphasize particular texture characteristics (scale, direction, smoothness, periodicity, etc.). Here as described in our previous work [26] dealing with supervised texture discrimination, we use a large set of various features computed for different parameters and we select the most discriminating ones. The following set of textural filters is considered:

- 121 co-occurrence distributions with parameters $\{(d_x, d_y) \in \{1, \ldots, 10\} \times \{1, \ldots, 10\}\}$, where d_x and d_y refers, respectively, to the horizontal and vertical displacement;
- 50 distributions of the magnitude of Gabor filter responses, computed for six radial frequencies $\left\{\sqrt{2}/2^k\right\}_{k=1:6}$, and five orientations: $\{0°,\ 25°,\ 45°,\ 90°,\ 135°\}$;
- 48 distributions of the energy of the image wavelet packet coefficient computed for different bands (we used different wavelet types: Haar, Daubechies and Coiflet).

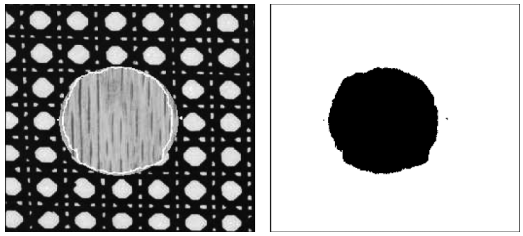

Fig. 5. Segmentation of the two-class mosaic (Fig. 1) by the proposed method.

Formally, we characterize each texture sample T by a set of the F first-order statistics of its responses to the predefined filters $\{D_f(T)\}_{f=1:F}$. Note that F accounts both for given filters and associated parameterizations. Subsequently, index f will refer to a given filter category with some parameterization. Given reference texture statistics $Q^k = \left\{Q_f^k\right\}_{f=1:F}$, the similarity measure $KL_w(Q^k, D(T))$ between texture sample T and the texture class indexed by k is defined as

$$KL_w\left(Q^k, D(T)\right) = \sum_{f=1}^{F} w_f^2 KL\left(Q_f^k, D_f(T)\right) \qquad (4)$$

where KL is the Kullback–Leibler divergence [29] and weights w_f verify $\sum_{f=1}^{F} w_f^2 = 1$. The estimation of the weights $\left\{w_f^2\right\}$ can be issued from the maximization of a supervised margin criterion detailed in [26].

III. Level Set Segmentation

We detail in the following the proposed region-level segmentation framework. Regarding the curvature-driven regularization criteria (E_2) and the multiclass image partition constraints, we use classical functionals detailed in [27]. The numerical implementation relies on is based upon a level set setting [30]. The proposed approach relies on the definition of the data-term E_1 at region-level according to the similarity measure KL_w between reference statistics Q^k and region statistics $D(\Omega_k) = \{D_f(\Omega_k)\}_{f=1:F}$:

$$E_1\left(\{\Omega_k\}_{k=1:K}\right) = \sum_{k=1}^{K} |\Omega_k| \, KL_w\left(Q^k, D\left(\Omega_k\right)\right) \qquad (5)$$

where, $D(\Omega_k) = \{D_f(\Omega_k)\}_{f=1:F}$ and $D_f(\Omega_k)$ is the marginal distribution of the image response to the filter indexed by f estimated on the region Ω_k.

Using the Gâteaux derivative introduced in [25], the evolution equations of the level set functions denoted by $\{\varphi_k\}_k$ [27]

associated to the energy E_1 are the following (see Appendix A for details):

$$\frac{\partial \varphi_k}{\partial t}(s,t) = \left[\underbrace{-KL_w(Q^k, D(\Omega_k))}_{\text{Global term}} + \underbrace{\sum_{f=1}^{F} w_f^2 \left(\frac{Q_f^k}{D_f(\Omega_k)} * g_\sigma(h_f(s)) - 1 \right)}_{\text{Local term}} \right] |\nabla \varphi_k| \quad (6)$$

where h_f is the filter response indexed by f (for instance, for a co-occurrence matrix with parameters $\mu = (d, \theta)$, $h_f : \Omega \rightarrow [1, Ng] \times [1, Ng]$ and $h_f(s) = (I(s), I(s+\mu))$ where $I(s)$ is the gray value at pixel s and Ng the total gray level number), g_{σ_f} is a centered Gaussian kernel with standard deviation σ_f and $*$ denotes the convolution symbol.

In contrast to classical functionals related to classical functionals described in Section I (2) which are of the form

$$\frac{\partial \varphi_k}{\partial t} = |\nabla \varphi_k| \Psi(p_k), \quad \forall k \in \{1 : K\} \quad (7)$$

the evolution equations related to the proposed method involve a global term and a local one.

- The global term $-KL_w(Q^k, D(\Omega_k))$: this term is always negative or null. It is a contraction force that reduces the size of heterogeneous regions: the lower the heterogeneity, the lower the force. This term will avoid to converge towards a local minimum that doses not give regions with the correct statistics mainly on multimodal features (see videos http://public.enst-bretagne.fr/rfablet/Demos/demoIKaroui/classic.avi and http://public.enst-bretagne.fr/rfablet/Demos/demoIKaroui/proposed.avi)
- The local term

$$\sum_{f=1}^{F} w_f^2 \left(Q_f^k / D_f(\Omega_k) * g_\sigma(h_f(s)) - 1 \right) :$$

this term compares locally the feature values at each pixel s. This term can be positive or negative and tends to locally fit region statistics to the prototype statistics. The contribution of each descriptors f is weighted by w_f^2.

We use as level set functions $\{\varphi_k\}_{k=1:K}$ signed distance functions. The initial segmentation is computed from a moving window approach: each image pixel s is characterized by a set of features estimated on an analysis window centered at s that we denote by W_s and the initial pixel-based classification is given by

$$\text{label(s)} = \arg\min_k KL_w\left(Q^k, D(W_s)\right) \quad (8)$$

where $D(W_s) = \{D_f(W_s)\}_{f=1:F}$ is the set of distributions associated to the different filters which are estimated locally within the neighborhood of pixel s.

IV. Unsupervised Texture Segmentation

For the unsupervised case, proposed approaches are also usually based upon energy criterion evaluated as a sum of punctual statistics [20], [31]. The most popular criteria are the entropy or mutual information maximization [20], [31] and likelihood maximization alternating class feature estimation and segmentation [13], [17], [32]. Here, we use the region based similarity KL_w to define an unsupervised segmentation criterion that consists in the maximization of the similarity measure between regions

$$E^1(\{\Omega_k\}_{k=1:K}) = \sum_{(k,k'),k' \neq k}^{K} KL_w(D(\Omega_k), D(\Omega'_k)). \quad (9)$$

For the unsupervised case two strategies might be considered: a uniform prior, $w_f^2 = 1/F$, $\forall f$, or iterations between region-level image segmentation and the estimation of weights $\left\{w_f^2\right\}$ from segmented regions.

We showed (Appendix B) that the proposed criterion allows to separate the image into homogeneous regions. Using the Gâteau derivative tools, the evolution equations associated with the proposed criterion in (10), shown at the bottom of the page. These evolution equations, involve a global term and a local one.

- Global term $-\sum_{k',k' \neq k}^{K} KL_w(D(\Omega_k), D(\Omega_{k'}))$: the larger the dissimilarity between the region and the others, the larger the contraction force: this term will penalize the expansion of the regions when the dissimilarities increase. This global constraint does not appear in classical approaches [20], [31].
- Local term:

$$\sum_{k',k' \neq k}^{K} \sum_{f=1}^{F} w_f^2$$

$$(\log D_f(\Omega_k)/D_f(\Omega_{k'}) - D_f(\Omega_{k'})/D_f(\Omega_k) + 1)$$

$$* g_{\sigma_f}(h_f(s)).$$

This term is quite similar to those of classical approaches. It compares punctual pixel likelihoods for the different regions: it tends to assign the pixel to the region with the maximal likelihood.

$$\frac{\partial \varphi_k}{\partial t} = \sum_{k',k' \neq k}^{K} \frac{1}{|\Omega_k|} \left[-KL_w(D(\Omega_k), D(\Omega_{k'})) + \sum_{f=1}^{F} w_f^2 \left(\log \frac{D_f(\Omega_k)}{D_f(\Omega_{k'})} - \frac{D_f(\Omega_{k'})}{D_f(\Omega_k)} + 1 \right) * g_{\sigma_f}(h_f(s)) \right] |\nabla \varphi_k| \quad (10)$$

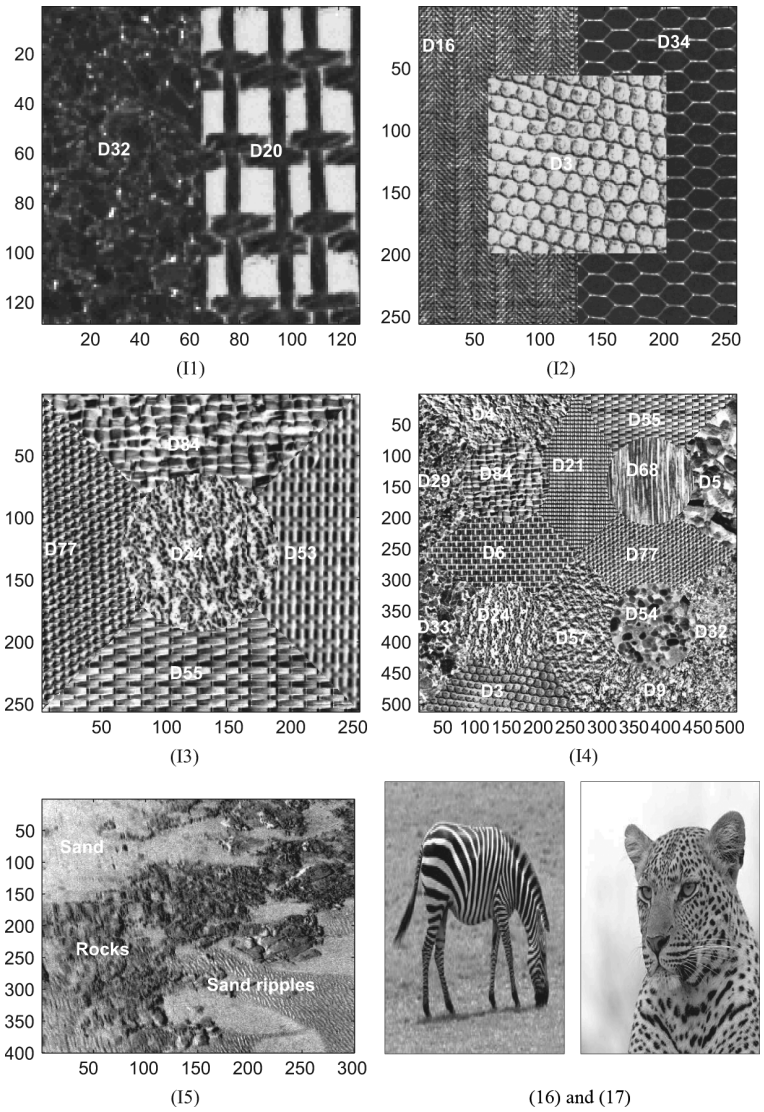

Fig. 6. Test images: I1, I2, I3, and I4 are, respectively, 2, 3, 5, and 16 Brodatz mosaics, I4 is a real sidescan image and I6 and I7 are, respectively, natural zebra and leopard images.

Here we consider the fully unsupervised case: neither the class number nor the class prototypes are known. For the estimation of the number of classes we use the method proposed in [33] and [34] based upon a two-term criterion: the intracluster distances and an entropy term. In our case, the intraclass distance is evaluated according to our similarity measure KL_w.

V. Results and Discussion

We report segmentation results on four Brodatz texture mosaics [21] with different complexities and on three natural images. The first image, denoted by I1, is a mosaic involving one homogeneous Brodatz-texture (D32) and a coarse Brodatz-texture (D20). The second image I2 is composed of three Brodatz textures (D34, D3, and D16). The third image I3 is a five-texture mosaic with histogram equalized Brodatz-textures (D77, D84, D55, D53 et D24). The fourth image I4 is a more complex mosaic composed of sixteen histogram equalized Brodatz textures (D3, D4, D5, D6, D9, D21, D24, D29, D32, D33, D54, D55, D57, D68, D77, and D84) and is denoted by I3. The latter two images were used in a comparative study carried out by Randen *et al.* [28] to evaluate several feature selection methods. Image I5 is a real sidescan sonar image composed of three seafloor types [35]: a coarse texture of rock, an homogeneous class of mud and oriented texture associated to sand ripples (Fig. 6). The last images I6 and I7 are, respectively, a zebra and a leopard image often used in previous works [11], [14], [17], [18].

For the supervised case, for each test image, we first select the most discriminant feature statistics keeping only features that account for more than 90% of the total weight sum. For image I1, three Gabor energy based distributions computed for parameters $(f_0, \theta) \in \left\{\left(2^{-8}\sqrt{2}, 0^\circ\right), \left(2^{-8}\sqrt{2}, 25^\circ\right), \left(2^{-5}\sqrt{2}, 135^\circ\right)\right\}$ are selected, for image I2, only two Gabor energy based distributions computed for parameters $(f_0, \theta) \in \left\{\left(2^{-6}\sqrt{2}, 0^\circ\right), \left(2^{-4}\sqrt{2}, 0^\circ\right)\right\}$ are selected with weights 0.45 and 0.42. For image I3, two co-occurrence distributions computed for $(d_x, d_y) \in$

TABLE I
SEGMENTATION ERROR RATES (%) COMPUTED FOR THE PROPOSED AND CLASSICAL APPROACHES: MEAN AND STD ARE THE MEAN AND THE STANDARD DEVIATION ERROR RATE

	V_H: 3	V_H: 9	V_H: 33	V_{cl}	V_{pS}	V_{pU}	Randen
I1	7%	$\tau = 6$	10	11	**2.7**	-	-
I2	9	5	4.6	2	**0.9**	1	-
I3	70	30	7	**3**	4.9	5.1	8.2
I4	80	70	19	63	**13.9**	17	37.2
I5	25	13	13	13.5	**7.5**	-	-
mean	38.2	24.8	10.8	18.5	**5.9**	7.7	22.7
std	34.5	27.2	5.6	25.3	**5**	8.3	20.5

$\{(2,1),(6,1)\}$ and a Gabor filter computed for parameters $(f_0,\theta) = \left(2^{-6}\sqrt{2}, 0°\right)\}$ are selected with weights 0.4, 0.3 and 0.1. For image I4, the segmentation is carried out using only three co-occurrence matrices computed for parameters: $(d_x,d_y) \in \{(0,3),(0,6),(2,2)\}$ with weights 0.25, 0.25, and 0.4. For image I5, the selected features are the two co-occurrence distributions computed for parameters $(d_x,d_y) \in \{(1,4),(2,1)\}$. For all the images, the selection step allows a drastic decrease in the dimension of feature space: an average of three selected features among the initial set of 219 features.

A comparative analysis in terms of classification error rates is reported in Table I. Several approaches are considered.

- The best segmentation results reported in the comparative study on texture feature discrimination power carried out by Randen *et al.* in [28]. These results are denoted by Randen.
- Classical variational approaches for which we use the energy form proposed by the authors but the texture features issued from our selection/fusion step.
  - — The Heiler *et al.* [19] method applied for three different sizes of square neighborhood, namely T_W =3, 9, and 33. This method is denoted by V_H.
  - — A variational level set setting, denoted by V_{cl}, using a pixel based data-driven energy term (2) with $\Psi(.) = \sum_{f=1}^{F} w_f^2 \log(p_f^k(.))$, where p_f^k is the distribution of texture k response to the filter indexed by f. This variational setting is the one exploited in [11] and [14]–[17] but with other texture features.
  - — The proposed region-based variational setting, denoted by V_{pS} for the supervised case and V_{pU} for the unsupervised case with $w_f^2 = 1/F$.

1) Performance of the Proposed Similarity Measure: Images I3 and I4 were used in [28] for the evaluation of a variety of texture feature selection methods. In [28], Randen *et al.* perform a comparative study on several filtering approaches including Laws masks, ring/wedge filters, dyadic Gabor filter banks, wavelet transforms, wavelet packets, wavelet frames, quadrature mirror filters, discrete cosine transform, eigenfilters, optimized Gabor filters, linear predictors, and optimized finite impulse response filters and nonfiltering approaches that are based upon co-occurrence and autoregressive features. We obtain better results than the most effective methods reported in [28]. For image I3, the obtained error rate is 4.9% whereas the best error rate reported in [28] is about 8.2% and the average classification error rate for all compared methods is about 23.6%. For image I4, the error rate for the proposed segmentation is about 14% and it is about 38% for the best method evaluated in [28] and the average error rate is 53.8% for this image. These results stress the relevance of the proposed similarity measure fusing various texture feature types. They also motivate the use of the feature sets issued from this selection step in the implementation of the different variational segmentation settings. More examples are given on our previous work [26].

2) Region-Based V_{pS} Versus Classical Approach V_{cl}: Using the same texture descriptors, segmentation results reported in Table I show that the proposed region-level setting significantly

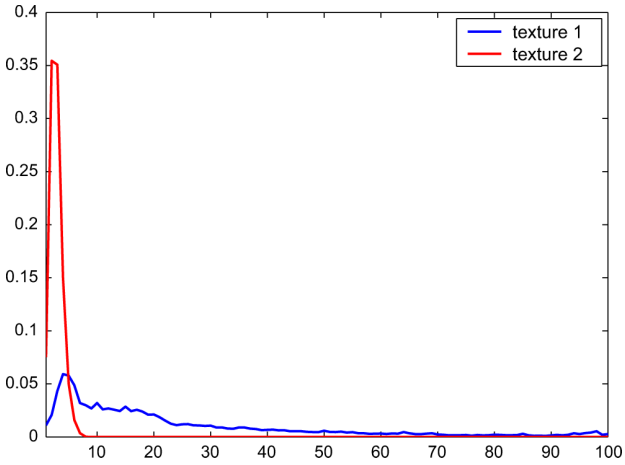

Fig. 7. Gabor energy based distributions for textures of image I1 (texture D32 in red and D68 in blue).

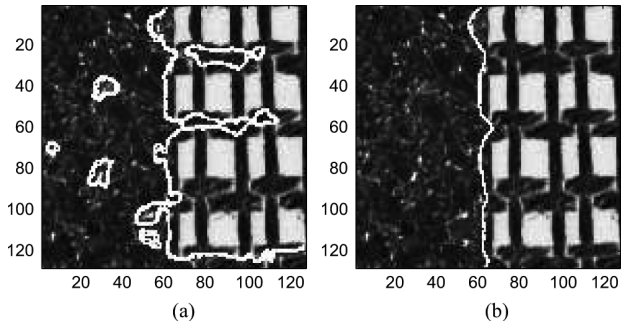

Fig. 8. Segmentation of image I1. (a) Classical approach (V_{cl}). (b) Proposed method (V_{pS}).

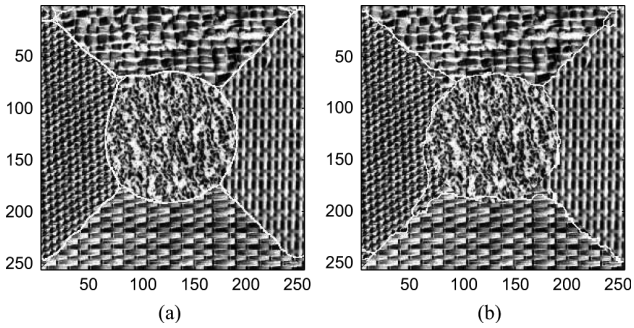

Fig. 9. Segmentation of image I3. (a) Classical method (V_{cl}). (b) Proposed approach (V_{pS}).

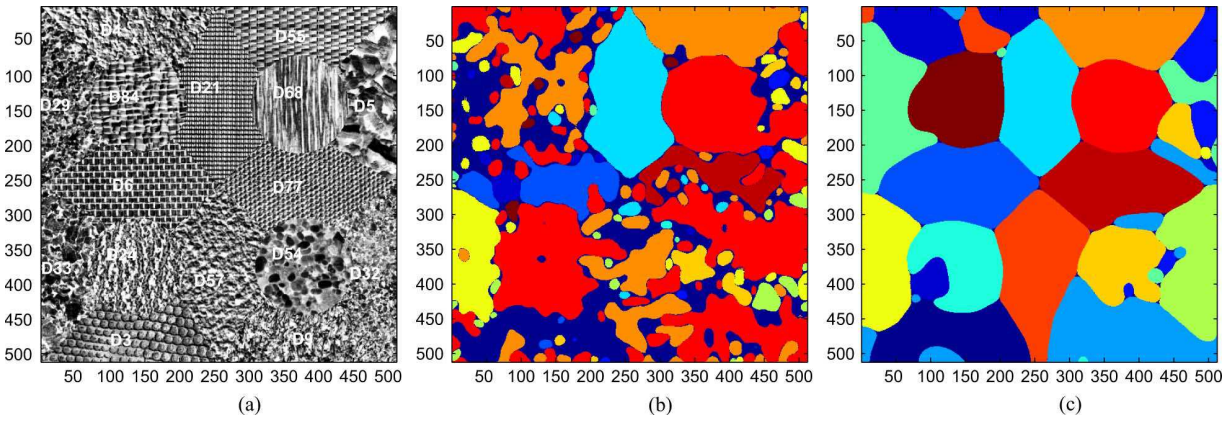

Fig. 10. Segmentation of image I4. (a) Original image. (b) Classical method (V_{cl}). (c) Proposed approach (V_{pS}).

outperforms the classical methods V_{cl}: the mean misclassification rate is about $5.9 \pm 5\%$ for the proposed method (Var_{propS}) where it is of $18.5 \pm 25.3\%$ for V_{cl}. Var_{propS} significantly outperforms V_{cl} in all cases, except for image I3. Significant improvements are brought in all cases compared to Var_{clas}, especially 2.7% versus 11% and 13.9% versus 63% for images I1 and I4, respectively. For image I3, the classical pixel-level variational scheme V_{cl} slightly outperforms the proposed approach (3% versus 4.9%). For this special case, image textures are well seperated in the feature space. In such case, the maximization of the pixel-level likelikood performed by the classical method may achieve a sligtly better detection of the region boundaries than the region-level scheme which seeks to reproduce region feature statistics similar to the reference class statistics. In contrast, when texture classes partially overlap in the considered feature space such as for images I1 and I4, the former strategy is misleading and poor segmentation performances may be achieved. For image I4, the misclassification rate is greater than 60% for V_{cl} where the region-level criterion V_{pS} reachs a satisfactory misclassification rate of only 13.9%. In the case of image I1, even if the mosaic is simple and the image contains only two textures, the classical method fails in discriminating between textures (Fig. 8) because of the overlap between the selected texture descriptors (Fig. 7).

3) Region-Based Versus Heiler et al. Approach (V_H): In contrast to classical methods based upon punctual pixel likelihoods V_{cl}, Heiler *et al.* approach exploits pixel neighborhood [19]. Segmentation results show that this method can be more relevant than V_{cl} if we use optimal analysis window size: the mean misclassification rate is about $10.8 \pm 5.6\%$ for V_H with $T_W = 33$ where it is of $18.5 \pm 25.3\%$ for Var_{clas}. However, results issued from V_H greatly depend upon the choice of the scale or window parameter: the mean misclassification rate is about $10.8 \pm 5.6\%$ for V_H with $T_W = 33$ and it is about $38.2 \pm 34.5\%$ for $T_W = 3$. Great values of this scale parameter produce better estimates of the texture statistics. But, they can also lead to undesirable situations where multiple texture classes are present in a common window [Fig. 4(c)]. In contrast, smaller analysis windows are less likely to contain multiple classes. But, the limited coverage may, however, produce misleading features [Fig. 4(a)].

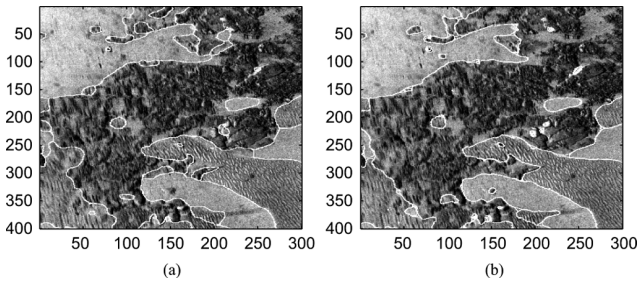

Fig. 11. Segmentation of image I5. (a) Classical method (V_{cl}). (b) Proposed approach (V_{pS}).

The proposed variational region-level segmentation circumvents the problem related to the choice of the neighborhood W_s size and accurately detects region boundaries (see Fig. 5) and significant improvements are brought in all cases compared to method V_H, especially 2.7% versus 6%, 0.9% versus 4.6%, and 7.5% versus 13% for images I1, I2, and I5, respectively.

Overall the performances of the two pixel-level approaches greatly depend upon the potential overlapping of the distributions of the considered feature and on the scale of the texture patterns. In contrast, the proposed region-level approach circumvent these limitations and satisfactory results are reported in all cases.

4) Robustness to Initialization: The proposed variational region-level segmentation is robust to initialization as illustrated in Figs. 12–14, where different initializations for the segmentation of I2 are considered namely a random initialization, an initialization with a maximum-likelihood segmentation using $T_W = 3 \times 3$ and an initialization according to the maximum-likelihood segmentation using $T_W = 33 \times 33$. Similar results (classification error rate of about 1%) are obtained in all cases (see http://public.enst-bretagne.fr/rfablet/Demos/demoIKaroui/Initialization1.avi, http://public.enst-bretagne.fr/rfablet/Demos/demoIKaroui/Initialization2.avi and http://public.enst-bretagne.fr/rfablet/Demos/demoIKaroui/Initialization3.avi).

5) Performance of the Unsupervised Criterion: As in the supervised case, the proposed unsupervised region-level method

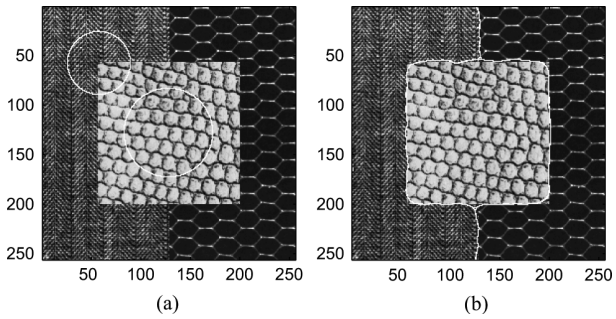

Fig. 12. Segmentation of image I2 using the proposed approach with a random initialization. (a) Random initialization. (b) Region based segmentation ($\gamma = 20, 5000$ iterations), $\tau = 0.9\%$.

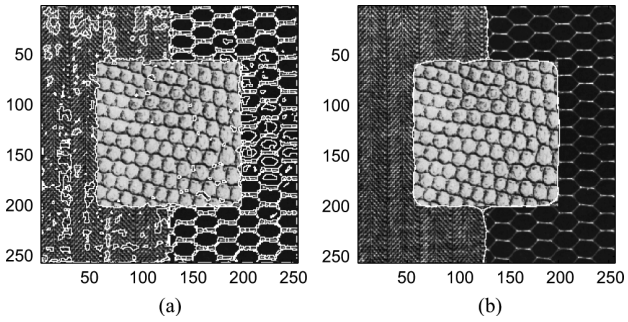

Fig. 13. Segmentation of image I2 using the region-level approach with an initialization issued from a maximum-likelihood criterion. (a) Using a 3×3 analysis window. (b) Region-level segmentation $\gamma = 20, 1000$ iterations), $\tau = 0.9\%$.

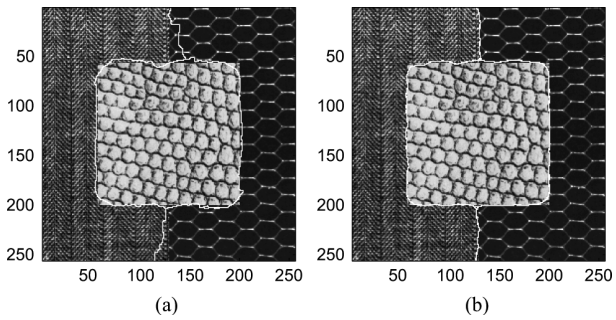

Fig. 14. Segmentation of image I2 using the region-level approach with an initialization issued from a maximum-likelihood criterion. (a) Using 33×33 analysis window. (b) Region based segmentation ($\gamma = 20, 600$ iterations), $\tau = 0.9\%$.

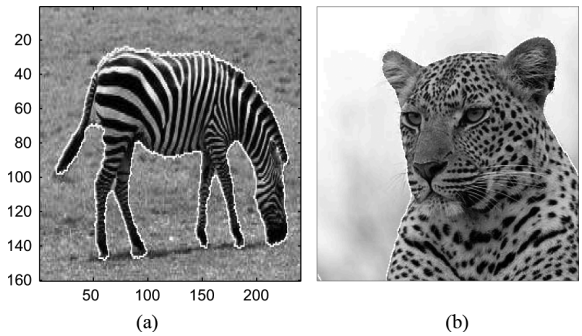

Fig. 15. Segmentation of natural images I6 and I7 using the proposed region-level approach. (a) Segmentation of image I6. (b) Segmentation of image I7.

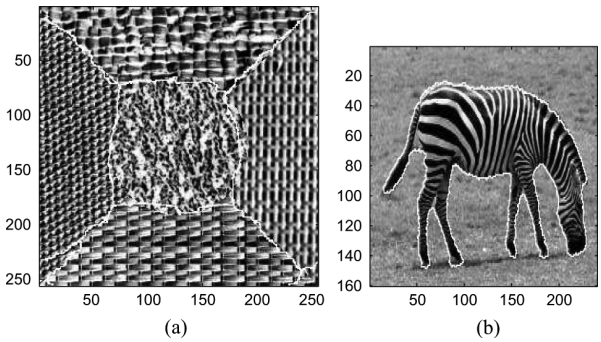

Fig. 16. Unsupervised segmentation. (a) I3. (b) I6.

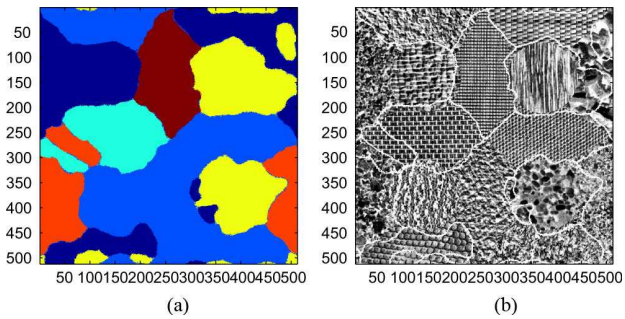

Fig. 17. Unsupervised segmentation of I4.

is shown to reach good classification performances even compared to classical supervised approaches. For example for the image I2, the error rate with the unsupervised method is about 1% whereas the average rate is about 5% for classical supervised approaches (see Table I). Good resulats were obtained for the other images (see Fig. 16).

The unsupervised criterion is however more dependent upon initialization and feature separability than the supervised case. Regarding the latter, the reference statistics are known and the method converges toward regions that conform these statistics regardless of the initialization. In contrast, the unsupervised case does not exploit any reference statistics and the partition that maximizes the dissimilarity between region statistics depends upon the separability of region in the chosen feature space. For example, for image I4 (see Fig. 17), only six classes were detected, quite similar textures were grouped:

- D29, D84, D3, and D55;
- D24, D57, D9, D77, and D57;
- D68, D5, and D54;
- D32 and D33.

The segmentation of the mosaic on the six detected classes is homogeneous and the segmentation rate of the proposed unsupervised segmentation is about 60% (if we consider 16 classes) which is still satisfactory compared to the classical supervised approaches (80% for Heiler supervised method using an analyzing window of 9×9 and pixel-likelihood based approaches 63%).

VI. Conclusion

In this paper, we propose and evaluate a region-level variational approach for supervised and unsupervised texture-based segmentation. Texture characterization is issued from nonparametric distributions of their responses to a set of filters. The variational segmentation consists in the minimization of an energy criterion defined over the set of image partitions and comprising two terms: a similarity measure between regions features and texture models and a boundary based functional that imposes smoothness and regularity on region boundaries. The proposed similarity criterion, is generic and permits optimally fusing various types of texture statistics and dealing with different image types. For example, in [27], an application to sidescan sonar images is considered. Experiments were carried out to compare our approach to previous work exploiting variational approaches [2], [3], [11], [14]–[19]. The following conclusions can be drawn.

- The proposed method defines an efficient similarity measure that naturally and optimally fuses a wide variety of texture features.
- The region-based observation-driven term is more robust than pixel-level formulation used in the classical approaches. Existing methods are mainly stated as the optimization of a criterion evaluating punctual pixel likelihoods or similarity measure computed within local neighborhood. These approaches require sufficient dissimilarity between used feature statistics and need the choice of the neighborhood size which may have a considerable impact on segmentation accuracy. The proposed variational setting solves for these two major drawbacks.

In [27], a complementary experimental comparison to Markovian pixel-level segmentation techniques was carried out for sonar images. Similar conclusions were drawn on the superiority brought by the variational region-level setting.

We have shown that the proposed region-level scheme could also be applied to unsupervised image segmentation. The region-level criterion then consists in the dissimilarity maximization between the texture statistics of the different regions. As perspectives for future work, we may mention that the proposed method can integrate automatically other texture features, it can also deal with other computer vision applications such as textured object tracking or detection, etc.

Appendix A
Evolution Equation Computation

Using the shape derivative tools, we want to differentiate the functional

$$F(\Omega_k) = |\Omega_k| \sum_f^F w_f^2 KL\left(Q_f^k, D_f(\Omega_k)\right). \quad (11)$$

The Gâteaux derivative of $F(\Omega_k)$ in the direction of a vector field $\vec{V}$ is then given by

$$dF\left(\Omega_k, \vec{V}\right) = \sum_{f=1}^F w_f^2 \left[d\left[|\Omega_k|\right] KL\left(Q_f^k, D_f(\Omega_k)\right) + |\Omega_k|\, d\left[KL\left(Q_f^k, D_f(\Omega_k)\right)\right]\right]. \quad (12)$$

Replacing KL by its expression, we get

$$d\left[KL\left(Q_f^k, D_f(\Omega_k)\right)\right] = \int_\alpha d\left[Q_f^k(\alpha) \log\left(\frac{Q_f^k(\alpha)}{D_f(\Omega_k,\alpha)}\right) d\alpha\right] \quad (13)$$

$$d\left[Q_f^k(\alpha)\log\left(\frac{Q_f^k(\alpha)}{D_f(\Omega_k,\alpha)}\right)d\alpha\right] = d\left[Q_f^k \log\left(Q_f^k\right)\right] - d\left[Q_f^k \log\left(D_f(\Omega_k,\alpha)\right)\right]. \quad (14)$$

Theorem [25]: The Gâteaux derivative of a functional of the type $K(\Omega) = \int_\Omega k(s,\Omega)\, ds$ is given by

$$dK\left(\Omega, \vec{V}\right) = \int_\Omega k_{sh}\left(s, \Omega, \vec{V}\right) ds - \int_\Gamma k(s,\Omega)\left(\vec{V}\vec{N}\right) da(s) \quad (15)$$

where $k_{sh}\left(s, \Omega, \vec{V}\right)$ is the shape derivative of $k(s,\Omega)$, da is an area element and $\vec{N}$ the inward unit normal vector of Γ.

Q_f^k does not depend upon the domain Ω_k, so its Gâteaux derivative is null, and we have

$$d\left[Q_f^k(\alpha)\log\left(\frac{Q_f^k(\alpha)}{D_f(\Omega_k,\alpha)}\right)d\alpha\right] = -Q_f^k d\left[\log\left(D_f(\Omega_k,\alpha)\right)\right] \quad (16)$$

$$d\left[\log\left(D_f(\Omega_k,\alpha)\right)\right] = \frac{1}{D_f(\Omega_k,\alpha)} d\left[D_f(\Omega_k,\alpha)\right] \quad (17)$$

$D_f(\Omega_k,\alpha) = 1/|\Omega_k| \int_{\Omega_k} g_{\sigma_f}(h_f(s)-\alpha)\, ds$, so

$$\begin{aligned} d\left[D_f(\Omega_k,\alpha)\right] &= \frac{-1}{|\Omega_k|^2} d\left[|\Omega_k|\right] \int_{\Omega_k} g_{\sigma_f}(h_f(s)-\alpha)\, ds \\ &\quad + \frac{1}{|\Omega_k|} d\left[\int_{\Omega_k} g_{\sigma_f}(h_f(s)-\alpha)\, ds\right] \\ &= \frac{-1}{|\Omega_k|} D_f(\Omega_k,\alpha)\, d\left[|\Omega_k|\right] \\ &\quad + \frac{1}{|\Omega_k|} d\left[\int_{\Omega_k} g_{\sigma_f}(h_f(s)-\alpha)\, ds\right]. \end{aligned} \quad (18)$$

The Gâteaux derivative of $|\Omega_k|$ is

$$d\left[|\Omega_k|\right]\left(\vec{V}\right) = -\int_{\Gamma_k}\left(\vec{V}.\vec{N}\right) d\vec{a}(s). \quad (19)$$

As $g_{\sigma_f}(h_f(s)-\alpha)$ does not depend upon the domain Ω_k, its shape derivative is null. So, we have

$$d\left[\int_{\Omega_k} g_{\sigma_f}(h_f(s)-\alpha)\, ds\right]\vec{V} = -\int_{\Gamma_k} g_{\sigma_f}(h_f(s)-\alpha)\vec{V}.\vec{N} d\vec{a}(s). \quad (20)$$

So

$$d\left[KL\left(Q_f^k, D_f(\Omega_k)\right)\right] = \int_\alpha \left[\frac{1}{|\Omega_k|}\int_{\Gamma_k}\left[\frac{Q_f^k(\alpha)}{D_f(\Omega,\alpha)} g_{\sigma_f}(h_f(s)-\alpha) - Q_f^k(\alpha)\right] (\vec{V}.\vec{N}) d\vec{a}(s)\right] d\alpha. \quad (21)$$

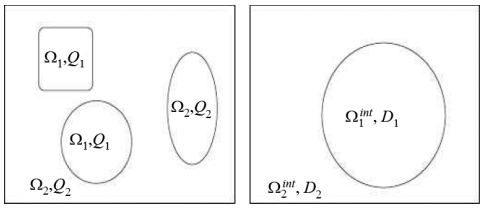

Fig. 18. Left: "true" segmentation. Right: random partition.

We have $\int_\alpha Q_f^k(\alpha)d\alpha = 1$, so we get

$$d\left[KL\left(Q_f^k, D_f\left(\Omega_k\right)\right)\right] = \frac{1}{|\Omega_k|} \times \int_{\Gamma_k}\left[\frac{Q_f^k}{D_f(\Omega_k)} * g_{\sigma_f}(h_f(s)) - 1\right](\vec{V}.\vec{N})d\vec{a}(s). \quad (22)$$

Finally, according to (12), we get

$$dF\left(\Omega_k, \vec{V}\right) = \int_{\Gamma_k} -KL_w\left(Q^k, D(\Omega_k)\right) + \sum_{f=1}^{F} w_f^2\left(\frac{Q_f^k}{D_f(\Omega_k)} * g_{\sigma_f}(h_f(s)) - 1\right)(\vec{V}.\vec{N})d\vec{a}(s). \quad (23)$$

APPENDIX B
UNSUPERVISED CRITERION

We show that image partition that maximizes E^1 (9) corresponds to the "right" segmentation. Without loss of generality we consider the two-class case, the generalization to multiclass case is straightforward. Let $\Omega = \{\Omega_1, \Omega_2\}$ be the true partition with statistics $Q_1\left(\Omega_1\right)$ and $Q_2\left(\Omega_2\right)$.

For an arbitrarily image partition $\Omega^{int} = \left\{\Omega_1^{int}, \Omega_2^{int}\right\}$ with region statistics $D\left(\Omega_1^{int}\right)$ denoted D_1 and $D\left(\Omega_2^{int}\right)$ denoted D_2, (see Fig. 18), we have

$$D_1 = \lambda Q_1 + (1-\lambda) Q_2$$

where $\lambda = \left|\Omega_1^{int} \cap \Omega_1\right| / \left|\Omega_1^{int}\right|$ For D_2 we also have

$$P_2 = \lambda' Q_2 + (1-\lambda') Q_1$$

where $\lambda' = \left|\Omega_2^{int} \cap \Omega_2\right| / \left|\Omega_2^{int}\right|$. For two class-case, our criterion is the following:

$$KL(D_1, D_2) + KL(D_2, D_1).$$

The Kullback–Leibler divergence $KL(Q, D)$ is convex with respect to (Q, D) (can easily demonstrated using Jensen inequality), so

$$\begin{aligned} &KL(D_1, D_2) \\ &\quad = KL(\lambda Q_1 + (1-\lambda) Q_2, \lambda D_2 + (1-\lambda) D_2) \\ &\quad \leq \lambda KL(Q_1, D_2) + (1-\lambda) KL(Q_2, D_2) \end{aligned}$$

or $KL(Q_1, D_2)$ can be expressed as follows:

$$\begin{aligned} &KL(Q_1, D_2)) \\ &\quad = KL(\lambda' Q_1 + (1-\lambda') Q_1, \lambda' Q_2 + (1-\lambda') Q_1) \\ &\quad \leq \lambda' KL(Q_1, Q_2) + (1-\lambda') KL(Q_1, Q_1) \\ &\quad \leq \lambda' KL(Q_1, Q_2). \end{aligned}$$

In the same way

$$KL(Q_2, D_2)) \leq (1-\lambda') KL(Q_2, Q_1).$$

So

$$\begin{aligned} &KL(D_1, D_2) \\ &\quad \leq \lambda\lambda' KL(Q_1, Q_2) + (1-\lambda)(1-\lambda') KL(Q_2, Q_1). \end{aligned}$$

Similarly, we show that

$$\begin{aligned} &KL(D_2, D_1) \\ &\quad \leq \lambda\lambda' KL(Q_2, Q_1) + (1-\lambda)(1-\lambda') KL(Q_1, Q_2). \end{aligned}$$

Finally, our functional can be majored as follows:

$$E^1 \leq (\lambda\lambda' + (1-\lambda)(1-\lambda')) \times (KL(Q_1, Q_2) + KL(Q_2, Q_1)).$$

The equality is reached for $\lambda = 1$ et $\lambda' = 1$, i.e., $D_1 = Q_1$ and $D_2 = Q_2$ or for $\lambda = 0$ and $\lambda' = 0$, i.e., $D_1 = Q_2$ and $D_2 = Q_1$.

REFERENCES

[1] M. N. Do and M. Vetterli, "Texture similarity measurement using Kullback–Leibler distance on wavelet subbands," in *Proc. Int. Conf. Image Process.*, 2000, vol. 3, pp. 730–733.
[2] M. Lianantonakis and Y. R. Petillot, "Sidescan sonar segmentation using active contours and level set method," *Oceans-Eur.*, vol. 1, pp. 719–724, 2005.
[3] T. Kadir and M. Brady, "Unsupervised non-parametric region segmentation using level sets," in *Proc. IEEE Int. Conf. Comput. Vis.*, Oct. 2003, vol. 2, pp. 1267–1274.
[4] L. Xiuwen and W. DeLiang, "Texture classification using spectral histograms," *IEEE Trans. Image Process.*, vol. 12, no. 6, pp. 661–670, Jun. 2003.
[5] R. O. Duda and P. E. Hart, *Pattern Classification and Scene Analysis*. Hoboken, NJ: Wiley, 1973.
[6] S. Shah and J. K. Aggarwal, "A Bayesian segmentation framework for textured visual images," *Comput. Vis. Pattern Recognit.*, pp. 1014–1020, Jun. 1997.
[7] G. Gimel'farb, "Texture modeling by multiple pairwise pixel interactions," *IEEE Trans. Pattern Anal. Mach. Intell.*, vol. 18, no. 11, pp. 1110–1114, Nov. 1996.
[8] R. Adams and L. Bischof, "Seeded region growing," *IEEE Trans. Pattern Anal. Mach. Intell.*, vol. 16, no. 6, pp. 641–647, Jun. 1994.
[9] P. Nammalwar, O. Ghita, and P. F. Whelan, "Integration of feature distributions for color texture segmentation," in *Proc. Int. Conf. Pattern Recognit.*, Aug. 2005, vol. 1, pp. 716–719.
[10] S. C. Zhu and A. Yuille, "Region competition: Unifying snakes, region growing, and Bayes/MDL for multiband image segmentation," *IEEE Trans. Pattern Anal. Mach. Intell.*, vol. 18, no. 9, pp. 884–900, Sep. 1996.
[11] J. F. Aujol, G. Aubert, and L. Blanc-Féraud, "Wavelet-based level set evolution for classification of textured images," *IEEE Trans. Image Process.*, vol. 12, no. 12, pp. 1634–1641, Dec. 2003.
[12] A. Luminita, A. Vese, and T. F. Chan, "A multiphase level set framework for image segmentation using the Mumford and Shah model," *Int. J. Comput. Vis.*, vol. 50, no. 3, pp. 271–293, 2002.

[13] C. Samson, L. Blanc-Féraud, G. Aubert, and J. Zerubia, "A level set method for image classification," *Int. J. Comput. Vis.*, vol. 40, no. 3, pp. 187–197, 2000.

[14] N. Paragios and R. Deriche, "Geodesic active regions and level set methods for supervised texture segmentation," *Int. J. Comput. Vis.*, vol. 46, no. 3, pp. 223–247, 2002.

[15] T. Brox and J. Weickert, "Level set based image segmentation with multiple regions," in *Pattern Recognition*, C. Rasmussen, H. Bulthoff, M. Giese, and B. Scholkopf, Eds. New York: Springer-Verlag, 2004, pp. 415–423.

[16] B. Sandberg, T. Chan, and L. Vese, "A level-set and Gabor-based active contour algorithm for segmenting textured images," Math. Dept., UCLA, Los Angeles, CA, 2002, Tech. Rep. 39.

[17] M. Rousson, T. Brox, and R. Deriche, "Active unsupervised texture segmentation on a diffusion based feature space," in *Proc. IEEE Comput. Soc. Conf. Comput. Vis. Pattern Recognit.*, Jun. 2003, vol. 2, pp. 699–704.

[18] S. P. Awate, T. Tasdizen, and R. T. Whitaker, "Unsupervised texture segmentation with nonparametric neighborhood statistics," in *Proc. Eur. Conf. Comput. Vis.*, 2006, pp. 494–507.

[19] M. Heiler and C. Schnorr, "Natural image statistics for natural image segmentation," in *Proc. IEEE Int. Conf. Comput. Vis.*, Oct. 2003, vol. 2, pp. 1259–1266.

[20] J. Kim, J. W. Fisher, and A. Yezzi, "A nonparametric statistical method for image segmentation using information theory and curve evolution," *IEEE Trans. Image Process.*, vol. 14, no. 10, pp. 1486–1502, Oct. 2005.

[21] P. Brodatz, *Textures: A Photographic Album for Artists and Designers*. New York: Dover, 1996.

[22] O. G. Cula and K. Dana, "3D texture recognition using bidirectional feature histograms," *Int. J. Comput. Vis.*, vol. 49, no. 1, pp. 33–60, Aug. 2004.

[23] Q. Xu, J. Yang, and S. Ding, "Texture segmentation using LBP embedded region competition," *Electron. Lett. Comput. Vis. Image Anal.*, vol. 5, no. 1, pp. 41–47, 2004.

[24] R. Fablet and P. Bouthemy, "Motion recognition using non parametric image motion models estimated from temporal and multiscale cooccurrence statistics," *IEEE Trans. Pattern Anal. Mach. Intell.*, vol. 25, no. 12, pp. 1619–1624, Dec. 2003.

[25] S. Jehan-Besson, M. Barlaud, and G. Aubert, "Image segmentation using active contours: Calculus of variations or shape gradients?," *SIAM J. Appl. Math.*, vol. 63, no. 6, pp. 2128–2154, 2003.

[26] I. K. Imen, R. Fablet, J. M. Boucher, W. Pieczynski, and J. M. Augustin, "Fusion of textural statistics using a similarity measure: Application to texture recognition and segmentation," *Pattern Anal. Appl.*, vol. 11, no. 3–4, pp. 425–434, Sep. 2008.

[27] I. Karoui, R. Fablet, J. M. Boucher, and J. M. Augustin, "Seabed segmentation using optimized statistics of sonar textures," *IEEE Trans. Geosci. Remote Sens.*, vol. 47, no. 6, pp. 1621–1631, Jun. 2008.

[28] T. Randen and J. H. Husoy, "Filtering for texture classification: A comparative study," *IEEE Trans. Pattern Anal. Mach. Intell.*, vol. 21, no. 4, pp. 291–310, Apr. 1999.

[29] S. Kullback, "On information and sufficiency," in *The Annals of Mathematical Statistics*. Hoboken, NJ: Wiley, 1951, vol. 22.

[30] J. A. Sethian, *Level Set Methods*. Cambridge, U.K.: Cambridge Univ. Press, 1996.

[31] A. Herbulot, S. Jehan-Besson, M. Barlaud, and G. Aubert, "Shape gradient for multimodal image segmentation using mutual information," in *Proc. Int. Conf. Image Process.*, 2004, vol. 4, pp. 2729–2732.

[32] T. F. Chan and L. A. Vese, "Active contours without edges," *IEEE Trans. Image Process.*, vol. 10, no. 2, pp. 266–277, Feb. 2001.

[33] G. Palubinskas, X. Descombes, and F. Kruggel, "An unsupervised clustering method using the entropy minimization," in *Proc. Int. Conf. Pattern Recognit.*, 1998, vol. 2, pp. 1816–1818.

[34] A. Lorette, X. Descombes, and J. Zerubia, "Fully unsupervised fuzzy clustering with entropy criterion," in *Proc. Int. Conf. Pattern Recognit.*, 2000, vol. 3, pp. 986–989.

[35] A. Ehrhold, D. Hamon, and B. Guillaumont, "The rebent monitoring network, a spatial integrated acoustic approach to survey nearshore macrobenthic habitats: Application to the bay of concarneau," *ICES J. Marine Sci.*, vol. 63, pp. 1604–1615, 2006.

Imen Karoui received the Engineering degree in telecommunications from the École Polytechnique de Tunis, Tunisia, in 2002, the DEA degree in signal, télécommunications, images, and radar from the Université de Rennes 1, Paris, France, in 2003, and the Ph.D. degree in signal processing and telecommunications from the Department Signal and Communications, Telecom Bretagne, Brest Cedex, France, in 2007.

She is currently a Postdoctoral Fellow at Ifremer, Plouzane, France. Her research interests include texture analysis and segmentation and shape recognition and tracking with application to acoustic imaging, fisheries, and oceanography.

Ronan Fablet received the M.Sc. degree in signal processing and telecommunications from École Nationale Supérieure de lAéronautique et de lEspace, Toulouse Cedex 4, France, in 1997, and the Ph.D. degree in signal processing and telecommunications from the University of Rennes 1, Rennes, France, in 2001.

In 2002, he was an INRIA Postdoctoral Fellow at Brown University, Providence. RI. From 2003 to 2007, he had a full-time research position at Ifremer Brest in the field of biological oceanography. Since 2008, he has been an Assistant Professor in the Signal and Communications Department, Telecom Bretagne, Brest Cedex, France. His main interests include sonar and radar imaging especially applied to biological and physical oceanography, and signal and image processing applied to biological archives.

Jean-Marc Boucher (M'83–SM'95) was born in 1952. He received the Engineering degree in telecommunications from the Ecole Nationale Supérieure des Telecommunications, Paris, France, in 1975 and the Habilitationà Diriger des Recherches degree from the University of Rennes 1, Rennes, France, in 1995.

He is currently a Professor in the Department of Signal and Communications, Telecom Bretagne, Brest Cedex, France, where he is also Education Deputy Director. He is also Deputy Manager of a National Scientific Research Center laboratory (FRE 3167 lab-STICC). His current researches are related to statistical signal analysis including estimation theory, Markov models, blind deconvolution, wavelets, and multiscale image analysis. These methods are applied to radar and sonar images, seismic signals, and electrocardiographic signals. He published about one hundred technical articles in these areas in international journals and conferences.

Jean-Marie Augustin received the M.S. degree in signal processing from the University of Rennes, France, in 1982.

He joined the Institut Français de Recherche et dExploitation de la Mer, Brest, France in 1984, and is presently a Senior Engineer in the Department of Acoustics and Seismics. His main interests include software development for sonar seafloor mapping and backscatter reflectivity analysis.

This article has been accepted for inclusion in a future issue of this journal. Content is final as presented, with the exception of pagination.

Keypoint-Based Analysis of Sonar Images: Application to Seabed Recognition

Huu-Giao Nguyen, Ronan Fablet, Axel Ehrhold, and Jean-Marc Boucher

***Abstract*—In this paper, we address seabed characterization and recognition in sonar images using keypoint-based approaches. Keypoint-based texture recognition has recently emerged as a powerful framework to address invariances to contrast change and geometric distortions. We investigate here to which extent keypoint-based techniques are relevant for sonar texture analysis which also involves such invariance issues. We deal with both the characterization of the visual signatures of the keypoints and the spatial patterns they form. In this respect, spatial statistics are considered. We report a quantitative evaluation for sonar seabed texture data sets comprising six texture classes such as mud, rock, and gravely sand. We clearly demonstrate the improvement brought by keypoint-based techniques compared to classical features used for sonar texture analysis such as cooccurrence and Gabor features. In this respect, we demonstrate that the joint characterization of the visual signatures of the visual keypoints and their spatial organization reaches the best recognition performances (about 97% of correct classification w.r.t. 70% and 81% using cooccurrence and Gabor features). Furthermore, the combination of difference of Gaussian keypoints and scale-invariant feature transform descriptors is recommended as the most discriminating keypoint-based framework for the analysis of sonar seabed textures.**

***Index Terms*—Acoustic remote sensing, log-Gaussian Cox process, maerly sand, megaripples, sonar texture, visual keypoint.**

I. Introduction

In RECENT years, the analysis of the physical properties of the seafloor and the mapping of seabed habitats has become increasingly important for both marine resource management and scientific research [1]–[4]. Many projects in coastal marine environment survey have been initiated to provide a baseline knowledge of seafloor and marine habitats [5]–[8]. The innovations in underwater acoustic signal processing have played a major role in the emergence of sidescan sonar as the privileged remote sensing device for *in situ* seabed observation. As an example, a sidescan sonar survey of the REBENT project has been carried out by IFREMER since 2000 [7]. An EdgeTech DF1000 sidescan sonar is deployed to survey a 200-km^2 area in the Bay of Concarneau on the south Brittany coast at different times, and it resulted in a high-resolution mapping of the marine habitats (Fig. 1). Sidescan sonar data refer to the backscatter energy from an insonified region of the seabed. Each line of a sonar image is built from one beam of the multibeam sidescan sonar system. The physical and biological properties of the seabed typically lead to the formation of textured images, different seabed types such as rock, mud, sand corresponding to different texture types (Fig. 4). Hence, sidescan sonar imaging is increasingly used for a variety of applications such as environmental monitoring, marine geosciences, and biology, as well as the oil industry or defense [9], [10], and the automated recognition and classification of sonar images in terms of seabed types are among the key issues [11]–[13].

Following the early development of texture descriptors in the field of image processing, sonar texture analysis [14], [15] usually relies on the extraction of statistics of the response to scale-space filters, as Gabor and wavelet analysis [15]–[17] or cooccurrence matrix [10]. However, as shown in Fig. 3, sonar texture characteristics strongly depend on the incidence angle. Variations of the incidence angle between the sonar beam and the insonified surface result both in local contrast changes as well as geometric distortions. These issues are not intrinsically embedded in the aforementioned techniques and are usually dealt with using texture models learned for different angular sectors. Recently, meaningful advances have been reported for visual texture recognition invariance to contrast and viewpoint change [18]–[21]. They mainly involved keypoint-based techniques, which primarily relied on the detection of interest points in visual textures [22]–[25]. Visual signatures of such keypoints also embedding such invariance properties were then proposed for image classification and categorization issues. The resulting texture characterization was regarded as the statistical analysis from the descriptor vector and local position of visual keypoints [26]–[28]. To our knowledge, the relevance of keypoint-based schemes in sonar seabed imaging has not been investigated. Here, we aim at evaluating to which extent keypoint-based techniques can improve the characterization and recognition of seabed textures. Regarding keypoint sets as realizations of multivariate point processes, our methodological contributions lie in the development of multivariate statistical descriptors and models of spatial keypoint patterns for sonar texture recognition. We focus on the analysis of the spatial covariance of keypoint patterns, namely, using second-order descriptive statistics and log-Gaussian Cox processes. These results open the door for other application of keypoint-based approaches in sonar imaging, e.g., registration-related issues.

This paper is organized as follows. In Section II, a sonar texture data set for seabed classification is introduced.

Manuscript received March 28, 2011; revised July 22, 2011; accepted July 31, 2011.

H.-G. Nguyen, R. Fablet, and J.-M. Boucher are with the Institut Telecom/Telecom Bretagne/LabSTICC and Université Européenne de Bretagne, 29238 Brest CEDEX 3, France (e-mail: huu.nguyen@telecom-bretagne.eu; ronan.fablet@telecom-bretagne.eu; jm.boucher@telecom-bretagne.eu).

A. Ehrhold is with the Department of Coastal Environment Dynamics—IFREMER, 29280 Plouzané, France (e-mail: axel.ehrhold@ifremer.fr).

Color versions of one or more of the figures in this paper are available online at http://ieeexplore.ieee.org.

Digital Object Identifier 10.1109/TGRS.2011.2165848

0196-2892/$26.00 © 2011 IEEE

This article has been accepted for inclusion in a future issue of this journal. Content is final as presented, with the exception of pagination.

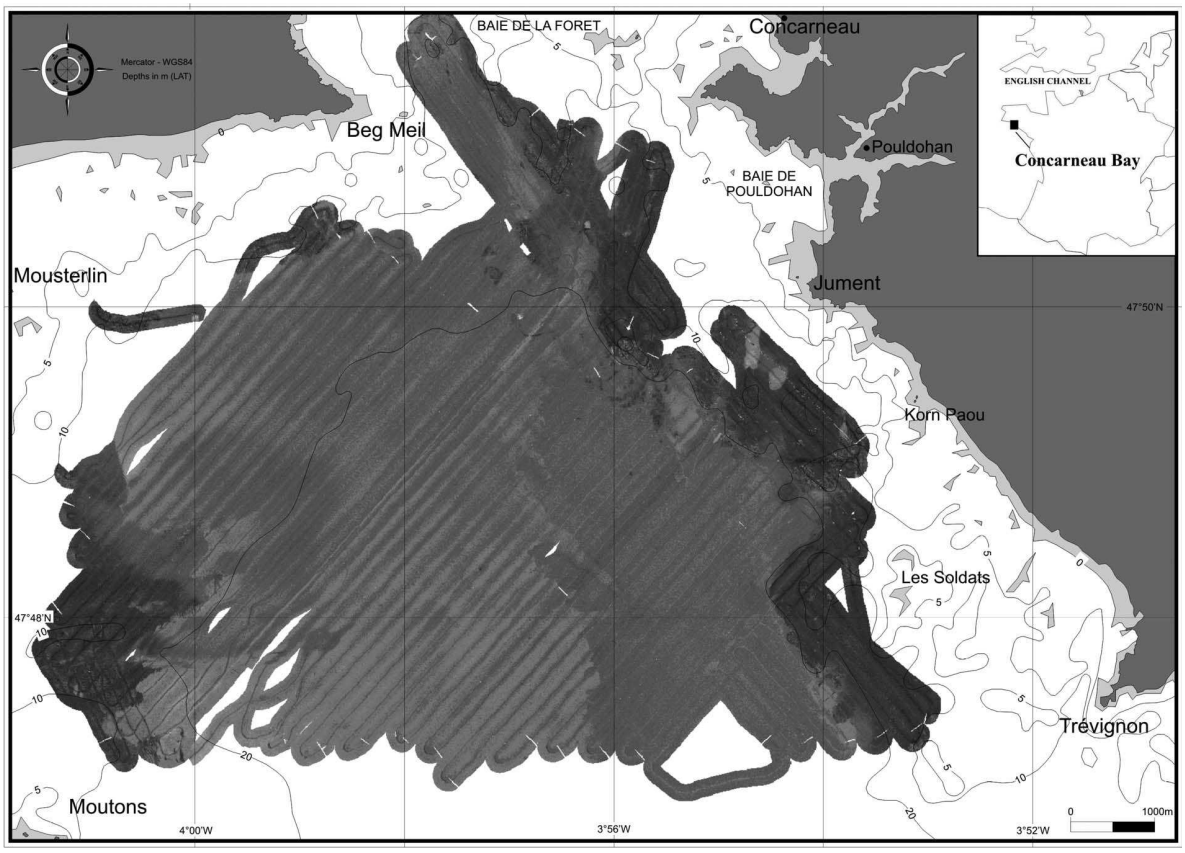

Fig. 1. Illustration of the surveyed area for marine habitat mapping as part of the REBENT project. The surveyed zone is located in the Bay of Concarneau (Britanny, France).

Keypoint detection and characterization in sonar seabed images are reviewed in Section III. In Section IV, we introduce keypoint statistics and associated probabilistic models, including spatial statistics of visual keypoint patterns. The application to sonar texture recognition and performance evaluations is reported in Section V. The main contributions of the proposed approach with respect to the previous work are further outlined in Section VI.

II. Sonar Texture Database

The sonar images considered in this paper were obtained from an EdgeTech DF1000 sidescan sonar as part of project REBENT, IFREMER. This database was used to survey coastal benthic habitats and to evaluate biodiversity changes in a 200-km^2 area in the Bay of Concarneau on the South Brittany, France (Fig. 1). The sidescan acquisition settings were chosen for the period from February 26, 2003, to March 21, 2003, as follows: 100-kHz backscatter signal, 110 m for swath width, and vertical beam titled down 20° from the horizontal. Moreover, 25 underwater video profile and diver observations and 93 grab samples were collected to provide a groundtruth knowledge of the structure of the seafloor.

Considering sidescan sonar data interpretation, acoustic backscatter can be regarded as a function of the incidence angle (i.e., the angle of incidence of the acoustic wavefront to the seafloor), surface roughness, impedance contrast across the sediment water interface, topography, and volume reverberation [29]. Sonar images are issued from the measurements of the backscattered echo of the seabed for successive sonar swaths. An example of sidescan sonar images with incident angles from $-85°$ to $+85°$ is shown in Fig. 2(a). The different seabeds correspond to different textural features. Fig. 2(a) contains two different seabed types, namely, maerly and gravelly sand and cleanly sand. Maerl biotopes [Fig. 2(c) and (d)] can build up over millennia to create carbonate-rich gravel deposits that often have high benthic biodiversity and productivity [30]. Maerl beds are protected by OSPAR convention. At the north of Mouton Island (Fig. 1), maerl beds are sculpted into a large-scale ripple pattern [Fig. 2(a) and (b)], indicating differential distributions of live and dead thalli between the tops of the ridges and the bottoms of the gullies. A better discrimination of megaripples sonar texture is important to recognize this sensitive habitat. Each column of this sonar image corresponds to a 25-m-wide band of the seafloor. For a given seabed type, the mean backscatter clearly depends on various incidence angles [9], [10]. Fig. 3(a) shows the mean backscatter evolution of two different seabed types in Fig. 2(a). In particular, for vertical incidences, poor discrimination among seabed types can be expected. Moreover, textural patterns may also vary depending on incidence angles, as shown in Fig. 3(b) and (c), where, in the specular domain $[5°, 40°]$, a loss in contrast is observed for maerly sand megaripples compared with the sector $[80°, 85°]$.

This article has been accepted for inclusion in a future issue of this journal. Content is final as presented, with the exception of pagination.

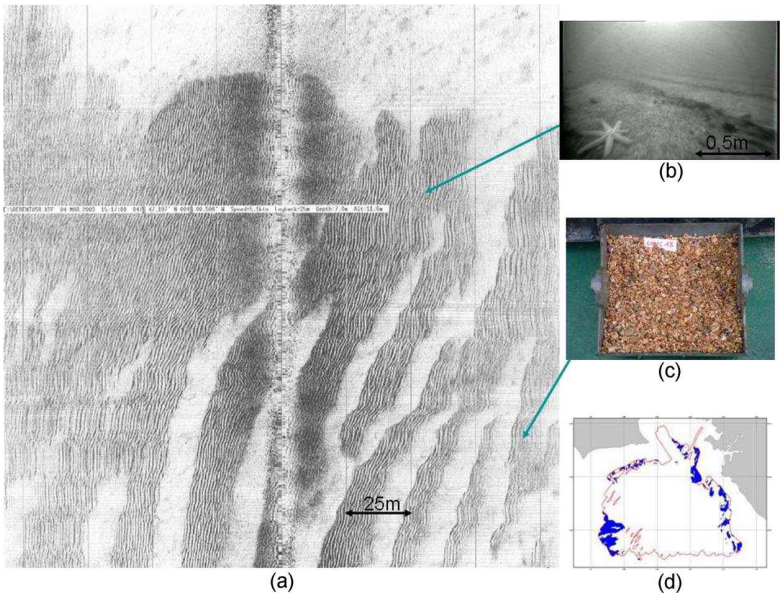

Fig. 2. (a) Example of sidescan sonar image (REBENT, IFREMER). Image extracted from (b) a video frame and (c) a grab observation of maerly and gravelly sand collected at the survey areas (in blue) in the (d) Bay of Concarneau.

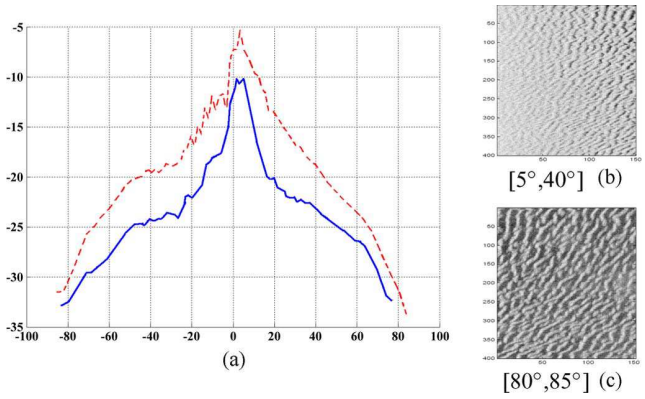

Fig. 3. (a) Backscatter evolution as a function of the incidence angle for two different seabed types: maerly-gravelly (M-G) sand (dotted line) and cleanly sand (solid line), from $-85°$ to $+85°$ with the incidence angle in Fig. 2. (b) and (c) Sonar image samples of the M-G sand for two angular sectors (REBENT, IFREMER).

Given the different physical and biological characteristics of the surveyed area, 50 sonar images were collected (Fig. 4). Six different seabed classes are identified for this paper, namely, *mud, sandy mud, maerly and gravelly (M-G) sand, clearly sand, rock, and mixed sediment*. Here, we used a database of 240 sonar textures images. Each class comprises 40 256 $\times$ 256 images with strong variations of incidence angles and scaling. This image database is made available.[1]

III. Keypoint Detection and Characterization in Sonar Images

We aim here at evaluating to which extent visual keypoints introduced for computer vision applications may be applied to sonar seabed imaging. Numerous approaches have been proposed to detect regions or points of interest in images. Among the most popular, the Harris detector detects corners [31], i.e., the points at which significant intensity changes in two directions occur. It relies on the eigen-decomposition of the structure tensor of the intensity function. Scale-space approaches based on the analysis of the Hessian matrix were also proposed to address scale adaption [32]. Scale-spaces of difference of Gaussians (DoG) are also widely considered as an approximation of the Laplacian [24]. More recently, Mikolajczyk *et al.* [33] has combined Harris or Hessian detector and the Laplacian operator (for scale adaption) to propose two scale-invariant feature detectors, namely, Harris–Laplace (Har-Lap) and Hessian–Laplace (Hes-Lap). Bay *et al.* [22] presented the fast-Hessian (FH) detector based on the Hessian matrix in the integral images. Other categories of keypoint detectors may be cited, e.g., the maximally stable extremal region detector [34], the edge-based region detector, the intensity extrema-based region detector [35], or the entropy-based region (such as salient regions) detector [36]. Comparisons between the different detectors for computer vision applications are given in [22], [33], and [37].

Given the pixel coordinates of the extracted keypoints, denoted by $\{s_1, \ldots, s_N\}$, many different schemes have been proposed to extract an invariant feature vector of each keypoint s_i [18], [26], [38]. The scale-invariant feature transform (SIFT) descriptor is certainly among the most popular. It is formed by local distributions of the orientations of the gradient of the intensity [24]. Intensity-domain features such as spin feature [37] may also be cited. The later relies on 2-D histogram encoding the distribution of the intensity value and the distance from the reference point. Rather than considering gradient orientations, the SURF descriptor [22] relies on the distribution of Haar-wavelet responses, whereas the Daisy descriptor [25] exploits responses to oriented Gaussian filters. The Brief descriptor

[1]This database is available for download at http://perso.telecom-bretagne.eu/ronanfablet.

This article has been accepted for inclusion in a future issue of this journal. Content is final as presented, with the exception of pagination.

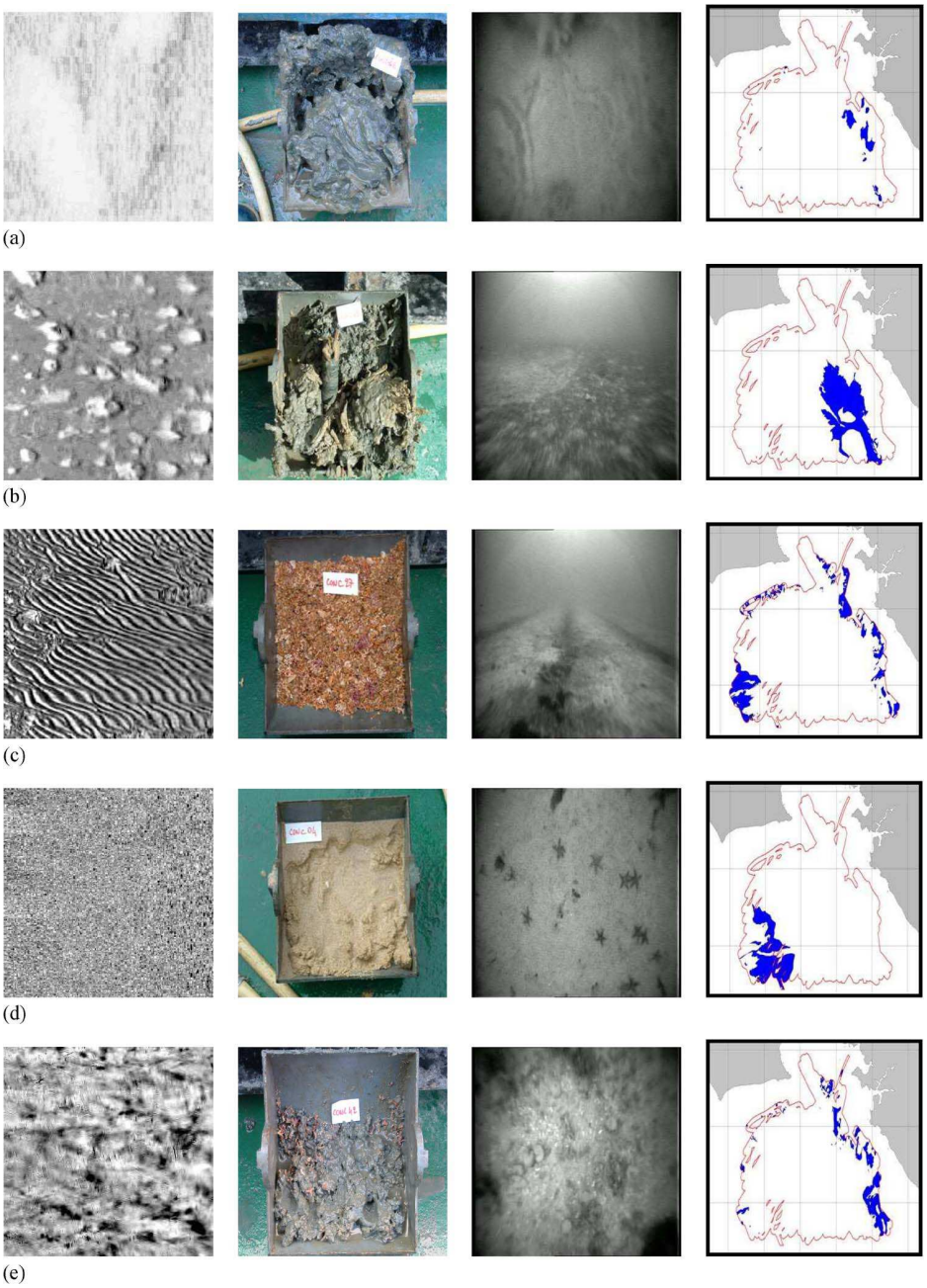

Fig. 4. Examples of sonar texture images with the corresponding video, grab observations, and survey location for the different seabed types. (a) Mud. (b) Sandy mud. (c) M-G sand. (d) Clearly sand. (e) Mixed sediment.

[23] was issued from a relatively small number of intensity of different image patches using binary string.

From computer vision reviews, we investigate five robust detector/descriptor types which were associated with the best performance for computer vision applications in [22]–[25] and [38], respectively: DoG+SIFT, (Har-Lap)+(SIFT–Spin), (Hes-Lap)+Daisy, FH+SURF, and FH+Brief. We briefly review the details of the implementation of each combination.

1) **DoG+SIFT**: This combination initially relies on the DoG detector to detect image keypoints. For each keypoint, a set of orientation histograms computed in 4×4 pixel neighborhoods with eight bins is evaluated. We therefore obtain a 128-dimensional feature vector. The implementation of DoG+SIFT is available at David Lowe's page.[2]
2) **(Har-Lap)+(SIFT–Spin)**: Following [33], we first apply the Har-Lap approach to detect the image keypoints. A 178-dimensional feature vector is formed from the 128-dimensional SIFT descriptor and the 50-dimensional Spin descriptor. The spin image is computed from the ten-bin normalized histogram of intensity in each of the five rings centered on the region. The implementation of

[2]http://www.cs.ubc.ca/~lowe/keypoints/

This article has been accepted for inclusion in a future issue of this journal. Content is final as presented, with the exception of pagination.

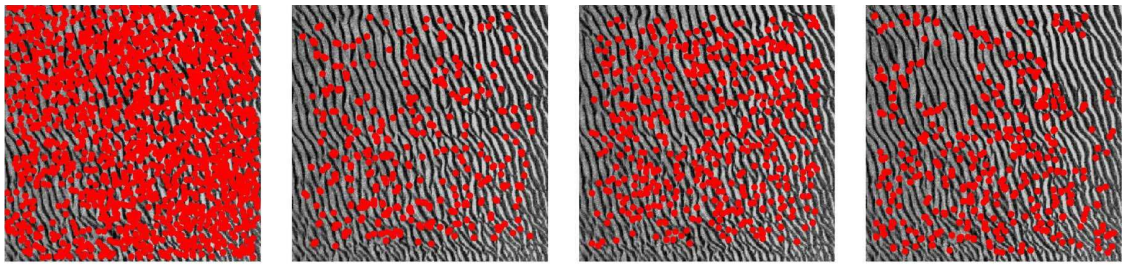

Fig. 5. Illustration of image keypoints detected in a sample of maerly and gravely sand using the different approaches. (a) DoG detector. (b) Har-Lap detector. (c) Hes-Lap detector. (d) FH detector. The mean number of keypoints per image for each method is presented in Table I.

this combination is available from the Visual Geometry group's page.[3]

3) **(Hes-Lap)+Daisy**: Following [25], we first apply the Hes-Lap approach to detect the image keypoints. The Daisy descriptor relies on histograms of oriented Gaussian filters. Here, we consider eight orientations, i.e., $(\pi/4)i$, $i = 1, 8$ at three levels of rings, where each level has eight rings with radius $R = 15$. The resulting feature vector is made of $8 + 8 \times 3 \times 8 = 200$-dimensional, extracted from 25 locations and 8 orientations. The implementation of this descriptor was taken from E. Tola's page.[4]
4) **FH+SURF**: A 64-dimensional orientation histogram of SURF descriptor is calculated from the distribution of four bins of Harr-wavelet responses in 4×4 windows around the FH keypoints. The code of this combination is available.[5]
5) **FH+Brief**: Following [23], we first apply the FH approach to detect the image keypoints, and the Brief descriptor is computed as the binary comparison between two values of N pairs of FH keypoints. The size of this vector descriptor is $N/8$. In our implementation, the dimension of Brief descriptor is fixed to 256. The code is available.[6]

As an example of the application of these keypoint detection schemes to sonar seabed images, we report detection results for a sonar texture corresponding to maerly and gravely sand (Fig. 5). Visually, detection results significantly differ among methods. While the DoG detector leads for this texture sample to a dense and homogeneous set of keypoints, Hes-Lap and Har-Lap detectors extract fewer points, and surprisingly, no keypoints are detected for some subregions. To further illustrate these aspects, we compare detection results using Har-Lap and DoG schemes for representative samples of each seabed texture class (Fig. 6) and report the mean number of detected points detected in the samples of each class (Table I).

Overall, visual keypoints in sonar seabed images are typically detected along the boundaries of shadow regions [e.g., for the mixed sediment class, Fig. 6(f)] or high-echo zones (e.g., for the sandy mud samples). As actual corners are not particularly characteristic of sonar images, the greater sensitivity of the DoG detector seems to make it more suited to the analysis of sonar images than Hessian-based detector. As detailed in the following section, keypoint-based recognition relies on keypoint statistics. In this respect, the DoG detector results in the greatest number of detected points, typically 1.8 (2.7 and 6.65) times more than Hes-Lap (respective Har-Lap and F.H) setting. This property is expected to be beneficial for characterization and classification issues.

[3]http://www.robots.ox.ac.uk/~vgg/research/affine/index.html
[4]http://cvlab.epfl.ch/~tola/daisy.html
[5]http://www.vision.ee.ethz.ch/~surf/
[6]http://cvlab.epfl.ch/software/brief/

IV. Keypoint-Based Statistics for Sonar Texture Characterization

Keypoint-based texture recognition typically relies on a statistical description of keypoint patterns. The first category of approaches relies on directly learning keypoint classification models in the feature space defined by the visual signatures of the keypoints [19], [20], [37]. Given a set of local keypoints in a texture image, the classification then relies on a simple voting procedure over all detected keypoints. A drawback of such approach is the requirement for learning classification models from very large training databases of keypoints.

By contrast, we investigate here actual statistical texture characterization and models for visual keypoint sets. As detailed in the subsequent section, such approaches benefit from the robustness of their visual signatures in terms of invariance to photometric and geometric image transformations while providing a more compact representation of the information [39], [40]. The bag-of-keypoints (BoKs) method [39], i.e., the distribution of the occurrences of the visual words in each texture sample, is the first solution. Moreover, with a view to jointly characterize the visual signatures of the keypoints along with their spatial distribution, we consider spatial descriptive statistics [40] and models [41] of spatial keypoint patterns. As shown in Fig. 7, for similar relative occurrences of visual signatures, different spatial patterns revealing differences in visual content of the textures may be observed.

A. BoKs

BoKs were inspired by bag-of-words characteristics widely used for text characterization and retrieval [39]. Given a set of keypoints, the BoK method relies on the construction of a codebook of the visual signatures of the keypoints using a k-means-like method. A discrete value is then assigned for

This article has been accepted for inclusion in a future issue of this journal. Content is final as presented, with the exception of pagination.

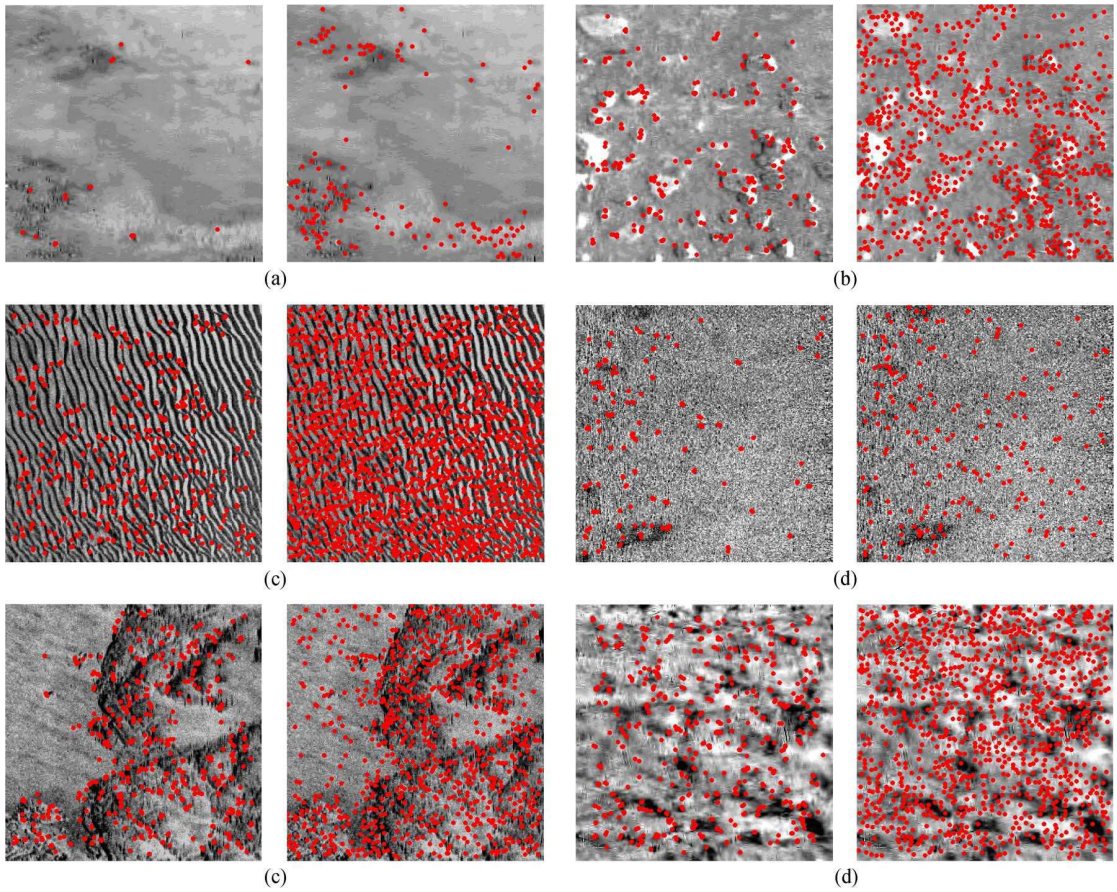

Fig. 6. Example of different spatial distributions of keypoint sets in sonar texture samples of the different seabed classes using the (left) Har-Lap detector and (right) DoG detector. (a) Mud: (Har-Lap) 19 points; (DoG) 190 points. (b) Sandy mud: (Har-Lap) 309 points; (DoG) 921 points. (c) M-G sand: (Har-Lap) 529 points; (DoG) 2287 points. (d) Clearly sand: (Har-Lap) 160 points; (DoG) 269 points. (e) Rock: (Har-Lap) 527 points; (DoG) 1002 points. (f) Mixed sediment: (Har-Lap) 569 points; (DoG) 1286 points.

TABLE I
MEAN NUMBER OF KEYPOINTS DETECTED FROM THE CONSIDERED SONAR TEXTURE DATABASE

	DoG	FH	Har-Lap	Hes-Lap
Mud	**334.85**	35.125	20.925	182.325
Sandy mud	**670.5**	166.65	230.95	534.65
M-G sand	**1777.275**	297.975	476.425	400.3
Clearly sand	**377.525**	143.825	205.55	368.5
Rock	**1070.7**	307.65	573.75	775.65
Mixed Sediment	**1350.175**	353.525	554.85	834.525
Overall	**930**	217.45	344	516

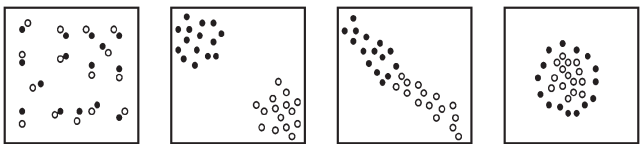

Fig. 7. Examples of different spatial distributions of marked point patterns.

each keypoint group, and the image is characterized by the occurrence statistics of each keypoint category (often referred to as visual words). Compared to approaches directly learning classification models in the feature space of the keypoint descriptors, each texture image is associated here with a feature vector such that the size of the training database is equal to the number of training images. However, BoK also ignores the spatial organization of the visual keypoints, as shown in Fig. 7.

B. Spatial Keypoint Statistics

With a view to jointly characterize the visual signatures of the keypoints along with their spatial distribution, we propose descriptors formed by spatial statistics of keypoint patterns [40]. Our approach consists in regarding the set of visual keypoint attached to a given sonar texture sample as the realization of a spatial point process.

A *spatial point process* $\mathbb{S}$ is defined as a locally finite random subset of a given bounded region $B \subset \mathbb{R}^2$. A realization of such a process is a spatial point pattern $s = \{s_1, \ldots, s_n\}$ of n points contained in B. Considering a realization of the point process, the moments of random variable are relevant descriptive statistics. In the general case, the pth-order moment of $\mathbb{S}$ is defined as

$$\mu^{(p)}(B_1 \times \ldots \times B_p) = E\left\{\mathbb{N}(B_1) \ldots \mathbb{N}(B_p)\right\} \qquad (1)$$

where $E\{.\}$ denotes the expectation and $\mathbb{N}(B_i)$ is the number of random points contained in a given Borel set B_i. The first-order moment is evaluated with $p = 1$

$$\mu(B) = E \sum_{s \in \mathbb{S}} \mathbb{I}_B(s) = \int_B \rho(s) ds \qquad (2)$$

This article has been accepted for inclusion in a future issue of this journal. Content is final as presented, with the exception of pagination.

where $\mathbb{I}_B(s)$ is an indicator function that takes the value of 1 when s falls in region B and $\rho(s)ds$ is the probability that one point falls in an infinitely small area ds of the neighborhood of point s. The normalized first-order moment $\lambda = \mu(B)/|B|$ is the mean density of expected points per surface unit, and $|B|$ is the surface of region B. This quantity fully characterizes Poisson point processes. For a homogeneous process, this density is spatially constant. For a Poisson process, the individual points of a realization are fully independent.

Beyond the first-order moment, with a view to encode spatial dependences, the covariance structure of the count variable, i.e., the descriptive statistics of the pairs of points of the finite random set, can be characterized by the second-order moment $\mu^{(2)}$ of $\mathbb{S}$ given by

$$\mu^{(2)}(B_1 \times B_2) = E \sum_{s_1 \in \mathbb{S}} \sum_{s_2 \in \mathbb{S}} \mathbb{I}_{B_1}(s_1)\mathbb{I}_{B_2}(s_2) \tag{3}$$

$$= \int_{B_1 \times B_2} \rho^{(2)}(s_1, s_2) ds_1 ds_2 \tag{4}$$

where the second-order density $\rho^{(2)}(s_1, s_2)$ is interpreted as the density per surface unit of the pair of points s_1 and s_2 in infinitely small areas ds_1 and ds_2. For a stationary and isotropic point process, this density function $\rho^{(2)}(s_1, s_2)$ states the correlation of pairs of points and only depends on distance $\|s_1 - s_2\|$ [42]. In the theory of spatial point processes [42]–[44], the second-order measure $\mu^{(2)}$ is frequently replaced by the factorial moment measure $\alpha^{(2)}$ as

$$\alpha^{(2)}(B_1 \times B_2) = E \sum_{s_1 \in \mathbb{S}} \sum_{\substack{s_2 \in \mathbb{S} \\ (s_2 \neq s_1)}} \mathbb{I}_{B_1}(s_1)\mathbb{I}_{B_2}(s_2) \tag{5}$$

where the relation between the second-order measure $\mu^{(2)}$ and the factorial moment measure $\alpha^{(2)}$ is given by

$$\alpha^{(2)}(B_1 \times B_2) = \mu^{(2)}(B_1 \times B_2) - \mu(B_1 \cap B_2). \tag{6}$$

In our application of spatial point process to image keypoint sets, each point of the realization is associated with a visual signature. Such spatial patterns can be regarded as realizations of a *marked point process*. A *marked point process*Ψ is defined as a spatial point process for which a mark m_i is associated to each point s_i in B. Following the BoK setting, we resort here to discrete marks and encode the signature associated with a given keypoint as a keypoint category. Such point processes associated with discrete marks can be referred to as multivariate point process [42], [44].

Similar to previous discussion, second-order moments [in (4)] can be derived for multivariate point patterns. Considering circular study region $D(.,r)$ with radius r [Fig. 5(f)], the second-order spatial cooccurrence statistics (SCS) of Ψ are characterized by the factorial moment measure as follows:

$$\alpha_{i,j}^{(2)}(r) = E\left\{ \sum_h \sum_{l \neq h} \delta_i(m_h)\delta_j(m_l)\mathbb{I}\left(\|s_h - s_l\| \leq r\right) \right\} \tag{7}$$

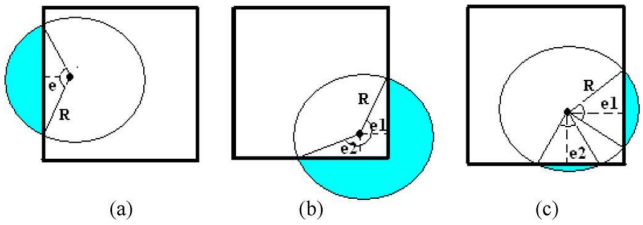

Fig. 8. Intersection cases of circular study window with the boundary of the image are presented. A very large neighborhood compared with the size of the image is not necessary to analyze the spatial texture pattern, i.e., we do not consider radius values greater than the width and the height of the image. Therefore, all cases of three-edge or four-edge effects and some particular cases of two-edge effect are not addressed. Considering the points located near the image's boundary with conditions of radius r in Table II, we obtain a total of 13 configurations of edge effect. The outside region is colored in green.

TABLE II
EXPLICIT FORMULAS OF ACTUAL CIRCUMFERENCE $b = 2\pi r - \tilde{b}$ OF THE CIRCULAR STUDY

Condition of radius	Outside area of the circular study
no-edge $r \leq e_1, e_2, e_3, e_4$	$\tilde{b} = 0$
one-edge $\begin{cases} r > e_1 \\ r \leq e_2, e_3, e_4 \end{cases}$	Fig. 8(a) $\tilde{b} = 2\arccos(\frac{e_1}{r})r$
two-edge1 $\begin{cases} e_1, e_2 < r \\ e_3, e_4 \geq r \\ r^2 > e_1^2 + e_2^2 \end{cases}$	Fig. 8(b) $\tilde{b} = \left(\frac{\pi}{2} + \arccos(\frac{e_1}{r}) + \arccos(\frac{e_2}{r})\right) r$
two-edge2 $\begin{cases} e_1, e_2 < r \\ e_3, e_4 \geq r \\ r^2 \leq e_1^2 + e_2^2 \end{cases}$	Fig. 8(c) $\tilde{b} = \left(\arccos(\frac{e_1}{r}) + \arccos(\frac{e_2}{r})\right) r$

where $\delta_i(m_h)$ is equal to one if the mark m_h of point s_h is i and zero otherwise. For statistical interpretation of second-order moment $\mu^{(2)}$ [42], Ripley's K function that is usually used to analyze the mean number of points of type j located in a study region of radius r centered at the points of type i (which itself is excluded) is measured as

$$K_{ij}(r) = \frac{1}{\lambda_i \lambda_j} \alpha_{ij}^{(2)}(r). \tag{8}$$

1) ***Correction of edge effects***: In practice, the computation of the aforementioned second-order descriptive statistics takes into account the edge effects. Several corrections for edge effects for points located near the boundary of the image have been proposed in the literature [45]. In Fig. 8, we present the visualization of one-edge effect [Fig. 8(a)] and two-edge effects [Fig. 8(b) and (c)] which are analyzed in this paper. Let us denote with e_1, e_2, e_3, e_4 the distances between a given point and the four sides of an image. In Table II, we present the explicit formulas of the actual circumference of the study circle for the intersection cases with the boundary of image.
2) ***Feature dimension reduction***: The aforementioned descriptive statistics refer to the mean occurrence of a keypoint of a given category in a ball of radius r centered at a keypoint of the pattern associated with another keypoint category. The feature vector size is $N_r k^2$-dimensional, where N_r is the number of balls of radius r and k is the number of keypoint categories. In practice, such

This article has been accepted for inclusion in a future issue of this journal. Content is final as presented, with the exception of pagination.

high-dimensional feature may affect recognition performance, where BoK [39] leads to a k-dimensional feature space. The spatial statistics combine cooccurrence statistics, i.e., occurrence statistics of pairs of keypoint categories in an image, and both spatial dependences through varying ball radii. A dimensional reduction procedure of second-order statistics was introduced in [40] from the determination of categories of keypoint pairs. The codebook of keypoint pairs, denoted by $u = M(s_h, s_l)$, is issued from an adapted clustering technique applied for each set of two categorized keypoints s_h and s_l. The second-order SCS in (7) are calculated as

$$\alpha_u^{(2)}(r) = E\left\{\sum_h \sum_{l\neq h} \delta_u\left(M(s_h, s_l)\right) \mathbb{I}\left(\|s_h - s_l\| \leq r\right)\right\}. \tag{9}$$

C. LGCM

The proposed second-order spatial statistics are the sufficient statistics describing the log-Gaussian Cox model (LGCM). Beyond their theoretical interest, parametric forms of these point process models provide a more compact representation of the spatial keypoint patterns.

A Cox process X with random intensity function Z is a point process such that $X|Z$ is a Poisson process with intensity function Z [42], [46]. For a *univariate log-Gaussian Cox process*X on a locally finite subset $S \subset \mathbb{R}^2$, the random intensity function is given by $Z = \exp(Y)$, where Y is a Gaussian field on S characterized by its mean $\mu = EY(s)$ and covariance functions $c(r) = \mathrm{Cov}(Y(s_1), Y(s_2))$, where $r = \|s_1 - s_2\|$ is defined and finite for all bounded $B \subset S$. The mean and covariance structure of Gaussian field Y relate to the first- and second-order moments of the point process [46]. More precisely, the following relations hold for intensity function ρ and pair correlation function g (see the Appendix):

$$\begin{cases} \rho(s) = \lambda = \exp(\mu + \sigma^2/2) \\ \rho^{(2)}(s_1, s_2)/\left(\rho(s_1)\rho(s_2)\right) = g(r) = \exp\left(c(r)\right) \end{cases} \tag{10}$$

where $\sigma^2 = \mathrm{Var}(Y(s))$ is the variance of the Gaussian process.

The extension to a *multivariate log-Gaussian Cox process* is derived as follows. Cox processes $\{X_i\}$ are conditionally independent w.r.t. a multivariate intensity field $Z = \{Z_i\}$, and $X_i|Z_i$ is a Poisson process with intensity measure $\{Z_i\}$. Z relates to a multivariate Gaussian field Y as $Z_i = \exp(Y_i)$. The multivariate Gaussian random field is characterized by its mean $\mu_i(s)$ and covariance functions $c_{ij}(r) = \mathrm{Cov}(Y_i(s_1), Y_j(s_2))$. Moreover, the intensity and pair correlation function become

$$\begin{cases} \lambda_i = \exp\left(\mu_i + \sigma_i^2/2\right) \\ g_{ij}(r) = \exp\left(c_{ij}(r)\right). \end{cases} \tag{11}$$

Fitting a stationary parametric log-Gaussian Cox process comes to the estimation of the mean and covariance parameters of the associated Gaussian field. Following [42] and [46], the proposed estimation procedure relies on the relation between the pair correlation function g_{ij} and the K function of Gaussian processes as

$$K_{ij}(R) = 2\pi \int_0^R r g_{ij}(r) dr \tag{12}$$

where R is a predefined value of the radius. Combining (8) and (12), the pair correlation function can be estimated as

$$g_{ij}(r) = \frac{1}{2\pi r \lambda_i \lambda_j} \sum_h \sum_{l\neq h} \delta_i(m_h)\delta_j(m_l)\xi\left(\|s_h - s_l\|, r\right) b_{s_h} \tag{13}$$

where $\xi(.)$ is a kernel (here, a Gaussian kernel is considered), λ_i is the intensity for class i estimated from (2), and b_{s_h} is the proportion of the circumference of the study circle lying within the image. Considering the edge effect correction for the computation of the descriptive statistics as detailed in the previous section, g_{ij} is not symmetric in i and j. The nonparametric estimation of the covariance function is then defined as

$$\begin{cases} c_{ii}(r) = \log\left(g_{ii}(r)\right) \\ c_{ij}(r) = \log\left(\frac{\lambda_i g_{ij}(r) + \lambda_j g_{ji}(r)}{\lambda_i + \lambda_j}\right). \end{cases} \tag{14}$$

To resort to a compact probabilistic model for the representations of visual textures, we investigate the parametric forms of the covariance function c. Given a chosen parameterization $\mathbb{L}(\beta, r)$ in Table III, the model parameters are estimated from the minimization of the following criterion:

$$\int_0^R \left\{\sigma_{ij}^2 \mathbb{L}(\beta_{ij}, r) - c_{ij}(r)\right\}^2 dr. \tag{15}$$

A gradient-based optimization procedure is applied to solve this minimization. The proposed probabilistic keypoint-based texture model is eventually given by intensity parameters λ_i, variances σ_{ij}, and scale parameters β_{ij}. The feature vector size is reduced from $k(k+2)$ to $3k^*$, where k and k^* are the number of categories of keypoints or pairs of keypoints.

TABLE III
COVARIANCE FUNCTIONS OF $\mathbb{L}(\beta, r)$

Exponential	Cardinal sine	Hyperbolic
$\exp(-(r/\beta)^\alpha)$	$\sin(r/\beta)/(r/\beta)$	$(1 + r/\beta)^{-1}$

1) **Feature dimension reduction**: The log-Gaussian Cox covariance model estimation gives a feature vector of dimensionality $k(k+2)$. The same procedure of complexity reduction as SCS is applied, i.e., the nonparametric estimation of the covariance function is calculated for the pairs of keypoint categories as

$$c_u(r) = \log\left(\frac{1}{2\pi r \lambda_u} \sum_h \sum_{l\neq h} \delta_u\left(M(s_h, s_l)\right) \times \xi\left(\|s_h - s_l\|, r\right) b_{s_h}\right) \tag{16}$$

and the estimation of intensity parameter λ_u, variances σ_u, and scale parameters β_u for each category of keypoint pairs follows as that previously from minimization (15).

This article has been accepted for inclusion in a future issue of this journal. Content is final as presented, with the exception of pagination.

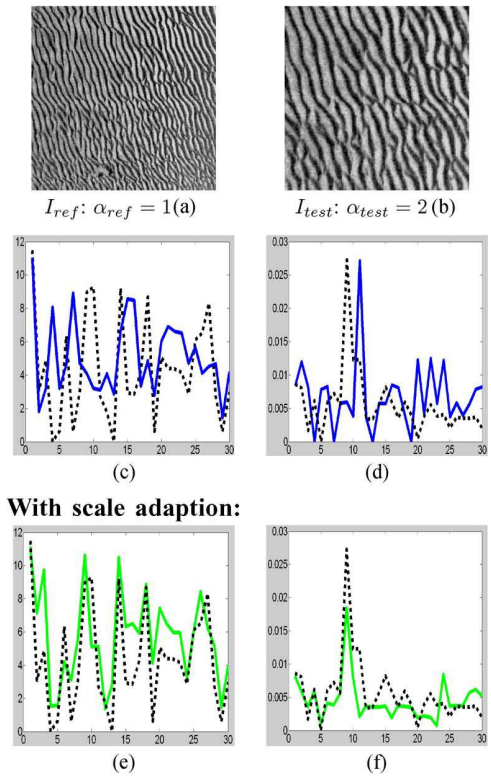

Fig. 9. Scaling effect on the estimation of the parameters of the LGCM of visual keypoint sets. (a) Reference image I_{ref} and (b) test image I_{test} at two scale factors. The dotted lines are the values of (c) and (d) variances σ_u and (e) and (f) scale parameters β_u of the reference image I_{ref} in all plots. The results of parameter estimation without (or with) scale adaption of the test image I_{test} are, respectively, showed on the second (or third) lines. These experiments were carried out with feature dimensionality reduction.

D. Invariance Properties

For the proposed approach based on the statistics of visual keypoint sets, invariance issues should be further analyzed. In all cases, invariance to contrast change is fully inherited from the definition of the keypoints and their visual signatures.

This is also the case for the invariance to geometric distortions of the BoK representation. For spatial statistics and associated models, image scaling clearly affects the second-order moments of the spatial patterns, where the radius value of the circular study region can be viewed as a scale-space parameter. Assuming that the detection and characterization of visual keypoints are scale invariant, scale adaption can be addressed. It should be stressed that this assumption is linked to the robustness of keypoint and characterization which is widely acknowledged in computer vision applications. Scale adaption proceeds here as follows. A scale factor is estimated from the rate of average point densities per surface unit compared to this rate for a reference image (corresponding to the reference (typically one) scale factor). The actual radius values R_i of the proposed estimation scheme were chosen depending on its scale factor. Fig. 9 shows the stability of the proposed scale-adapted features for different image scalings in the case of the log-Gaussian model.

V. Experimental Evaluation

Given the textural features defined in the previous section, an application to sonar texture classification is addressed, i.e., an unknown texture sample is assigned to one of a set of known texture classes using a discriminative classifier. The evaluation of the proposed descriptor involves the computation of classification performances for models learned from N_t training texture samples per class. Training images are randomly selected among the 40 samples per class. The remaining $40 - N_t$ images per class are used as test images. The random selection of training samples is repeated 50 times to evaluate the mean and the standard deviation of the correct classification rate. The reported experiments comprise both an evaluation of different parameter settings, particularly in terms of considered type of keypoint and discriminative classifiers. Moreover, a comparison to state-of-the-art techniques is also carried out. The later involves both standard sonar texture descriptors based on cooccurrence statistics and Gabor features [17], [47] as well as state-of-the-art techniques for invariant visual texture recognition [21], [38].

A. Discriminative Classifiers

These experiments were carried out using different discriminative classifiers. We selected the K nearest-neighbor (k-NN) classifier for its nonparametric nature and its simplicity, support vector machine (SVM) [48], and random forest (RF) [49], which are among the most accurate classification schemes [50].

The following parameter settings were considered.

1) The nonparametric k-NN classifier was implemented with a varied k parameter depending on the number of training samples N_t

$$\begin{cases} k = N_t & \text{if } N_t \leq 5 \\ k = 5 & \text{if } N_t > 5. \end{cases} \tag{17}$$

2) Regarding SVM classifiers [48], a one-versus-all strategy is exploited to train a multiclass SVM, and a Gaussian kernel is chosen

$$G(H, K) = \exp\left(-\frac{d(H, K)}{2\sigma^2}\right) \tag{18}$$

where H and K are the feature vectors of the texture sample and σ is the standard deviation of the Gaussian distribution.

3) The RF classifier relies on the construction of an ensemble of classification trees using some form of randomization. A texture sample is classified by sending it down every tree and by aggregating the reached leaf distributions. The RF classifier uses a voting rule to assign a class to an unknown texture sample [49]. We used the RF with 500 trees (default value), and 100 features were randomly selected for the optimization of each split of the tree $(\text{mtry} = 100)$.

SVM and k-NN classifiers require the definition of a distance in the considered feature space. We investigate here different distances accounting for the characteristics of the considered

This article has been accepted for inclusion in a future issue of this journal. Content is final as presented, with the exception of pagination.

TABLE IV
RECOGNITION PERFORMANCE OF THE LGCM TEXTURE FEATURE COMBINED WITH DIFFERENT CLASSIFIERS (K-NN, SVM, AND RF) AND SIMILARITY MEASURES (EUCLIDEAN, χ^2, AND JEFFREY DIVERGENCE)

N_t	k-NN			SVM			RF
	Euclidean	χ^2	Jeffrey	Euclidean	χ^2	Jeffrey	
5 samples	87.45%	88.17%	89.56%	88.11%	88.95%	91.34%	91.34%
10 samples	93.12%	94.83%	95.37%	94.18%	95.07%	96.95%	97.14%

TABLE V
RECOGNITION PERFORMANCE OF THE LGCM TEXTURE FEATURE USING DIFFERENT DETECTOR/DESCRIPTOR TYPES, NAMELY, DOG+SIFT, FH+SURF, (HAR-LAP)+(SIFT–SPIN), (HES-LAP)+DAISY, AND FH+BRIEF. AN RF CLASSIFIER WAS TRAINED IN EACH CASE

N_t	DoG+Sift	FH+Surf	(Har-Lap)+(Sift-Spin)	(Hes-Lap)+Daisy	FH+Brief
1 sample	73.85±1.75	71.15±1.91	72.67±1.95	73.67±1.52	**74.85±1.65**
3 samples	**82.95±1.13**	79.95±1.41	82.31±1.55	82.35±1.23	81.62±1.28
5 samples	**91.34±0.72**	90.17±1.37	91.05±1.31	91.24±0.81	90.84±1.13
8 samples	**93.87±0.61**	92.08±0.82	92.12±0.95	92.75±0.73	92.07±1.11
10 samples	**97.14±0.37**	95.67±0.51	96.12±0.62	96.63±0.47	95.92±0.59

descriptive statistics and models. Namely, three different dissimilarity measures are evaluated:

1) the Euclidean distance: $d_E(H,K) = \sum_i |h_i - k_i|^2$;
2) the χ^2 distance: $d_{\chi^2}(H,K) = \sum_i ((h_i - m_i)^2/m_i)$;
3) the Jeffrey divergence

$$d_J(H,K) = \sum_i \left(h_i \log \frac{h_i}{m_i} + k_i \log \frac{k_i}{m_i} \right) \qquad (19)$$

where $m_i = (h_i + k_i)/2$.

B. Parameter Setting of the Evaluated Texture Descriptors

Overall, we evaluated eight texture feature sets, namely, cooccurrence matrix [47] and Gabor [17] features which are classically used for sonar texture classification and state-of-the-art techniques for visual texture recognition such as Xu's method [21], BoK [39], Zhang's method [38], and Ling's method [51]. The most discriminative features from the different settings of each method were reported. The following parameter settings were considered.

1) **Gabor features** [17]: Gabor features are extracted as the statistics of the response to Gabor scale-space filters. The Gabor texture features were considered in this paper at orientations $\theta = \{0, \pm(\pi/2), \pi\}$ and frequencies $f = \{0, 4, 8\}$.
2) **Cooccurrence features** [47]: Cooccurrence matrix evaluates the occurrences of pairs of intensity values for neighboring pixels. Considered neighborhoods were parameterized by a distance $d = \{1, 2, 4\}$ of an orientation $\theta = \{0, \pm(\pi/4), \pm(\pi/2), \pm(3\pi/4), \pi\}$.
3) **BoK** [39]: The BoK method exploits relative occurrence statistics of the different visual words based on the SIFT descriptor. The number of classes of visual keypoints was set to $k = \{35, 50, 60\}$. We used the same k-means-like technique as that for spatial statistics.
4) **Ling's method** [51]: Ling's feature is a histogram of cooccurrence statistics of pair visual keypoint categories. We extend Ling' feature to a set of logarithmically increased neighborhood sizes $N_r = 128\log(x)$, where x varies between 1 and exp(1) according to a 0.05 linear step.

TABLE VI
RECOGNITION PERFORMANCE OF THE LGCM TEXTURE FEATURE WITH AND WITHOUT SCALE ADAPTION AND DIMENSION REDUCTION SCHEMES. HERE, A COMPLETE MODEL IS OBTAINED WHEN TWO OF THE AFOREMENTIONED SCHEMES ARE APPLIED

N_t	without scaling effect	without dimensional reduction	complete model
1 sample	72.63±1.75	**74.41±1.62**	73.85±1.75
3 samples	82.27±1.53	**83.11±1.25**	82.95±1.13
5 samples	89.85±1.11	91.05±0.95	**91.34±0.72**
8 samples	91.72±0.85	92.37±0.62	**93.87±0.61**
10samples	95.15±0.55	96.28±0.45	**97.14±0.37**

TABLE VII
RECOGNITION PERFORMANCE OF THE LGCM TEXTURE FEATURE FOR DIFFERENT COVARIANCE MODELS

N_t	Gaussian	Cardinal sine	Hyperbolic
1 sample	**73.85±1.75**	73.60±1.79	73.42±1.91
3 samples	**82.95±1.13**	82.47±1.21	82.15±1.23
5 samples	**91.34±0.72**	90.84±0.67	90.52±0.81
8 sample	**93.87±0.61**	93.11±0.65	92.57±0.75
10samples	**97.14±0.37**	96.81±0.48	96.12±0.58

5) **Xu's method** [21]: Xu's approach relies on a multifractal description of textures invariant to viewpoint changes, nonrigid deformations, and local affine contrast change. We tested different parameter settings for Xu's method: density level $ind = \{1, 8\}$, dimension of MFS $f = \{16, 64\}$, and iteration level $ite = \{8, 10\}$.
6) **Zhang's method** [38]: Zhang *et al.* proposed a technique of texture classification using SVM classifier and earth move distance for the combination of two keypoint detectors (Har+Lap) and two local descriptors (SIFT+Spin) with the same number of clusters of visual keypoints $k = \{35, 50, 60\}$.
7) **SCS** [40]: The same parameter setting as the Ling's method was used for the SCS approach. However, SCS involves a correction of edge effects and scale adaption as well as a feature dimension reduction with $k^* = 30$ categories of visual keypoint pairs.
8) **LGCM** [41]: LGCM was implemented with $k = \{35, 50, 60\}$ and $k^* = 30$, which are the categories of visual keypoints and visual keypoint pairs.

This article has been accepted for inclusion in a future issue of this journal. Content is final as presented, with the exception of pagination.

TABLE VIII
CLASSIFICATION RATES AND STANDARD DEVIATIONS OF THE EVALUATED TEXTURE RECOGNITION METHOD FOR THE CONSIDERED SONAR TEXTURE DATABASE, NAMELY, GABOR FEATURE, COOCCURRENCE FEATURE, BOKS, KEYPOINT COOCCURRENCE STATISTICS [51], MULTIFRACTAL FEATURE [21], KEYPOINT CLASSIFIER [38], SCS, AND LGCM

N_t	1	3	5	8	10
Gabor filter[17]	51.71±3.24	55.34±2.84	59.27±1.97	62.53±1.72	69.81±1.48
Cooccurrence matrix[47]	62.13±3.17	69.72±2.44	72.15±1.53	76.22±1.41	81.21±1.27
BoK[39]	67.15±2.55	76.27±2.08	85.42±1.56	90.35±1.42	92.03±1.21
Ling[51]	66.83±2.33	78.12±2.21	85.27±1.83	90.68±1.35	91.92±1.24
Xu[21]	67.54±2.49	79.33±2.11.	87.12±1.91	90.14±1.63	91.85±1.12
Zhang[38]	73.33±2.17	82.62±1.83	90.67±1.15	93.43±0.91	94.25±0.73
SCS[40]	**74.57±1.69**	**83.23±1.19**	91.17±1.08	93.25±0.58	96.67±0.35
LGCM	73.85±1.75	82.95±1.13	**91.34±0.72**	**93.87±0.61**	**97.14±0.37**

C. Performance Result

We first evaluated the importance of the parameter setting (keypoint types, dimension reduction, scaling invariance, classifier type, and associated parameterization) for the proposed spatial keypoint statistics and models. We detail here these experiments for the descriptors issued from the LGCMs. Similarly, results were obtained for the SCS. Considering the performances of the different classifiers and similarity measures in Table IV, Jeffrey divergence improves the classification performance with an approximate gain greater than 1.5% (3%) compared to χ^2 distance (respectively, Euclidean distance) when five (or ten) training images were used. SVM and RF classifiers lead to similar recognition performances for our sonar data set, but the gain compared to k-NN classifier was greater than 2%. We further evaluated the relevance of the different types of visual keypoints (Table V). It should be pointed out that recognition performances appeared relevant whatever the considered keypoint type is. DoG+SIFT descriptors however outperform the other keypoint types, with a gain slightly greater than 1% over (Har-Lap)+(SIFT–Spin) and (Hes-Lap)+Daisy and 2% over FH+SURF and FH+Brief. These results might be explained by the greater number of keypoints using DoG+SIFT schemes compared to the other combinations such that a finer characterization of the textures can be reached as well as a more robust estimation of the considered statistics.

Selecting DoG+SIFT descriptors as the reference keypoint setting, we emphasize the relevance of the proposed scale adaption and dimension reduction schemes in Table VI. While scale adaption leads to a gain of about 2%, dimension reduction also improves the correct classification rate by about 1.5% when 5–10 training images are available. The choice of the covariance model also affects recognition performance (Table VII). The best performances were obtained with a Gaussian covariance model with 97.14 $\pm$ 0.37 versus 96.81 $\pm$ 0.48 for a cardinal sine model and 96.12 $\pm$ 0.58 for a hyperbolic model when ten training images are used.

The comparison of the different categories of texture descriptors is reported in Table VIII. These results clearly stressed the relevance of the proposed spatial keypoint statistics for sonar texture recognition. Compared to classical cooccurrence and Gabor texture features, the gains were, respectively, greater than 16% and 27%. These improvements were direct benefits from the robustness and invariance of visual keypoints for the analysis of sonar textures which depicted local contrast variations as well as geometric distortions. It should be pointed out that, even

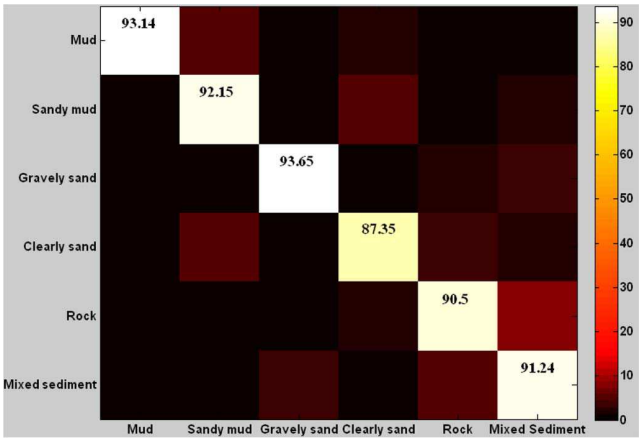

Fig. 10. Confusion matrix of sonar texture classification using the LGCM texture feature. These experiments were carried out using five training images per class.

with the increase of the number of training samples available for each class, cooccurrence and Gabor features would not lead to such high recognition performances greater than 95%. In this respect, all methods exploiting visual keypoints [38], [39], [51] or invariant local features [21] reached correct classification rates greater than 90% when five training images or more are available.

This quantitative evaluation also demonstrated the meaningfulness of the considered spatial keypoint statistics. They outperformed by, respectively, 5% and 2% the BoK feature and the most popular local keypoint (H+L)(SIFT+Spin) method of Zhang's method. Where these two approaches only rely on the discrimination of visual keypoint signatures, spatial keypoint statistics jointly characterize the visual information conveyed by these visual keypoint signatures as well as the spatial distributions of the keypoints. As expected from the observation of keypoint distributions in sonar textures (Fig. 6), the spatial organization of keypoint sets is also a discriminative information that is used to distinguish seabed types. It might be noted that straighforward keypoint cooccurrence statistics proposed by Ling *et al.* [51] were significantly outperformed (97.14% versus 91.92% when ten training images were considered). The combination of scale adaption, dimension reduction, and edge effect corrections explained these improvements.

The proposed spatial statistics, namely, SCS and estimated covariance models, led to very similar recognition

This article has been accepted for inclusion in a future issue of this journal. Content is final as presented, with the exception of pagination.

performances, although covariance models were slightly more robust, e.g., 97.14% $\pm$ 0.37 versus 96.67% $\pm$ 0.35 when ten training images were considered. Covariance models should however be preferred as they provide a more compact representation (typically, covariance models lead to $3k^*$-dimensional feature space when the dimensionality of the SCS reach $(N_r + 1)k^*$, where k^* is the size of the codebook of keypoint pairs and N_r is the number of bounded regions; here, $N_r = 20$, and $k^* = 30$) and benefit from a solid theoretical background.

We further detail the class-by-class recognition performances issued from the parametric LGCM when five training images were used (Fig. 10). The reported confusion matrix was nicely balanced over seabed classes, with the mean correct classification rate ranging from 87.35% to 93.65%. The greatest confusions retrieved between clearly sand and sandy mud (5.75%) were consistent in terms of visual similarities of the sonar images.

VI. Conclusion

This paper has addressed the development of invariant descriptors of sonar textures for seabed classification using keypoint-based approaches. We have showed that visual keypoints, developed for computer vision applications and visual texture analysis, also provide meaningful signatures of sonar images to deal with local contrast change and geometric distortions observed in the sonar observations of the seabed. In this respect, statistical descriptors and models of the covariance structure of the multivariate spatial patterns formed by keypoint sets in sonar textures were highly relevant to improve sonar texture characterization and recognition.

The analysis of keypoint detection statistics for various seabed types indicated that DoG keypoints may be more appropriate to deal with the structures observed in sonar images. Whereas visual keypoints were initially developed as corner detectors in natural images, sonar images do not intrinsically involve such corner-like structures. They are rather characterized by the presence of highly reflective areas along with shadow zones. Whereas some keypoint detectors seem too conservative to spatially cover all the structures of interest (e.g., sand ripples in Fig. 2), the detection of the DoG keypoints appears highly correlated to the geometric structures of interest in sonar images. This qualitative evaluation was confirmed by the reported results for seabed recognition. These results open the door for other applications of keypoint-based sonar imaging, including autonomous underwater vehicle navigation [52] and mine detection [53]. Future work might also pursue the development of sonar-specific local signatures.

Regarding the application to seabed recognition, we have reported a quantitative evaluation for a sonar data set involving six different types of seabed, namely, mud, sandy mud, maerly and gravelly sand, clearly sand, rock, and mixed sediment. We have demonstrated that keypoint-based sonar texture characterization can actually achieve very high recognition performances compared to classical cooccurrence and Gabor texture features, which are typically exploited in sonar imaging, while only considering a few training images to learn seabed texture models (typically, 5–10 training samples per class). This aspect is of critical importance for operational applications, in which only a limited subset of the acquired sonar data set is generally groundtruthed by an expert. We believe that this paper could provide a reference benchmarked database for future work on sonar texture analysis. In this respect, the sonar data set is made freely available to the community through a Web access.[7]

From a methodological point of view, we have shown that spatial point processes provide a mathematically sound framework to analyze the spatial organization and the visual signatures of keypoint sets in sonar images. These descriptors that are invariant to local contrast change as well as geometric distortions, especially scaling, provided significant improvements over state-of-the-art techniques. The advantages of parametric point process models were further pointed out in their ability to provide more compact representation of the sonar texture patterns. In future work, the potential of such models will be further explored. Compared to simple descriptive statistics, they can be associated with powerful statistical tools, including goodness-of-fit or hypothesis test. Such tools are of key interest for marine seabed applications to statistically evaluate the significance of the changes of seabed textures over time [54]. Other classes of statistical models may also be investigated, such as Neyman–Scott, shot-noise Cox, or Gibbs processes [42], [55], keeping in mind that we should balance model flexibility and complexity. Combining spatial keypoint process and advanced segmentation schemes is also among the key issues that should be addressed in future work.

Appendix
Intensity and Pair Correlation Function Computation

Considering a univariate log-Gaussian Cox process X on a locally finite subset $S \subset \mathbb{R}^2$, the random intensity function is given by $Z = \exp(Y)$ and covariance functions $c(r) = Cov(Y(s_1), Y(s_2))$, where Y is a Gaussian field on S and $r = \|s_1 - s_2\|$.

1) **The intensity function**

$$\begin{aligned}\rho(s) = E[Z] &= \int_B \exp(y) \frac{1}{\sqrt{2\pi\sigma^2}} \exp\left(-\frac{(y-\mu)^2}{2\sigma^2}\right) dy \\ &= \frac{1}{\sqrt{2\pi\sigma^2}} \int_B \exp\left(-\frac{y^2 - 2y(\mu+\sigma^2) + \mu^2}{2\sigma^2}\right) dy \\ &= \exp\left(-\frac{\mu^2}{2\sigma^2}\right) \exp\left(\frac{(\mu+\sigma^2)^2}{2\sigma^2}\right) A_1 \\ &= \exp(\mu + \sigma^2/2) \end{aligned} \quad (20)$$

where $A_1 = (1/\sqrt{2\pi\sigma^2}) \int_B \exp(-((y-(\mu+\sigma^2))^2/2\sigma^2))dy = 1$.

2) **The pair correlation function**:

Regarding the case of $\mu = 0$ with $\hat{r}$ as the correlation coefficient of the Gaussian field, the second-order

[7]The sonar image database is made available from the authors' Web page.

This article has been accepted for inclusion in a future issue of this journal. Content is final as presented, with the exception of pagination.

moment is given by

$$\begin{aligned}\rho^{(2)}(s_1,s_2) &= E[Z_1,Z_2] \\ &= \int\limits_{B_1\times B_2} \frac{\exp(y_1+y_2)\exp\left(-\frac{\left(y_1^2-\hat{r}y_1y_2+y_2^2\right)}{(1-\hat{r}^2)\sigma^2}\right)}{2\pi\sigma^2\sqrt{1-\hat{r}^2}}dy_1dy_2 \\ &= \int\limits_{B_1\times B_2} \frac{exp\left(-\frac{A_2}{(1-\hat{r}^2)\sigma^2}\right)}{2\pi\sigma^2\sqrt{1-\hat{r}^2}}dy_1dy_2 \qquad (21)\end{aligned}$$

where $A_2 = y_1^2-(2\hat{r}y_1y_2+2(1-\hat{r}^2)\sigma^2(y_1+y_2))+y_2^2$. Considering the identification

$$\begin{aligned}&y_1^2-\left(2\hat{r}y_1y_2+2(1-\hat{r}^2)\sigma^2(y_1+y_2)\right)+y_2^2 \\ &\quad=(y_1-\kappa)^2-2\hat{r}\left((y_1-\kappa)(y_2-\kappa)\right)+(y_2-\kappa)^2+A_3 \\ &\quad=y_1^2-(2\hat{r}y_1y_2-(2\hat{r}\kappa-2\kappa)(y_1+y_2)) \\ &\qquad+y_2^2+A_3+2\kappa^2-2\hat{r}\kappa^2. \qquad (22)\end{aligned}$$

We get

$$\begin{cases}2(1-\hat{r}^2)\sigma^2=-2(\hat{r}-1)\kappa \\ A_3+2\kappa^2-2\hat{r}\kappa^2=0\end{cases} \qquad (23)$$

$$\begin{cases}\kappa=\sigma^2(1+\hat{r}) \\ A_3=2\kappa^2(\hat{r}-1)=2\hat{r}^4(\hat{r}^2-1)(\hat{r}+1).\end{cases} \qquad (24)$$

Replacing κ and A_3 into (21), we have

$$\rho^{(2)}(s_1,s_2)=\exp\left(-\frac{A_3}{2(1-\hat{r}^2)\sigma^2}\right)=\exp\left((1+\hat{r})\sigma^2\right). \qquad (25)$$

The correlation function is given by

$$\begin{aligned}g(s_1,s_2)&=\frac{\rho^{(2)}(s_1,s_2)}{\rho^{(1)}(s_1)\rho^{(1)}(s_2)}=\frac{\exp\left((1+\hat{r})\sigma^2\right)}{\exp(\sigma^2/2)\exp(\sigma^2/2)} \\ &=\exp(\hat{r}\sigma^2)=\exp\left(c(r)\right) \qquad (26)\end{aligned}$$

where $\hat{r}\sigma^2=E[Y_1,Y_2]=c(r)$.

REFERENCES

[1] C. Brown, K. Cooper, W. Meadows, D. Limpenny, and H. Rees, "Small-scale mapping of sea-bed assemblages in the eastern English Channel using sidescan sonar and remote sampling techniques," *Estuarine, Coastal Shelf Sci.*, vol. 54, no. 2, pp. 263–278, 2002.

[2] G. Cochrane and K. Lafferty, "Use of acoustic classification of sidescan-sonar data for mapping benthic habitat in the Northern Channel Islands, California," *Continental Shelf Res.*, vol. 22, pp. 683–690, 2002.

[3] W. Dierking, "Mapping of different sea ice regimes using images from Sentinel-1 and ALOS synthetic aperture radar," *IEEE Trans. Geosci. Remote Sens.*, vol. 48, no. 3, pp. 1045–1058, Mar. 2010.

[4] X. Li, C. Li, Q. Xu, and W. Pichel, "Sea surface manifestation of along-tidal-channel underwater ridges imaged by SAR," *IEEE Trans. Geosci. Remote Sens.*, vol. 47, no. 8, pp. 2467–2477, Aug. 2009.

[5] J. Davies, J. Baxter, M. Bradley, D. Connor, J. Khan, E. Muray, W. Sanderson, C. Turnbull, and M. Vincent, *Marine Monitoring Handbook (UK Marine SACs Project)*. Peterborough, U.K.: Joint Nature Conservation Committee, 2001.

[6] S. Degraer, V. van Lancker, G. Moerkerke, G. V. Hoey, M. V. P. Jacobs, and J. P. Henriet, "Intensive evaluation of the evolution of a protected benthic habitat: HABITAT. Final report of the Federal Office for Scientific, Technical and Cultural Affairs (OSTC) e ministry of the Flemish community, environment and infrastructure," Waterways Marine Affairs Admin., Coastal Waterways, Belgium, 2002.

[7] A. Ehrhold, D. Hamon, and B. Guillaumont, "The REBENT monitoring network, a spatially integrated, acoustic approach to surveying nearshore macrobenthic habitats: Application to the Bay of Concarneau (France)," *ICES J. Mar. Sci.*, vol. 63, no. 9, pp. 1604–1615, 2006.

[8] C. Hu, F. Muller-Karger, B. Murch, D. Myhre, J. Taylor, R. Luerssen, C. Moses, C. Zhang, L. Gramer, and J. Hendee, "Building an automated integrated observing system to detect sea surface temperature anomaly events in the Florida keys," *IEEE Trans. Geosci. Remote Sens.*, vol. 47, no. 6, pp. 1607–1620, Jun. 2009.

[9] G. L. Chenadec, J.-M. Boucher, and X. Lurton, "Angular dependence of k-distributed sonar data," *IEEE Trans. Geosci. Remote Sens.*, vol. 45, no. 5, pp. 1124–1235, May 2007.

[10] I. Karoui, R. Fablet, J.-M. Boucher, and J.-M. Augustin, "Seabed segmentation using optimized statistics of sonar textures," *IEEE Trans. Geosci. Remote Sens.*, vol. 47, no. 6, pp. 1621–1631, Jun. 2009.

[11] M. Mignotte, C. Collet, P. Perez, and P. Bouthemy, "Sonar image segmentation using an unsupervised hierarchical MRF model," *IEEE Trans. Image Processing*, vol. 9, no. 7, pp. 1216–1231, Jul. 2000.

[12] J.-M. Bell, M.-J. Chantler, and T. Wittig, "Sidescan sonar: A directional filter or seabed texture?," *Proc. Inst. Elect. Eng.—Radar, Sonar Navig.*, vol. 146, no. 1, pp. 65–72, Feb. 1999.

[13] S. Reed, Y. Petillot, and J. Bell, "An automatic approach to the detection and extraction of mine features in sidescan sonar," *IEEE J. Ocean. Eng.*, vol. 28, no. 1, pp. 90–105, Jan. 2003.

[14] A. Martin, "Comparative study of information fusion methods for sonar images classification," in *Proc. Int. Conf. Inf. Fusion*, 2005, vol. 2, pp. 1420–1426.

[15] Y. Wang, Z. Liu, E. Sang, and H. Ma, "Sonar image classification based on directional wavelet and fuzzy fractal dimension," in *Proc. IEEE Conf. Ind. Electron. Appl.*, 2007, pp. 118–120.

[16] N. Sun and T. Shim, "Sonar images classification of seabed physiognomy based on the information fusion methods," in *Proc. Congr. Image Signal Process.*, 2008, pp. 813–819.

[17] T. Randen and J. H. Husøy, "Filtering for texture classification: A comparative study," *IEEE Trans. Pattern Anal. Mach. Intell.*, vol. 21, no. 4, pp. 291–310, Apr. 1999.

[18] M. Heikkilä, M. Pietikäinen, and C. Schmid, "Description of interest regions with local binary patterns," *Pattern Recognit.*, vol. 42, no. 3, pp. 425–436, Mar. 2009.

[19] T. Ojala, M. Pietikäinen, and T. Mäenpää, "Multiresolution grayscale and rotation invariant texture classification with local binary patterns," *IEEE Trans. Pattern Anal. Mach. Intell.*, vol. 24, no. 7, pp. 971–987, Jul. 2002.

[20] M. Varma and A. Zisserman, "Classifying images of materials: Achieving viewpoint and illumination independence," in *Proc. Eur. Conf. Comput. Vis.*, 2002, pp. 255–271.

[21] Y. Xu, H. Ji, and C. Fermuller, "Viewpoint invariant texture description using fractal analysis," *Int. J. Comput. Vis.*, vol. 83, no. 1, pp. 85–100, Jun. 2009.

[22] H. Bay, T. Tuytelaars, and L. Gool, "SURF: Speeded up robust features," in *Proc. Eur. Conf. Comput. Vis.*, 2006, pp. 404–417.

[23] M. Calonder, V. Lepetit, C. Strecha, and P. Fua, "Brief: Binary robust independent elementary features," in *Proc. Eur. Conf. Comput. Vis.*, 2010, vol. IV, pp. 778–792.

[24] D. Lowe, "Distinctive image features from scale-invariant keypoints," *Int. J. Comput. Vis.*, vol. 60, no. 2, pp. 91–110, Nov. 2004.

[25] E. Tola, V. Lepetit, and P. Fua, "Daisy: An efficient dense descriptor applied to wide baseline stereo," *IEEE Trans. Pattern Anal. Mach. Intell.*, vol. 32, no. 5, pp. 815–830, May 2010.

[26] K. Mikolajczyk and C. Schmid, "A performance evaluation of local descriptors," *IEEE Trans. Pattern Anal. Mach. Intell.*, vol. 27, no. 10, pp. 1615–1630, Oct. 2005.

[27] J. Liu and M. Shah, "Scene modeling using co-clustering," in *Proc. Int. Conf. Comput. Vis.*, 2007, pp. 1–7.

[28] S. Lazebnik, C. Schmid, and J. Ponce, "Beyond bags of features: Spatial pyramid matching for recognizing natural scene categories," in *Proc. Comput. Vis. Pattern Recog.*, 2006, pp. 2169–2178.

[29] R. J. Urick, *Principles of Underwater Sound*. New York: McGraw-Hill, 1983, p. 423.

[30] D. Birkett, C. Maggs, and M. Dring, Marl (Volume V). An Overview of Dynamic and Sensitivity Characteristics for Conservation Management of Marine SACs. Scottish Association for Marine Science (UK Marine SACs Project), p. 1161998.

This article has been accepted for inclusion in a future issue of this journal. Content is final as presented, with the exception of pagination.

[31] C. Harris and M. Stephens, "A combined corner and edge detector," in *Proc. Alvey Vis. Conf.*, 1988, pp. 147–151.
[32] T. Lindeberg, "Feature detection with automatic scale selection," *Int. J. Comput. Vis.*, vol. 30, no. 2, pp. 79–116, Nov. 1998.
[33] K. Mikolajczyk, T. Tuytelaars, C. Schmid, A. Zisserman, J. Matas, F. Schaffalitzky, T. Kadir, and L. Van Gool, "A comparison of affine region detectors," *Int. J. Comput. Vis.*, vol. 65, no. 1/2, pp. 43–72, Nov. 2005.
[34] J. Matas, O. Chum, M. Urban, and T. Pajdla, "Robust wide baseline stereo from maximally stable extremal regions," in *Proc. Brit. Mach. Vis. Conf.*, 2002, pp. 384–393.
[35] T. Tuytelaars and L. Van Gool, "Matching widely separated views based on affine invariant regions," *Int. J. Comput. Vis.*, vol. 59, no. 1, pp. 61–85, Aug. 2004.
[36] T. Kadir, A. Zisserman, and M. Brady, "An affine invariant salient region detector," in *Proc. Eur. Conf. Comput. Vis.*, 2004, pp. 345–457.
[37] S. Lazebnik, C. Schmid, and J. Ponce, "A sparse texture representation using local affine regions," *IEEE Trans. Pattern Anal. Mach. Intell.*, vol. 27, no. 8, pp. 1265–1278, Aug. 2005.
[38] J. Zhang, M. Marszalek, S. Lazebnik, and C. Schmid, "Local features and kernels for classification of texture and object categories: A comprehensive study," *Int. J. Comput. Vis.*, vol. 73, no. 2, pp. 213–238, Jun. 2007.
[39] G. Csurka, C. Bray, C. Dance, and L. Fan, "Visual categorization with bags of keypoints," in *Proc. Eur. Conf. Comput. Vis.*, 2004, pp. 1–22.
[40] H.-G. Nguyen, R. Fablet, and J.-M. Boucher, "Spatial statistics of visual keypoints for texture recognition," in *Proc. Eur. Conf. Comput. Vis.*, 2010, vol. IV, pp. 764–777.
[41] H.-G. Nguyen, R. Fablet, and J.-M. Boucher, "Visual textures as realizations of multivariate log-Gaussian Cox processes," in *Proc. CVPR*, 2011, pp. 2945–2952.
[42] D. Stoyan and H. Stoyan, *Fractals, Random Shapes and Point Fields*. Chichester, U.K.: Wiley, 1994.
[43] P. Diggle, *Statistical Analysis of Spatial Point Patterns*. London, U.K.: Academic, 1983.
[44] M. Schlather, "On the second-order characteristics of marked point process," *Bernoulli*, vol. 7, no. 1, pp. 99–117, Feb. 2001.
[45] F. Goreaud and R. Pélissier, "On explicit formulas of edge effect correction for Ripley's K-function," *J. Vegetation Sci.*, vol. 10, no. 3, pp. 433–438, Jun. 1999.
[46] J. Møller, A. Syversveen, and R. Waagepetersen, "Log Gaussian Cox processes," *Scand. J. Statist.*, vol. 25, no. 3, pp. 451–482, Sep. 1998.
[47] R. Haralick, "Statistical and structural approaches to textures," *Proc. IEEE*, vol. 67, no. 5, pp. 786–804, May 1979.
[48] C. Burges, "A tutorial on support vector machines for pattern recognition," *Data Mining Knowl. Discov.*, vol. 2, no. 2, pp. 121–167, Jun. 1998.
[49] F. Breiman, "Random forests," *Mach. Learn.*, vol. 45, no. 1, pp. 5–32, 2001.
[50] A. Bosch, A. Zisserman, and X. Munoz, "Image classification using random forests and ferns," in *Proc. Int. Conf. Comput. Vis.*, 2007, pp. 1–8.
[51] H. Ling and S. Soatto, "Proximity distribution kernels for geometric context in category recognition," in *Proc. Int. Conf. Comput. Vis.*, 2007, pp. 1–8.
[52] S. Botelho, P. Junior, M. Figueiredo, C. Rocha, and G. Oliveira, "Appearance-based odometry and mapping with feature descriptors for underwater robots," *J. Brazilian Comput. Soc.*, vol. 15, no. 3, pp. 47–54, 2009.
[53] T. Wang, I. Gu, and T. Tjahjadi, "Enhanced landmine detection from low resolution IR image sequences," in *Proc. Comput. Anal. Images Patterns*, 2009, vol. 5702, pp. 1236–1244.
[54] T. Nelson, S. Gillanders, J. Harper, and M. Morris, "Nearshore aquatic habitat monitoring: A seabed imaging and mapping approach," *J. Coastal Res.*, vol. 27, no. 2, pp. 348–355, 2011.
[55] F. Lafarge, G. Gimel'farb, and X. Descombes, "Geometric feature extraction by a multi-marked point process," *IEEE Trans. Pattern Anal. Mach. Intell.*, vol. 32, no. 9, pp. 1597–1609, Sep. 2010.

Huu-Giao Nguyen received the B.S. degree from the University of Science, Hochiminh City, Vietnam, in 2004 and the M.S. degree from the University of La Rochelle, La Rochelle, France, in 2008. He is currently working toward the Ph.D. degree in signal processing and communication at the Institut Telecom/Telecom Bretagne, Brest, France.

His research interests include computer vision, machine learning, and statistical methods applied to signal processing.

Ronan Fablet graduated from the Ecole Nationale Supérieure de l'Aéronautique et de l'Espace (SUPAERO), Toulouse, France, in 1997 and received the Ph.D. degree in signal processing and telecommunications from the University of Rennes, Rennes, France, in 2001.

In 2002, he was an INRIA Postdoctoral Fellow at Brown University, Providence, RI. From 2003 to 2007, he held a full-time research position at IFREMER Brest in the field of biological oceanography. Since 2008, he has been an Associate Professor with the Signal and Communications Department, Telecom Bretagne, Brest, France. In 2011, he is a Visiting Researcher at IMARPE, Peru (Peruvian Sea Research Institute). His main interests include statistical methods for signal processing and computer vision, and applications to ocean remote sensing.

Axel Ehrhold received the Ph.D. degree in marine geoscience from the University of Caen, Caen, France, in 1999.

He is a Marine Geologist specializing in recent sedimentary processes. From 1998 to 2005, he was with the Sedimentology Division, Naval Hydrographic and Oceanographic Service. Since 2005, he has been working with biologists on marine benthic habitat mapping projects with the French Research Institute for Exploration of the Sea (IFREMER), Plouzané, France. His research interests are mapping the offshore sea-bed geology and quaternary geology using side-scan sonar, multibeam echosounder, shallow seismic, video acquisition, and grab sampler in coastal environment and investigating the relationship between seabed substrate and associated biological communities.

Jean-Marc Boucher was born in 1952. He received the Engineering degree in telecommunications from the Ecole Nationale Supérieure des Telecommunications, Paris, France, in 1975 and the "Habilitation à Diriger des Recherches" degree from the University of Rennes 1, Rennes, France, in 1995.

He is currently a Professor with the Telecom Bretagne, Brest, France, where he is also the Deputy Dean and Deputy Head of the UMR CNRS 3192 lab-STICC research unit. His current research is related to statistical signal analysis, including estimation theory, Markov models, spatial point processes, wavelets, and multiscale image analysis. These methods are applied to radar and sonar images, seismic signals, and electrocardiographic signals. He has published about 150 papers in these areas in national and international journals and conferences.

Weakly Supervised Classification of Objects in Images Using Soft Random Forests

Riwal Lefort[1,2], Ronan Fablet[2], and Jean-Marc Boucher[2]

[1] Ifremer/STH, Technopole Brest Iroise, 29280 Plouzane
[2] Telecom-Bretagne/LabSticc, Technopole Brest Iroise, 29280 Plouzane
{riwal.lefort,ronan.fablet,jm.boucher}@telecom-bretagne.eu

Abstract. The development of robust classification model is among the important issues in computer vision. This paper deals with weakly supervised learning that generalizes the supervised and semi-supervised learning. In weakly supervised learning training data are given as the priors of each class for each sample. We first propose a weakly supervised strategy for learning soft decision trees. Besides, the introduction of class priors for training samples instead of hard class labels makes natural the formulation of an iterative learning procedure. We report experiments for UCI object recognition datasets. These experiments show that recognition performance close to the supervised learning can be expected using the propose framework. Besides, an application to semi-supervised learning, which can be regarded as a particular case of weakly supervised learning, further demonstrates the pertinence of the contribution. We further discuss the relevance of weakly supervised learning for computer vision applications.

1 Introduction

The paper focuses on weakly supervised learning that includes both the supervised and semi-supervised learning. It considers probability vectors that indicate the prior of each class for each sample of the training set. The same notations are used throughout the paper. Let $\{x_n, \pi_n\}_n$ be the training dataset, where x_n is the feature vector for sample n and $\pi_n = \{\pi_{ni}\}_i$ is the prior vector for sample n, i indexing the classes. π_{ni} gives the likelihood for the example x_n to belong to class i. A supervised case corresponds to priors π_{ni} set to 0 or 1 whether or not sample n belongs to class i. The semi-supervised learning is also a specific case where training priors π_{ni} are given as 0 or 1 for the subset of the fully labelled training samples and as uniform priors for the remaining unlabelled samples.

Weakly supervised learning covers several cases of interest. Especially, in image and video indexing issue, object recognition dataset may involve training images labelled with the presence or the absence of each object category [1] [2] [3] [4] [5] [6]. Again such presence/absence dataset can be regarded as specific cases of training priors. As an other example, one can imagine an annotation by experts with some uncertainty measure [7]. This situation would be typical from photo-interpretation applications especially remote sensing applications [8].

K. Daniilidis, P. Maragos, N. Paragios (Eds.): ECCV 2010, Part IV, LNCS 6314, pp. 185–198, 2010.
© Springer-Verlag Berlin Heidelberg 2010

A further generalization can be issued from expert-driven or prior automated analysis providing some confidence or uncertainty measure of the classification of objects or group of objects. This is typical from remote sensing applications. For instance, in the acoustics sensing of the ocean for fisheries management [9], images of fish schools are labelled with class proportions that lead to individual priors for each fish school. Such training dataset provided with class priors instead of hard class labels could also be dealt with when a cascade of classifiers or information could be processed before the final decision. In such cases, one could benefit from soft decisions to keep all relevant information in the cascade until the final decisions. This is typical of computer vision applications where multiple sources of information may be available [10] [11].

In this paper, we address weakly supervised learning using decision trees. The most common probabilistic classifiers are provided by generative models learnt using Expectation Maximization algorithm [12] [13]. These generative probabilistic classifiers are also used in ensemble classifiers [14] as in boosting schemes or with iterative classifiers [11]. In contrast, we investigate the construction of decision trees with weakly supervised dataset. Decision tree and random forest are among the most flexible and efficient techniques for supervised object classification [15]. However to our knowledge, previous works only deal with decision trees that consider hard input and probabilistic output [16]. The second contribution of this work is to develop an iterative procedure for weakly supervised learning. The objective is to iteratively refine the class priors of the training data in order to improve the classification performance of the classifier at convergence. We report different experiments to demonstrate the relevance of these contributions. The focus is given to examples demonstrating the genericity of the proposed weakly supervised framework, including applications to semi-supervised learning. In all cases, the proposed approach favourably compares to previous work, especially hard decision trees, generative classification models, and discriminative classification models.

This paper is organized as follows. In section 2, we present the weakly supervised learning of decision trees. In section 3, the iterative procedure for weakly supervised learning is detailed. The application to semi-supervised learning is presented in section 4 while experiments and conclusions are given in sections 5 and 6.

2 Decision Trees and Random Forest

2.1 Supervised Decision Trees and Random Forests

In supervised learning, the method consists in splitting the descriptor space into sub-sets that are homogeneous in terms of object classes. More precisely, the feature space is split based on the maximization of the gain of information. Different split criteria have been proposed such as the Gini criterion [17], the Shannon entropy [18] [19], or other on statistical tests such as ANOVA [20] or χ^2 test [21]. All of these methods have shown to lead to rather equivalent classification performances.

We focus here on the C4.5 decision trees which are among the most popular [19]. During the training step, at a given node of the tree, the procedure chooses descriptor d and associated split value S_d that maximize information gain G:

$$\arg\max_{\{d,S_d\}} G(S_d) \tag{1}$$

where gain G is issued from the Shannon entropy of object classes [19]:

$$\begin{cases} G = \left(\sum_m E^m\right) - E^0 \\ E^m = -\sum_i p_{mi} log(p_{mi}) \end{cases}. \tag{2}$$

where E^0 indicates the entropy at the parent considered node, E^m the entropy at children node m, and p_{mi} the likelihood of class i at node m.

A test sample is passed trough the tree and follows the test rules associated with each node. It is assigned to the class of the terminal node (or descriptor subspace) that it reaches.

Random forests combine a "bagging" procedure [22] and the random selection of a subset of descriptors at each node [23]. The random forest [15] can provide probabilistic outputs given by the posterior distribution of the class votes over the trees of the forest. Additional randomization-based procedures can be applied during the construction of the tree [24]. In some cases, they may lead to improve performances. Here, the standard random forests will be considered [15].

2.2 Weakly Supervised Learning of Soft Decision Trees

In this section, we introduce a weakly supervised procedure for learning soft decision trees. Let us denote by $\{x_n, \pi_n\}$ the provided weakly supervised dataset.

In contrast to the standard decision tree, any node of the tree is associated with class priors. In the weakly supervised setting, the key idea is to propagate class priors through tree nodes rather than class labels as in the supervised case. Consequently, given a constructed decision tree, a test sample will be passed trough the tree and be assigned the class priors of the terminal it will reache.

Let us denote by p_{mi} the class priors at node m of the tree. The key aspect of the weakly supervised learning of the soft decision tree is the computation of class prior p_{mi} at any node m. In the supervised case it consists in evaluating the proportion of each class at node m. In a weakly supervised learning context, real classes are unknown and class proportions can not be easily assessed. We propose to compute p_{mi} as a weighted sum over priors $\{\pi_{ni}\}$ for all samples attached to node m. For descriptor d, denoting x_n^d the instance value and considering the children node m_1 that groups together data such as $\{x_n^d\} < S_d$, the following fusion rule is then proposed:

$$p_{m_1 i} \propto \sum_{\{n\}|\{x_n^d\}<S_d} (\pi_{ni})^\alpha \tag{3}$$

For the second children node m_2 that groups data such as $\{x_n^d\} > S_d$, the equivalent fusion rule is suggested:

$$p_{m_2 i} \propto \sum_{\{n\}|\{x_n^d\}>S_d} (\pi_{ni})^{\alpha} \tag{4}$$

The considered power α weighs low-uncertainty samples, i.e. samples such that class priors closer to 1 should contribute more to the overall cluster mean p_{mi}. An infinite exponent values resorts to assigning the class with the greatest prior over all samples in the cluster. In contrast, an exponent value close to zero withdraws from the weighted sum low class prior. In practice, for α from 0.1 to 8, performances are more or less the same accuracy. After experiments, α is set to 0.8. This setting comes to give more importance to priors close to one. If $\alpha < 1$, high class priors are given a similar greater weight compared to low class priors. If $\alpha > 1$, the closer to one the prior the greater the weight.

Considering a random forest, the output from each tree t for a given test data x is a prior vector $p_t = \{p_{ti}\}$. p_{ti} is the prior for class i at the terminal node reached for tree t. The overall probability that x is assigned to class i, i.e. posterior likelihood $p(y = i|x)$, is then given by the mean:

$$p(y = i|x) = \frac{1}{T} \sum_{t=1}^{T} p_{ti} \tag{5}$$

where $y_n = i$ denotes that sample x_n is assigned to class i. A hard classification resorts to selecting the most likely class according to posteriors (5).

In this paper, experiments are carried out to fix the mean optimal number of tree per forest. Results show that 100 trees per forests are optimal on average. Furthermore, following the random forest process, there is no pruning.

3 Iterative Classification

3.1 Naive Iterative Procedure

The basic idea of the iterative scheme is that the class priors of the training samples can be refined iteratively from the overall knowledge acquired by the trained classifier such that these class priors finally converge to the real class of the training samples. The classifier at a given iteration can then be viewed as a filter that should reduce the noise or uncertainty on the class priors of training samples. Note that this iterative method is only applied to the training dataset.

Such an iterative procedure has previously been investigated in different contexts, especially with probabilistic generative classifier [11]. Theoretical results regarding convergence properties can hardly be derived [25] [26], though good experimental performances have been reported [27]. The major drawbacks of this approach are possible over-training effects and the propagation of early classification errors [28]. Bayesian models may contribute to solve for these over-training issues.

Table 1. Naive iterative procedure for weakly supervised learning (IP1)

Given an initial training data set $T_1 = \{x_n, \pi_n^1\}$ and M iterations,

1. For m from 1 to M
   - Learn a classifier C_m from T_m.
   - Apply the classifier C_m to T_m.
   - Update $T_{m+1} = \{x_n, \pi_n^{m+1}\}$ with $\pi_n^{m+1} \propto \pi_n^1 p(x_n|y_n = i, C_m)$.
2. Learn the final classifier using T_{M+1}.

The implementation of this naive iterative procedure proceeds as follows for weakly supervised learning. At iteration m given the weakly supervised dataset $\{x_n, \pi_n^m\}$, a random forest C_m can be learnt. The updated random forest could be used to process any training sample $\{x_n, \pi_n^m\}$ to provide an updates class prior π^{m+1}. This update of class prior π^{m+1} should exploit both the output of the random forest and the initial prior π^1. Here, the updated priors are given by: $\pi_n^{m+1} \propto \pi_n^1 p(x_n|y_n = i, C_m)$ where $y_n = i$ denotes the classe variable for sample n.

This algorithm is sketched in Tab. 1. In the subsequent, this procedure will be referred to as IP1 (Iterative Procedure 1).

3.2 Randomization-Based Iterative Procedure without over Training

A major issue with the above naive iterative procedure is that the random forest is repeatedly applied to the training data such that over-training effects may be expected. Such over-training effects should be avoided.

To this end, we propose a second iterative procedure. The key idea is to exploit a randomization-based procedure to distinguish at each iteration separate training and test subsets. More precisely, we proceed as follows. At iteration m, the training dataset $T_m = \{x_n, \pi_n^m\}$ is randomly split into a training dataset Tr_m and a test dataset Tt_m according to a given proportion β. Tr_m is exploited to build a weakly supervised random forest C_m. Samples in Tt_m are passed

Table 2. Randomization-based iterative procedure for weakly supervised learning (IP2)

Given a training data set $T_1 = \{x_n, \pi_n^1\}$ and M iterations,

1. for m from 1 to M
   - Randomly split T_m in two groups: $Tr_m = \{x_n, \pi_n^m\}$ and $Tt_m = \{x_n, \pi_n^m\}$ according to a split proportion β.
   - Learn a classifier C_m from subset Tr_m.
   - Apply classifier C_m to subset Tt_m.
   - Update $Tt_{m+1} = \{x_n, \pi_n^{m+1}\}$ with $\pi_n^{m+1} \propto \pi_n^1 p(x_n|y_n = i, C_m)$.
   - Update training dataset T_{m+1} as Tt_{m+1}: $T_{m+1} = \{Tr_m, Tt_{m+1}\}$.
2. Learn the final classifier using T_{M+1}.

through random forest C_m and updated class priors are issued from the same rule as previously: $\pi_n^{m+1} \propto \pi_n^1 p(x_n|y_n = i, C_m)$. β gives the proportion of training examples in the training set Tr_m while the remainder $(1-\beta)$ training examples fall in the test set Tt_m. Setting β obeys to a trade-off: for a good assessment of random forest C_m, the number of samples in Tr_m must be high enough. But if β is too high, only very few samples will be updated at each iteration leading to a very slow convergence of the algorithm. In practice β is typically set to 0.75.

The algorithm is shown in the table 2. In the subsequent, this procedure will be denoted as IP2 (Iterative Procedure 2).

4 Application to Semi-supervised Learning

4.1 Related Work

Semi-Supervised Learning is reviewed in [28]. Four types of methods can be distinguished. The first type includes generative models often exploiting Expectation Maximization schemes that assess parameters of mono-modal Gaussian models [29] [28] or multi-modal Gaussian models [30]. Their advantages are the consistency of the mathematical framework with the probabilistic setting. The second category refers to discriminative models such as the semi-supervised support vector machine (S3VM) [31] [28]. Despite a mathematically-sound basis and good performances, S3VM are subject to local optimization issues and S3VM can be outperformed by other models depending on the dataset. Graph-based classifier is an other well known category in semi-supervised learning [32] [28]. The approach is close to the K-nearest-neighbour approach but similarities between examples are also taken in account. The principal drawback is that this classifier is mostly transductive: generalization properties are rather weak and performances decrease with unobserved data. The last family of semi-supervised models is formed by iterative schemes such as the self-training approach [33] or the co-training approach [34] that is applicable if observation features can be split into two independent groups. The advantage is the good performance reached by these methods and the simplicity of the approach. Their drawbacks mostly lie in the difficulties to characterize convergence properties.

4.2 Self Training with Soft Random Forests

A semi-supervised version of the iterative procedure proposed in the previous section can be derived. Following a self training strategy, it conststs in initially training a random forest from groundtruthed training samples only. Then, at each iteration, unlabelled data are processed by the current classifier and the K samples with the greatest class posteriors are appended to the training database to retrain the classifier. If should be stressed that in the standard implementation of semi-supervised learning with SVMs and random forest the new samples appended to training set at each iteration are assigned class labels. In contrast, we benefit from the proposed weakly supervised decision trees. This is expected to reduce the propagation of classification errors. The sketch of semi-supervised learning is given in table 3.

Table 3. Soft self-training procedure for semi-supervised learning

Given an initial training data set $T = \{T_L, T_U\}$, where T_L contains labelled data and T_U unlabelled data, and M iterations.

1. For m from 1 to M
   - Learn a classifier C_m from T_L.
   - Apply classifier C_m to T_U.
   - For each classes, transfer from T_U to T_L the most confident examples, with weak label, according to the probabilistic classification.
2. Generate the final classifier using T_L.

5 Experiments

5.1 Simulation Protocol

In this section, we compare four classification models: IP1 using soft random forests, IP2 using soft random forests, soft random forests alone, and the generative model proposed in [2] for weakly labelled data.

Given a supervised dataset, a weakly supervised training dataset is built. We distribute all the training examples in several groups according to predefined target class proportions (table 4). All the instances in a given group are assigned the class proportion of the group. In table 4, we show an example of target class proportions for a three-class dataset. In this example, we can create groups containing from one class (supervised learning) to three classes. For each case of class-mixture, different mixture complexities can be created: from one class dominating the mixture, i.e. the prior of one class being close to one, to equiprobable class, i.e. equal values for non-zeros class priors.

To evaluate the performances of the proposed weakly supervised learning strategies, we consider different reference datasets of the UCI machine learning repository so that reported experiments could be reproduced. The three considered datasets have been chosen to provide representative examples of the datasets to be dealt with in computer vision applications. We do not consider datasets with two classes because they do not allow us to generate complex class-mixtures. D1 is an image segmentation dataset containing 7 classes of texture and 330 instances per class. Each sample is characterized by a 19-dimensional real feature vector. D1 is a typical computer vision dataset drawn from a database of 7 outdoor images (brickface, sky, foliage, cement, window, path, grass). D2 is the classical Iris dataset containing 3 classes and 50 instances per class. Each objectis characterized by geometric features, i.e. length and width of the petals. D3 is the Synthetic Control Chart Time Series dataset, containing 6 classes of typical line evolutions, 100 instances per classes, and 5 quantified descriptors. An interesting property of this dataset is that the distribution of the features within each class is not unimodal and cannot be easily modelled using a parametric approach. This is particularly relevant for computer vision applications where objects classes often lead non-linear manifolds in the feature space. Dataset D3

Table 4. Example of training class priors for a dataset with 3 classes. Different cases are carried out: from the supervised labelling to the high complexity mixture.

Dataset with 3 classes, 1-class mixture labels:
$\begin{pmatrix}1\\0\\0\end{pmatrix}$ $\begin{pmatrix}0\\1\\0\end{pmatrix}$ $\begin{pmatrix}0\\0\\1\end{pmatrix}$ (supervised learning)
Dataset with 3 classes, 2-class mixture labels:
$\begin{pmatrix}0.8\\0.2\\0\end{pmatrix}$ $\begin{pmatrix}0.2\\0.8\\0\end{pmatrix}$ $\begin{pmatrix}0.6\\0.4\\0\end{pmatrix}$ $\begin{pmatrix}0.4\\0.6\\0\end{pmatrix}$ $\begin{pmatrix}0.8\\0\\0.2\end{pmatrix}$ $\begin{pmatrix}0.2\\0\\0.8\end{pmatrix}$ $\begin{pmatrix}0.6\\0\\0.4\end{pmatrix}$ $\begin{pmatrix}0.4\\0\\0.6\end{pmatrix}$ $\begin{pmatrix}0\\0.8\\0.2\end{pmatrix}$ $\begin{pmatrix}0\\0.2\\0.8\end{pmatrix}$ $\begin{pmatrix}0\\0.6\\0.4\end{pmatrix}$ $\begin{pmatrix}0\\0.4\\0.6\end{pmatrix}$
Dataset with 3 classes, 3-class mixture labels:
$\begin{pmatrix}0.8\\0.1\\0.1\end{pmatrix}$ $\begin{pmatrix}0.1\\0.8\\0.1\end{pmatrix}$ $\begin{pmatrix}0.1\\0.1\\0.8\end{pmatrix}$ $\begin{pmatrix}0.4\\0.2\\0.2\end{pmatrix}$ $\begin{pmatrix}0.2\\0.4\\0.2\end{pmatrix}$ $\begin{pmatrix}0.2\\0.2\\0.4\end{pmatrix}$

was also chosen to investigate the classification of time series depicting different behaviours (cyclic, increasing vs. decreasing trend, upward vs. downward shift). This is regarded as a mean to evaluate the ability to discriminate dynamic contents particularly relevant for video analysis, i.e. activity recognition, trajectory classification, event detection.

Cross validation over 100 tests allows assessing a mean classification rate. 90% of data are used to train classifier while the 10% remainders are used to test. Dataset is randomly split every test and the procedure that affects weak labels to the training data is carried out every test. A mean correct classification rate is extracted over the cross validation.

5.2 Experiments on Weakly Supervised Dataset

We report weakly supervised experiments in table 5 for the tree datasets. Results are provided as a function of the training dataset and as a function of the class mixture complexity, from the supervised learning (1-class mixture) to the maximum complexity mixture (mixture with all classes). Results are reported for the iterative procedures IP1 (section 3.1) and IP2 (section 3.2), the weakly supervised learning of soft random forests, the generative and discriminant models previously proposed in [2] and [9]. The later respectively exploit Gaussian mixtures and a kernel Fisher discrimination technique.

Overall, the iterative process IP2 outperforms the other models. Even if random forests alone are outperformed by the generative model with D2, the iterative procedure leads to improved classification. The explanation is that class priors are iteratively refined to finally resort to less fuzzy priors. Experiments with dataset D3, particularly stress the relevance of the introduction of soft decision trees. Due to the interlaced structure of the feature distribution for each class of dataset D3, the generative and discriminative models perform poorly. In contrast the weakly supervised random forests reach correct classification rates close to the supervised reference even with complex 6-class training mixtures. For instance, considering D3 and 6-classes mixture labels, the iterative procedure IP2 combined to soft forest reach 98.8% (vs. 100% in the supervised case) where the generative end discriminative models only reach 58.3% and 59.8% of correct classification.

Table 5. Classification performances for datasets D1, D2, and D3: the mean correct classification rate (%) is reported as a function of the complexity of the mixture label for the 5 classification models IP1 + soft trees, IP2+ soft trees, soft trees and random forest alone, a EM-based generative algorithm [2], and a discriminative-based algorithm [9]

Dataset, type of mixtures	IP1 + soft trees	IP2 + soft trees	soft trees	Naive bayes [2]	Fisher + K-pca [9]
D1, 1 classes mixture	-	-	**96.1%**	83.7%	89.7%
D1, 2 classes mixture	90.7%	**96.1%**	92.3%	83.6%	89.2%
D1, 3 classes mixture	88.7%	**95.9%**	91.2%	84.4%	89.5%
D1, 4 classes mixture	88.3%	**94.4%**	88.4%	83.7%	89.1%
D1, 5 classes mixture	85.0%	**94.1%**	88.8%	83.8%	89.1%
D1, 6 classes mixture	75.2%	**92.7%**	84.6%	83.1%	89.1%
D1, 7 classes mixture	55.1%	81.4%	62.6%	75.1%	**85.9%**
D2, 1 classes mixture	-	-	**97.3%**	94.6%	96.0%
D2, 2 classes mixture	**97.3%**	**97.3%**	90.6%	95.3%	87.3%
D2, 3 classes mixture	84.0%	**92.6%**	81.3%	85.3%	76.6%
D3, 1 classes mixture	-	-	**100%**	77.1%	66.8%
D3, 2 classes mixture	90.5%	**100%**	90.0%	62.2%	63.6%
D3, 3 classes mixture	91.3%	**99.5%**	89.3%	62.1%	61.5%
D3, 4 classes mixture	82.1%	**98.1%**	75.6%	45.5%	62%
D3, 5 classes mixture	74.6%	**97.3%**	82.1%	47.3%	59.1%
D3, 6 classes mixture	94.0%	**98.8%**	88.6%	58.3%	59.8%

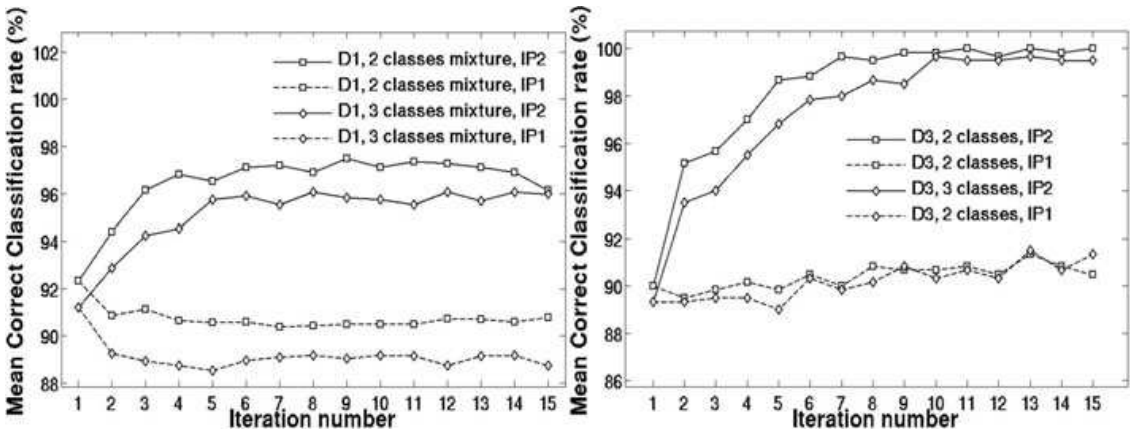

Fig. 1. Evolution of the performances of the iterative procedures IP1 and IP2 through iteration: dataset D1 (left), dataset D3 (right)

To further illustrate the behaviour of the iterative procedures IP1 and I2, we report in figure 1 the evolution of the mean correct classification rate (for the test set) as a function of the iteration for dataset D1 and D2 and several types of class mixtures. These plots state the relevance of the procedure IP2 compared to procedure IP1. Whereas the later does not lead to significant improvement over iterations, the gain in the correct classification rate can be up to 10% after the convergence of the IP2 procedure, for instance for dataset D2 and 2-class mixtures. The convergence is typically observed on a ten of iterations. These results can be explained by the fact that the IP2 procedure distinguishes at each iteration separate training and test set to update the random forests and the class priors.

5.3 Application to Fish School Classification in Sonar Images

Weakly supervised learning is applied to fisheries acoustics data [9] formed by a set of fish schools automatically extracted in sonar acoustics data. Fish schools are extracted as connected components using a thresholding-based algorithm. Each school is characterized by a X-dimensional feature vector comprising geometric (i.e. surface, width, height of the school) and acoustic (i.e. backscattered energy) descriptors. At the operation level, training samples would issue from the sonar in trawled areas, such any training school would be assigned the relative priors of each class. With a view to performing a quantitative evaluation, such weakly supervised situations are simulated from a groundtruthed fish school dataset. The later has been built from sonar images in trawled regions depicting only one species.

From results given in table 6, we perform a comparative evaluation based on the same methods than in section 5.2 as shown in table 5. Class proportions have been simulated as presented in table 4. Similar conclusions can be drawn. Overall the iterative procedure with soft random forests (IP2-SRF) outperforms the other techniques including the generative and discriminative models presented in [2] [9], except for the four-class mixture case where soft random forests alone perform better (58% vs. 55%). The operational situations typically involve mixtures between two or three species and the reported recognition performances (between 71% and 79%) are relevant w.r.t. ecological objectives in terms of species biomass evaluation and the associated expected uncertainty levels.

Table 6. Classification performances for sonar image dataset D4: the mean correct classification rate (%) is reported as a function of the complexity of the mixture label for the 5 classification models IP1 + soft trees, IP2+ soft trees, soft trees and random forest alone, a EM-based generative algorithm [2], and a discriminative-based algorithm [9].

Dataset, type of mixtures	**IP1 + soft trees**	**IP2 + soft trees**	**soft trees**	**Naive bayes** [2]	**Fisher + K-pca** [9]
D4, 1 classes mixture	-	-	**89.3%**	66.9%	69.9%
D4, 2 classes mixture	72.3%	**79.4%**	71.9%	52%	71.7%
D4, 3 classes mixture	62.9%	**70%**	68.3%	51.2%	65.9%
D4, 4 classes mixture	45.3%	55%	**58.7%**	47.9%	56.2%

5.4 Semi-supervised Experiments

Semi-supervised experiments have been carried out using a procedure similar to the previous section. Training and test sets are randomly built for a given dataset. Each training set is composed of labelled and unlabelled samples. We here report results for datasets D2 and D3 with the following experimental setting. For dataset D3 the training dataset contains 9 labelled examples (3 for each class) and 126 unlabelled examples (42 for each class). For dataset D3, we focus on a two-class example considering only samples corresponding to normal and cyclic pattern. Training datasets contain 4 labelled samples and 86 unlabelled samples per class. This particular experimental setting is chosen to illustrate the relevance of the semi-supervised learning when only very fulled labelled training

samples are available. In any case, the upper bound of the classification performances of a semi-supervised scheme is given by the supervised case. Therefore, only weak gain can be expected when a representative set of fully labelled samples is provided to the semi-supervised learning.

Five semi-supervised procedure are compared: three based on self-training (ST) strategies [28], with soft random forests (ST-SRF), with standard (hard) random forests (ST-RF), with a nave Bayes classifier (ST-NBC), a EM-based nave Bayes classifier (EM-NBC) [2] and the iterative procedure IP2 to soft random forest (IP2-SRF). Results are reported in figure 2.

These semi-supervised experiments first highlight the relevance of the soft random forests compared to their standard versions. For instance, when comparing both to a self-training strategy, the soft random forests lead to a gain of 5% of correct classification with dataset D3. This is regarded as a direct consequence of a reduced propagation of initial classification errors with soft decisions. The structure of the feature space for dataset D3 further illustrates as previously the flexibility of the random forest schemes compared to the other ones, especially generative models which behave poorly.

These experiments also demonstrate the relevance of the weakly supervised learning IP2-SRF in a semi-supervised context. The later favourably compares to the best self-training strategy (i.e. 90% vs 82.5% of correct classification for dataset D2 after 10 iterations). This can be justified by the relations between the two procedures. As mentioned in section 4, the self training procedure with soft random forests can be regarded as a specific implementation of the iterative procedure IP2. More precisely, the self-training strategy consists in iteratively appending unlabelled samples to the training dataset. At a given iteration, among the samples not yet appended to the training set, those with the greatest measures of the confidence in the classification are selected. Hence the classification decisions performed for the samples in the training set are never re-evaluated. In contrast

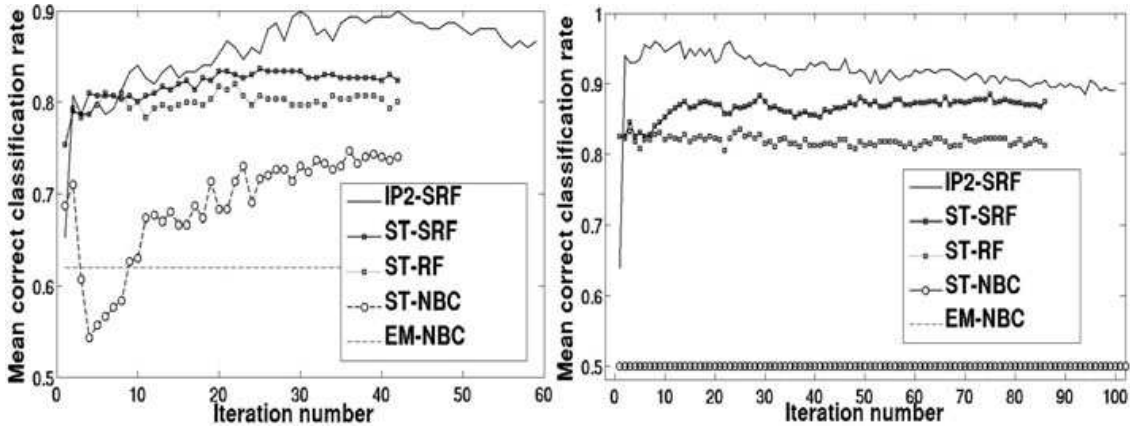

Fig. 2. Classification performances in semi-supervised contexts: dataset D2 (left) and dataset D3 (right) restricted to classes "standard patterns" and "cyclic pattern". Five approaches are compared: ST-SRF, ST-RF, ST-NBC, EM-NBC, and IP2-SRF (cf. text for details).

to this deterministic update of the training set, the weakly supervised iterative procedure IP2 exploits a randomization-based strategy where unlabelled sample are randomly picked to build at each iteration a training set. Therefore, soft classification decisions are repeatedly re-evaluated with respect to the updated overall knowledge. Then, the proposed entropy criterion (equation (3)) implies that fully labelled samples are also implicitly given more weight as in the soft training procedures. These different features support the better performances reported here for the iterative procedure IP2 combined to soft random forests.

6 Conclusion

We have presented in this paper methodological contributions for learning object class models in a weakly supervised context. The key feature is that classification information in the training datasets are given as the priors of the different classes for each training sample. This weakly supervised setting covers the supervised situations, the semi-supervised situations, and computer vision applications as the object recognition scheme that only specifies the presence or absence of each class in each image of the training dataset.

Soft random forests for weakly supervised learning: From a methodological point of view, a first original contribution is a procedure to learn soft random forests in a weakly supervised context. Interestingly the later is equivalent to the C4.5 random forest [15] if a supervised dataset is available such that recognition performances for low uncertainty priors can be granted. The second methodological contribution is an iterative procedure aimed at iteratively improving the learning model.

The experimental evaluation of these methodological contributions for several reference UCI datasets demonstrate their relevance compared to previous work including generative and discriminative models [2] [9]. We have also shown that these weakly supervised learning schemes are relevant for semi-supervised datasets for which they favourably compare to standard iterative techniques such as self-training procedures. The experiments support the statement widely acknowledged in pattern recognition that, when relevantly iterated, soft decisions perform better than hard decisions.

Weakly supervised learning for computer vision applications: The reference UCI datasets considered in the reported experiments are representative of different types of computer vision datasets (i.e. patch classification, object recognition, trajectory analysis). For these datasets, we have shown that recognition performances close to upper bounds provides by the supervised learning could be reached by the proposed weakly learning strategy even when the training set mostly high uncertainty class priors.

This is of particular importance as it supports the relevance of the weakly supervised learning to process uncertain or contradictory expert or automated preliminary interpretations. In any case, such a learning scheme should make in computer vision applications the construction of training datasets which is task

often a very tedious task. The later observation initially motivated the introduction of the semi-supervised learning and of the weakly supervised case restricted to presence and absence information. Our work should be regarded as a further development of these ideas to take into account more general prior information. As illustrated for instance by the fisheries acoustics dataset, we believe that this generalization may permit reaching relevant classification performances when the knowledge of presence and/or absence information only leads to unsatisfactory classification rates [35] [2].

Given the central role of the randomization-based sampling in the iterative procedure, future work will focus on its analysis both form experimental and theoretical points of view. The objectives will be to characterize the convergence of this procedure as well to evaluate different random sampling beyond the uniform sampling tester in the reported experiments. A stopping criteria might also be considered.

References

1. Crandall, D.J., Huttenlocher, D.P.: Weakly supervised learning of part-based spatial models for visual object recognition. In: Leonardis, A., Bischof, H., Pinz, A. (eds.) ECCV 2006. LNCS, vol. 3951, pp. 16–29. Springer, Heidelberg (2006)
2. Ulusoy, I., Bishop, C.M.: Generative versus discriminative methods for object recognition. In: CVPR, vol. 2, pp. 258–265 (2005)
3. Ponce, J., Hebert, M., Schmid, C., Ziserman, A.: Toward Category-Level Object Recognition. LNCS, vol. 4170. Springer, Heidelberg (2006)
4. Weber, M., Welling, M., Perona, P.: Unsupervised learning of models for object recognition. In: Vernon, D. (ed.) ECCV 2000. LNCS, vol. 1842, pp. 18–32. Springer, Heidelberg (2000)
5. Fergus, R., Perona, P., Zisserman, A.: Weakly supervised scaled-invariant learning of models for visual recognition. IJCV 71, 273–303 (2006)
6. Schmid, C.: Weakly supervised learning of visual models and its application to content-based retrieval. IJCV 56, 7–16 (2004)
7. Rossiter, J., Mukai, T.: Bio-mimetic learning from images using imprecise expert information. Fuzzy Set and Systems 158, 295–311 (2007)
8. van de Vlag, D., Stein, A.: Incorporing uncertainty via hierarchical classification using fuzzy decision trees. IEEE Transaction on GRS 45, 237–245 (2007)
9. Lefort, R., Fablet, R., Boucher, J.M.: Combining image-level and object-level inference for weakly supervised object recognition. Application to fisheries acoustics. In: ICIP (2009)
10. Maccormick, J., Blake, A.: A probabilistic exclusion principle for tracking multiple objects. IJCV 39, 57–71 (2000)
11. Neville, J., Jensen, D.: Iterative classification in relational data. In: AAAI workshop on learning statistical models from relational data, pp. 42–49 (2000)
12. Neal, R., Hinton, G.: A view of the EM algorithm that justifies incremental, sparse and other variants. Kluwer Academic Publishers, Dordrecht (1998)
13. Lachlan, G.M., Krishnan, T.: The EM algorithm and extentions. Wiley, Chichester (1997)
14. Kotsiantis, P., Pintelas, P.: Logitboost of simple bayesian classifier. Informatica Journal 29, 53–59 (2005)

15. Breiman, L.: Random forests. Machine Learning 45, 5–32 (2001)
16. Calonder, M., Lepetit, V., Fua, P.: Keypoint signatures for fast learning and recognition. In: Forsyth, D., Torr, P., Zisserman, A. (eds.) ECCV 2008, Part I. LNCS, vol. 5302, pp. 58–71. Springer, Heidelberg (2008)
17. Breiman, L., Friedman, J., Olshen, R., Stone, C.: Classification and regression trees. Chapman and Hall, Boca Raton (1984)
18. Quinlan, J.: Induction of decision trees. Machine Learning 1, 81–106 (1986)
19. Quinlan, J.: C4.5: Programs for machine learning. Morgan Kaufmann Publishers, San Francisco (1993)
20. Loh, W.Y., Shih, Y.Y.: Split selection methods for classification trees. Statistica Sinica 7, 815–840 (1997)
21. Kass, G.V.: An exploratory technique for invesgating large quantities of categorical data. Journal of applied statistics 29, 119–127 (1980)
22. Breiman, L.: Bagging predictors. Machine Learning 26, 123–140 (1996)
23. Ho, T.K.: Random decision forest. ICDAR (1995)
24. Geurts, P., Ernst, D., Wehenkel, L.: Extremely randomized trees. Machine Learning 36, 3–42 (2006)
25. Culp, M., Michailidis, G.: An iterative algorithm for extending learners to semi-supervised setting. In: The 2007 Joint Statistical Meetings (2007)
26. Haffari, G., Sarkar, A.: Analysis of semi-supervised learning with the yarowsky algorithm. In: 23rd Conference on Uncertainty in Artificial Intelligence (2007)
27. Macskassy, S.A., Provost, F.: A simple relational classifier. In: Proceedings of the second workshop on multi-relational data mining, pp. 64–76 (2003)
28. Chapelle, O., Schölkopf, B., Zien, A.: Semi-supervised learning. MIT Press, Cambridge (2006)
29. Nigam, K., McCullum, A., Thrun, S., Mitchel, T.: Learning to classify text from labeled and unlabeled documents. In: AAAIJ (1998)
30. Nigam, K., McCallum, A., Thrun, S., Mann, G.: Text classification from labeled and unlabeled documents using em. Machine Learning 39, 103–134 (2000)
31. Joachims, T.: Transductive inference for text classification using support vector machines. In: ICML, pp. 200–209 (1999)
32. Zhu, X., Ghahramani, Z., Lafferty, J.: Semi-supervised learning using gaussian fields and harmonic functions. In: ICML, pp. 912–919 (2003)
33. Rosenberg, C., Hebert, M., Schneidermann, H.: Semi-supervised self-training of object detection models. In: WACV (2005)
34. Blum, A., Mitchel, T.: Combining labeled and unlabeled data with co-training. In: WCLT, pp. 92–100 (1998)
35. Fablet, R., Lefort, R., Scalabrin, C., Mass, J., Boucher, J.M.: Weakly supervised learning using proportion based information: an application to fisheries acoustic. In: International Conference on Pattern Recognition (2008)

IV Exploitation des bases d'observation de l'océan : quels outils de traitement de l'information pour l'aide à la caractérisation et la modélisation des dynamiques des écosystèmes marins ?

IV.1 Tera-octets de données d'observation de l'océan : quel potentiel ? Quels enjeux et quels outils nécessaires ?

La compréhension et la prédiction des dynamiques des écosystèmes marins constituent des enjeux sociétaux majeurs dans le contexte actuel de changement climatique. Le rapport Stern sur l'évaluation des coûts économiques du changement climatique (Stern 2006) met notamment en exergue l'impact potentiel des changements à grande échelle et des évènements extrêmes :" The costs of climate change for developed countries could reach several percent of GDP as higher temperatures lead to a sharp increase in extreme weather events and large-scale changes" ((Stern 2006), p137).

Des tera-octets de données d'observation de l'océan. Appréhender l'impact des évènements extrêmes et changements à grande échelle nécessite en premier lieu de disposer des outils et moyens permettant de les observer. Dans ce contexte, les développements scientifiques et technologiques dans le domaine de la télédétection de l'environnement, en particulier l'observation satellitaire, au cours des trente dernières années constituent des avancées décisives. L'observation opérationnelle de l'océan dans son ensemble est un aboutissement relativement récent : l'observation satellitaire de la surface de l'océan a réellement démarré au milieu des années 80 et l'observation in situ de l'océan ouvert grâce au déploiement de bouées dérivantes (e.g., projet ARGO) est opérationnel depuis une vingtaine d'années. La communauté scientifique dispose donc actuellement de séries d'observation de paramètres géophysiques (e.g., température de surface, hauteur de mer, vent de surface, couleur de l'eau, extension des zones de glace,..., cf. Figure 26) de 15 à 25 ans. L'accroissement de la résolution des capteurs, le déploiement d'un nombre croissance de systèmes satellitaires opérationnels d'observation de l'océan (e.g., le satellite européen SMOS lancé en 2009 pour l'observation de la salinité en surface) conduit à une augmentation considérable des masses de données qui doivent être archivées et ensuite explorées. A titre d'exemple, le CERSAT (Center for Satellite Exploitation and Research) de l'Ifremer traite et archive de manière journalière plus de 150Go de données uniquement pour les observations satellitaires de la température de l'océan issus de plus de 10 capteurs différents pour des résolutions spatiales de 1km à 40km et des modalités d'observation différentes (e.g., capteur micro-onde, capteur infra-rouge). On peut souligner que les données acquises dans le cadre de campagnes océanographiques récurrentes, le déploiement d'observatoires sous-marins comme la modélisation opérationnelle conduit aux mêmes constats de croissance exponentielle des masses de données disponibles pour aborder les questions scientifiques d'intérêt.

Des approches intégrées pour l'étude des dynamiques du système océan. Conjointement à cet accroissement des capacités d'observation et modélisation opérationnelle de l'océan se développe un nombre croissant d'approches intégrées visant à promouvoir une compréhension d'ensemble des différentes composantes (physiques, biogéochimiques, biologiques, voire socio-écomoniques) des écosystèmes marins et de leurs interactions. Le développement de l'approche écosystémique des pêches en est une parfaite illustration (e.g., (Garcia, Cochrane 2005; Fromentin, Planque et al. 2007)). La gestion des ressources halieutiques est traditionnellement fondée sur une évaluation spécifique à chaque stock[5] de poissons. La définition du stock utilisé comme unité de gestion des pêcheries ne revêt toutefois pas toujours une réalité biologique et ne permet pas d'appréhender les interactions possibles entre les différentes sous-populations d'une même espèce, les autres espèces de poissons et plus largement les autres composantes de l'écosystème. Ce changement de paradigme s'accompagne d'un profond changement des méthodologies à considérer, les modèles de dynamique de populations utilisés à l'échelle du stock ne pouvant être étendus simplement pour appréhender l'ensemble d'un écosystème exploité. Le développement d'outil de modélisation à l'échelle d'un écosystème constitue un défi scientifique majeur. Même si certains outils tels que le modèle Ecopath (Pauly, Christensen et al. 2000), fournissent déjà des plateformes de simulation et prédiction pertinentes pour certains aspects, la caractérisation et la compréhension des mécanismes clés déterminants la dynamique des différentes composantes d'un écosystème (forçage "bottom-up", rôle et impact des différentes échelles spatiales et temporelles caractéristiques des systèmes étudiés, ..., e.g. dans le cas du système du courant de Humboldt (Chavez, Ryan et al. 2003; Chavez, Bertrand et al. 2008)) doivent être complétées.

[5] Le terme "stock de poissons" désigne généralement un population de poissons particulière, plus ou moins isolée des autres stocks de la même espèce. (Source : www.millenniumassessment.org).

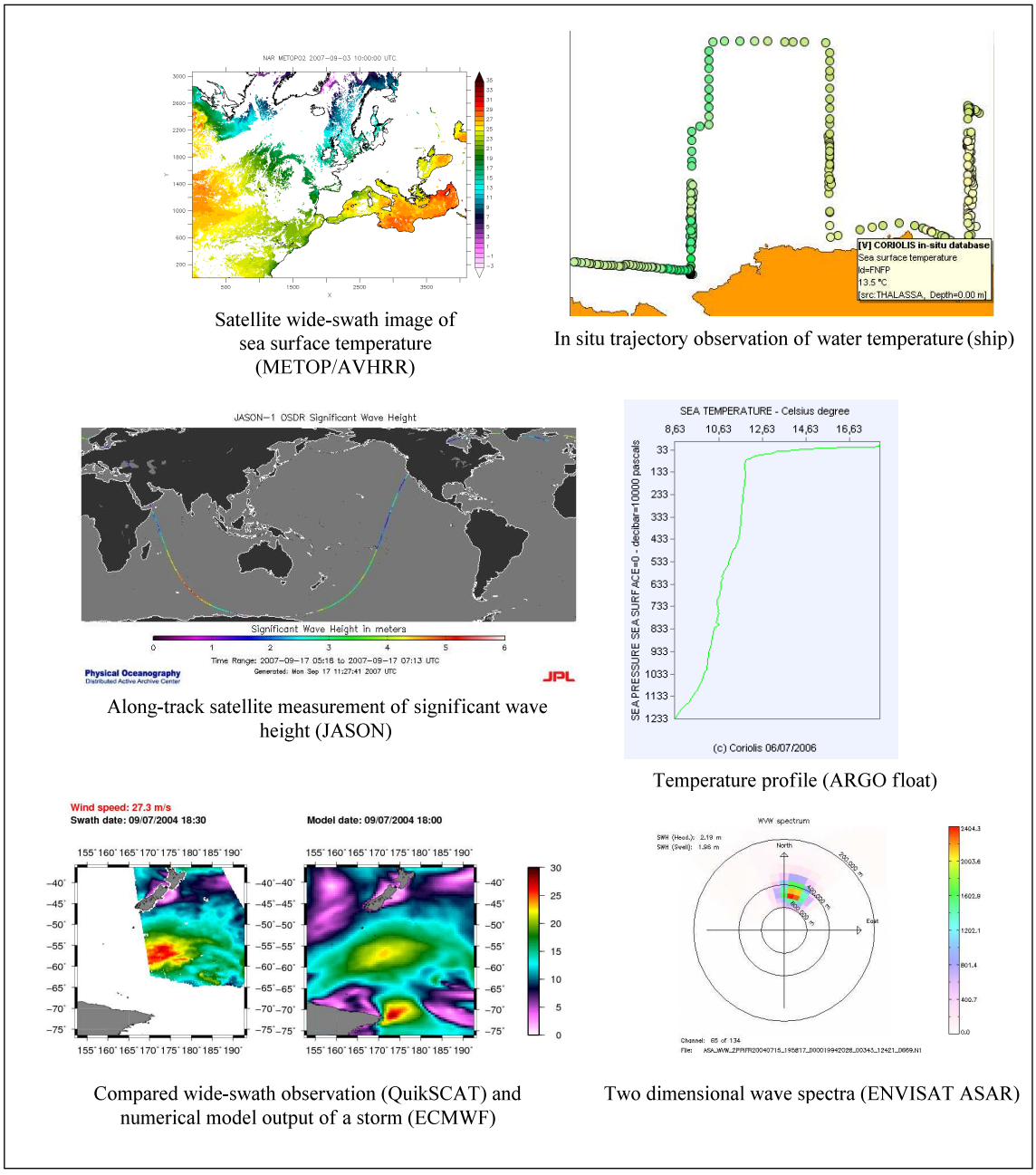

Figure 26. Diversité des données d'observations satellitaires et in situ de l'océan : de gauche à droite et haut en bas, image satellitaire de la température de surface, observation in situ de la température de surface (sur la trajectoire d'un navire), hauteur de mer acquise sur la trajectoire orbitale du satellite JASON, profil *in situ* de température acquis par un profileur dérivant, observation des champs de vent en surface de l'océan (données satellitaires QuikSCAT) vs. prédiction de modèle numérique ECMWF, spectre 2D des vagues estimé à partir d'une observation SAR de la surface de l'océan.

Enjeux du traitement de l'information et projet de recherche. Dans ce contexte, les outils et méthodes de traitement de l'information peuvent compléter les outils classiques de l'océanographie. L'objectif central du projet de recherche envisagé est le développement de tels outils et méthodes permettant d'exploiter pleinement l'ensemble des données/observations disponibles, en particulier les données de télédétection spatiale (observation de la surface de l'océan), l'observation acoustique sous-marine et les marqueurs individuels (notamment issus des biocarbonates marins et de données trajectométriques), et de contribuer à l'identification, la caractérisation et la modélisation de processus et interactions clés des dynamiques des composantes d'un écosystème marin. En s'appuyant sur l'expertise acquise tant du point de vue méthodologique (e.g., scènes dynamiques, géométrie des images, méthodes de classification, problèmes inverses) que thématique (otolithométrie, acoustique sous-marine, télédétection), ce projet de recherche vise à promouvoir cette démarche originale en collaboration étroite avec

des thématiciens (océanographe physicien, biogéochimiste, écologue, ...) dans le cadre d'approches intégrées mises en oeuvre pour différents chantiers (par exemple, le système du courant de Humboldt (cf. collaboration avec le LMI DISCOH)). Ce projet s'articule plus spécifiquement autour de trois questions méthodologiques :

- **Comment analyser et modéliser la structuration géométrique multi-échelle de signaux multivariées** (signaux 1D, courbes planes, trajectoires, images) (Partie IV.2) ?
  Le caractérisation et la modélisation de la structuration des échelles géométriques caractéristiques de nombreux processus géophysiques et écologiques des systèmes étudiés (e.g., distribution spatio-temporelle des structures géophysiques à subméso- et méso-échelle[6], échelles caractéristiques des distributions spatiales de populations, échelles caractéristiques de données trajectométriques,...) sont des questions fondamentales par exemple exploitées pour définir des typologies de processus (e.g., processus à méso-échelle et subméso-échelle en océanographie physique), auxquelles des méthodes d'analyse et modélisation multi-échelle des déformations géométriques de signaux mutivariés (signaux 1D, courbes planes, trajectoires, images) doivent permettre de répondre.

- **Comment améliorer la résolution spatiale et temporelle des structures géophysiques de l'océan à partir des différentes sources d'observations disponibles** (Partie IV.3) ?
  Analyser et modéliser les déterminants des dynamiques de processus géophysiques et écologiques (e.g., impact des structures géophysiques de surface de l'océan sur le déplacement des oiseaux marins (Tew Kai, Rossi et al. 2009), impact des dynamiques subméso- et méso-échelle sur la structuration de l'écosystème pélagique (Bertrand, Ballon et al. 2010; Grados, Fablet et al. 2012)) nécessitent de disposer d'observations des différents processus étudiés cohérentes en termes de résolution spatiale et temporelle. A titre d'exemple il est a priori difficile d'envisager d'analyser des interactions entre des processus de déplacement à des échelles caractéristiques de l'ordre de quelques mètres et des observations de processus géophysiques de surface (e.g., circulation en surface à partir de données altimétriques à une résolution de l'ordre de 50km). Dans ce contexte, l'accroissement de la gamme des capteurs satellitaires disponibles pour l'observation de la surface de l'océan comme la disponibilité de sorties de modèles numériques réalistes ouvre de nouvelles possibilités pour accroître la résolution spatiale et temporelle et la qualité des produits géophysiques opérationnels de la surface de l'océan (e.g., température, salinitié, couleur de l'eau, circulation, vent).

- **Quelles stratégies de fouille dans les bases de données multi-modales d'observations de l'océan pour l'étude et la modélisation des processus caractéristiques déterminant les dynamiques de composantes d'un écosystème marin** (Partie IV.4)?
  La disponibilité de bases de données multimodales d'observation d'un écosystème marin rend aujourd'hui possible l'exploration des relations et déterminismes des dynamiques de différentes composantes du système (structures physiques, processus biogéochimiques, structurations des espèces pélagiques, comportements des prédateurs supérieurs,...). Les masses de données à manipuler aussi bien que l'hétérogénéité de ces données nécessitent de développer des outils et méthodes appropriés pour aborder ces questions thématiques.

On peut souligner que ces questions méthodologiques ne sont pas limitées au seul champ thématique privilégié ici mais au contraire génériques à un grand nombre de domaines scientifiques (e.g., astronomie, biologie moléculaire, imagerie biologique, médecine,...) qui ont également vu s'accroître de manière importante les outils d'observation et modélisation des processus étudiées et les masses de données disponibles aujourd'hui pour leur étude. Pour ces différents champs thématiques, exploiter le potentiel représenté par ces masses de données, i.e. identifier, caractériser et modéliser les processus caractéristiques, est une question centrale à laquelle peut contribuer significativement les outils et méthodes de traitement de l'information.

Le développement de ces axes de recherche a pu être initié dans le cadre du projet "Region Bretagne" CREATE (2009-2012) et s'appuie sur des collaborations régionales étroites dans le cadre de l'Europôle Mer (Ifremer Brest (LOS, STH), LEMAR) et avec le LMI DISCOH. Cette dernière collaboration s'est notamment engagée dans le cadre d'un séjour d'étude d'un an à l'IMARPE (Lima, Pérou; accueil en mise à disponibilité à l'IRD, UMR EME).

[6] La méso-échelle fait typiquement référence à des structures géophysiques dont les échelles caractéristiques sont comprises entre quelques dizaines de kilomètres et quelques centaines de kilomètres, la subméso-échelle correspondant à des échelles caractéristiques de quelques centaines de mètres à quelques kilomètres (cf., par exemple Capet, X., J. C. McWilliams, M. J. Molemaker, A. F. Shchepetkin, 2008: Mesoscale to Submesoscale Transition in the California Current System. Part II: Frontal Processes. *J. Phys. Oceanogr.*, **38**, 44–64).

Les parties suivantes détaillent chacun de ces trois points et présentent certains résultats préliminaires.

IV.2 Analyse et modélisation de la structuration géométrique multi-échelle de signaux multivariés

Résumé des objectifs : *L'analyse et la modélisation des informations de déformation géométrique sont des enjeux importants pour de nombreux processus, e.g. mouvement des organismes, processus physiques (turbulence), processus de structuration spatiale des différentes composantes d'un écosystème. L'objectif méthodologique portera notamment sur le développement d'outils et méthodes de caractérisation et modélisation de la distribution multi-échelle de signatures géométriques locales de signaux multivariés associés à ces processus (courbes planes, trajectoires, images,...). Différents résultats préliminaires démontrent la pertinence de l'approche proposée.*

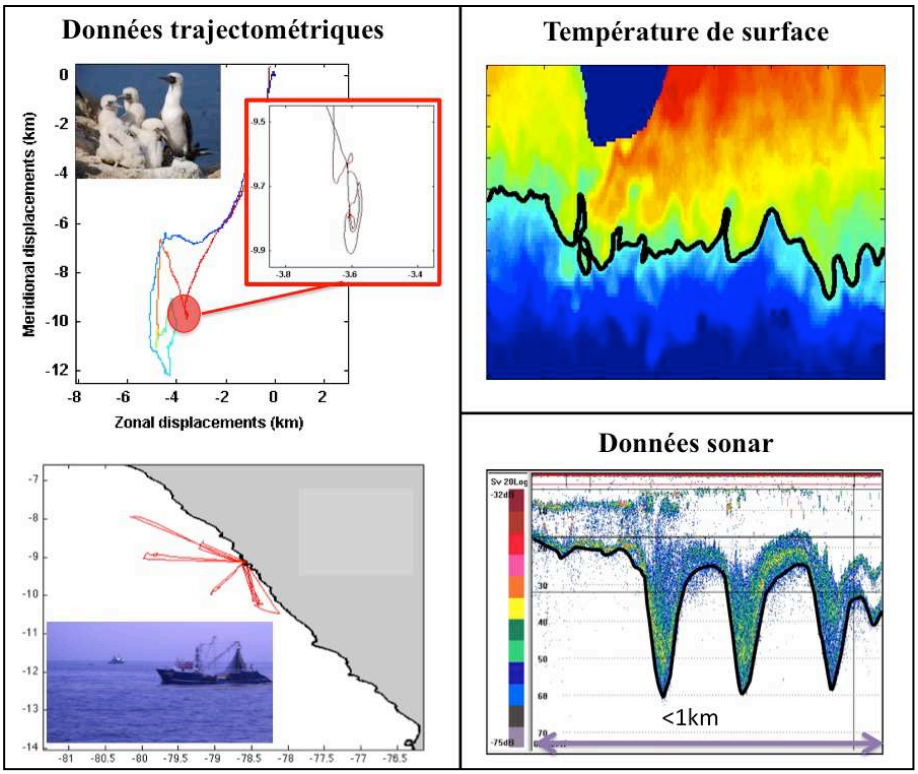

Figure 27. Les déformations géométriques comme marqueurs des dynamiques de différentes composantes d'un écosystème : exemples de données trajectométriques de suivi par satellite de prédateurs supérieurs présentant des caractéristiques géométriques à différentes échelles (cf. texte) (gauche), iso-ligne (en noir) de la température de surface de l'océan dont les déformations géométriques sont associées aux dynamiques turbulentes dans cette région de l'océan (sud de l'Afrique du Sud) (haut, droite), données acoustiques sonar acquises dans le cadre d'une campagne océanographique permettant d'estimer la profondeur de la couche superficielle de l'océan (profondeur de la zone de minimum d'oxygène) et de mettre en évidence les déformations de la couche superficielle de l'océan à subméso-échelle (<10km) (Bertrand, Ballon et al. 2010) (bas, droite).

Comme illustré ci-dessus (Figure 27) la géométrie, et plus particulièrement la distribution espace-échelle des structures et/ou motifs géométriques élémentaires, sont des caractéristiques clés de nombreux processus géophysiques et écologiques. Nous l'avons déjà illustré en matière de caractérisation des textures sonar des fonds marins et de distributions des bancs de poissons (Partie III.1). D'autres exemples sont illustrés ici :

- La diversité des échelles spatiales exhibées par le comportement des prédateurs de supérieurs (ici des oiseaux marins) lors de voyages de nourrissage (Figure 27, gauche, haut) ;
- Les caractéristiques de diffusion/exploration associées aux stratégies de pêche des prédateurs supérieurs, illustrées ici par les données trajectométriques de navires industriels de pêche à l'anchois au Pérou (Figure 27, gauche, bas) ;

- Les propriétés de régularité et d'invariance géométrique (précisément d'invariance conforme (Bernard, Boffetta et al. 2006)) exhibé par des iso-niveaux de champs géophysiques pour certaines dynamiques turbulentes (Figure 27, droite, haut) ;
- Les déformations géométriques pour des échelles spatiales de quelques dizaines de mètres à plusieurs centaines de kilomètres exhibées par la couche superficielle de l'océan (ici, illustrée par la profondeur de la zone de minimum d'oxygène, Figure 27, droite, bas).

La compréhension et la modélisation des déterminismes définissant la distribution espace/temps-échelle de ces propriétés géométriques représentent des enjeux majeurs. A titre d'exemple, l'analyse comparative des dynamiques physiques à subméso-échelle (typiquement des échelles inférieure à quelques kilomètres) et méso-échelle (de quelques kilomètres à quelques dizaines de kilomètres) sont des questions ouvertes de même que leur impact que sur les dynamiques des autres composantes (y compris les prédateurs supérieurs). Des études récentes ont, par exemple, démontré l'effet structurant de structures de méso-échelle sur les stratégies de déplacement d'oiseaux marins (Tew Kai, Rossi et al. 2009). Avant de mettre en évidence ce type d'interactions (cf. Partie IV.4), il est nécessaire de développer des outils et méthode d'extraction et modélisation des propriétés géométriques des signaux observés.

De manière générale, trois aspects complémentaires sont explorés :

- **Invariance en échelle et processus fractals** : Le premier aspect consiste à explorer des propriétés d'invariance des processus géométriques, en particulier des invariances en échelle des processus fractals (Mandelbrot 1982; Shlesinger, Zaslavsky et al. 1995). Du point de vue thématique, ces processus présentent l'intérêt de fournir une interprétation physique directe. Dans le cas des trajectoires, le modèle fractal peut être associé à un comportement de type marche de Lévy caractérisé par une super-diffusion (i.e., la capacité à explorer un domaine avec une loi dépendant en puissance du temps là où la diffusion conduit à une exploration linéaire en fonction du temps) (Fritz, Said et al. 2003; Bertrand, Bertrand et al. 2007; Humphries, Queiroz et al. 2010). Dans le cas des dynamiques turbulentes, la dimension fractale d'iso-niveaux de quantités géophysiques peut être associée à un paramètre physique de diffusivité (Bernard, Boffetta et al. 2006; Cardy 2006). Nous avons commencé à explorer le modèle fractal pour ces deux situations. Du point de vue méthodologique, notre attention se porte notamment sur la capacité à évaluer la significativité de l'hypothèse d'invariance en échelle pour la queue de distribution de la quantité considérée. Une méthode originale est proposée et permet de mettre en évidence pour des jeux de données trajectométriques de prédateurs supérieurs (ici des navires de pêche) aussi bien des comportements de type Lévy que des comportements non-Lévy, là où l'analyse de l'état de l'art pointe les limites méthodologiques des approches existantes pour démontrer l'existence de comportements de type Lévy (Bertrand, Joo et al. Soumis). Une application aux observations satellitaires de la température de surface dans des zones dynamiques de l'océan (e.g., au sud de l'Afrique du Sud) met en évidence l'intérêt de descripteurs de la régularité des lignes de niveaux de ces images pour caractériser la dynamique des zones de frontogénèse (Ba, Autret et al. 2012);
- **Détection de signatures géométriques élémentaires :** Une deuxième approche vise à extraire et caractériser l'ensemble des déformations géométriques élémentaires significatives observées sur les signaux traités. Dans le cas de signaux monodimensionnels (par exemple, pour l'analyse de la profondeur de la couche superficielle de l'océan (Bertrand, Ballon et al. 2010)) les outils d'analyse temps-fréquence classiques peuvent être utilisés (Torrence, Compo 1998; Mallat 2008) et conduisent à des résultats prometteurs (Grados, Fablet et al. 2012). Dans le cas de l'analyse de courbes planes, c.-à-.d. de données trajectométriques ou d'iso-lignes dans des images et/ou champs 2D ou 3D), ces outils se révèlent inadaptés du fait de l'absence d'une paramétrisation intrinsèque des courbes valide à toutes les échelles. Ceci nous a conduit à proposer une première approche de décomposition espace-échelle des déformations géométriques des courbes planes (Fablet, Chaigneau et al. 2012; Fablet, Chaigneau et al. Soumis), décomposition qui combine une analyse temps-fréquence de la série des orientations des tangentes à la courbe et une représentation espace-échelle de la courbe (Figure 28). L'approche proposée permet également de détecter des déformations géométriques (oscillation, boucles) d'intérêt le long d'une courbe comme des régions d'énergie significative vis-à-vis d'un modèle a contrario. Des résultats préliminaires démontrent l'intérêt de la méthodologie proposée par rapport à l'état de l'art (aussi bien les méthodes d'analyse mono-échelle de trajectoires, e.g. (Fauchald, T. 2003; Benhamou 2004; Tremblay, Roberts et al. 2007; Barraquand, Benhamou 2008) que des méthodes d'analyse de formes (Chuang, Kuo 1996; Zhang, Lu 2003)). Appliquée aux iso-lignes de champs géophysiques de surface, elle ouvre également des perspectives de caractérisation et modélisation de la déformation géométrique associée aux différentes échelles caractéristiques des dynamiques océaniques (Fablet, Chaigneau et al. 2012; Fablet, Chaigneau et al. Soumis);

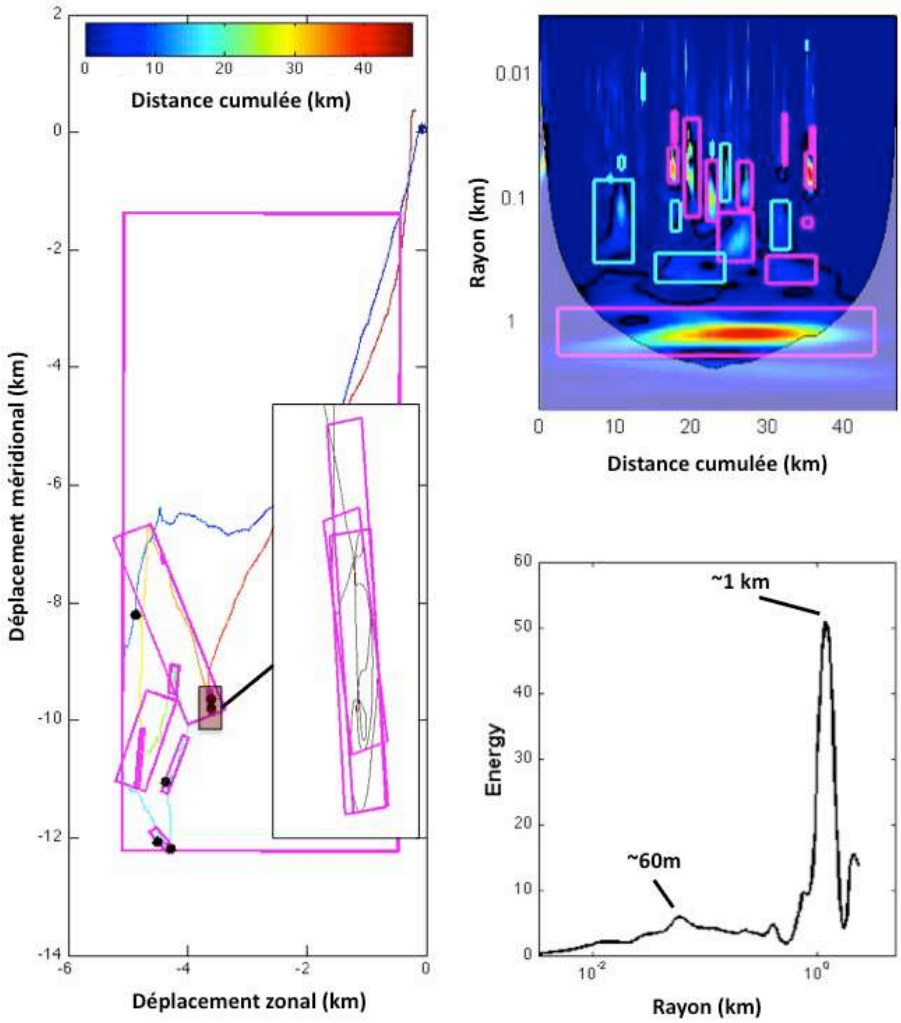

Figure 28. Analyse multi-échelle des déformations géométriques le long d'une trajectoire : trajectoire d'un oiseau marin (fou) sur les côtes péruviennes et structures bouclantes significatives détectées (gauche) ; spectre d'ondelette des déformations géométriques le long de la trajectoire (droite, haut), les déformations géométriques (structures bouclantes (magenta), oscillations (cyan)) significatives sont détectées comme des zones de forte énergie du spectre ; distribution des énergies de déformation le long de la trajectoire (bas, droite), cette distribution fait apparaître deux gammes d'échelle principale de l'ordre de quelque dizaines de mètres et de l'ordre du kilomètre. D'après (Fablet, Chaigneau et al. 2012).

- **Caractérisation et modélisation de la distribution espace-échelle des déformations géométriques:** le troisième aspect portera sur le développement de modèle stochastique multi-échelle des déformations géométriques exhibées par les processus étudiés. Contrairement aux modèles de type fractals évoqués ci-dessus, l'objectif sera ici de pouvoir étudier d'éventuels déterminismes (cascade directe, cascade inverse, forçage externe) de la distribution des déformations géométriques le long d'une courbe. Deux classes de modèle sont privilégiées : des modèles espace-état, fondés sur des marches aléatoires corrélées (Barraquand, Benhamou 2008; Calenge, Dray et al. 2009), des modèles de cascades multiplicatives (Chainais 2007) formulés comme des modèles de processus ponctuels dans des espaces espace-échelle pour pouvoir appréhender explicitement les cascades en échelle (directes ou inverses). Ce dernier point pourra exploiter une extension de l'approche développée pour la modélisation de la distribution des signatures locales dans les images (Descombes 2011; Nguyen, Fablet et al. 2011).

Ces différentes approches fourniront les représentations (en termes de caractéristiques des motifs géométriques détectés, de statistiques globales (e.g., distribution en échelle des déformations géométriques), et/ou des paramètres des modèles développés pour étudier les interactions entre les différents processus étudiés (Partie IV.4). Ces développements méthodologiques s'appuieront notamment sur les travaux menés dans le cadre des thèses de R. Joo et D. Grados (collaboration IMARPE /IRD/Telecom Bretagne) et de E. Autret (collaboration Ifremer/Telecom Bretagne).

IV.3 Super-résolution spatio-temporelle de champs géophysiques à partir de données multi-modales d'observation de l'océan

Résumé des objectifs : *L'un des enjeux actuels majeurs de l'océanographie spatiale est de proposer des produits géophysiques opérationnels permettant de tirer partie au mieux de la diversité des modalités d'observations et modélisations disponibles pour accroître la résolution spatiale et temporelle des champs géophysiques estimés (e.g., température, couleur de l'eau, salinité, vitesse). Les solutions envisagées seront fondées sur le cadre formel de l'assimilation variationnelle dans un contexte multi-échelle et multi-modal et exploiteront de nouveaux opérateurs définis par des a priori géophysiques et/ou par apprentissage statistique à partir d'observations et/ou simulations numériques.*

Afin de mettre en évidence et modéliser les interactions entre différents processus il est critique de disposer d'observations de ces processus à des échelles pertinentes vis-à-vis de leur dynamique spatiale et temporelle. Les observations satellitaires (à l'exception notable des capteurs SAR) présentent classiquement des résolutions d'observation de l'ordre de quelques kilomètres à la centaine de kilomètres suivant le type de capteurs et modalités (cf. Figure 29) pour des échantillonnages temporels de quelques heures à quelques jours. En outre, certains capteurs (cf. Figure 29) sont affectés par la couverture nuageuse et peuvent présenter de ce fait un grand nombre de données manquantes. D'autres capteurs, tels que les capteurs SAR pour l'observation et l'estimation de la rugosité et de champs de vent à la la surface de l'océan (Chapron, Johnsen et al. 2001; Kerbaol, Collard 2005), founissent des résolutions spatiales extrêmement élevées (quelques mètres) mais pour une couverture temporelle parcellaire (tous les dix à quinze jours dans certains cas). Pour pouvoir croiser au mieux ces différentes observations de la dynamique physique avec par exemple des données trajectométriques issus du suivi GPS de prédateurs supérieurs dont les résolutions sont de l'ordre de quelques mètres et quelques secondes et étudier l'impact du forçage physique sur le comportement des prédateurs (Tew Kai, Rossi et al. 2009), il est essentiel de pouvoir disposer de données d'observations géophysiques à la meilleure résolution possible (en temps et en espace). Ce cas particulier est générique au questionnement sur le croisement de données d'observations de processus différents suivant des modalités associées à différentes résolutions spatiales et temporelles.

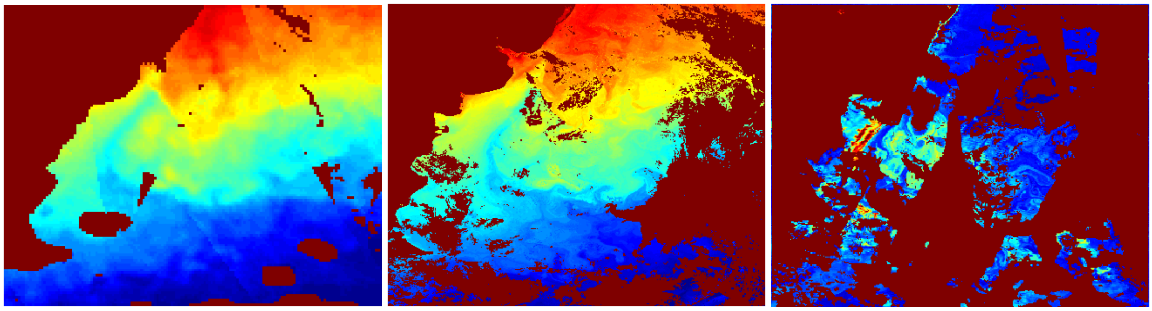

Figure 29. Observations satellitaires multi-modales de l'océan et données maquantes : de gauche à droite, image de la température de surface à une résolution de 25km (données AMSRE), image de la température de surface à une résolution de 4km (données METOP), image de la couleur de l'eau à une résolution de 10km (données MERIS). La zone observée correspond à la zone Atlantique sud-ouest au large des côtes de l'Argentine. Les observations présentent des niveaux de données manquantes différents suivant le capteur utilisé, certains capteurs (e.g., données METOP et MERIS) se révèlent notamment plus sensibles à la couverture nuageuse.

Nous proposons d'aborder la reconstruction de champs géophysiques en surface à haute-résolution (en temps et en espace) en exploitant l'ensemble des observations disponibles suivant deux approches complémentaires :

- **Assimilation variationnelle multi-modale multi-échelle** : La première se base sur une formulation multi-échelle de l'assimilation varitionnelle (Le-Dimet, Talagrand 1986; Papadakis, Corpetti et al. 2007) pour exploiter des observations et des a priori à différentes échelles. De manière générale, la formulation mathématique considérée repose sur la définition d'un système dynamique, c.à.d. d'une part sur un modèle de la dynamique de la variable d'état X représentant le champ géophysique à reconstruire

  $$\frac{\partial X}{\partial t} = M\left(X(t)\right)$$

  où t est la variable temporelle et M l'opérateur définissant le modèle dynamique, et d'autre part sur un opérateur d'observation

  $$Y(t) \sim \Psi\left[H\left(X(t)\right)\right]$$

où H est un opérateur d'observation faisant le lien entre l'état X(t) et l'observation Y(t) et Ψ un modèle de bruit et/ou incertitude (par exemple, une distribution gaussienne de moyenne H(X(t)). La reconstruction de la dynamique de X à partir d'une séquence d'observations de Y consiste classiquement en une maximisation de la probabilité de la séquence d'observation sous contrainte que la séquence suive la dynamique définie par l'opérateur M. Cette reconstruction repose sur des méthodes de descente de gradient faisant intervenir le calcul d'opérateurs adjoints (Le-Dimet, Talagrand 1986; Papadakis, Corpetti et al. 2007). L'originalité porte ici sur trois aspects: des dynamiques de l'état X définies à différentes échelles, la présence de données manquantes dans l'observation Y, des états X non-directement observés (e.g., reconstruction de la circulation à partir d'observations de la température de surface), des observations Y multi-modales et multi-résolution (e.g., température et couleur de l'eau à différentes résolutions, cf. Figure 29). L'enjeu se situe ici dans la définition d'opérateurs permettant de contraindre la géométrie spatio-temporelle à haute-résolution du champ géophysique. Cela peut passer par la définition de modèles a priori appropriés (modèles de turbulence et/ou des déformations géométriques évoqués précédemment (Partie IV.3) et/ou l'ajout de contraintes multi-modales (par exemple, via une contrainte conjointe des géométries de champs géophysiques différents). Cette dernière solution a déjà fourni des résultats prometteurs (Ba, Fablet 2011; Ba, Chapron et al. Soumis). L'une des contributions attendues porte sur l'évaluation de l'impact du choix du modèle a priori sur les caractéristiques des champs scalaires reconstruits ainsi que sur les dynamiques sous-jacentes estimés conjointement à l'interpolation des données manquantes ;

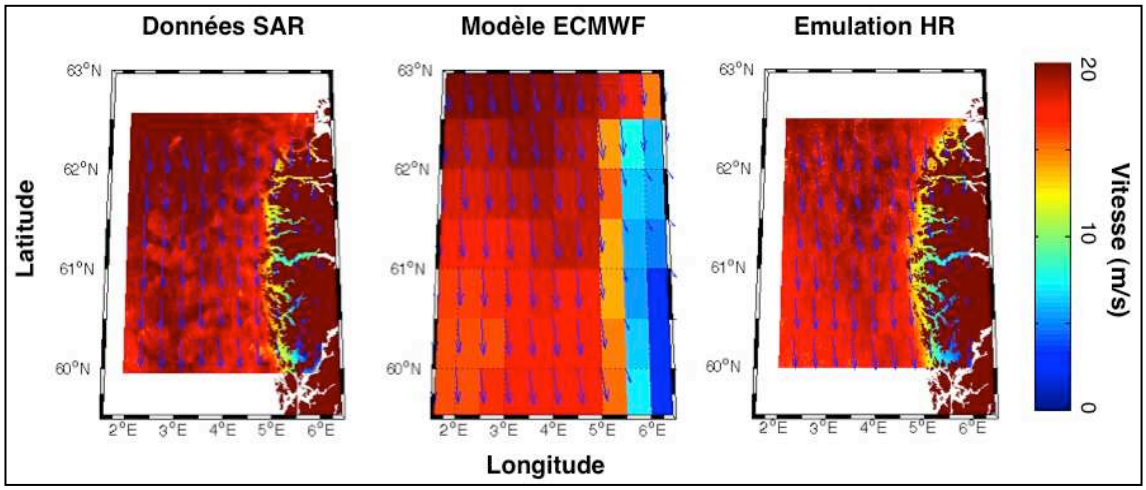

Figure 30. Principe de l'émulation haute-résolution de champs de vent à la surface de l'océan par apprentissage statistique : de gauche à droite, données SAR haute-résolution (~1x1km), prédiction basse-résolution (~50x50km) du modèle ECMWF, exemple d'émulation haute-résolution (HR) à partir de la prédiction basse-résolution ECMWF par apprentissage statistique à partir d'une base de données conjointes SAR/ECMWF.

- **Définition de nouveaux opérateurs d'observation par apprentissage statistique** : La deuxième approche vise à exploiter les techniques d'apprentissage statistique pour développer de nouveaux opérateurs d'observation H à haute résolution à partir d'observations et/ou sorties de modèles basse-résolution. L'estimation de champs de vent de surface en constitue une parfaite illustration (Figure 30). Alors que les champs de vent SAR (Chapron, Johnsen et al. 2001; Kerbaol, Collard 2005) fournissent des observations à haute-résolution (de l'ordre de 1 km), la récurrence spatio-temporelle de ces observations satellitaires est faible (de l'ordre de 10 jours pour les latitudes tempérées). Dans le même temps, les sorties de modèle (e.g., modèle ECMWF, http://www.ecmwf.int/) fournissent des prédictions avec une résolution spatiale relativement basse (50 km) mais pour un échantillonnage temporel régulier, typiquement de 6 heures. Ces prédictions présentent aussi des biais systématiques dans le domaine côtier du fait de caractéristiques locales (phénomènes d'abris près des îles ou d'accélération dans des fjords) non prises en compte dans les modèles opérationnels. En exploitant une base de données de champs de vent SAR haute-résolution pour une zone donnée et les sorties de modèle basse-résolution associées, l'objectif est d'apprendre la fonction de transfert entre basse résolution et haute résolution. Ce problème peut être vu comme une extension des méthodes de super-résolution d'images par apprentissage statistique (Baker, Kanade 2002). Une spécificité se situe ici dans la nécessité de spatialiser la fonction de transfert pour appréhender les biais systématiques du modèlebasse-résolution, là où elle est supposée stationnaire en traitement d'images. Il faut également souligner la nécessité de

prendre en compte des caractéristiques à différentes échelles (i.e., à la fois locales et globales) pour appréhender la variabilité des dynamiques observées (dans le cas des images naturelles, on se limite à des caractéristiques locales au sens d'une fenêtre autour de chaque point). Cette approche évaluée initialement pour les champs de vent (Figure 30) sera étendue à d'autres grandeurs géophysiques, y compris la définition de nouveaux opérateurs d'observation de champs de vitesse à partir de grandeurs scalaires advectées.

Le couplage de ces deux approches sera envisagé afin de combiner les nouveaux opérateurs d'observation définis par apprentissage statistique et des modèles dynamiques garantissant la consistance spatio-temporelle des champs reconstruits. Du point de vue méthodologique, on étudiera plus particulièrement la forme des opérateurs adjoints associés aux opérateurs d'observation introduits. Ces travaux sont développés en collaboration avec le LIAMA (T. Corpetti) et l'Ifremer/LOS (B. Chapron) dans le cadre du projet FI2O, et plus particulièrement de la thèse de Liyun He-Guelton (co-encadrement Ifremer/Telecom Bretagne) et du postdoctorat de S. Ba (Telecom Bretagne).

IV.4 Stratégie de fouille dans les bases d'observation de l'océan

Résumé des objectifs : *ce projet a pour objectif de développer des stratégies de fouille dans les bases d'observation de l'océan pour fournir aux thématiciens des outils opérationnels d'exploitation des bases de données disponibles et d'identification de processus et interactions-clés des systèmes étudiés. La démarche générale envisagée consiste à exploiter des méthodes de détection de signatures/évènements élémentaires (localisés en temps/espace-fréquence/échelle) des signaux considérés (séries temporelles, séries d'images mono-variées ou multi-variées,...) et modélisation des dépendances et/ou relations entre ces signatures élémentaires. Cette démarche sera déployée sur différents cas d'étude (e.g., structuration bottom-up à subméso- et méso-échelle du système du Humboldt, stratégies individuelles des prédateurs supérieurs, les biocarbonates marins comme marqueurs des évènements climatiques extrêmes).*

L'un des objectifs thématiques importants de ce projet de recherche est de mettre à disposition des thématiciens (e.g., océanographes, écologues) des outils et méthodes quantitatifs permettant de révéler les processus et interactions caractéristiques en jeu. D'un point de vue méthodologique, il s'agit de tirer partie des bases de données d'observation constituées et de proposer des stratégies de fouille de données permettant d'aller au-delà de l'analyse de corrélation classique.

Evènements et signatures élémentaires. L'originalité de l'approche proposée réside dans la définition et l'extraction d'évènements ou signatures élémentaires des processus étudiés. Alors que l'approche classique consiste généralement en une analyse et/ou décomposition des corrélations globales de séries d'observations associées aux processus étudiés (e.g., coefficient de corrélation, analyse en composantes principales) (Torrence, Compo 1998; Ghil, Allen et al. 2002; Rouyer, Fromentin et al. 2008), ces séries peuvent souvent être vues comme un ensemble d'évènements élémentaires (e.g., des motifs bouclants ou oscillants pour des données trajectométriques (cf. Figure 28), des motifs d'oscillation spécifiques dans des séries temporelles de paramètres géophysiques, des structures d'intérêt telles que les zones frontales ou les efflorescences algales pour les séries d'observation de la surface de l'océan, etc..). La détection et la caractérisation de ces évènements élémentaires permettront de passer de bases de données d'observations à des bases de données d'évènements élémentaires. Cette approche peut être vue comme une extension des approches fondées sur l'extraction de signatures locales pour l'analyse d'images et de vidéos (e.g., les points d'intérêt). La méthodologie d'analyse de signatures géométriques élémentaires de signaux multivariés (Partie IV.2) correspond à cette approche dans le cas de processus géométriques. On cherchera ici à l'étendre à d'autres types de processus (séries temporelles, séries d'images,...). L'objectif est ici double : 1) réaliser une compression d'information pour permettre une réelle exploration de la masse de données disponibles, 2) identifier les informations élémentaires utiles et caractéristiques des processus étudiés. Il s'agit très clairement de l'étape critique de la stratégie proposée et une attention particulière sera portée sur les critères statistiques de détection de ces signatures élémentaires (e.g., apprentissage de modèles a contrario).

Caractère multi-échelle des processus étudiés. La pertinence de cette stratégie de fouille résidera notamment dans la prise en compte du caractère intrinsèquement multi-échelle des processus étudiés. L'approche classique par corrélation, même lorsqu'elle utilise des techniques de décomposition multi-échelle (Rouyer, Fromentin et al. 2008; Rouyer, Fromentin et al. 2008) ou de décomposition spectrale (Ghil, Allen et al. 2002) repose sur l'évaluation d'un critère de corrélation globale, ne permet pas d'identifier directement des déterminismes impliquant des gammes d'échelles différentes ni de prendre en compte des évènements ponctuels (i.e, des corrélations significatives sur une certaine extension temps/espace-fréquence/échelle) ou d'éventuels déphasages

temporels. L'approche proposée devra permettre une telle analyse et reposera sur l'identification d'évènements élémentaires temps-fréquence ou espace-échelle (i.e., caractérisés par une certaine extension en temps/espace et fréquence/échelle). La décomposition et l'identification multi-échelle des déformations géométriques élémentaires le long de trajectoires constituent une illustration de cette approche pour des données trajectométriques (Fablet, Chaigneau et al. 2012; Fablet, Chaigneau et al. Soumis). On cherchera à l'étendre aux autres types de données traitées (séries temporelles, séries d'images) en combinant des techniques de décomposition multi-échelle des signaux et images et des méthodes de détection statistique de structures significatives dans les représentations temps-fréquence ou espace-échelle proposées. Le cadre d'analyse proposé devra également s'appliquer à l'analyse de tendance, correspondant généralement à un signal faible occulté par des variabilités à plus haute fréquence, la tendance pouvant être définie comme une composante basse-fréquence signficative.

La stratégie de fouille à proprement parler comportera deux étapes complémentaires :

- **la typologie des évènements élémentaires**. Cette typologie résultera de méthodes de classification non-supervisée (e.g., modèle de mélange, regroupement hiérarchique) sur la base des signatures des évènements considérés. On cherchera notamment à exploiter des métriques invariantes vis-à-vis de certains types de variabilité (e.g., déphasages locaux dans les séries temporelles, variabilité spatiales et temporelles des évènements identifiées dans des séries d'images satellitaires); Les catégories ainsi déterminées pourront notamment être exploités pour mettre en oeuvre des méthodes de type "sacs de mots visuels" (Sivic, Zisserman 2003) à l'échelle des séries d'observation ;
- **un processus de fouille des bases d'évènements élémentaires** pour identifier et caractériser les relations et associations caractéristiques entre ensembles d'évènements élémentaires. Différentes stratégies seront explorées, en premier lieu l'identification de règles d'association à partir d'analyse de cooccurrences de types d'évènements élémentaires. On cherchera également à exploiter les avancées récentes en termes d'apprentissage de modèles de classification et régression (e.g., méthodes SVM (Séparateurs à Vaste Marges), forêts aléatoires, réseaux de neurones et techniques associées d'apprentissage semi-supervisé et faiblement supervisé) pour mettre en évidence des relations significatives (mais non-linéaires) entre différents types d'évènements ;

Cette étape de fouille de données aura pour objectif premier de déterminer des représentations conceptuelles des déterminismes régissant les interactions entre les processus étudiés et fournira la base au développement de modèles numériques (en particulier stochastiques) de ces représentations. La thèse de B. Saulquin vise à explorer certains de ces aspects méthodologiques pour l'analyse de séries d'observation de la surface de l'océan (notamment les séries d'observations température de surface et de couleur de l'eau à des échelles régionales et globales).

Cette démarche générique sera plus particulièrement mise en œuvre dans le cadre de trois cas d'études :

- **L'analyse de l'impact des dynamiques physiques à mésoéchelle et submésoéchelle sur la structuration de l'environnement pélagique** (biogéochimie, macrozooplancton et poissons pélagiques) **dans le système du courant de Humboldt**. Ce cas d'étude développé dans le cadre du LMI DISCOH (collaborations avec l'IRD (A. Bertrand, A. Chaigneau) et l'IMARPE (J. Tam)) reposent sur l'analyse conjointe de données acoustiques sonar (cf. Figure 27), d'observations satellitaires (notamment les données altimétriques permettant d'estimer les dynamiques de mésoéchelle) et de données issues des campagnes océanographiques (notamment les mesures physiques et biogéochimiques sur des profils verticaux). Il s'appuie notamment sur la thèse de D. Grados (2011-2014) ;
- **La modélisation des stratégies des prédateurs supérieurs** (oiseaux marins et pêcheurs) en relation à la distribution spatiale des champs de proie et à la structuration physique dans le système du courant de Humboldt. Ces travaux menés dans le cadre du LMI DISCOH (collaborations avec l'IRD (UMRs EME et LEGOS) et l'IMARPE (J. Tam)) reposent sur l'analyse conjointe de données trajectométriques, de données acoustiques sonar et de séries de paramètres géophysiques issus d'observations satellitaires et sorties numériques de modèle (e.g., activité de l'upwelling, couleur de l'eau, activité à méso-échelle,...). Ils s'articulent notamment autour du co-encadrement de la thèse de R. Joo (2010-2013) ;
- **L'évaluation du potentiel des biocarbonates marins comme marqueurs individuels des évènements climatiques extrêmes** (cyclones, tempêtes). L'objectif est ici de mettre en relation les dynamiques de signatures surfaciques des extrêmes climatiques de vent observées par satellite (température de surface, salinité, champs de vent,..) et les dynamiques de signatures structurelles et biogéochimiques de biocarbonates marins (e.g., des coquilles de bivalves) pour définir de nouvelles variables des extrêmes climatiques. Ce cas d'étude fait l'objet d'une proposition de projet en cours de montage à l'interface des LabEx Mer et CominLabs avec l'Ifremer/LOS (B. Chapron) et le LEMAR (L. Chauvaud).

IV.5 Valorisation des travaux et insertion locale

Valorisation académique. Dans le prolongement des activités menées depuis 10 ans, ce projet de recherche a pour objectif de proposer des avancées significatives tant du point de vue méthodologique que du point de vue thématique. Dans cet esprit, la valorisation académique se fera dans des conférences et revues internationales à la fois du domaine du traitement du signal et des images et de la télédétection, et des conférences et revues thématiques (océanographie, écologie). On s'attachera également à développer de possibles valorisations opérationnelles (par exemple, de nouveaux produits d'océanographie spatiale en collaboration avec le CERSAT).

Insertion locale. Au-delà de cette valorisation académique devant contribuer à la visibilité des activités de recherche de Telecom Bretagne et du laboratoire LabSTICC (e.g., participations à des comités de programme), ce projet s'inscrit également dans une volonté de développer les dynamiques initiées au sein du département Signal & Communications de Telecom Bretagne et de l'équipe de TOMS du laboratoire LabSTICC, à travers différentes collaborations internes (cf. co-encadrements de thèses en cours). A l'échelle du LabSTICC, il a également pour objectif de développer une activité transversale entre les équipes TOMS et DECIDE sur les thématiques de fouilles de données signal/image. Cette contribution devra notamment se structurer à travers des participations et/ou coordinations de projets nationaux et/ou internationaux (e.g., ANR, FP7,...) s'appuyant notamment pour les orientations thématiques Mer sur les collaborations académiques et industrielles développés dans le cadre des structures "régionales" Europôle Mer et pôle Mer (e.g., Ifremer, IRD, LEMAR pour les partenaires académiques; Sercel, iXSea, CLS pour les partenaires industriels). Ce projet vise également à développer les collaborations nationales et internationales existantes (e.g., UMR EME, LIAMA (Chine), IMARPE/LMI DISCOH (Pérou)) ainsi que de nouvelles collaborations (e.g., Woods Hole Oceanographic Institution, EU).

Retombées méthodologiques. Il peut être souligné que les avancées méthodologiques attendues (e.g. caractérisation et la modélisation stochastique de la géométrie de courbes planes, super-résolution spatio-temporelle variationnelle, méthodes de fouille de données multi-échelle/multivariées) pourront trouver des applications dans d'autres champs applicatifs que ceux privilégiés ici (e.g., données multimédia, télédétection terrestre, imagerie médicale, problématiques de surveillance, astronomie, ...).

Contributions à la formation. Il est également attendu de ce projet de recherche des contributions directes aux activités d'enseignement de Telecom Bretagne au-delà de l'encadrement de thèses et projets d'étudiants en relation thématique directe avec ce projet, plus particulièrement à deux niveaux : la proposition de nouveaux modules de formation en lien avec les thématiques de recherche développées (UVs de dernière année, formation continue) et de développement des relations internationales en termes de programme d'échanges étudiants au niveau ingénieur/master et thèse.

V Bibliographie

Allemand, D., N. Mayer-Gostan, H. de Pontual, G. Boeuf et P. Payan (2007). Fish Otolith Calcification in Relation to Endolymph Chemistry. Handbook of biomineralization. E. Bäuerlein, Behrens, P., and Epple, M. (eds.), Wiley. 1**:** 291-308.

Anderson, C. I. H., J. K. Horne et J. Boyle (2007). Classifying multi-frequency fisheries acoustic data using a robust probabilistic classification technique. Journal of the Acoustical Society of America, 121(6): EL230-EL237.

Aoki, I. (1980). An analysis of the schooling behavior of fish: internal organisation and communication process. Bulletin of the Oceanic Research Institute of the University of Tokyo, 12: 1-65.

Aujol, J. F., G. Aubert et L. Blanc-Féraud (2003). Wavelet-based level set evolution for classification of textured images. IEEE Trans. on Image Processing, 12(12): 1634-1641.

Axelsen, B. E., T. Anker-Nilssen, P. Fossum, C. Kvamme et L. Nøttestad (2001). Pretty patterns but a simple strategy: predator-prey interactions between juvenile herring and Atlantic puffins observed with multibeam sonar. Canadian Journal of Zoology, 79(9): 1586–1596.

Ba, S., E. Autret, B. Chapron et R. Fablet (2012). Statistical descriptors of ocean regimes from the geometric regularity of Sea Surface Temperature observations. IEEE Geoscience and Remote Sensing Letters, Sous Presse.

Ba, S., B. Chapron, T. Corpetti et R. Fablet (Soumis). Multi-resolution missing data interpolation in geophysical image sequences.

Ba, S. et R. Fablet (2011). Multi-resolution missing data interpolation in SST image series. Proc. 18th IEEE Int. Conf. on Image Processing, ICIP'2011, Brussels, septembre.

Baker, S. et T. Kanade (2002). Limits on super-resolution and how to break them. IEEE Trans. on Pattern Analysis and Machine Intelligence, 24(9): 1167-1183.

Ballon, M., A. Bertrand, A. Lebourges-Dhaussy, M. Gutierrez, P. Ayon, et al. (2011). Is there enough zooplankton to feed forage fish populations off Peru? An acoustic (positive) answer. Progress In Oceanography, 9(4): 360–381.

Barraquand, F. et S. Benhamou (2008). Animal movements in heterogeneous landscapes: identifying profitable places and homogeneous movement bouts. Ecology, 89: 3336-3348.

Begg, G. et R. Brown (2000). Stock identification of haddock melanogrammus aeglefinus on georges bank based on otolith shape analysis. Trans. of the American Fisheries Society, 129(1): 935-945.

Benhamou, S. (2004). How to reliably estimate the tortuosity of an animal's path: straightness, sinuosity, or fractal dimension? . Journal of Theoretical Biology, 229: 209-220.

Bernard, D., G. Boffetta, A. Celani et G. Falkovich (2006). Conformal invariance in two-dimensional turbulence. Nature Physics, 2(2): 124-128.

Bertrand, A., M. Ballon et A. Chaigneau (2010). Acoustic Observation of Living Organisms Reveals the Upper Limit of the Oxygen Minimum Zone. PLoS ONE, 5(4): e10330.

Bertrand, S., A. Bertrand, R. Guevara-Carrasco et F. Gerlotto (2007). Scale-invariant movements of fishermen: The same foraging strategy as natural predators. Ecological Applications, 17: 331-337.

Bertrand, S., E. Díaz et M. Ñiquen (2004). Interactions between fish and fisher's spatial distribution and behaviour: the anchovy (Engraulis ringens) fishery of Peru. ICES Journal of Marine Science, 61: 1127-1136.

Bertrand, S., R. Joo et R. Fablet (Soumis). Do foragers move Lévy or not? Let Generalized Pareto decide.

Black, M. et A. Rangarajan (1996). On the unification of line processes, outlier rejection and robust statistics with applications in early vision. International Journal of Computer Vision, 19(5): 57-92.

Block, B. A., S. L. H. Teo, A. Walli, A. Boustany, M. J. W. Stokesbury, et al. (2005). Electronic tagging and population structure of Atlantic bluefin tuna. Nature, 434(7037): 1121-1127.

Blondel, P. (2009). The handbook of sidescan sonar. Springer.

Burgos, J. M. et J. K. Horne (2008). Acoustic characterization and classification of pelagic organism distributions. ICES Journal of Marine Science, 65: 1235-1247.

Calenge, C., S. Dray et M. Royer-Carenzi (2009). The concept of animals trajectories from a data analysis perspective. Ecological Informatics, 4: 34-41.

Campana, S. et J. Casselman (1993). Stock discrimination using otolith shape analysis. Canadian Journal of Fisheries and Aquatic Sciences, 50: 1062-1083.

Campana, S. E. (1990). How Reliable are Growth Back-Calculations Based on Otoliths? Canadian Journal of Fisheries and Aquatic Sciences, 47(11): 2219–2227.

Campana, S. E. (2001). Accuracy, precision and quality control in age determination, including a review of the use and abuse of age validation methods. Journal of Fish Biology, 59(2): 197-242.

Cao, F. et R. Fablet (2006). Automatic morphological detection of otolith nucleus. Pattern Recognition Letters, 27(6): 658-666.

Cardy, J. (2006). The power of two dimensions. Nature Physics, 2: 67-68.

Caselles, V., J. M. Morel et C. Sbert (1998). An axiomatic approach to image interpolation. IEEE Trans. on Image Processing, 7(3): 376-386.

Chainais, P. (2007). Infinitely Divisible Cascades to Model the Statistics of Natural Images. IEEE Trans. on Pattern Analysis and Machine Intelligence, 29(12): 2105-2119.

Chapelle, O., B. Schölkopf et A. Zien (2006). Semi-supervised learning. MIT Press.

Chapron, B., H. Johnsen et R. Garello (2001). Wave and wind retrieval from sar images of the ocean. Annals of Telecommunications, 56(11): 682-699.

Charef, A., S. Ohshimo, I. Aoki et N. Al Absi (2010). Classification of fish schools based on evaluation of acoustic descriptor characteristics. Fisheries Science, 76(1): 1-11.

Chauvaud, L., A. Lorrain, R. B. Dunbar, Y.-M. Paulet, G. Thouzeau, et al. (2005). Shell of the Great Scallop Pecten maximus as a high-frequency archive of paleoenvironmental changes. Geochem. Geophys. Geosyst., 6(8): 1-15.

Chavez, F., A. Bertrand, R. Guevara-Carrasco, P. Soler et J. Csirke (2008). The northern Humboldt Current System: Brief history, present status and a view towards the future. Progress in Oceanography, 79: 95-105.

Chavez, F. P., J. Ryan, S. E. Lluch-Cota et M. Ñiquen (2003). From anchovies to sardines and back: multidecadal change in the Pacific Ocean. Science, 299: 217-221.

Chessel, A. (2007). Otolithes et vision par ordinateur: de la perception visuelle à une représentation des connaissances. Univsersité Rennes 1. Thèse de doctorat.

Chessel, A., F. Cao et Fablet (2006). Interpolation of orientation: an axiomatic approach. Proc. European Conference on Computer Vision, ECCV06, LNCS 3954:241-254, Graz, Autriche, mai.

Chessel, A., R. Fablet et F. Cao (2008). Computer vision and otolith: towards a modelisation of the morphogenesis of accretionary processes. European series in applied and industrial mathematics - ESAIM, 22: 150-154.

Chuang, G. C. et C. Kuo (1996). Wavelet descriptor of planar curves: theory and applications. IEEE Trans. on Image Processing, 5(1): 56–70.

Courbin, N., R. Fablet, C. Mellon et H. l. n. de Pontual (2007). Are hake otolith macrostructures randomly deposited? Insights from an unsupervised statistical and quantitative approach applied to Mediterranean hake otoliths. ICES Journal of Marine Science, 64(6): 1191-1201.

Dance, C., J. Willamowski, L. Fan, C. Bray et G. Csurka (2004). Visual categorization with bags of keypoints. ECCV International Workshop on Statistical Learning in Computer Vision, Prague, République Tchèque, mai.

Dannevig, E. H. (1956). Chemical Composition of the Zones in Cod Otoliths. ICES Journal of Marine Science, 21(2): 156-159.

Daverat, F., J. Martin, R. Fablet et C. Peycheran (2010). Colonisation tactics of three temperate catadromous species, Eel Anguilla anguilla, mullet Liza ramada and flounder Plathychtys flesus, revealed by Bayesian multielemental otolith microchemistry approach. Ecology of Freshwater Fish, 20: 42-51.

de Pontual, H. (2009). Concepts et méthodes en sclérochronologie pour l'halieutique. Université Paris XIII. Mémoire d'Habilitation à Diriger les Recherches.

de Pontual, H., M. Bertignac, A. Battaglia, G. Bavouzet, P. Moguedet, et al. (2003). A pilot tagging experiment on European hake (Merluccius merluccius): methodology and preliminary results. ICES Journal of Marine Science, 60(6): 1318-1327.

de Pontual, H. et A. J. Geffen (2002). Otolith Microchemistry Manual of fish sclerochronolgy. J. Panfili, H. de Pontual, H. Troadec and P. J. Wright, Ifremer- IRD coédition, Brest, France, 464 p**:** 243-302.

de Pontual, H., A. Jolivet, M. Bertignac et R. Fablet (Soumis). How does European hake Merluccius merluccius move? In what thermal environment? Insights from a pilot archival tagging experiment.

Dempster, A., N. Laird et D. Rubin (1977). Likelihood from incomplete data via the em algorithm. Journal of the Royal Statistic Society Series B, 39(1): 1-38.

Deriche, R. (1987). Using Canny's criteria to derive a recursively implemented optimal edge detector. Int. Journal on Computer Vision, 1: 167-187.

Descombes, X. (2011). Stochastic geometry for image analysis. Wiley.

Desolneux, A., L. Moisan et J. M. More (2003). A Grouping principle and four applications. IEEE Trans. on Pattern Analysis and Machine Intelligence, 25(4): 508-513.

Desolneux, A., L. Moisan et J. M. More (2008). From Gestalt Theory to Image Analysis. A Probabilistic Approach. Springer.

Devereux, I. (1967). Temperature measurements from oxygen isotope ratios of fish otoliths. Science, 155: 1684-1685.

Duarte-Neto, P., R. Lessa, B. Stosic et M. E. (2008). The use of sagittal otoliths in discriminating stocks of common dolphinfish (coryphaena hippurus) off northeastern brazil using multishape descriptors. ICES Journal of Marine Science, 65(7): 1144-1152.

Elsdon, T. S. et B. M. Gillanders (2006). Temporal variability in strontium, calcium, barium, and manganese in estuaries: Implications for reconstructing environmental histories of fish from chemicals in calcified structures. Estuarine Coastal and Shelf Science, 66(1-2): 147-156.

Elsdon, T. S., B. K. Wells, S. E. Campana, B. M. Gillanders, C. M. Jones, et al. (2008). Otolith chemistry to describe movements and life-history parameters of fishes: Hypotheses, assumptions, limitations and inferences. Oceanography and Marine Biology: an Annual Review, Vol 46. Boca Raton, Crc Press-Taylor & Francis Group. 46**:** 297-330.

Fablet, R. (2006). Semi-local extraction of ring structures in images of biological hard tissues: application to the Bayesian interpretation of fish otoliths for age and growth estimation. Canadian Journal of Fisheries and Aquatic Sciences, 63(7): 1414-1428.

Fablet, R. et J.-M. Augustin (2006). Unsupervised calibrated sonar imaging for seabed observation using hidden Markov Random fields. Proc. IEEE Int. Conf. on Acoustics, Speech and Signal Processing, ICASSP'2006, Toulouse, mai.

Fablet, R., J.-M. Augustin et A. Isar (2005). Multi-wavelet variational image denoising. Proc. of 12th IEEE Int. Conf. on Image Processing, ICIP'2005, Genoa, septembre.

Fablet, R., A. Benzinou et C. Doncarli (2003). Robust time-frequency model estimation in otolith images for fish age and growth analysis. IEEE Int. Conf. on Image Processing, ICIP'2003, Barcelone, Catalogne, septembre.

Fablet, R., A. Chaigneau et S. Bertrand (2012). Analyse multi-échelle de la géométrie des courbe planes. 18ème Congrès Francophone AFRIF-AFIA de Reconnaissance des Formes et Intelligence Artificielle, RFIA'2012, Lyon, janvier.

Fablet, R., A. Chaigneau et S. Bertrand (Soumis). Multiscale geometric deformations along planar curves: application to satellite tracking and ocean observation data.

Fablet, R., F. Daverat et H. De Pontual (2007). Unsupervised Bayesian reconstruction of individual life histories from otolith signatures: case study of Sr : Ca transects of European eel (Anguilla anguilla) otoliths. Canadian Journal of Fisheries and Aquatic Sciences, 64(1): 152-165.

Fablet, R., P. Gay, S. Peraltilla, C. Peña, R. Castillo, et al. (Accepté). Bags-of-Features for fish school cluster characterization in pelagic ecosystems: application to the discrimination of juvenile and adult anchovy clusters off Peru.

Fablet, R. et N. Le Josse (2005). Automated fish age estimation from otolith images using statistical learning. Fisheries Research, 72(2-3): 279-290.

Fablet, R., R. Lefort, I. Karoui, L. Berger, J. Massé, et al. (2009). Classifying fish schools and estimating their species proportions in fishery-acoustic surveys. ICES Journal of Marine Science, 66(6): 1136-1142.

Fablet, R., L. Pecquerie, H. de Pontual, H. Hoie, R. Millner, et al. (2011). Shedding Light on Fish Otolith Biomineralization Using a Bioenergetic Approach. PLoS ONE, 6(11): e27055.

Fablet, R., S. Pujolle, A. Chessel, A. Benzinou et F. Cao (2008). 2D Image-based reconstruction of shape deformation of biological structures using a level-set representation. Computer Vision and Image Understanding, 111(3): 295-306.

Fauchald, P. et T. T. (2003). Using First-Passage Time in the analysis of area-restricted search and habitat selection. Ecology, 84: 282-288.

Fergus, R., P. Perona et A. Zisserman (2006). Weakly supervised scaled- invariant learning of models for visual recognition. International Journal of Computer Vision, 71(3): 273-303.

Fernandes, P. G. (2009). Classification trees for species identification of fish-school echotraces. ICES Journal of Marine Science, 66(6): 1073-1080.

Fréon, P. et O. A. Misund (1999). Dynamics of Pelagic Fish Distribution and Behaviour: Effects on Fisheries and Stock Assessment. Blackwell Science, London.

Fritz, H., S. Said et H. Weimerskirch (2003). Scale-Dependent Hierarchical Adjustments of Movement Patterns in a Long-Range Foraging Seabird. Philosophical Transactions of the Royal Society B: Biological Sciences, 270(1520): 1143-1148.

Fromentin, J.-M., B. Ernande, R. Fablet et H. de Pontual (2009). Importance and future of individual markers for the ecosystem approach to fisheries. Aquatic Living Resources, 22(04): 395-408.

Fromentin, J.-M., B. Planque et O. Thébaud (2007). L'approche écosystémique des pêches : quelles priorités pour la recherche ? Rapport Ifremer.

Gaillard, F., E. Autret, V. Thierry, P. Galaup, C. Coatanoan, et al. (2009). Quality Control of Large Argo Datasets. Journal of atmospheric and oceanic technology, 26(2): 337-351.

Garcia, S. M. et K. L. Cochrane (2005). Ecosystem approach to fisheries: a review of implementation guidelines. ICES Journal of Marine Science, 62(3): 311-318.

Gauldie, R. W. et C. R. Romanek (1998). Orange roughy otolith growth rates: a direct experimental test of the Romanek-Gauldie otolith growth model. Comparative Biochemistry and Physiology - Part A: Molecular & Integrative Physiology, 120(4): 649-653.

Ghil, M., M. R. Allen, M. D. Dettinger, K. Ide, D. Kondrashov, et al. (2002). Advanced spectral methods for climatic time series. Rev. Geophys., 40(1): 1003.

Gould, J., D. Roemmich, S. WIJFFELS, H. FREELAND, M. IGNASZEWSKY, et al. (2004). Argo Profiling Floats Bring New Era of In Situ Ocean Observations. EOS, 85(19).

Grados, D., R. Fablet, M. Ballon, N. Bez, R. Castillo, et al. (2012). Multiscale analysis of the spatial interactions between ecosystem components from acoustic survey data: application of the Northern SCH off Peru. Canadian Journal of Fisheries and Aquatic Sciences, Sous presse.

Gutierrez, M., G. Schwartzman, A. Bertrand et S. Bertrand (2007). Anchovy (Engraulis ringens) and sardine (Sardinops sagax) spatial dynamics and aggregation patterns in the Humboldt Current ecosystem, Peru, from 1983–2003. Fisheries Oceanography, 16(2): 155–168.

Hammond, T. R., G. L. Swartzman et T. S. Richardson (2001). Bayesian estimation of fish school cluster composition applied to a Bering Sea acoustic survey. ICES Journal of Marine Science, 58(6): 1133-1149.

Haralambous, J. et S. Georgakarakos (1996). Artificial neural networks as a tool for species identification of fish schools. ICES Journal of Marine Science, 53(2): 173-180.

Heiler, M. et C. Schnorr (2003). Natural image statistics for natural image segmentation. Proc. IEEE Int. Conf. on Computer Vision, ICCV'2003, Nice, France, octobre.

Hellequin, L., J. M. Boucher et X. Lurton (2003). Processing of high-frequency multibeam echo sounder data for seafloor characterization. IEEE Journal of Oceanic Engineering, 28(1): 78-89.

Høie, H., A. Folkvord, H. Mosegaard, L. Li, L. A. W. Clausen, et al. (2008). Restricted fish feeding reduces cod otolith opacity. Journal of Applied Ichthyology, 24: 138-143.

Humphries, N. E., N. Queiroz, J. R. M. Dyer, N. G. Pade, M. K. Musyl, et al. (2010). Environmental context explains Lévy and Brownian movement patterns of marine predators. Nature, 465(7301): 1066-1069.

Hunter, E., J. D. Metcalfe et J. D. Reynolds (2003). Migration route and spawning area fidelity by North Sea plaice. Proceedings of the Royal Society of London. Series B: Biological Sciences, 270(1529): 2097-2103.

Hussy, K. et H. Mosegaard (2004). Atlantic cod (Gadus morhua) growth and otolith accretion characteristics modelled in a bioenergetics context. Canadian Journal of Fisheries and Aquatic Sciences, 61(6): 1021-1031.

Iturbe, I., P. Roux, B. Nicolas, J. Virieux et J. I. Mars (2009). Shallow-Water Acoustic Tomography Performed From a Double-Beamforming Algorithm: Simulation Results. IEEE Journal of Oceanic Engineering, 34(2): 140-149.

Jech, J. M. et W. L. Michaels (2007). A multifrequency method to classify and evaluate fisheries acoustics data (vol 63, pg 2225, 2006). Canadian Journal of Fisheries and Aquatic Sciences, 64(2): 386-386.

Jehan-Besson, S., M. Barlaud et G. Aubert (2003). Image segmentation using active contours: calculus of variations or shape gradients? SIAM Journal of Applied Mathematics, 63(6): 2128-2154.

Jolivet, A. (2009). Compréhension des mécanismes de Biominéralisation de l'otolithe : quantification spatialisée des fractions minérale et organique et influence des facteurs environnementaux. Université de Bretagne Occidentale. Thèse de doctorat.

Jolivet, A., J.-F. Bardeau, R. Fablet, Y.-M. Paulet et H. de Pontual (2008). Understanding otolith biomineralization processes: new insights into microscale spatial distribution of organic and mineral fractions from Raman microspectrometry. Analytical and Bioanalytical Chemistry, 392(3): 551-560.

Jolivet, A., H. de Pontual, M. Hervy, Y.-M. Paulet et R. Fablet (2012). Preliminary observations of survival and growth of European hake in captivity. Aquaculture Research, sous presse.

Kanizsa, G. (1996). La grammaire de voir. Diderot.

Karoui, I. (2007). Segmentation par méthodes markoviennes et variationnelles des images texturées : application à la caractérisation sonar des fonds marins. Institut Telecom, Telecom Bretagne. Thèse de doctorat.

Karoui, I., R. Fablet, J. M. Boucher et J.-M. Augustin (2010). Variational region-based segmentation using multiple texture statistics. IEEE Trans. on Image Processing, 30(3): 3146-3156.

Karoui, I., R. Fablet, J. M. Boucher et J. M. Augustin (2008). Fusion of textural statistics using a similarity measure: application to texture recognition and segmentation. Pattern Analysis and Applications, 11(3-4): 425-434.

Karoui, I., R. Fablet, J. M. Boucher et J. M. Augustin (2008). Segmentation d'images sonar texturées par une approche variationnelle basée région. Traitement du Signal, 25(1-2): 73-85.

Karoui, I., R. Fablet, J. M. Boucher et J. M. Augustin (2009). Seabed segmentation using optimized statistics of sonar textures. IEEE Trans. on Geoscience and Remote Sensing, 47(6): 1621-1631.

Kenny, A. J., I. Cato, M. Desprez, G. Fader, R. T. E. Sch√ºttenhelm, et al. (2003). An overview of seabed-mapping technologies in the context of marine habitat classification. ICES Journal of Marine Science, 60(2): 411-418.

Kerbaol, V. et F. Collard (2005). SAR-Derived coastal and marine applications: from research to operational products. IEEE Journal of Oceanic Engineering, 30(3): 472-486.

Kilfoyle, D. B. et A. B. Baggeroer (2000). The state of the art in underwater acoustic telemetry. IEEE Journal of Oceanic Engineering, 25(1): 4-27.

Kim, W. Y. et Y. S. Kim (2000). A region-based shape descriptor using zernike moments. Signal Processing: Image Communication, 16: 95-102.

Kloser, R. J., T. Ryan, P. Sakov, A. Willliams et J. A. Koslow (2002). Species identification in deep water using multiple acoustic frequencies. Canadian Journal of Fisheries and Aquatic Sciences, 59: 1065–1077.

Kloser, R. J., T. E. Ryan, J. W. Young et M. E. Lewis (2009). Acoustic observations of micronekton fish on the scale of an ocean basin: potential and challenges. ICES Journal of Marine Science, 66(6): 998-1006.

Kooijman, S. A. L. M. (2010). Dynamic Energy Budget theory for Metabolic Organisation. Cambridge University Press.

Korneliussen, R. J., Y. Heggelund, I. K. Eliassen et G. O. Johansen (2009). Acoustic species identification of schooling fish. ICES Journal of Marine Science, 66(6): 1111-1118.

Koslow, J. A. (2009). The role of acoustics in ecosystem-based fishery management. ICES Journal of Marine Science, 66(6): 966-973.

Landa, J., I. Quincoces, R. Duarte, A. C. Fari√±a et H. Dupouy (2008). Movements of black and white anglerfish (Lophius budegassa and L. piscatorius) in the northeast Atlantic. Fisheries Research, 94(1): 1-12.

Latecki, L. J. et R. Lakamper (2002). Shape similarity measure based on correspondence of visual parts. IEEE Trans. on Pattern Analysis and Machine Intelligence, 22(10): 1185-1190.

Lazebnik, S., C. Schmid et J. Ponce (2005). A sparse texture representation using local affine regions. IEEE Trans. on Pattern Analysis and Machine Intelligence, 27(8): 1265-1278.

Le Chenadec, G. et J. M. Boucher (2007). Angular dependence of K-distributed sonar data. IEEE Trans. on Geoscience and Remote Sensing, 45(5-6): 1224-1235.

Le-Dimet, F. X. et O. Talagrand (1986). Variational algorithms for analysis and assimilation of meteorological observations: theoretical aspects. Tellus: 97-110.

Lebourges-Dhaussy, A., J. Coetzee, L. Hutchings, G. Roudaut et C. Nieuwenhuys (2009). Zooplankton spatial distribution along the South African coast studied by multifrequency acoustics, and its relationships with environmental parameters and anchovy distribution. ICES Journal of Marine Science, 66(6): 1055-1062.

Lefort, R. (2010). Apprentissage et classification faiblement supervisée : Application en acoustique halieutique. Institut Telecom, Telecom Bretagne. Thèse de doctorat.

Lefort, R., R. Fablet, L. Berger et J. M. Boucher (2012). Spatial Statistics of Objects in 3-D Sonar Images: Application to Fisheries Acoustics. Geoscience and Remote Sensing Letters, 9(1): 56-59.

Lefort, R., R. Fablet et J. M. Boucher (2010). Weakly Supervised Classification of Objects in Images Using Soft Random Forests. Proc. Eur. Conf. on Computer Vision, ECCV'2010, LNCS 6314:185-198, Heraklion, Chypre, septembre.

Lefort, R., R. Fablet et J. M. Boucher (2011). Object recognition using proportion-based prior information: Application to fisheries acoustics. Pattern Recognition Letters, 32(2): 153-158.

Lefort, R., R. Fablet et J. M. Boucher (2011). Spatial Statistics of Objects in 3-D Sonar Images: Application to Fisheries Acoustics. Geoscience and Remote Sensing Letters: 56-59.

Ling, H. et S. S. (2007). Proximity distribution kernels for geometric context in category recognition. Int. Conference on Computer Vision, ICCV2007, Rio de Janeiro, Brésil, octobre.

Lions, J. L. (1971). Optimal Control of Systems Governed by Partial Differential Equations. Springer-Verlag.

Lurton, X. (2002). An introduction to underwater acoustics: principles and applications. Springer.

Maître, H. (2008). Processing of Synthetic Aperture Radar Images. Wiley.

Mallat, S. (2008). A Wavelet Tour of Signal Processing. Academic Press.

Mandelbrot, B. (1982). The Fractal Geometry of Nature. Hardback.

Mikolajczyk, K. et C. Schmid (2005). A performance evaluation of local descriptors. IEEE Trans. on Pattern Analysis and Machine Intelligence, 27(10): 1615-1630.

Mikolajczyk, K., T. Tuytelaars, C. Schmid, A. Zisserman, J. Matas, et al. (2005). A comparison of affine region detectors. International Journal of Computer Vision, 65: 43-72.

Mitsuguchi, T., E. Matsumoto, O. Abe, T. Uchida et P. J. Isdale (1996). Mg/Ca Thermometry in Coral Skeletons. Science, 274(5289): 961-963.

Mokhtarian, F. et A. K. Mackworth (1986). Scale-based description and recognition of planar curves and two-dimensional shapes. IEEE Trans. on Pattern Analysis and Machine Intelligence, 8(1): 34-43.

Møller, J., A. Syversveen et R. Waagepetersen (1998). Log gaussian cox processes. Scandinavian Journal of Statistics, 25(3): 451-462.

Nasreddine, K., A. Benzinou et R. Fablet (2009). Shape geodesics for the classification of calcified structures: Beyond Fourier shape descriptors. Fisheries Research, 98(1-3): 8-15.

Nasreddine, K., A. Benzinou et R. Fablet (2010). Variational shape matching for shape classification and retrieval. Pattern Recognition Letters, 31(12): 1650-1657.

Nguyen, H.-G. (2011). Caractérisation et modélisation de la distribution spatiale de signatures locales dans les images : application à la cartographie des fonds marins. Institut Telecom, Telecom Bretagne. Thèse de doctorat.

Nguyen, H.-G., R. Fablet et J. M. Boucher (2010). Spatial statistics of visual keypoints for texture recognition. Proc. Eur. Conf. on Computer Vision, ECCV'2010, LNCS 6314:764-777, Heraklion, Chypre, septembre.

Nguyen, H.-G., R. Fablet et J. M. Boucher (2011). Visual textures as realizations of multivariate log-Gaussian Cox processes. Proc. IEEE Conf. on Computer Vision and Pattern recognition, CVPR'2011, Colorado Springs, juin.

Nguyen, H.-G., R. Fablet et J. M. Boucher (2012). Keypoint-based analysis of sonar images: application to seabed recognition. IEEE Trans. on Geoscience and Remote Sensing, sous presse.

Nystuen, J. A. et H. D. Selsor (1997). Weather Classification Using Passive Acoustic Drifters. Journal of atmospheric and oceanic technology, 14: 656-666.

Panfili, J., H. de Pontual, H. Troadec et P. Wright (2002). Manual of Fish Sclerochronology. Eds. Ifremer.

Papadakis, N., T. Corpetti et E. Mémin (2007). Dynamically consistent optical flow estimation. IEEE International Conference on Computer Vision, ICCV'07, Rio de janeiro, Brésil, octobre.

Pauly, D., V. Christensen et C. Walters (2000). Ecopath, Ecosim, and Ecospace as tools for evaluating ecosystem impact of fisheries. ICES Journal of Marine Science, 57(3): 697-706.

Pecquerie, L., R. Fablet, P. Petitgas, M. Alunno-Bruscia, H. de Pontual, et al. (2012). Reconstructing individual food and growth histories from biogenic carbonates. Marine Ecology Progress Series, 447: 151-164.

Petitgas, P. et J. J. Levenez (1996). Spatial organisation of pelagic fish: echogram structure, spatio-temporal condition, and biomass in Senegalese waters. ICES Journal of Marine Science, 53(2): 147-153.

Petitgas, P., J. Masse, P. Beillois, E. Lebarbier et A. Le Cann (2003). Sampling variance of species identification in fisheries-acoustic surveys based on automated procedures associating acoustic images and trawl hauls. ICES Journal of Marine Science, 60(3): 437-445.

Pieczynski, W. (1992). Statistical image segmentation. Machine Graphics and Vision, 1(2): 261-268.

Quinlan, J. (1993). C4.5: Programs for machine learning. Morgan Kaufmann Publishers.

Rabaste, O. et T. Chonavel (2007). Estimation of Multipath Channels With Long Impulse Response at Low SNR via an MCMC Method. IEEE Trans. on Signal Processing, 55(4): 1312-1325.

Rabiner, L. R. (1989). A tutorial on hidden markov models and selected applications in speech recognition. Proceedings of the IEEE: 257-286.

Randen, T. et J. H. Husoy (1999). Filtering for texture classification: a comparative study. IEEE Trans. on Pattern Analysis and Machine Intelligence, 21(4): 291-310.

Robertson, S. et A. Morison (1999). A trial of artificial neural networks for automatically estimating the age

of fish. Marine and Freshwater Research, 50(1): 73-82.

Romanek, C. S. et R. W. Gauldie (1996). A predictive model of otolith growth in fish based on the chemistry of the endolymph. Comp. Biochem. Phys. A, Physiology, 114(1): 71-79.

Rouyer, T., J. M. Fromentin, F. Ménard, B. Cazelles, K. Briand, et al. (2008). Complex interplays among population dynamics, environmental forcing, and exploitation in fisheries. Proceedings of the National Academy of Sciences, 105(14): 5420-5425.

Rouyer, T., J. M. Fromentin, N. C. Stenseth et B. Cazelles (2008). Analysing multiple time series and extending significance testing in wavelet analysis. Marine Ecology Progress Series, 359: 11-23.

Roy, N., Y. Simard et C. d. Gervaise (2010). 3D tracking of foraging belugas from their clicks: Experiment from a coastal hydrophone array. Applied Acoustics, 71(11): 1050-1056.

Scalabrin, C., N. Diner, A. Weill, A. Hillion et M. C. Mouchot (1996). Narrowband acoustic identification of monospecific fish shoals. ICES Journal of Marine Science, 53(2): 181-188.

Sebastian, T. B., P. N. Klein et B. B. Kimia (2003). On aligning curves. IEEE Trans. on Pattern Analysis and Machine Intelligence, 25(1): 116-125.

Shlesinger, M. F., G. Zaslavsky et U. Frisch (1995). Lévy Flights and Related Topics in Physics. Springer.

Simmonds, J. et D. MacLennan (2005). Fisheries acoustics: theory and practice. Oxford: Blackwell Science Ltd.

Sivic, J. et A. Zisserman (2003). Video Google: A Text Retrieval Approach to Object Matching in Videos. Proc. Int. Conf. on Computer Vision, ICCV'2003, Nice, France, octobre.

Socheleau, F.-X., C. Laot et J.-M. Passerieux (2011). Stochastic Replay of non-WSSUS Underwater Acoustic Communication Channels Recorded at Sea. IEEE Trans. on Signal Processing, 59(10): 4838-4849.

Sole, A., V. Caselles, G. Sapiro et F. Arandiga (2004). Morse description and geometric encoding of digital elevation maps. IEEE Trans. on Image Processing, 13(9): 1245-1262.

Stanton, T., D. Chu et P. H. Wiebe (1996). Acoustic scattering characteristics of several zooplankton groups. ICES Journal of Marine Science, 53: 289-295.

Stern, N. (2006). Stern Review on The Economics of Climate Change.HM Treasury, London.

Stoyan, D. et H. Stoyan (1994). Fractals, random shapes and point fields. Wiley.

Tew Kai, E., V. Rossi, J. Sudre, H. Weimerskirch, C. Lopez, et al. (2009). Top marine predators track Lagrangian coherent structures. Proceedings of the National Academy of Sciences, 106(20): 8245-8250

Torrence, C. et G. P. Compo (1998). A Practical Guide to Wavelet Analysis. Bulletin of the American Meteorological Society, 79(1): 61–78.

Tremblay, Y., A. J. Roberts et D. P. Costa (2007). Fractal landscape method: an alternative approach to measuring area-restricted searching behavior. Journal of Experimental Biology, 210: 935-945.

Trenkel, V. M., V. Mazauric et L. Berger (2008). The new fisheries multibeam echosounder ME70: description and expected contribution to fisheries research. ICES Journal of Marine Science, 65(4): 645-655.

Troadec, H., A. Benzinou, V. Rodin et J. L. Bihan (2000). Use of deformable templates for otolith 2D growth ring detection by digital image processing. Fisheries Research, 46(1-3): 155-163.

Tschumperlé, D. (2006). Fast Anisotropic Smoothing of Multi-Valued Images using Curvature-Preserving PDE's. International Journal of Computer Vision, 68(1): 65-82.

Ulusoy, I. et C. Bishop (2005). Generative versus discriminative methods for object recognition. Proc. IEEE Conf. on Computer Vision and Pattern Recognition, CVPR'2005, San Diego, Californie, juin.

Wright, P. J., P. Fallon-Cousins et J. D. Armstrong (2001). The relationship between otolith accretion and resting metabolic rate in juvenile Atlantic salmon during a change in temperature. Journal of Fish Biology, 59(3): 657 - 666.

Xia, G.-S., J. Delon et Y. Gousseau (2010). Shape-based invariant texture indexing. International Journal of Computer Vision, 88(3): 382-403.

Xu, Y., H. Ji et C. Fermuller (2009). Viewpoint invariant texture description using fractal analysis. International Journal of Computer Vision, 83(1): 85-100.

Yang, J., Z. Jin, J. Y. Yang, D. Zhang et A. F. Frangi (2004). Essence of kernel Fisher discriminant: KPCA plus LDA. Pattern Recognition, 37(10): 2097-2100.

Younes, L. (2000). Optimal matching between shapes via elastic deformations. Image and Vision Computing, 17(5): 381-389.

Zhang, D. et G. A. Lu (2003). Comparative study of curvature scale space and fourier descriptors for shape-based image retrieval. Visual Communication and Image Representation, 14(1): 41-60.

Zhang, J., M. Marszalek, S. Lazebnik et C. Schmid (2007). Local features and kernels for classification of texture and object categories: a comprehensive study. International Journal of Computer Vision, 73(2): 213-238.

ANNEXES

A Curriculum vitae

Ronan Fablet — Maître de Conférence, TELECOM Bretagne/UMR 3192 LabSTICC
37 ans, 3 enfants

Diplômes

1998-2001 : Doctorat en Traitement du signal, Univ. de Rennes I/IRISA
1996-1997 : DEA de Mathématiques Appliqués, SUPAERO/Université Paul Sabatier
1997-1994 : ingénieur SUPAERO

Parcours professionnel

2010-2011 : Séjour d'étude au sein du LMI DISCOH (IRD-IMARPE, Lima, Pérou)
Depuis 2008 : Maître de Conférence à Telecom Bretagne/UMR 3192 LabSTICCC
2002-2008 : Chercheur à l'Ifremer département Sciences et Technologies Halieutiques
2001-2002 : Postdoctorat à Brown University (USA), Computer Science Departement
1997-1998 : Assistant de recherche et d'enseignement à l'Ecole Navale

Expérience d'enseignement et formation

Domaines : probabilités, traitement du signale et des images, informatique
Types de formation : cycle ingénieur, master II recherché, formation continue

Expérience de montage et de coordination projet de recherche

FI2O, 2009-2012, projet CREATE Région Bretagne, 3 partenaires, aide : 180kE
OTOCAL, 2005-2008, ANR Jeune Chercheur, 4 partenaires, aide ANR : 150kE
AFISA, 2007-2008, projet européen STREP 7 partenaires, aide UE : 600kE
ITIS/ACSYS, 2007-2008, projet « pôle Mer »/DGE , 5 partenaires, aide DGE: 350kE

Publications

Nombre de publications dans des journaux avec comité de lecture: 37
Nombre de publications dans des conférences internationales avec comité de lecture: 52
Sélection de publications représentatives:

R. Fablet, L. Pecquerie, H. de Pontual, H. Hoie, R. Millner, H. Mosegaard, S.A.L.M Kooijman. Shedding light on fish otolith biomineralization using a bioenergetic approach. PLOS One, 2011.
I. Karoui, R. Fablet, J.M. Boucher, J.M. Augustin. Variational region-based segmentation using multiple texture statistics. IEEE Trans. on Image Processing, 30(3):3146-3156, 2011.
H.-G. Nguyen, R. Fablet, J.M. Boucher. Visual textures as realizations of multivariate log-Gaussian Cox processes, IEEE Conf. on Computer Vision and Pattern recognition, CVPR'2011, Colorado Springs, juin 2011.
Pecquerie, R. Nisbet, R. Fablet, A. Lorrain, S.A.L.M. Kooijman. The impact of metabolism on stable isotope dynamics: a theoretical framework. Phil. Trans. Roy. Soc. B: Biological Sciences, 2010.
R. Fablet, S. Pujolle, A. Chessel, A. Benzinou, F. Cao 2D Image-based reconstruction of shape deformation of biological structures using a level-set representation. Comp. Vision and Image Understanding, 111(3):295-306, 2008.
R. Fablet et P. Bouthemy. Non parametric motion recognition using temporal multiscale Gibbs models. IEEE Trans. on Pat. Anal. and Machine Intelligence, 25(12):1619-1624, décembre 2003.

Divers

Prix de la meilleure communication en reconnaissance des formes et traitement d'images au symposium Otolith Research and Applications, 2004.
Prix AFRIF 2002 de l'Association Française de Reconnaissance et d'Interprétation des Formes

B Activités d'enseignement

Formations dispensées

2002-2007	Formation d'ingénieur de l'ENIB, 5ème année ▪ Interventions dans le cadre du module de vision par ordinateur ▪ 6h/an ▪ Master II IUEM Sciences de la mer et du littoral ▪ Intervention dans le cadre du module Enregistrements biologiques ▪ 4h/an Formation continue dans le cadre des activités du département Ifremer/STH ▪ Formation Ifremer/IRD en sclérochronologie, intervention pour le volet Image & TNPC, 10 pers., Brest, septembre 2005. ▪ Formation Ifremer TNPC, organisation et intervention, public : experts Ifremer en estimation d'âge, 15p., Brest, octobre 2005. ▪ Formation de chercheurs et techniciens au traitement numérique des pièces calcifiées dans le cadre des missions du LASAA (3/4 stagiaires par an)
2008-actuellement	Formations dispensées : ▪ Formation d'ingénieur de l'ENIB (cf. supra) ▪ Formation d'ingénieur généraliste (FIG), Télécom Bretagne ▪ Formation d'ingénieur en partenariat (FIP), Télécom Bretagne ▪ Formations continues en traitement du signal, Télécom Bretagne Volume horaire : de l'ordre de 130h/an Répartition du volume horaire : ▪ Cours : 17h ▪ TD et TP : 65h ▪ Tutorat de projet en pédagogie active : 40h

Responsabilités d'enseignement

Depuis mon arrivée à TELECOM Bretagne en 2008, j'ai eu la responsabilité de mettre en place plusieurs modules d'enseignements dont notamment :

- Une formation continue en traitement du signal avancé (3,5 jours) couvrant l'analyse spectrale, l'analyse temps-fréquence, les modèles espace-état. Les aspects théoriques sont illustrés par des exemples pratiques sur différents types de signaux (e.g., signal de parole, suivi de cibles,…)
- Un module de vision par ordinateur en en 3ème année de la formation d'ingénieur généraliste (17h). Ce module vise à introduire les concepts et modèles mathématiques utilisés en vision par ordinateur (e.g., équations au dérivées partielles et approches variationnelles, notions d'invariance, filtrage particulaire) en s'appuyant plus particulièrement sur trois types d'application, la régularisation d'images, l'analyse de textures et l'analyse du mouvement dans des séquences d'images.

Je suis également investi dans la formation par projets dispensée à Télécom Bretagne à travers ma participation aux comités de pilotage des projets « Créativité » et « Gestion de Projet » de la formation d'ingénieur généraliste de Télécom Bretagne.

Depuis 2009, je suis en outre en charge de la coordination du domaine « Systèmes d'ingénierie des Télécommunications » de la formation d'ingénieur FIP de Télécom Bretagne. Ce domaine qui regroupe 5 UVs dispensés au cours de la première et deuxième année de cette formation a pour objectif de promouvoir une vision transversale des compétences et savoir-faire que doivent acquérir les élèves ingénieurs.

C Activités d'encadrement de la recherche

Encadrement de thèses soutenues

Imen Karoui	Segmentation par méthodes Markoviennes et variationelles des images texturées : application à la caractérisation des fonds marins ▪ Thèse débutée le 1er octobre 2003 et soutenue le 20 mars 2006 ▪ Université : Université de Rennes I ▪ Directeur de thèse : Jean-Marc Boucher, Telecom Bretagne ▪ Taux d'encadrement: 50% Imen Karoui est chercheur postdoctorante à l'Ifremer.
Anatole Chessel	Otolithes et vision par ordinateur: de la perception visuelle à une représentation des connaissances, ▪ Thèse débutée le 1er octobre 2004 et soutenue le 10 décembre 2007 ▪ Université : Université de Rennes I ▪ Directeur de thèse : Frédéric Cao, IRISA/INRIA Rennes ▪ Taux d'encadrement: 75% Anatole Chessel est chercheur postdoctorant à Gordon Institute.
Aurélie Jolivet	Contribution à la calibration de l'archive otolithe: extraction et analyse des informations structurelles et chimiques" ▪ Thèse débutée le 1er février 2006 et soutenue le 18 février 2009 ▪ Université : Université de Bretagne Occidentale ▪ Directeur de thèse : Yves-Marie Paulet, Univeristé de Bretagne Occidentale ▪ Taux d'encadrement : 50% Aurélie Jolivet est chercheur postdoctorant à l'IUEM. ○
Kamal Nasrredine	Analyse multimodalités et fusion d'information pour le décryptage de l'otolithe ▪ Thèse débutée le 1er octobre 2006 et soutenue le 9 novembre 2010 ▪ Université : Université de Bretagne Occidentale ▪ Directeur de thèse : Jean Le Bihan, ENIB ▪ Taux d'encadrement : 25% (Co-encadrement avec Abdesslam benzinou, ENIB) Kamal Nasrredine est Maître de Conférence à l'ENIB.
Riwal Lefort	Apprentissage et classification faiblement supervisée : application en acoustique halieutique" ▪ Thèse débutée le 1er octobre 2007 et soutenue le 29 novembre 2010 ▪ Université : Université Rennes I ▪ Directeur de thèse : Jean-Marc Boucher, Telecom Bretagne ▪ Taux d'encadrement : 50% Riwal Lefort est chercheur postdoctorant à l'IDIAP.
Giao Huu Nguyen	Caractérisation et modélisation invariante des textures visuelles : application à la cartographie des fonds marins ▪ Thèse soutenue le 29 octobre 2011 ▪ Université : Université Rennes I ▪ Directeur de thèse : Jean-Marc Boucher, Telecom Bretagne ▪ Taux d'encadrement : 50% Huu Giao Nguyen est chercheur postdoctorant à l'INRIA Grenoble.

Encadrement de thèses en cours

Emmanuel Autret	Caractérisation et modélisation de la régularité géométrique des dynamiques océaniques à méso-échelle ▪ Débutée le 1er octobre 2010 ▪ Université : Université Rennes I ▪ Directeur de thèse : Valérie Mombet, Univ. Rennes I ▪ Taux d'encadrement : 20%
Liyun He-Guelton	Analyse spatio-temporelle multi-échelle d'observations et simulations de l'océan à très haute résolution ▪ Thèse débutée le 1er octobre 2010 ▪ Université : Université Rennes I ▪ Directeur de thèse : Jean Tournade, Ifremer ▪ Taux d'encadrement : 40%
Bertrand Saulquin	Qualification de données satellitaires pour l'étude de tendances ▪ Débutée le 1er octobre 2010 ▪ Université : Université Rennes I ▪ Directeur de thèse : Grégoire Mercier, Telecom Bretagne ▪ Taux d'encadrement : 50%
Rocio Joo	Comment les interactions biotiques et les conditions environnementales déterminent les mouvements des prédateurs marins ? Une approche par modélisation bayésienne hiérarchique. ▪ Débutée le 1er octobre 2010 ▪ Université : Université Montpellier II ▪ Directeur de thèse : Arnaud Bertrand, IRD Sète ▪ Taux d'encadrement : 30%
Daniel Grados	Caractérisation et modélisation statistique multi-échelle des dynamiques subméso- et méso-échelle des composantes de u Système du Nord du Courant de Humboldt ▪ Débutée le 1er novembre 2011 ▪ Université : Université de Bretagne Occidentale ▪ Directeur de thèse : Ronan Fablet, Telecom Bretagne ▪ Taux d'encadrement : 40%

Encadrement d'ingénieur de recherche et post-doctorant

Silèye Ba	postdoctorant, projet FI20 (2009-)
Erwan Hascoët	ingénieur de recherche, projet ATSO (2010-2011)
Sebastien Carbini	postdoctorant, projet DEBSIM (2010)
Imen Karoui	ingénieur de recherche, projet ITIS (2008-2009)

Accueil de chercheurs et doctorants :

Chercheurs	Vicenç Parisi-Barabad, Professeur assistant, Université Polytechnique de Catalogne, 2005 (3 mois)
Doctorants	Dennis Lefkaditis, Doctorant, Univ. de Brighton, 2005 (une semaine) Paulo Duarte, Doctorant, DIMAR (Brésil), 2004 (un mois)

Encadrement de stagiaires

Stages de Master II recherche	N. Le Josse, stage Télécom Bretagne/Master II STIR de l'Université de Rennes I, avril-septembre 2003. Estimation automatique de l'âge des poissons par apprentissage statistique. A. Elmoden, stage ENIB/DEA UBO Signaux et Circuits, février-juin 2004, co-encadrement avec D. Leguen (ENIB). Détection a contrario multi-échelles de ruptures dans des signaux d'otolithes. A. Jolivet, stage ENSAR/DAA, avril-septembre 2004, co-encadrement avec H. de Pontual (Ifremer/STH/LASAA) et F. Largardère (CREMA). Relations entre croissance somatique, structure et composition microchimique de l'otolithe: approche expérimentale en mésocosme sur la sole du Golfe de Gascogne (Solea solea, L.). A. Chessel, stage DEA MVA ENS Cachan, avril-septembre 2004, co-encadrement avec F. Cao (IRISA). Analyse d'images faiblement contrastées : application à l'extraction de structures dans les images d'otolithes. N. Guerrot, stage ENIB/Master II UBO Sciences, Technologies et Santé, février-juin 2005, co-encadrement avec A. Benzinou (ENIB). Recalage de signaux 1D : application aux signaux d'otolithes. N. Courbin, stage de Master II en Océanographie, Université de Marseille, février-juin 2005, co-encadrement avec C. Mellon (Ifremer/HMT) et H. de Pontual (Ifremer/STH/LASAA). Méthode d'analyse quantitative des signaux structuraux sur les otolithes. Application aux merlus du golfe du Lion. G. Le Lan, stage Télécom Bretagne, avril-septembre 2010, co-encadrement avec D. Pastor. Classification dans des enregistrements acoustiques sous-marins. P. Gay, stage INSA Rouen, mars-juillet 2011, co-encadrement avec S. Peraltilla. Caractérisation de la distribution des bancs dans des échogrammes acoustique - application à la discrimination des populations d'anchois du Pérou.
Stages de fin d'étude d'école d'ingénieur	E. d'Angelo, stage SUPAERO, avril-août 2003, co-encadrement avec F. Cao (IRISA). Extraction a contrario de structures géométriques dans les images d'otolithes. G. Foucault, stage ENIB, février-juin 2004. Acquisition automatique de séries d'images de pièces calcifiées. S. Pujolle, Mastère Télécom Bretagne, avril-septembre 2005. Extraction dense de champs d'orientation et reconstruction de la morphogenèse de l'otolithe. P. Cauchy, stage Ecole Centrale de Marseille, avril-septembre 2006, co-encadrement avec C. Scalabrin (Ifremer/STH/LTH). Apprentissage faiblement supervisé pour la classification des échos sonars.

Participation à des jurys de thèse

Imen Karoui	Segmentation par méthodes Markoviennes et variationelles des images texturées : application à la caractérisation des fonds marins, Université de Rennes I, le 20 mars 2006. (examinateur)
Anatole Chessel	Otolithes et vision par ordinateur: de la perception visuelle à une représentation des connaissances, Université de Rennes I, le 10 décembre 2007. (examinateur)
Aurélie Jolivet	Contribution à la calibration de l'archive otolithe: extraction et analyse des informations structurelles et chimiques, Université de Bretagne Occidentale, le 18 février 2009. (examinateur)
Riwal Lefort	Apprentissage et classification faiblement supervisée : application en acoustique halieutique, Université de Rennes I, le 29 novembre 2010. (examinateur)
Giao Huu Nguyen	Caractérisation et modélisation invariante des textures visuelles : application à la cartographie des fonds marins, Université Rennes I, le 29 octobre 2011. (examinateur)

D Activités d'administration de la recherche

Responsabilité de projets nationaux et européens

2005-2008	***OTOCAL (Projet ANR Jeune Chercheur, L'otolithométrie au service de l'écologie marine: approche mécaniste et modélisation numérique de l'archive biologique)*** Thématique : développement d'outils de calibration et modélisation numérique de la formation de l'otolithe Partenaires et collaborateurs du projet : Ifremer, CSM, ENIB/RESO, LASAA LEMAR, Institut Pasteur, LPEC, Univ. Paris XI Valorisation : rapport d'étude, publications, thèse de A. Jolivet (2006-2009). Implication dans le projet : montage et coordination du projet.
2006-2008	***AFISA (Automated Fish Ageing) [2007-2008]*** Thématique : Développement d'un système logiciel opérationnel d'estimation automatique de l'âge des poissons à partir des images d'otolithes Partenaires et sous-traitants : AZTI, CEFAS, DIFRES, Ifremer (LASAA), IMR, MRI, UPC (partenaires); ENIB, NOESIS (sous-traitants) Valorisation : logiciels, publications. Implication dans le projet : montage et coordination du consortium pour la réponse à l'appel d'offre européen (2006), coordination du projet (2007-2008)
2007-2010	***ITIS (Instrumentation & Technologie Innovantes au service du développement durable du Secteur halieutique)*** Thématique : Développement de systèmes innovants de capture durable Partenaires : IPSIS, iXtrawl, Le Drezen (partenaires indutriels), Telecom Bretagne, Ifremer/STH-NSE-TSI, IMP, IRD/ACAPELLA (partenaires académiques), CRPMEM Bretagne (représentant des professionnels de la pêche) Valorisation : logiciels, rapports d'étude, publications, postdoctorat I. Karoui (2008). Implication dans le projet : coordination du consortium pour le montage du dossier de labellisation par le pôle MER et du dossier de financement FCE (Fonds de Compétitivité des Entreprises) (2005-2006), coordination Ifremer du projet (2007-2009)
2009-2012	***FI2O (Projet Région Bretagne CREATE, Fouille de données intelligente dans les bases d'observation de l'océan) [2009-2012]*** Thématique : développement d'outils de fouille de données pour l'exploitation des bases d'observations de l'océan Partenaires et collaborateurs du projet : Ifremer, Telecom Bretagne, LIAMA Valorisation : rapports d'étude, publications, postdoctorat S. Ba (2009-). Implication dans le projet : montage et coordination du projet.
2010-2012	***IFIG (Projet « Mobilité internationale » de l'Axe 5 de l'Europôle Mer, extraction d'Information et FouIlle dans les Grandes bases de données d'observation des écosystèmes marins)*** Thématique : développement d'outils de fouille de données pour l'exploitation des bases d'observations de l'océan Partenaires et collaborateurs du projet : Telecom Bretagne, LIAMA, LMI DISCOH Valorisation : publications. Implication dans le projet : montage et coordination du projet.

Participation à des projets européens

2002-2006	**TACADAR (Concerted Action Q5CA-2002-01891, Towards Accreditation and Certification of Age Determination of Aquatic Ressources)** Thématique : assurance qualité et contrôle qualité pour l'estimation de l'âge des poissons en routine Partenaires : principaux instituts européens de recherche en sciences halieutiques Valorisation : rapport. Implication dans le projet : participation à l'ensemble des workshops de l'action concertée.
2003-2006	**IBACS (QQLRT-2001-01610 Integrated Approach for Biological Basis of Age Determination of Commercially Important Species)** Thématique : caractérisation, compréhension et modélisation du processus de formations des structures calcifiées pour l'estimation de l'âge des poissons Partenaires : CEFAS, DIFRES, Ifremer, IMEDEA, Marlab, Univ. Bergen, UPC Valorisation : publications. Implication dans le projet : participation à la tâche 1 portant sur l'estimation automatique de l'âge à partir des images d'otolithe.

Contrats d'étude

2008-2009	**REGULISO** Thématique : étude de descripteurs de la régularité des iso-températures dans les images de température de surface. Valorisation : rapport d'étude, publications, postdoctorat de S. Ba. Implication dans le projet : coordination scientifique et administrative du contrat Financement : Ifremer
2009-2010	**ATSO** Thématique : Méthodes d'assimilation variationnelle pour l'analyse des observations de température de surface Valorisation : rapport d'étude, publications, postdoctorat de S. Ba et de E. Hascoët. Implication dans le projet : coordination scientifique et administrative du contrat Financement : Ifremer
2009-2010	**DEBSIM [2009-2010]** Thématique : Développement d'algorithmes de simulation 2D et d'inversion du modèle DEB-otolithe pour l'analyse et la reconstruction de traits de vie individuels Valorisation : rapport d'étude, postdoctorat de S. Carbini. Implication dans le projet : coordination scientifique et administrative du contrat Financement : Ifremer
2009-2010	**DETPAS** Thématique : Développement et évaluation de techniques de traitement du signal pour la détection passive de mammifères marins Valorisation : rapport d'étude, stage de fin d'étude de Télécom Bretagne. Implication dans le projet : coordination scientifique et administrative du contrat Financement : SERCEL
2010-2013	**QTEND** Thématique : Qualification de données satellitaires pour l'étude de tendances Valorisation : thèse de B. Saulquin (2010-2013) Implication: encadrement scientifique Financement : ACRI-ST

E Production et valorisation scientifique

Bilan de la production scientifique

Publications dans des revues internationales	37 (+ 5 soumissions)
Chapitres d'ouvrage	2
Communications dans des actes de conférences internationales avec comité de lecture	52
Communications dans des actes de conférences nationales avec comité de lecture	12
Autres communications dans des colloques nationaux et internationaux	36

Liste complète des publications

Manuscrit de thèse

- Modélisation statistique non paramétrique et reconnaissance du mouvement dans des séquences d'images ; application à l'indexation vidéo. R. Fablet. Thèse de l'Université de Rennes 1, mention Traitement du signal et télécommunication, Juillet 2001.

Chapitre de livre

- P. Gros, **R. Fablet** et P. Bouthemy - New descriptors for image and video indexing. - *State-of-the-Art in Content-Based Image and Video Retrieval,* H. Burkhardt, H.-P. Kriegel et R. Veltkamp (eds.), Kluwer Academic Publishers, 2001.
- R. Lefort, **R. Fablet**, J.-M. Boucher. Weakly supervised learning: application to fish school recognition. In New advances in Intelligent Signal Processing, Springer. 2012.

Publications dans des revues à comité de lecture

A1. **R. Fablet**, P. Bouthemy. Non-parametric scene analysis modelling for statistical retrieval with partial query - *Journal of Mathematical Imagining and Vision* - 14(3), 2001.

A2. **R. Fablet**, P. Bouthemy, P. Perez. Non Parametric Motion Characterization using Temporal Gibbs Models for Content-Based Video Indexing and Retrieval. IEEE Transactions on Image Processing, 11(4):393-407, 2002.

A3. **R. Fablet**, P. Bouthemy. Motion recognition using non parametric image motion models estimated from temporal and multiscale cooccurrence statistics. IEEE Trans. on Pattern Analysis and Machine Intelligence, 25(12):1619-1624, 2003.

A4. **R. Fablet,** N. Le Josse. Automated fish age estimation from otolith images using statistical learning. Fisheries Research, 72(2-3): 279-290, 2005.

A5. F. Cao, **R. Fablet**. Automatic morphological detection of otolith nucleus. Pattern Recognition Letters, 27(6): 656-666, 2006

A6. **R. Fablet**. Semi-local extraction of ring structures in images of biological hard tissues: application to the Bayesian interpretation of fish otoliths for age and growth estimation. Canadian Journal of Fisheries and Aquatic Science, 63(7): 1414-1428, 2006.

A7. **R. Fablet**. Statistical learning applied to computer-assisted fish age and growth estimation from otolith images. Fisheries Research, 81:219-228, 2006.

A8. **R. Fablet**, F. Daverat, H. de Pontual. Unsupervised Bayesian reconstruction of individual life histories from otolith signatures: case study of Sr:Ca transects of eel (Anguilla anguilla) otoliths. Canadian Journal of Fisheries and Aquatic Science. 64:152-165, 2007.

A9. N. Courbin, **R. Fablet**, C. Mellon, H. de Pontual. Are hake otolith macrostructures randomly deposited? Insights from an unsupervised statistical and quantitative approach applied to Mediterranean hake otoliths. ICES Jal of Marine Science. 64(6): 1191-1201, 2007.

A10. A. Chessel, R. Fablet, F. Cao. Computer vision and otolith : toward a model of the morphogenesis of accretionary processes. European series in applied and industrial mathematics - ESAIM, 2008, 22, pp. 150-154.

A11. I. Karoui, **R. Fablet**, J.M. Boucher, J.M. Augustin. Segmentation d'images sonar texturées par une approche variationnelle basée région. Traitement du Signal. 25(1-2), 73-85, 2008.

A12. I. Karoui, **R. Fablet**, J.M. Boucher, J.M. Augustin Similarity measure for the fusion of textural statistics: application to texture recognition and segmentation. Pattern Analysis and Applications, 11(3-4):425-434, 2008.

A13. **R. Fablet**, S. Pujolle, A. Chessel, A. Benzinou, F. Cao 2D Image-based reconstruction of shape deformation of biological structures using a level-set representation. Comp. Vision and Image Understanding, 111(3):295-306, 2008.

A14. A. Jolivet, J.-F. Bardeau, **R. Fablet**, Y.-M. Paulet, H. de Pontual. Understanding otolith biomineralization process: new insights on microscale spatial distribution of organic and mineral fractions from Raman micro-spectrometry. Analytical and Bioanalytical Chemistry, 392(3), 551-560, 2008.

A15. I. Karoui, **R. Fablet**, J.M. Boucher, J.M. Augustin. Seabed segmentation using optimized statistics of sonar textures. IEEE Trans. on Geoscience and Remote Sensing, 47(6):1621 - 1631, 2009.

A16. **R. Fablet**, A. Chessel,S. Carbini, A. Benzinou, H. de Pontual. Reconstructing individual shape histories of fish otoliths: a new image-based tool for otolith growth analysis and modeling. Fisheries Research, 2009, 96(2-3):148-159.

A17. S. Bourguignon, L. Berger, C. Scalabrin, **R. Fablet**, V. Mazauric. Methodological developments for improved bottom detection with the ME70 multibeam echosounder. ICES Jal of Marine Science. 66(6):1015-1022, 2009.

A18. **R. Fablet**, R. Lefort, I. Karoui, L. Berger, J. Massé, C. Scalabrin, J.M. Boucher. Classifying fish schools and estimating their species proportions in fishery-acoustic surveys. ICES Jal of Marine Science. 66(6):1136-1142, 2009.

A19. K. Nasreddine, A. benzinou, **R. Fablet**. Shape geodesics for the classification of calcified structures: beyond Fourier shape descriptors. Fisheries Research, 98(1-3):8-15, 2009.

A20. J.-M. Fromentin, B. Ernande, **R. Fablet**, H. de Pontual. Importance and future of individual markers for the ecosystem approach to fisheries. Aquatic living resources, 22(4):395-408, 2009.

A21. V.M. Trenkel, L. Berger, S. Bourguignon, M. Doray, **R. Fablet**, J. Massé, V. Mazauric, C. Poncelet, G. Quemener, C. Scalabrin, H. Villalobos. Overview of recent progress in fisheries acoustics made by Ifremer with examples from the Bay of Biscay. Aquatic Living Resources, 22(4):433-446.

A22. K. Nasreddine, A. benzinou, **R. Fablet**. Recalage de signaux et d'images: Application au décryptage d'archives biologiques marines. Traitement du Signal, 26(4), 255-268, 2009

A23. L. Pecquerie, R. Nisbet, **R. Fablet**, A. Lorrain, S.A.L.M. Kooijman. The impact of metabolism on stable isotope dynamics: a theoretical framework. Phil. Trans. Roy. Soc. B: Biological Sciences, 365(1557):3455-3468, 2010.

A24. I. Karoui, **R. Fablet**, J.M. Boucher, J.M. Augustin. Variational region-based segmentation using multiple texture statistics. IEEE Trans. on Image Processing, 30(3):3146-3156, 2011.

A25. K. Nasreddine, A. Benzinou, **R. Fablet**. Variational Shape Matching For Shape Classification and Retrieval. Pattern Recognition Letters, 31(12):1650-1657, 2010.

A26. F. Daverat, J. Martin, **R. Fablet**, C. Peycheran. Colonisation tactics of three temperate catadromous species, Eel Anguilla anguilla, mullet Liza ramada and flounder Plathychtys flesus, revealed by Bayesian multielemental otolith microchemistry approach. Ecology of Freshwater Fish. 20:42-51, 2010.

A27. R. Lefort, **R. Fablet**, J.-M. Boucher. Weakly supervised learning based on proportion labelling. Application to Fisheries acoustic. Pattern Recognition Letters. 31(12): 1650-1657 (2010).

A28. R. Lefort, **R. Fablet**, J.-M. Boucher. Classification faiblement supervisée: arbre de décision probabiliste et apprentissage iterative. Revue National de Traitement de l'Information, Special issue "Fouille de Données Complexes : données multiples". Sous presse.

A29. A. Jolivet, H. de Pontual1, M. Hervy, Y.-M. Paulet, **R. Fablet**. Preliminary observations of survival and growth of European hake in captivity. Aquaculture Research. Sous presse.

A30. Q.-T. Nguyen, **R. Fablet**, D. Pastor. Protein Interaction Hotspot Identification Using Sequence-based Frequency-derived Features. IEEE Trans. on Biomedical Engineering. Sous presse.

A31. R. Lefort, **R. Fablet**, L. Berger, J-M. Boucher. Spatial statistics of objects in 3D sonar image: application to fisheries acoustics IEEE Geoscience and Remote Sensing Letters. Sous presse.

A32. S.O. Ba, **R. Fablet**, E. Autret, B. Chapron. Statistical descriptors of ocean regimes from the geometric regularity of Sea Surface Temperature observations. IEEE Geoscience and Remote Sensing Letters. Sous presse.

A33. H.-G. Nguyen, **R. Fablet**, J.M. Boucher, A. Erhold. Keypoint-based analysis of sonar images: application to seabed recognition. IEEE Trans. on Geoscience and Remote Sensing. Sous presse.

A34. L. Pecquerie, **R. Fablet**, P. Petitgas, H. de Pontual, S. Bonhommeau, S.A.L.M. Koijman. Reconstructing individual food and growth histories from biogenic carbonates. Marine Ecology Progress Series. Sous presse.

A35. **R. Fablet**, L. Pecquerie, H. de Pontual, H. Hoie, R. Millner, H. Mosegaard, S.A.L.M Kooijman. Shedding light on fish otolith biomineralization using a bioenergetic approach. PLOS One, 6(11): e27055 (2011).

A36. D. Grados, **R. Fablet**, M. Ballón, N. Bez, R. Castillo, A. Lezama, A. Bertrand. Multiscale analysis of the spatial interactions between ecosystem components from acoustic survey data: application of the Northern SCH off Peru. Canadian Journal of Fisheries and Aquatic Science, sous presse.

A37. **R. Fablet**, P. Gay, S. Peraltilla, C. Peña, R. Castillo, A. Bertrand. Bags-of-Features for fish school cluster characterization in pelagic ecosystems: application to the discrimination of juvenile and adult anchovy clusters off Peru. Canadian Journal of Fisheries and Aquatic Science, accepté.

Articles soumis et en préparation

A38. F. Daverat, P. Morais, E. Dias, J. Martin, J. Babaluk, **R. Fablet**, C. Peycheran, C. Antunes. Plasticity of European flounder life history patterns discloses alternatives to catadromy. Marine Ecology Progress Series. En révision.

A39. R. Lefort, **R. Fablet**, J.-M. Boucher. Learning with prior information: iterative methods and soft decision trees. Soumis.

A40. H. de Pontual, A. Jolivet, M. Bertignac, **R. Fablet**. How does European hake Merluccius merluccius move? In what thermal environment? Insights from a pilot archival tagging experiment. Soumis.

A41. S. Bertarand, R. Joo, **R. Fablet**. Do foragers move Lévy or not? Let Generalized Pareto model decide. Soumis.

A42. S.O. Ba, B. Chapron, T. Corpetti, **R. Fablet**. Variational data assimilation for missing data interpolation in series of sea surface temperature observations. Soumis.

A43. **R. Fablet**, A. Chaigneau, Y. Tremblay, H. Weimerkirsch, S. Bertrand. Multiscale analysis of seabird GPS trakcs. En préparation.

A44. H.-G. Nguyen, **R. Fablet**, J.M. Boucher. Spatial statistics of keypoints for visual texture recognition. En préparation.

A45. R. Joo, **R. Fablet**, S. Bertrand. Bayesian reconstruction of fishermen activities from VMS data. En préparation.

Communications dans des conférences internationales avec comité de lecture

C1. **R. Fablet** et P. Bouthemy – Motion characterization from temporal cooccurrences of local motion-based measures for video indexing. - 13th IAPR Int. Conf. on Pattern Recognition, ICPR'98, août 1998, Brisbane.

C2. **R. Fablet,** P. Rostaing et C. Collet - Motion segmentation and cloud tracking on noisy infrared image sequences. - SPIE Conf. on Visual Communications and Image Processing, VCIP'99, janvier 1999, San Jose.

C3. **R. Fablet** et P. Bouthemy – Motion-based feature extraction and ascendant hierarchical classification for video indexing and retrieval. -4th Int. Conf. on Visual Information Systems, VISUAL'99, LNCS Vol. 1614, juin 1999, Amsterdam.

C4. **R. Fablet**, P. Bouthemy et M. Gelgon - Moving object detection in color image sequences using region-level graph labeling. - 6th Int. Conf. on Image Processing, ICIP'99, octobre 1999, Kobe.

C5. **R. Fablet,** P. Bouthemy et P. Pérez –Statistical motion-based video indexing and retrieval. - 6ème conf. int. Sur la Recherche d'Information Assistée par Ordinateur, RIAO'2000, avril 2000, Paris.

C6. **R. Fablet** et P. Bouthemy – Statistical motion-based object indexing using optic flow fields. - 5th IAPR Int. Conf. on Pattern Recognition, ICPR'2000, septembre 2000, Barcelona.

C7. **R. Fablet** et P. Bouthemy – Statistical motion-based retrieval with partial query. -4th Int. Conf. On Visual Information Systems, VISUAL'2000, LNCS Vol. 1929, novembre 2000, Lyon.

C8. A. Benzougar, P. Bouthemy et **R. Fablet.** -MRF-based moving object detection from MPEG coded video. - IEEE Int. Conf. on Image Processing, 8th ICIP'2001, octobre 2001, Thessalonique.

C9. **R. Fablet** et P. Bouthemy – Motion recognition using spatio-temporal Random Walks in Sequence of 2D Motion-Related Measurements. - 8th IEEE Int. Conf. on Image Processing, ICIP'2001, octobre 2001, Thessalonique.

C10. **R. Fablet** et P. Bouthemy - Non parametric motion recognition using temporal multiscale Gibbs models - *IEEE Conf. Computer Vision and Pattern Recognition, CVPR'2001*, décembre 2001, Hawaii.

C11. **R. Fablet**, M. Black Automatic detection and tracking of human motion with a view-based representation. LNCS 2350, 476-491, Proc. Eur. Conf. on Computer Vision, ECCV'2002, Copenhaguen, mai 2002.

C12. **R. Fablet**, P. Bouthemy Segmentation of regions of interest in images from non-parametric statistical modelling of motion activity. Proc. of 9th Int. Conf. on Information Processing and Management of Uncertainty in Knowledge-Based Systems, IPMU'2002, Annecy, juillet 2002.

C13. **R. Fablet**, A. Benzinou, C. Doncarli. Robust time-frequency model estimation in otolith images for fish age and growth analysis. Proc. of 10th IEEE Int. Conf. on Image Processing, ICIP'2003, vol.3, pp593-596, Barcelona, septembre 2003.

C14. F. Rousseau, **R. Fablet**, C. Barillot. Robust Statistical Registration of 3D Ultrasound Images Using Texture Information. Proc. of 10th IEEE Int. Conf. on Image Processing, ICIP'2003, vol.1, pp581-584, Barcelona, septembre 2003.

C15. F. Cao, P. Bouthemy, **R. Fablet**. Automatic morphological detection of otolith nucleus. 17th Int. Conf. on Pattern Recognition, ICPR'2004, vol.4, pp606-609, Cambridge, UK, août 2004.

C16. **R. Fablet**, N. Le Josse, A. Benzinou. Automatic fish ageing from otolith images using statistical learning. Proc. of 17th IAPR Int. Conf. on Pattern Recognition, ICPR'2004, vol.3, pp503-506, Cambridge, UK, août 2004.

C17. I. Keraoui, J.-M. Boucher, **R. Fablet**, J.-M. Augustin. Multiscale segmentation of textured sonar images using cooccurrence statistics. Proc. of 11th IEEE Int. Conf. on Image Processing, ICIP'2004, vol.3, pp1691-1694, Singapore, octobre 2004.

C18. I. Karoui, J.-M. Boucher, **R. Fablet**,J.-M. Augustin. Segmentation multi-échelle d'images sonar. 2nd Int. Symp. on Image and Video Communications over fixed and mobile networks, ISIVC'2004, juillet, Brest, France, 2006.

C19. R. Fablet, J.-M. Augustin, A. Isar. Speckle denoising using a variational multi-wavelet approach. IEEE Conf. Oceans 2005, vol.1, pp539-544, Brest, juin 2005.

C20. I. Keraoui, J.M. Boucher, R. Fablet, J.-M. Augustin. Statistical discrimination of seabed textures in sonar images using cooccurrence statistics. IEEE Conf. Oceans 2005, vol.1, pp605-610, Brest, juin 2005.

C21. R. Fablet. Extraction and interpretation of ring structures in images of biological hard tissues: application to fish age and growth estimation. Proc. of 12th IEEE Int. Conf. on Image Processing, ICIP'2005, vol.3, pp830-833, Genoa, septembre 2005.

C22. **R. Fablet,** J.-M. Augustin and A. Isar. Multi-wavelet variational image denoising. Proc. of 12th IEEE Int. Conf. on Image Processing, ICIP'2005, vol.3, pp305-308, Genoa, septembre 2005.

C23. **R. Fablet,** J.-M. Augustin. Unsupervised calibrated sonar imaging for seabed observation using hidden Markov Random fields. Proc. of IEEE Int. Conf. on Acoustics, Speech and Signal Processing, ICASSP'2006, vol.2, pp817-820, Toulouse, mai 2006.

C24. I. Karoui, **R. Fablet**, J.-M. Boucher, J.-M. Augustin. Region-based image segmentation using texture statistics and level-set methods. Proc. of IEEE Int. Conf. on Acoustics, Speech and Signal Processing, ICASSP'2006, vol.1, pp693-696, Toulouse, mai 2006.

C25. I. Karoui, **R. Fablet,** J.-M. Boucher, J.-M. Augustin. Region-based and incidence angle dependent segmentation of seabed sonar images using a level-set approach combined to local texture statistics. IEEE Ocean Confe., OCEAN'06, Singapore, mai 2006. ***[2ème prix du meilleur papier d'étudiant de la conférence OCEAN'06]***

C26. I. Karoui, **R. Fablet**, J.-M. Boucher, J.-M. Augustin. Separability-Based Kullback Divergence Weighting and Filter Selection for Texture Classification and Segmentation. 18th IAPR Int. Conf. on Pattern Recognition, ICPR'2006, Hong-Kong, août 2006.

C27. A. Chessel, **R. Fablet**, F. Cao and C. Kervrann. Orientation Interpolation and Applications. Proc of 13th IEEE Int. Conf. on Image Processing, ICIP'2006, Atlanta, octobre 2006.

C28. **R. Fablet**, S. Pujolle, A. Chessel, A. Benzinou, F. Cao. Variational level-set reconstruction of accretionary morphogenesis from images. Proc. of 13th IEEE Int. Conf. on Image Processing, ICIP'2006, Atlanta, octobre 2006.

C29. A. Chessel, F. Cao, **R. Fablet**. Interpolation of orientation: an axiomatic approach. LNCS 3954, 241-254, Proc. European Conference on Computer Vision, ECCV06, Graz, mai 2006.

C30. I. Karoui, **R. Fablet**, J.-M. Boucher, J.-M. Augustin. Segmentation de textures par une approche combinée contours actifs basés région et distributions de co-occurrence. 3rd Int. Symp. on Image and Video Communications over fixed and mobile networks, ISIVC'2006, September, Hammamet, Tunisia, 2006

C31. I. Karoui, **R. Fablet**, J.-M. Boucher, J.-M. Augustin. Unsupervised region-based image segmentation using texture statistics and level-set methods. IEEE Int. Symp. on Intelligent Signal Processing, WISP'2007, Madrid, octobre 2007.

C32. A. Chessel, **R. Fablet**, C. Kervrann, F. Cao. Otolith image by computer vision: extraction growth rings and recovering shape evolution of accretionary structures. Int. Conf. on Bio-Inspired Signal Processing Systems, Biosignal 2008, janvier 2008.

C33. K. Nasrredine, A. Benzinou, **R. Fablet**. Non-rigid registration of fish otolith images. 8th IASTED Int. Conf. on Visualization, Imaging and Image Processing, VIIP'2008, Mallorca, septembre 2008.
C34. K. Nasrredine, A. Benzinou, **R. Fablet**. Non-Rigid Registration Of Shape Sequence Images: Applications To Biological And Medical Images. 9th Int. Conf. on Signal Processing, ICSP'08, Beijing, octobre 2008.
C35. I. Karoui, **R. Fablet**, J.-M. Boucher. Fast marching and acoustic descriptors based method for fish proportion interpolation. IEEE Conf. OCEANS'2008, Quebec, septembre 2008.
C36. R. Lefort, **R. Fablet**, J.-M. Boucher, L. Berger, S. Bourguignon. Automatic fish school classification for acoustic sensing of marine ecosystem. IEEE Conf. OCEANS'2008, Quebec, septembre 2008.
C37. **R. Fablet**, R. Lefort, C. Scalabrin, J. Massé, J.-M. Boucher. Weakly Supervised Learning Using Proportion-Based Information: An Application to Fisheries Acoustics. Int. Conf. on Pattern Recognition, ICPR'2008, Tampa, FL, décembre 2008.
C38. R. Lefort, **R. Fablet**, J.-M. Boucher. Combining image-level and object-level inference for weakly supervised object recognition. Application to fisheries acoustics. Proc. 16th Int. Conf. on Image Processing, ICIP'2009, Cairo, Egypt, novembre 2009.
C39. K. Nasrredine, A. Benzinou, **R. Fablet**. Shape Geodesics For Boundary-Based Object Recognition and Retrieval. Proc. 16th Int. Conf. on Image Processing, ICIP'2009, Cairo, Egypt, novembre 2009.
C40. R. Lefort, **R. Fablet**, J-M. Boucher. Weakly supervised classification with bagging in fisheries acoustics. IEEE International symposium on Intelligent Signal Processing, WISP'2009, Budapest, Hungary, août 2009.
C41. Z. Bouhroum, T. Chonavel, **R. Fablet**. Target tracking in the time-frequency domain for a driving aid application. 9th Int. Conf. on Intelligent Transport Systems Telecommunication, ITST'2009, Lille, France, octobre 2009.
C42. H.-G. Nguyen, **R. Fablet**, J.-M. Boucher. Invariant descriptors of sonar textures from spatial statistics of local features. Proc. 35th Int. Conf. on Acoustics, Speech and Signal Processing, ICASSP'2010, Dallas, mars 2010.
C43. R. Lefort, **R. Fablet**, J.-M. Boucher. Weakly supervised learning with decision trees applied to fisheries acoustics. Proc. 35th Int. Conf. on Acoustics, Speech and Signal Processing, ICASSP'2010, Dallas, mars 2010.
C44. S. Ba, T. Corpetti, B. Chapron, **R. Fablet**. Variational data assimilation for missing data interpolation in SST images. IEEE Int. Geoscience and Remote Sensing Symp., IGARSS'2010, juillet 2010.
C45. S. Ba**, R. Fablet**, D. Pastor, B. Chapron. Descriptors for sea surface temperature front regularity characterization. IEEE Int. Geoscience and Remote Sensing Symp., IGARSS'2010, juillet 2010.
C46. S. Ba, **R. Fablet**. Variational front tracking in Sea Surface Temperature images. Proc. 16th Int. Conf. on Image Processing, ICIP'2010, Hong-Kong, septembre 2010.
C47. H.-G. Nguyen, **R. Fablet**, J.M. Boucher. Spatial statistics of visual keypoints for texture recognition. Proc. Eur. Conf. on Computer Vision, ECCV'2010, Heraklion, septembre. 2010.
C48. R. Lefort, **R. Fablet**, J.M. Boucher. Weakly supervised classification of objects in images using soft random forests. Proc. Eur. Conf. on Computer Vision, ECCV'2010, Heraklion, septembre 2010.
C49. H.-G. Nguyen, **R. Fablet**, J.M. Boucher. log-Gaussian Cox processes of visual keypoints for sonar texture recognition. Proc. 36th Int. Conf. on Acoustics, Speech and Signal Processing, ICASSP'2011, Prague, mars 2011.
C50. H.-G. Nguyen, **R. Fablet**, J.M. Boucher. Visual textures as realizations of multivariate log-Gaussian Cox processes, IEEE Conf. on Computer Vision and Pattern recognition, CVPR'2011, Colorado Springs, juin 2011.
C51. S. Ba**, R. Fablet.** Multi-resolution missing data interpolation in SST image series. Proc. 18th IEEE Int. Conf. on Image Processing, ICIP'2011, Brussels, Belgium, septembre 2011.
C52. H.-G. Nguyen, **R. Fablet**, J.M. Boucher. Multivariate log-Gaussian Cox models of elementary shapes for recognizing natural scene categories. Proc. 18th IEEE Int. Conf. on Image Processing, ICIP'2011, Brussels, Belgium, septembre 2011.

Communications dans des conférences internationales

C53. **R. Fablet**. Combining the extraction of partial 2D rings within otolith images and statistical growth modeling for the Bayesian estimation of fish age and growth. 3rd international symposium on fish otolith research and application, Townsville, Australia, juillet 2004.
C54. **R. Fablet**, G. Foucault, F. Germain, H. Troadec. Automatic multiple acquisition of otolith images for routine aging 3rd international symposium on fish otolith research and application, Townsville, Australia, juillet 2004.
C55. **R**. **Fablet**, N. Le Josse. Statistical learning applied to fish age and growth analysis. 3rd international symposium on fish otolith research and application, Townsville, Australia, juillet 2004. ***[prix de la meilleure communication du symposium en traitement d'image]***

C56. **R. Fablet**, F. Daverat, H. de Pontual. How to Decode Individual Fish Movements Archived by Fish Otoliths? A Bayesian Perspective. 1st Int. Sclerochronology Conf., San-Petersburg, FL, juillet 2007.

C57. A. Jolivet, J.-F. Bardeau, H. de Pontual, **R. Fablet**. Characterization and Quantification of Organic and Mineral Contents of Fish Otoliths using Micro-Raman Spectrometry: Application to European Hake. 1st Int. Sclerochronology Conf., San-Petersburg, FL, juillet 2007.

C58. H. de Pontual, A. Jolivet, **R. Fablet**, M. Bertignac, Diel rhythm in diving behaviour of European hake and associated thermal changes revealed by archival tagging. 2nd Int. Symp. on tagging and tracking marine fish with electronic devices, San Sebastian, Spain, octobre 2007.

C59. **R. Fablet**, R. Lefort, P. Cauchy, C. Scalabrin, J. Massé, J.-M. Boucher. Probabilistic models for inferring species mixture from acoustic data in multi-specific environment. ICES Symp. on Ecosystem Approach with Fisheries Acoustics and Complementary technologies, SEAFACTS, juin 2008.

C60. L. Pecquerie, **R. Fablet**, A. Lorrain, E. Dufour, R. Nisbet, S.A.L.M. Kooijman. Modeling δ13C dynamics in soft tissues and calcified structures of aquatic organisms in the context of the Dynamic Energy Budget (DEB) theory. 6th Int. Conf. On Applications of Stable Isotope Techniques to Ecological Studies, IcoEcol VI, Honolulu, Hawaii, USA, août 2008.

C61. **R. Fablet,** L. Pecquerie, H. Hoie, A. Jolivet, R. Millner, H. Mosegaard, S.A.L.M. Kooijman, H. de Pontual. A DEB-based framework for analyzing individual life traits recorded by fish otoliths. DEB. International Symposium, Brest, avril 2009.

C62. A. Jolivet, J.F. Bardeau, **R. Fablet**, H. de Pontual,. Understanding otolith biomineralization process: new insights on spatial distribution of organic and mineral fractions from Raman micro-spectrometry. International Otolith Symposium, Monterrey, août 2009.

C63. **R. Fablet,** L. Pecquerie, H. Hoie, A. Jolivet, R. Millner, H. Mosegaard, S.A.L.M. Kooijman, H. de Pontual. Can we model otolith growth and opacity patterns as a response to environmental factors and fish metabolism? A DEB-based framework. International Otolith Symposium, Monterrey, août 2009.

C64. L. Pecquerie, **R. Fablet,** A. Lorrain, E. Dufour, S.A.L.M. Kooijman. Dynamics of d13C isotope ratio in fish otoliths and bivalve shells in the context of the Dynamic Energy Budget (DEB) Theory..International Otolith Symposium, Monterrey, août 2009.

C65. A. Lorrain, C. Poulain, L. Pecquerie, **R. Fablet**, Y.-M. Paulet, L. Chauvaud, D. Gillikin. Deepening our understanding of the delat-13C black box in biogenic carbonates through a comparative analysis of bivalve shells and otoliths. 2009 Portland GSA Annual Meeting Portland, Oregon, octobre 2009.

C66. Bertrand A., Ballón M., Chaigneau A., **Fablet R**., Graco M., Grados D., Monetti, F. & Paulmier. Towards new tools for OMZs and hypoxia detection (acoustical approach). Eur-Ocean conference on ocean desoxygenation. Toulouse, France octobre 24-26, 2011.

Autres communications

C67. **R. Fablet**, P. Bouthemy et M. Gelgon - Étiquetage statistique d'un graphe de régions pour la détection d'objets mobiles dans des séquences d'images couleur. - Actes du 17ème colloque Gretsi sur le Traitement du Signal et des Images, GRETSI'99, septembre 1999, Vannes

C68. **R. Fablet** et P. Bouthemy -Extraction d'attributs de mouvement et classification hiérarchique pour l'indexation vidéo par le contenu. *–Actes des journées francophones des jeunes chercheurs en analyse d'images et perception visuelle, ORASIS'99*, Aussois, avril 1999.

C69. P. Bouthemy, Y. Dufournaud, **R. Fablet**, R. Mohr, S. Peleg et A. Zomet -Video hyper-link creation for content-based browsing and navigation. - 1st Workshop on Content-Based Multimedia Indexing, octobre 1999, Toulouse.

C70. **R. Fablet** et P. Bouthemy – Modélisation statistique non paramétrique et reconnaissance du mouvement –Actes du Congrès sur la Reconnaissance des Formes et l'Intelligence Artificielle, RFIA'2002, janvier 2002, Angers. Cet article a reçu le prix AFRIF'02 de la meilleure communication en reconnaissance des formes du congrès RFIA'2002.

C71. C. Lacoste, **R. Fablet**, P. Bouthemy et J.F. Yao –Création de résumés de vidéos par une approche statistique –Actes du Congrès sur la Reconnaissance des Formes et l'Intelligence Artificielle, RFIA'2002, janvier 2002, Angers.

C72. A. Isar, **R. Fablet**, J.-M. Augustin. Multi-wavelet denoising for speckle removal in underwater sonar images. Symposimum on In situ sea bed characterization, SeaTech Week, Brest, octobre 2004.

C73. H. Yalcin, M. Black, **R. Fablet**. The Dense Estimation of Motion and Appearance. IEEE Workshop on Image and Video Registration, IVR'04, Washington, juin 2004.

C74. **R. Fablet**. Le traitement des images d'otolithes : application à l'estimation de l'âge et de la croissance. Workshop Mathématiques, Image et Gelstat, Berder, juin 2004.

C75. **R. Fablet**. Statistical learning for age and growth analysis from otolith images. Annual Workshop TACADAR (Towards Accreditation and Certification of Age Determination of Aquatic Ressources), Ancona, Italy, septembre 2004.

C76. **R. Fablet**. TNPC 4: digital processing of calcified structures for QA/QC. Annual Workshop TACADAR (Towards Accreditation and Certification of Age Determination of Aquatic Ressources), Ancona, Italy, septembre 2004.

C77. M. Bertignac, **R. Fablet**, O. Guyader, S. Mahévas, H. de Pontual, J.-C. Poulard. Le merlu dans le golfe de Gascogne : bilan et prospective. Colloque Defi Gascogne, Brest, 22-24 mars 2005.

C78. A. Chessel, **R. Fablet**, F. Cao. Fish otolith analysis via computer vision. 4ème forum JSPS (Japan Society for the Promotion of Science). Strasbourg, novembre 2005.

C79. J.M. Fromentin, B. Ernande, **R. Fablet**, H. de Pontual. Importance and future of individual markers for the ecosystem approach to fisheries. Colloque Approche Systémiques des Pêches, Boulogne, France, novembre 2008.

C80. A. Chessel, **R. Fablet**, C. Kervrann, F. Cao. Detection a contrario multi-modale de structures curvilineaire. 15ème Congrès Francophone AFRIF-AFIA de Reconnaissance des Formes et Intelligence Artificielle, RFIA'2008, Angers, janvier 2008.

C81. H. de Pontual A. Jolivet, F. Garren, M. Bertignac, **R. Fablet**,. First archival tagging on European hake: what have we learnt? Colloque Approche Systémiques des Pêches, Boulogne, France, novembre 2008.

C82. **R. Fablet**, J.F. Bardeau, A. Benzinou, A. Chessel, A. Jolivet, M. Labonne, A. Lorrain, Y.M. Paulet, V. Rodin, H. de Pontual. Understanding otolith biomineralization: from physico-chemical signatures to numerical modelling. Colloque Approche Systémiques des Pêches, Boulogne, France, novembre 2008.

C83. S. Carbini, A. Chessel, A. Benzinou, **R. Fablet**, K. Mahé, H. De Pontual. A review of image-based tools for automatic fish ageing from otolith features. Colloque Approche Systémiques des Pêches, Boulogne, France, novembre 2008.

C84. V.M. Trenkel, L. Berger, S. Bourguignon, **R. Fablet**, J. Massé, V. Mazauric, C. Scalabrin, H. Villalobos. Recent methodological progress in fisheries acoustics for studying fish stocks and communities with examples from the Bay of Biscay. Colloque Approche Systémiques des Pêches, Boulogne, France, novembre 2008.

C85. H.-G. Nguyen, **R. Fablet**, J.-M. Boucher.. Invariant texture descriptors based on spatial statistics Workshop on Advances in Seafloor-Mapping Sonar, novembre 2009.

C86. R. Lefort, **R. Fablet**, J-M. Boucher. Classification et apprentissage faiblement supervisé en acoustique halieutique. Actes du 22ème colloque Gretsi sur le Traitement du Signal et des Images, GRETSI 2009, septembre 2009, Dijon, France.

C87. Z. Bouhroum, T. Chonavel, **R. Fablet.** Suivi de cibles radar dans l'espace temps-fréquence par filtrage. Actes du 22ème colloque Gretsi sur le Traitement du Signal et des Images, GRETSI 2009, septembre 2009, Dijon, France.

C88. H.-G. Nguyen, **R. Fablet**, J.-M. Boucher. Statistiques spatiales de points d'intérêt pour la reconnaissance invariante de textures. 5ème Congrès Francophone AFRIF-AFIA de Reconnaissance des Formes et Intelligence Artificielle, RFIA'2008, Caen, janvier 2010.

C89. R. Lefort, **R. Fablet**, J.-M. Boucher. Méthodes d'apprentissage faiblement supervisé: arbres de classification et approche itérative. 5ème Congrès Francophone AFRIF-AFIA de Reconnaissance des Formes et Intelligence Artificielle, RFIA'2010, Caen, janvier 2010.

C90. S. Liberge, **R. Fablet**, S. Ba, P. Lenca. Prévision de trajectoires de cyclones à l'aide de forêts aléatoires avec arbres de regression. Conférence EGC 2011, Brest, janvier 2011.

C91. R. Lefort, **R. Fablet**, J.-M. Boucher. Apprentissage itératif pour une connaissance a priori des labels. 11ème Conf. Int. sur l'Extraction et la Gestion des Connaissances, EGC 2011, Atelier "Fouille de Données Complexes", Brest, janvier 2011.

C92. **R. Fablet**, A. Chaigneau, S. Bertrand. **Analyse multi-échelle de la géométrie des courbe planes.** 18ème Congrès Francophone AFRIF-AFIA de Reconnaissance des Formes et Intelligence Artificielle, RFIA'2012, Lyon, janvier 2012.

C93. S. Ba, T. Corpetti, **R. Fablet**. **Interpolation de données manquantes dans des séquences multi-modales d'images géophysiques satellitaires.** 18ème Congrès Francophone AFRIF-AFIA de Reconnaissance des Formes et Intelligence Artificielle, RFIA'2012, Lyon, janvier 2012.

Rapports

- **R. Fablet**, A. Ogor. Manuel utilisateur du logiciel TNPC 4. 45p. 2005.
- A. Ogor, **R. Fablet**. Manuel de formation au logiciel TNPC. 35p. 2005

Autres

- Article de vulgarisation – Montre-moi ton oreille….. je te dirai quel âge tu as. – Science Ouest (Recherche et Innovation en Bretagne), avril 2003.

Conférences invitées

C94. **R. Fablet** et P. Bouthemy -Spatio-temporal segmentation and general motion characterization for video indexing and retrieval. - 10th DELOS Workshop on Audio-Visual Digital Libraries, Santorin, juin 1999.
C95. **R. Fablet,** P. Bouthemy – Non parametric scene activity modelling for statistical retrieval with partial query –Mathematics and Image Analysis Workshop, MIA'00, Paris, septembre 2000.
C96. **R. Fablet,** P. Bouthemy – Non parametric scene activity modelling for statistical retrieval with partial query – Brown University, Comp. Science Dpt, février 2001.
C97. **R. Fablet** et P. Bouthemy - Statistical modeling for motion-based video classification and retrieval – Workshop on Multimedia content-Based Indexing and Retrieval, MMCBIR'2001, Rocquencourt, septembre 2001.
C98. **R. Fablet**. Acquisition, analysis and interpretation of multimodal signals extracted from calcified structures: structural information and CS interpretation from multimodal information. EFARO workshop on Otolith Research . Brest, décembre 2004.
C99. A. Chessel, **R. Fablet**, F. Cao. Vision par ordinateur et otolithes : vers une modélisation de la morphogenèse. 38ème congrès national d'analyse numérique, CANUM 2006, Guidel, FR, juin 2006.
C100. **R. Fablet.** Visual keypoints in sonar images: application to invariant seabed recognition. Workshop MOQESM, Monitoring Quantitatif de l'Environnement Sous-Marin, Brest, juin 2010.
C101. **R. Fablet** et al. Characterizing the spatial distribution of objects and local signatures in images: application to ocean sensing data. LIAMA (French-Chinese Computer Science and Applied Math. Lab.), Beijing, April 2010.
C102. **R. Fablet** et al. Characterizing the spatial distribution of objects and local signatures in images: application to ocean sensing data. Microsoft Research, Beijing, April 2010.
C103. **R. Fablet** et al. Tracking and characterizing temperature front regions in SST image series for the statistical analysis of oceanic regimes. Institute of Atmospheric Physics, Beijing, April 2010.
C104. **R. Fablet** et al. Texture-based classification of sonar images: visual keypoints and region-level segmentation. Thales Underwater Systems, Brest, France, June 2010.
C105. **R. Fablet** et al. Characterizing the spatial distribution of objects and local signatures in images: application to ocean sensing data. INICTEL (Peruvian Telecommunications Institute), Lima, Peru, Aug. 2011.
C106. **R. Fablet** et al. Characterizing the spatial distribution of objects and local signatures in images: application to ocean sensing data. INICTEL (Peruvian Telecommunications Institute), Lima, Peru, Aug. 2011.
C107. **R. Fablet** et al. Des fous croisant Humboldt à la géométrie multi-échelle des trajectoires et des images. UMR EME, Sète, France, Sept. 2011.

Autres activités

Evaluation d'articles de revue nationales et internationals : environ 5 articles par an
IEEE Trans. on Image Processing
IEEE Geoscience and Remote Sensing Letters
IEEE Trans. on Circuit System and Video Technology
Pattern Recognition Letters
Canadian Journal of Fisheries and Aquatic Sciences
Fisheries Research
Journal of Fish Biology
ICES Jal on Marine Science

Evaluation d'articles de conférences nationales et internationales : environ 20 articles par an
IEEE Conf. on Acoustics Speech and Signal Processing
IEEE Conf. on Image Processing
Colloque Gretsi sur le Traitement du Signal et des Image
Congrès Francophone AFRIF-AFIA de Reconnaissance des Formes et Intelligence Artificielle

Membre du comité d'organisation du colloque GRETSI 2013.
Membre du Conseil d'Administration de l'AFRIF (Association Française de Reconnaissance et d'Interprétation des Formes)

F Acronymes

Instituts et laboratoires

- **AZTI** : Instituto Tecnológico Pesquero y Alimentario, Pays Basque, Espagne
- **CEFAS** : Center for Environment, Fisheries and Aquatic Science, Royaume Uni
- **CEMAGREF** : Centre national du machinisme agricole, du génie rural, des eaux et des forêts
- **DIFRES** : Danish Institute for Fisheries Research, Danemark
- **ENIB** : Ecole Nationales des Ingénieurs de Brest
- **IDIAP** : Institut de recherche autonome lié à l'EPFL dans le domaine des technologies de l'information, Martigny, Suisse.
- **IEEE** : Institute of Electrical and Electronics Engineering
- **Ifermer** : Institut français pour l'exploitation de la mer
- **Ifremer/STH** : Département Science et Technologies Halieutiques, Ifremer Brest
- **Ifremer/LOS** : Laboratoire d'Océanographie Spatiale, Ifremer Brest
- **IMARPE** : Instituto del Mar del Peru
- **IMEDEA** : Institut Mediterrani d'Estudis Avançats, Espagne
- **IMR** : Institute for Marine Research, Norvège
- **IRD** : Insitut de Recherche pour le Développement
- **IRISA** : Institut de Recherche en Informatique et Systèmes Aléatoires, UMR CNRS-INSA Rennes-Univ. Rennes 1
- **LabSTICC :** Laboratoire de Sciences et Techniques de l'Information, de la Communication et de la Connaissance, UMR CNRS-UBO-UBS-Télécom Bretagne
- **LEMAR** : Laboratoire IUEM des Sciences de l'Environnement MARin, UMR CNRS-IRD-Univ. Bretagne Occidentale
- **LMI DISCOH** : Labratoire Mixte International "Dynamiques du système du Courant de Humboldt"
- **MRI** : Marine Research Institute, Islande
- **TOMS** : équipe Traitements, Observation et Méthodes Statistiques du LabSTICC
- **UBO** : Univesité de Bretagne Occidentale
- **UBS** : Université de Bretagne Sud
- **UPC** : Université Polytechnique de Catalogne

Programmes

- **ANR JC** : programme "Jeune Chercheur(se)" de l'Agence Nationale de la Recherche
- **FUI** : Fond Unifié Interministériel
- **CREATE** : programme CREATivitE et thématiques exploratoires de la Région Bretagne
- **UE STREP** : programme STREP (Specfic Targeted Research Project) du 6ème Programme Commun de Recherche et Développement de l'Union Européenne

www.telecom-bretagne.eu

Campus de Brest
Technopôle Brest-Iroise
CS 83818
29238 Brest Cedex 3
France
Tél. : + 33 (0)2 29 00 11 11
Fax : + 33 (0)2 29 00 10 00

Campus de Rennes
2, rue de la Châtaigneraie
CS 17607
35576 Cesson Sévigné Cedex
France
Tél. : + 33 (0)2 99 12 70 00
Fax : + 33 (0)2 99 12 70 19

Campus de Toulouse
10, avenue Edouard Belin
BP 44004
31028 Toulouse Cedex 04
France
Tél. : +33 (0)5 61 33 83 65
Fax : +33 (0)5 61 33 83 75

TELECOM Bretagne